IN-SITU VISCOELASTIC SOIL PARAMETER ESTIMATION USING LOVE WAVE INVERSION

by

Michael Wayne Morrison

A dissertation
submitted in partial fulfillment
of the requirements for the degree of
Doctor of Philosophy in Geophysics
Boise State University

May 2014

BOISE STATE UNIVERSITY GRADUATE COLLEGE

DEFENSE COMMITTEE AND FINAL READING APPROVALS

of the dissertation submitted by

Michael Wayne Morrison

Dissertation Title: In-Situ Viscoelastic Soil Parameter Estimation Using Love Wave Inversion

Date of Final Oral Examination: 11 April 2014

The following individuals read and discussed the dissertation submitted by student Michael Wayne Morrison, and they evaluated his presentation and response to questions during the final oral examination. They found that the student passed the final oral examination.

Paul Michaels, Ph.D.	Chair, Supervisory Committee
John Bradford, Ph.D.	Member, Supervisory Committee
Jodi L. Mead, Ph.D.	Member, Supervisory Committee
Joseph C. Guarino, Ph.D.	Member, Supervisory Committee
Nenad Gucunski, Ph.D.	External Examiner

The final reading approval of the dissertation was granted by Paul Michaels, Ph.D., Chair of the Supervisory Committee. The dissertation was approved for the Graduate College by John R. Pelton, Ph.D., Dean of the Graduate College.

To the daughters of Mnemosyne.

ACKNOWLEDGMENT

Of course, I must begin by thanking my graduate committee for the many hours that they have invested in me.

I am indebted to my graduate advisor, Dr. Paul Michaels, whose patience, good counsel, and occasional prodding have been essential to my success. It would be difficult to overstate the magnitude of Paul's contribution to the present work. Suffice it to say, his imprint can be found throughout the document. In particular, the method for reducing receiver walk-away data was Paul's idea. Long before I knew what a Geophysicist was, I met Paul when we were debating opposing sides of a continuing education resolution at an *Idaho Society of Professional Engineers* forum, and we have been bumping into each other ever since.

Dr. John Bradford's *Physics of the Earth* course at BSU convinced me to change careers and become a geophysicist. Dr. Jodi Mead's excellent course on inversion was foundational for the way that I approached the Love wave inversion problem. I drew heavily from the papers I wrote for her class when considering potential inversion methods.

I met Dr. Joe Guarino while taking a computational fluid dynamics course through BSU's mechanical engineering department, and he was very helpful getting me connected to a thing called the *cloud*. I was quite happy when he agreed to join my graduate committee. The problem he gave me during my comprehensive exams was an excellent introduction to vibrational modes.

It is not possible for me to name all of those whose encouraging words and kind acts have helped me along the way, but a few folks deserve some mention. Conversations with Dr. Grady Wright of BSU's math department led me to conjure-up the root finding method detailed in Chapter 4, and my understanding of soil mechanics and the relationships between soil properties was fostered by Dr. Arvin Farid. My friends Jeff, Deb, Sherri, Ernie, Bob, Betty, Brent, Janet, Vaughn, and Ellen have been steady sources of encouragement.

And of course, I must thank my dear wife, whose enthusiastic support has bordered on indulgence. I only hope that some day she will let me repay the favor.

AUTOBIOGRAPHICAL SKETCH

At the tender age of forty-eight, I was blessed with an opportunity to return to school, and pursue a goal I have had since I was an undergraduate student.

Like many my age, my scientific interests were piqued by the spectacle of men scooping-up rocks and dust while bouncing across the surface of Earth's moon. That interest was reinforced, a few years later, when a group of JPL geoscientists visited my elementary school bearing bits of moon rock for our inspection. They showed us how instruments left on the moon were used to detect meteorite impacts, and how seismic waves thus generated enabled a better understanding of the moon's structure.

In the ensuing years, my scientific interests broadened to include all of the natural sciences, as well as the technological uses to which scientific knowledge could be employed in service to humanity. I had originally wished to study Geology and Paleontology in college, but was sidetracked by a U.S. Air Force scholarship that required me to obtain an engineering degree. By dint of a delightfully tortuous career path, which included a stint as a B-52 bomber navigator, I found myself working in the semiconductor industry, where I was privileged to help develop the materials and gadgets of modern society. Twenty-one years later, my daughters had finished college, and I was pondering what I ought to do for the rest of my life. At the behest of my sister, and the cajoling of my indulgent wife, I opted to quit work and return to school.

I have always believed science to be an activity that is valuable for its own sake, and that it is made even more precious by its ability to provide goods and services that improve the human condition. Over the past several years, however, I have come to appreciate the importance of living in harmony with nature, accepting her limits, and viewing our little planet as more than just a repository of materials for exploitation. It is this realization, together with my long-standing interest in Earth's inner-workings, that prompted my decision to embark on a second career in the earth sciences. A belief that the knowledge, skills, and experience gleaned during my engineering career would be of greatest use when applied to the problems of geophysics led me to my second career choice.

ABSTRACT

Industry best practices for estimating viscoelastic soil properties employ either cross hole seismic surveys, or ex-situ laboratory testing. The former method can be costly, and its area of investigation limited to a few meters. The latter method samples only a tiny volume from the research area, and requires that samples be disturbed from their native condition. We investigated an alternative method that uses Love wave inversion to estimate layer geometry, shear modulus, and soil viscosity. We derived a method for determining the complex velocity of Love wave modes in horizontally layered viscoelastic media, and used the method to investigate the behavior and propagation of the Love wave fundamental mode and first three overtones in one, two, and three layered media. We studied the evolution of Love wave modes with increasing frequency, and found that roots representing the complex velocities of Love wave modes evolve in pairs, with one root originating from along the real axis, and the other root originating from along the imaginary axis. In all cases studied, we observed that only one root from each pair was expressed as a propagating wave.

The simultaneous propagation of multiple Love wave modes poses a challenge to their separation and analysis. We developed a technique for separating Love wave modes and used the information thus obtained to produce dispersion and attenuation relationships. We characterized the technique, and demonstrated its viability using synthetic data.

Using these dispersion and attenuation relationships, we used the Gauss-Newton inversion method to deduce best-fit layer property models. We investigated the method's sensitivity to constraints on model properties, and to the types of data used in inversion.

For a single-layer soil model, we found that the method gives reasonable estimates of layer thickness, shear modulus, and viscosity. For two and three-layer systems, we found it necessary to constrain layer thickness in order to obtain consistent estimates of shear modulus and velocity. We thus conclude that the Love wave method is best used for extending estimates obtained using crosshole or downhole information as a control.

In some cases, we found it difficult to ascertain, a-priori, which of the modes from each pair was manifested in the data. When the wrong root is chosen, the model may converge to erroneous soil property estimates. We recommend that future work be directed at developing techniques for ensuring that the correct root is used in the inversion model. So long as the correct root is used, Love wave inversion offers a viable in-situ method for estimating viscoelastic soil properties.

TABLE OF CONTENTS

ACKNOWLEDGMENT v

AUTOBIOGRAPHICAL SKETCH vii

ABSTRACT ix

LIST OF TABLES xvii

LIST OF FIGURES xviii

1 BACKGROUND AND HISTORICAL CONTEXT 1
- 1.1 Evolution of the Love Wave Analytical Model 3
- 1.2 Constitutive Soil and Rock Models 13
  - 1.2.1 Coulombic Soil Damping Models 14
  - 1.2.2 Viscoelastic Models 19
- 1.3 Testing Methods 25
  - 1.3.1 The Resonant Column Test 25
  - 1.3.2 In-Situ Methods 31
  - 1.3.3 Surface Wave Methods 35
- 1.4 The Need for Accurate Viscoelastic Soil Property Estimates 38

2 THE VISCOELASTIC SHEAR WAVE EQUATION 42
- 2.1 Choosing a Constitutive Soil Model 42
- 2.2 The Viscoelastic Equation of Motion 43

2.2.1 An Alternative Formulation of the Viscoelastic Wave Equation 46
2.2.2 Shear Wave Velocity and Wave Number Relationships 47
2.2.3 Viscoelastic Damping 48
2.3 The 2-D Viscoelastic Shear Equation for a Homogeneous Medium . . 50

3 LOVE WAVE PROPAGATION IN LAYERED VISCOELASTIC MEDIA 54
3.1 Introduction 54
3.2 The Shear Wave Equation for a Layered Viscoelastic Medium over a Half-Space 55
3.2.1 Propagator Matrix for a Layered Medium–$\boldsymbol{P(z_n, z_0)}$ 58
3.2.2 Propagator Matrices for a Half-Space and for an Arbitrary Depth–$\boldsymbol{P(z_\infty, z_n)}$ and $\boldsymbol{P(z, z_n)}$ 62
3.2.3 The Objective Function 64
3.2.4 Love Wave Velocity and Wave Number Relationships 65
3.3 Geometric Dispersion 66
3.3.1 The Wave Equation in Cylindrical Coordinates 67
3.3.2 Solution to the Wave Equation in Cylindrical Coordinates . . 69
3.3.3 Correction for Geometric Spreading 70
3.3.4 Finding Solutions to the Love Wave Equation 73

4 LOVE WAVE MODES IN LAYERED VISCOELASTIC SOILS 76
4.1 Single Elastic Layer over a Half-Space 76
4.1.1 Love Wave Modes and Depth Dependent Behavior 77
4.1.2 Elastic Scaling Relationships 81
4.2 Evolution of Complex Modes with Viscosity 82

4.3 Single Viscoelastic Layer over a Half-Space 87

4.3.1 Effects of Half-Space Viscosity 89

4.3.2 Viscoelastic Scaling Relationships 91

4.4 Two Layers over a Half-Space 92

4.4.1 Two Elastic Layers over a Half-Space 92

4.4.2 Two Viscoelastic Layers over a Half-Space 97

4.5 Three Layers over a Half-Space 102

4.5.1 Some Observations on Higher Order Modes 106

5 DATA COLLECTION AND REDUCTION 109

5.1 Partitioning Waveforms 110

5.2 Practical Considerations 112

5.2.1 Depth vs. Wavelength 112

5.2.2 Temporal and Spatial Resolution and Aperture 114

5.2.3 Measuring Attenuation 118

5.2.4 Near Field Considerations 120

5.3 Data Reduction 121

5.4 Synthetic Data and Data Reduction Methods 123

5.4.1 Synthetic Data 123

5.4.2 Reducing Source Walk-Away Data 124

5.4.3 Reducing Receiver Walk-Away Data 125

5.5 Results 127

5.5.1 One-Layer Model 128

5.5.2 Two-Layer Model 132

5.5.3 Three-Layer Model 134

5.6 Summary: Data Reduction 134

6 DATA INVERSION 137

6.1 Joint Inversion Using the Gauss-Newton Method 137

6.1.1 Estimating Error 141

6.1.2 Constraining Layer Thickness 141

6.2 Methods 145

6.2.1 Inversion Procedure 145

6.2.2 Characterization Models 147

6.3 Single Layer Property Estimates Using Only Fundamental Mode Data 148

6.3.1 Effects of Varying Half-Space Parameters 149

6.3.2 Effects of Model Bias 151

6.3.3 Models Using Only Dispersion Data 151

6.3.4 Models Using Only Attenuation Data 152

6.4 Single-Layer Property Estimates Using Several Modes 152

6.4.1 Joint Inversion of Dispersion and Attenuation Data 152

6.4.2 Sequential Inversion of Dispersion and Attenuation Data . . . 155

6.4.3 Notes on Single-Layer Inversion 155

6.5 Two-Layer Model 156

6.5.1 Two-Layer Model Using Only Dispersion Data 158

6.5.2 Using a One-Layer Model with Two-Layer Data and Vice Versa 158

6.5.3 Three-Layer Model 159

6.6 Parameter Error Estimates 160

6.7 Summary 161

7 CONCLUSIONS AND RECOMMENDATIONS FOR FURTHER RESEARCH 163

7.1 Lessons Learned 165

7.2 Recommendations for Further Research 167

7.3 Concluding Remarks 168

REFERENCES 169

APPENDICES 179

A FORWARD MODELING UTILITIES: DOCUMENTATION 179

A.1 Getting Started 179

A.2 LoveObjects 181

A.3 RootFinder 182

A.4 RootTracker 184

A.5 RootHunter 185

A.6 RootReports 187

A.7 FineRoot 189

A.8 PropagateZ 189

A.9 Propagate 190

A.10 Cauchy 191

A.11 SignalBuilder 191

B FORWARD MODELING MATLAB® CODE 194

B.1 About the Forward Modeling Utilities 194

B.2 LoveObjects 195

B.3 RootFinder 197

B.4 RootTracker 199

B.5 RootHunter 201

B.6 RootReport 203

B.7 FineRoot 205

B.8 PropagateZ 207

B.9 Propagate 210

B.10 Cauchy 212

B.11 SignalBuilder 213

C INVERSION UTILITIES: DOCUMENTATION 215

C.1 Getting Started 215

C.2 WigglePlot 216

C.3 Kfreq 217

C.4 FilePrep 218

C.5 Jacob 220

C.6 LoveInv 221

D INVERSION MATLAB® CODE 223

D.1 About the Inversion Utilities 223

D.2 WigglePlot 224

D.3 Kfreq 225

D.4 FilePrep 226

D.5 Jacob 228

D.6 LoveInv 230

LIST OF TABLES

5.1 Normalized amplitudes of the partition function. 111

5.2 Frequency ranges for low and high density lay-outs. 117

6.1 Parameter estimates for the two layer model using one, two, or all modes. 158

6.2 Reasonable viscosity estimates could be obtained using dispersion data, alone with two-layer data. 159

6.3 Parameter estimates for the three-layer using different types of constraint. 160

6.4 Typical standard deviations of estimated model parameters obtained from the model covariance matrix. 161

LIST OF FIGURES

1.1 Refraction Nomenclature 7

1.2 Relationship between shear wave velocity and apparent surface wave velocity 8

1.3 Phase shift in a post critical wave 10

1.4 Comparison of Coulombic and elastic models. 15

1.5 The Coulombic damping model and its hysteresis loop. 16

1.6 The elasto-plastic model and its hysteresis loop. 17

1.7 The Kelvin-Voigt model and its hysteresis loop. 20

1.8 Asymptotic behavior of a Kelvin-Voigt system 22

1.9 Maxwell viscoelastic model. 23

1.10 The KVMB (Kelvin-Voigt-Maxwell-Biot) system 24

1.11 Resonant Column Apparatus used by Ishimoto and Iida (1937). . . . 26

1.12 Resonant Column Apparatus (excerpted from ASTM-D-4015 (92)). . 29

1.13 Preferred borehole configuration for crosshole testing (excerpted from ASTM-D-4428(91)). 32

1.14 The seismic cone penetrometer test (SCPT). 34

1.15 Downhole test set-up and graphs 35

1.16 Idealized soil-structure system 39

1.17 Magnification factor versus frequency for an idealized viscoelastic system with a natural resonance frequency of 1 Hz. 40

2.1 Forces acting on a horizontal soil element. 43

2.2 Viscoelastic attenuation of a plane wave with different loss tangents. . 49
2.3 Coordinate system used in the derivation of shear and Love wave equations. 51

3.1 Nomenclature and layer properties for a single layer over a half-space 55
3.2 Nomenclature and layer properties for a layered system over a half-space 56
3.3 Coordinate system used in the polar coordinate derivation of the shear and Love wave equations. 67
3.4 Bessel function and an approximation using Equation (3.54). 71
3.5 Comparison between scaled Bessel function and cosine function . . . 72
3.6 The argument principle 73
3.7 Finding roots using the argument principle 75

4.1 Soil properties used to model a single elastic layer over a half-space. . 77
4.2 The motion stress vector versus depth 78
4.3 Elastic mode evolution with increasing frequency 80
4.4 Dispersion curves of the fundamental mode and first three overtones for a single elastic layer over a half-space (Figure 4.1). 81
4.5 Complex frequency plot for a purely elastic model 83
4.6 Effect of viscosity on complex velocity 84
4.7 The loss tangent is greater than unity when $C_i > C_r$. 86
4.8 Soil properties used to model a single viscoelastic layer over a half-space. 87
4.9 Viscoelastic mode evolution with increasing frequency (single layer over a half-space) 88
4.10 Dispersion curves for a single viscoelastic layer over a half-space. . . . 89

4.11 Attenuation as a function of frequency for a single viscoelastic layer over a half-space 90
4.12 Loss tangent as a function of frequency for a single viscoelastic layer over a half-space 90
4.13 Ray path in a two layer system 93
4.14 Soil properties used to model two elastic layers over a half-space. . . . 94
4.15 Mode evolution with frequency for two elastic layers over an elastic half-space 95
4.16 Motion-stress displacement component for two elastic layers over a half-space 96
4.17 Dispersion curves for two elastic layers over a half-space 97
4.18 Soil properties used to model two viscoelastic layers over a half-space. 98
4.19 Viscoelastic mode evolution with frequency (Two layers over a half-space). 99
4.20 Dispersion curves for two viscoelastic layers over a half-space 100
4.21 Attenuation as a function of frequency for two viscoelastic layers over a half-space 100
4.22 Loss tangent as a function of frequency for two viscoelastic layers over a half-space. 101
4.23 Soil properties used to model three viscoelastic layers over a half-space. 101
4.24 Love wave modes as a function of frequency for a three-layer elastic system (Figure 4.23). 102
4.25 Dispersion curves for three elastic layers over a half-space 103

4.26 Love wave modes as a function of frequency for a three-layer viscoelastic system 104
4.27 Dispersion curves for three viscoelastic layers over a half-space 105
4.28 Attenuation as a function of frequency for three viscoelastic layers over a half-space 105
4.29 Loss tangent as a function of frequency for three viscoelastic layers over a half-space 106
4.30 Higher order Love wave modes as a function of frequency for a three-layer viscoelastic system (Figure 4.23). 107

5.1 Source and receiver lay-out. 115
5.2 Gaussian white noise was added to the data from each trace. 123
5.3 Synthetic data shot gathers 124
5.4 Masking a K-f plot before converting to frequency-space domain . . . 126
5.5 Comparison of K-f plots from low and high density lay-outs. 127
5.6 Constant wave number *slices* obtained from Figure 5.5. 128
5.7 Expanded K-f plot of high density lay-out data. 129
5.8 Dispersion curves obtained from the low density lay-out. 130
5.9 Dispersion curves obtained from the high-density lay-out. 130
5.10 Attenuation curves from the low density lay-out. 131
5.11 Selected attenuation curves. 131
5.12 Attenuation curve obtained from fundamental mode. 132
5.13 Dispersion curves for synthetic two layer data. 133
5.14 Attenuation curves for two layer synthetic data. 133
5.15 Dispersion curves for three-layer synthetic data. 134

5.16 Attenuation curves for three layer viscoelastic data. 135

6.1 Convergence history for single mode data 150

6.2 Convergence history for inversion of all four modes 154

6.3 Convergence history for a two layer viscoelastic model. 157

LIST OF SYMBOLS

$\boldsymbol{A}$	Motion Stress Coefficient Matrix.
C^*	complex Love wave velocity $(\frac{\mathrm{m}}{\mathrm{s}})$.
C_r	real Love wave velocity component $(\frac{\mathrm{m}}{\mathrm{s}})$.
C_i	imaginary Love wave velocity component $(\frac{\mathrm{m}}{\mathrm{s}})$.
C_L	Love wave phase velocity component $(\frac{\mathrm{m}}{\mathrm{s}})$.
D	Damping factor for a viscous damping element $(\frac{1}{s^2})$.
DR	ASTM-D-4015 Damping Factor (Dimensionless).
DR_c	Damping factor used in the International Building Code (Dimensionless).
G_c	Frictional force on a Coulombic damping element (Nt).
G_e	Spring coefficient (Hooke's coefficient) $(\frac{Nt}{m})$.
G_v	Viscous force on a viscous damping element $(\frac{Nt}{m})$.
$\overline{h}$	Equivalent single layer thickness $(m.)$
h_j	Layer j thickness (m).
i	Imaginary Unit.
I_1 and I_2	Energy Integrals.
k^*	Complex shear angular wave number $(\frac{\mathrm{rad}}{\mathrm{m}})$.
K	Real cyclical shear wave number $(\frac{cycles}{s})$.
k_r	Real angular shear wave number $(\frac{\mathrm{rad}}{\mathrm{m}})$.
k_i	Imaginary angular shear wave number/attenuation coefficient. $(\frac{\mathrm{rad}}{\mathrm{m}})$,$(\frac{1}{m})$
K^*	Complex Love angular wave number $(\frac{\mathrm{rad}}{\mathrm{m}})$.
K_r	Real Love angular shear wave number $(\frac{\mathrm{rad}}{\mathrm{m}})$.
K_i	Imaginary Love angular shear wave number/attenuation coefficient. $(\frac{\mathrm{rad}}{\mathrm{m}})$,$(\frac{1}{m})$

$\boldsymbol{l_j}$	Layer j motion-stress vector.
l_{mj}	Layer j motion-stress vector displacement component.
l_{sj}	Layer j motion-stress vector stress component.
$\mathbf{m}, \hat{\mathbf{m}}, \Delta\mathbf{m}$	vector of model parameters, estimates, and differential values.
R(x)	Horizontal wave equation eigenfunction in Cartesian coordinates (x) direction.
L(z)	Wave equation eigenfunction for the vertical (z) direction.
$\boldsymbol{Q}$	Eivenvecor matrix of $\boldsymbol{A}$
s_d, s_u	Upward and downward propagation coefficients.
$S(r)$	Horizontal wave equation eigenfunction in cylindrical coordinates (r) direction.
T(t)	Wave equation eigenfunction for time (t).
t	Time.
u,v,w	Displacement in, respectively, x, y, and z directions.
U	Group velocity $(\frac{m}{s})$
v(x,y,t)	Horizontal (y) displacement function.
x	Ordinate in direction of wave propagation.
y	Transverse ordinate.
z	Vertical ordinate, measured from the surface.
α	p wave phase velocity $(\frac{\mathrm{m}}{\mathrm{s}})$.
α_L	Love Wave Attenuation Ratio $(\frac{rad}{m})$.
α_s	Shear Wave Attenuation Ratio $(\frac{rad}{m})$.
β^*	complex shear wave velocity $(\frac{\mathrm{m}}{\mathrm{s}})$.
β_i	imaginary shear wave velocity component $(\frac{\mathrm{m}}{\mathrm{s}})$.
β_r	real shear wave velocity component $(\frac{\mathrm{m}}{\mathrm{s}})$.
β_s	shear wave phase velocity $(\frac{\mathrm{m}}{\mathrm{s}})$.

$\Gamma(n, \omega)$	Partition Function.
ϵ	Error vector.
ε	Phase delay (rad)
λ_j	first Lamé Parameter (Pa), or spatial wave number $(1/m)$.
$\boldsymbol{\Lambda}$	Eigenvalue matrix of $\boldsymbol{A}$.
μ_j	Layer j shear modulus (Pa).
μ_j^*	Layer j complex shear modulus (Pa).
η_j	Layer j effective viscosity $(Pa - s)$.
ξ_s	shear waveattenuation ratio.
ξ_L	Love wave attenuation ratio.
ρ_j	Layer j density $(\frac{\mathrm{kg}}{\mathrm{m}^3})$.
$\tau_{j,k}$	Stress component.
ω	Angular frequency $(\frac{\mathrm{rad}}{\mathrm{s}})$.
ω_d	Damped resonant angular frequency $(\frac{\mathrm{rad}}{\mathrm{s}})$.
ω_0	Undamped resonant angular frequency $(\frac{\mathrm{rad}}{\mathrm{s}})$.

CHAPTER 1:

BACKGROUND AND HISTORICAL CONTEXT

Both the instrumentation and the theoretical apparatus for studying seismic waves evolved rapidly during the last two decades of the nineteenth century, and scientists were putting the devices to use exploring Earth's deep structure. By the nineteen twenties, it was widely recognized that Earth consisted of a solid inner core, surrounded by a liquid core, wrapped in a mantle, and covered with a thin outer crust. That the destructive power of earthquakes was primarily due to waves traveling through, and interacting with, this thin crustal layer was also generally accepted (Fowler, 2005).

Cogent explanations for the visible manifestations of an earthquake's destructive power were more problematic: A structure might be demolished, while a nearby structure might suffer little or no damage at all. By the late nineteen fifties, structural and geotechnical engineers had concluded that a structure's behavior in an earthquake could best be understood in terms of a resonant system, consisting of the structure and ground to which that structure is attached. Modern building codes reflect this understanding by requiring that critical structures be designed to withstand lateral loads caused by the resonant behavior of the earth-structure system.

Shear wave velocity is an important predictor of dynamic soil response, and the shear wave properties of the upper 30 meters of soil are used to predict the frequency spectrum and amplitude that a structure could expect to experience during an earthquake (ICC, 2000). Traditionally, measurements for these computations have been made using cross-borehole experiments as described in ASTM-D-4428 (1996). This method allows in-situ testing to determine shear wave velocities, but because it requires three or more bore holes, it can be expensive (Michaels, 1998).

In recent years, Spectral Analysis of Surface Waves (SASW) and Multi Channel Spectral Analysis of Surface Waves (MASW) have been promoted as economical alternatives to cross-borehole methods. SASW inverts Rayleigh wave dispersion curves to obtain a one dimensional profile of shear wave velocity versus depth. The MASW method extends SASW to two or three dimensions (Xia *et al.*, 1999). The use of Rayleigh waves, which effect both vertical and horizontal surface displacements, permits the use of relatively inexpensive vertical component geophones, which are in common use by geotechnical engineering companies; however, as noted earlier, Rayleigh waves are produced by the interaction of both compressional and shear waves, so shear wave velocity estimates can be biased by erroneous compressional velocity estimates.

A second important factor determining a site's earthquake response is internal friction, caused by intra-frame or fluid-frame interactions. Although an obvious source of attenuation, it is less obvious that internal friction will effect a shear wave velocity increase. Unlike shear wave velocity, which is typically studied in-situ, frictional effects are normally measured in a laboratory setting using a resonant column apparatus such as that described in ASTM-D-4015 (1996). Shear velocity and attenuation measurements thus obtained are usually interpreted using a modified Kelvin-Voigt viscoelastic model. Unfortunately, resonant column methods are limited to small soil samples that have been disturbed, and it is nearly impossible to conduct resonant column tests at the same conditions of stress and moisture experienced under field conditions, so laboratory results may not predict the actual behavior of soils, in-situ.

The advent of inexpensive horizontal-component geophones has made collection and inversion of shear wave data economically viable. In the present work, we will develop a novel method for estimating viscoelastic soil properties in-situ. Because Love wave velocity and attenuation are functions only of viscoelastic shear properties, Love wave inversion avoids the pitfalls that might result when erroneous compressional properties are included in Rayleigh wave inversion schemes such as SASW and MASW.

1.1 Evolution of the Love Wave Analytical Model

Love waves result from interactions of horizontally polarized shear waves, within a zone of low velocity material, near Earth's surface. Unlike Rayleigh waves, which arise from the interaction of vertically polarized shear waves with dilational waves at Earth's surface, Love wave behavior depends solely on material shear properties.

Poisson (1830) derived general equations for wave propagation in elastic media, and demonstrated that within a homogeneous, isotropic solid body, there exist two distinct propagation modes. Dilational wave propagation is parallel to particle motion, and its velocity is given by the relationship $\alpha = \sqrt{\frac{\lambda+2\mu}{\rho}}$. Shear wave propagation is perpendicular to the direction of particle motion, and its velocity is given by the relationship $\beta = \sqrt{\frac{\mu}{\rho}}$. Thus, dilational wave propagation is necessarily faster than shear wave propagation, and by the mid-19th century, the monikers primary (P) and secondary (S) were being used describe the order in which these waves manifest themselves in seismic instrumentation (Stokes, 1849).

Seismometers capable of detecting and recording wave patterns made their debut in 1889, and seismograms obtained from actual earthquakes followed a characteristic pattern: A weak preliminary tremor followed by a main shock. The causes of this pattern were the subject of scientific scrutiny through the first decades of the 20th century. Early on, it was believed that the preliminary tremor and main shock corresponded, respectively, to P and S waves; however, this simple description was soon abandoned (Love, 1911). Although seismologists were in general agreement that the earliest signals corresponded with the arrival of P waves at Earth's surface, neither the magnitudes nor the behavior of subsequent arrivals were consistent with S waves.

A potential explanation was given by Lord Rayleigh. In 1885, Rayleigh predicted the existence of surface waves, and described a means by which they could be generated through the interaction of P waves and vertically polarized S waves with the surface of an elastic body (Rayleigh, 1887). He demonstrated that these waves would travel somewhat more slowly than S-waves, and that unlike body waves, which decay directly with the distance from the source, Rayleigh's eponymous waves decay with the square root of distance. Thus, at long distances, Rayleigh waves could be much stronger than body waves. Rayleigh also predicted that these waves would manifest themselves through elliptical particle motion at the surface, providing a theoretical underpinning for some of the late motions observed in seismograms.

Rayleigh's theory was dependent on an earlier work by Lamb (1882), and Rayleigh himself noted that it was possible to derive his predictions using formulae derived in Lamb's paper on elliptical waves in elastic spheres. In his discussion, Rayleigh disputed Lamb's assertion that only positive real values of the bulk modulus and Poisson's ratio yield stable solutions to his wave equations. Asserting that the only necessary conditions for stability are that shear modulus, μ, and bulk modulus, $\lambda+\frac{2}{3}\mu$, be non-negative, Rayleigh provided theoretical counterexamples demonstrating that bulk modulus could be as small as zero, and that Poisson's ratio could be as small as negative one.

Rayleigh discussed the mathematical possibility of complex solutions to the wave equations, but dismissed such solutions as lacking physical interpretation. In the present work, we will discuss a framework wherein complex solutions of wave equations not only have physical meaning, but utility, as well.

In 1900, Oldham published a system for seismic interpretation that associated events in the preliminary tremor with P and S body waves, and those in the main shock with Rayleigh waves (Oldham, 1900). Oldham's interpretation of the preliminary tremor was consistent with seismic data, and generally well received; however, the notion that the main shock consisted of Rayleigh waves was more controversial. Although velocities and magnitudes were consistent with those predicted for Rayleigh waves, other aspects of their behavior were not. For example, Rayleigh waves were predicted to operate in two dimensions, with the vertical component of motion larger than the horizontal component by a factor of between 1.5 and 2, yet the earlier portions of the main shock often exhibited little or no vertical motion. Furthermore, these early portions often exhibited substantial horizontal movement perpendicular to the direction of wave propagation (Love, 1911).

Between 1903 and 1904, Lamb developed a source theory that offered a partial explanation for the lack of vertical motion in the main shock (Lamb, 1903, 1904). Lamb investigated wave propagation for a single impulse, and posited that more complicated signals could be explained by superposition. Lamb's source theory did not satisfactorily explain the lateral motion observed in seismic records. Furthermore, Lamb's theory did not predict the high periodicity associated with these motions, and although he suggested that such periodicity could be explained by periodicity of the source, he was unable to explain the mechanism by which this might occur.

In 1911, A.E.H. Love published an essay entitled, *Some Problems of Geodynamics*, which won Cambridge University's 1911 Adams prize. Love's book tackles problems as diverse as isostacy, gravity anomalies, and ocean tides. In Chapter 11, after reviewing the theories of Rayleigh, Lamb, and Oldham, he proposed a mechanism to explain the lateral seismic motions that had vexed the Geosciences since the first accurate seismometers had become available.

Love proposed that a superficial layer of relatively slow material over a faster half space might act as a wave guide for horizontally polarized transverse waves (SH waves). Love demonstrated that such a system would be *dispersive*: Low frequency waves would travel more quickly than high frequency waves. Accordingly, the interaction between Earth's crust and the mantle could sort a relatively short burst of seismic energy, such as is produced by an earthquake, into a long train of periodic, large amplitude, lateral waves similar to those observed in the seismic record. In his essay, Love also developed a theory of Rayleigh wave propagation in layered media, but he did not extend the method to the propagation of Love waves in layered media. In Chapter 3, our development of Love wave relationships will begin in a manner reminiscent of Love's own work; however, our treatment will diverge so that we can extend it to layered media with viscoelastic properties. We will also derive relationships that will allow us to account for the effects of geometric spreading.

We can visualize Love waves as horizontally polarized waves that are trapped in a half space, producing different modes via constructive interference. When layer velocity, β_1, is less than half-space velocity, β_2, it is possible for a wave impinging

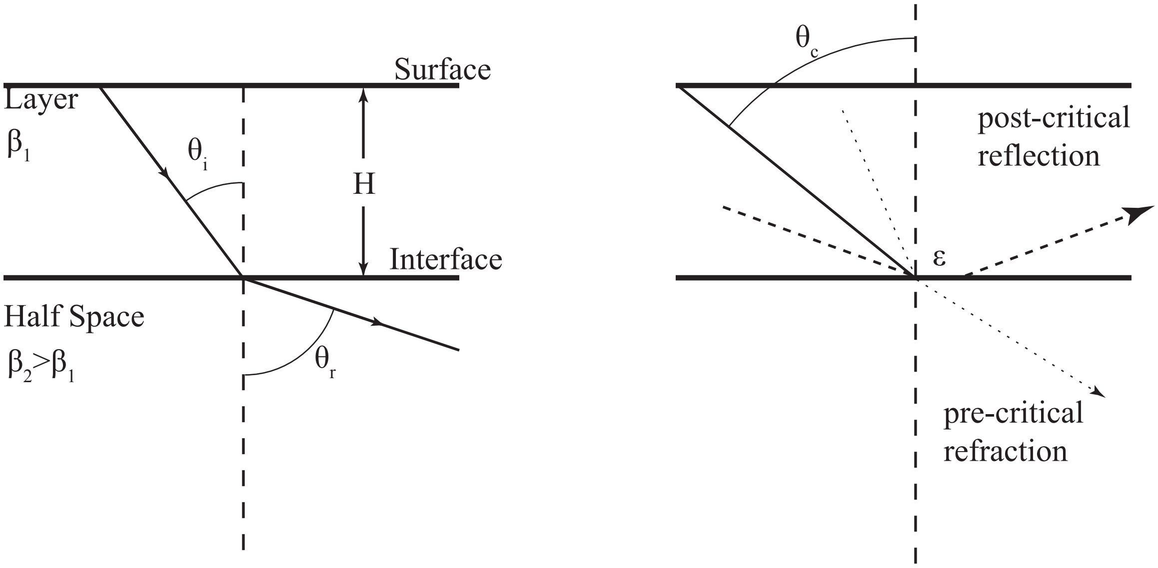

Figure 1.1: (l) Refraction nomenclature. θ_i is the incidence angle, and θ_r may represent either the angle of refraction or reflection, depending on whether the wave is refracted into the half-space (pre-critical) or reflected back into the layer (post-critical). Both angles are measured from the vertical. (r) Waves impinging on the interface at low grazing angles $(\theta_i > \theta_c)$ reflect back into the layer with with a phase delay, ε.

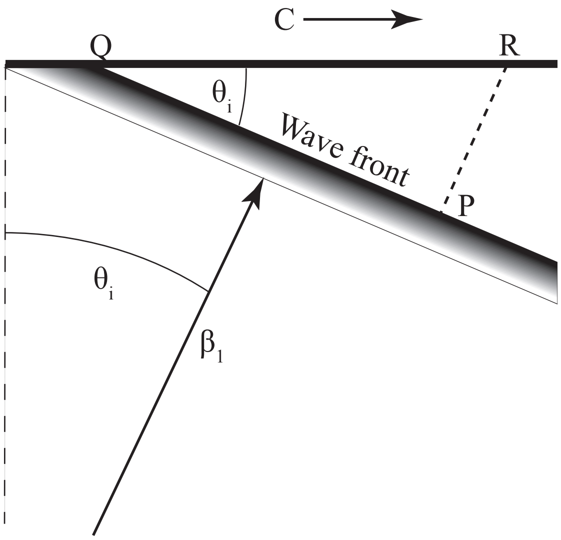

Figure 1.2: Relationship between shear wave velocity and apparent surface wave velocity, C. The wave front is moving at an angle θ_i and velocity β_1. In the time it takes a point, P, on the wavefront to move to a point, R, on the surface, the surface expression of the wave front will have moved from point Q to point R. $\overline{QR}$ is greater than $\overline{PR}$, so the apparent velocity, C, is greater than β_1. Thus, surface wave phase velocity, C, is greater than or equal to β_1.

the interface from above to be reflected back into the layer. According to Snell's law (Stein and Wysession, 2003), a shear wave traveling across the interface between a layer and a half-space will refract at an angle that depends on the incidence angle, θ_i, and on β_1 and β_2. Beyond a certain critical angle, the wave will reflect back into the original layer. The critical angle, θ_c, is found using Snell's law:

$$sin\theta_c = sin\left(\frac{\pi}{2}\right)\frac{\beta_1}{\beta_2} = \frac{\beta_1}{\beta_2} \tag{1.1}$$

Incidence angle also affects measured wave velocity. A wave traveling horizontally would have an apparent velocity equal to shear wave velocity; however, a wave impinging on Earth's surface with an incidence angle, θ_i, would exhibit an apparent phase velocity equal to:

$$C_L = \frac{\beta_1}{sin\theta_i} \tag{1.2}$$

To an observer on Earth's surface, a wave traveling upward and perpendicular to the surface, would appear to have an infinite velocity. If a wave's incidence angle at the half-space boundary is less than θ_c, its energy will propagate into the half-space and be lost, and the wave will be unsustainable. This places an upper limit on the apparent velocity of Love wave propagation. Substituting Equation 1.1 into Equation 1.2, we see that maximum possible apparent Love wave velocity is β_2, thus placing upper and lower bounds on possible Love wave phase velocities: $\beta_1 < C_L < \beta_2$.

Below the critical angle, a significant fraction of incident energy is transmitted downward into the half-space and lost. Although it is possible for the energy reflected back into the layer to interfere constructively and form *leaky modes*, these typically decay so quickly that they won't be of concern to us in the present work. The inquisitive reader is referred to Section 7.6 of Aki and Richards (2009).

At post-critical angles, all of the energy incident upon the interface is reflected back into the layer; however, its phase is delayed by an angle, ε, that depends on the incidence angle and material properties of both layers. To understand the cause of this phase shift, recall that the apparent velocity of a post-critical wave on the layer side of the interface will be less than wave velocity in the half-space, β_2. This asymmetry induces a stress field in the half-space side that acts as a sort of wave. This *evanescent* wave decays quickly, and extends only a short distance into the half space, but its effect is to increase the effective path length of the wave–As if the wave were reflecting from a plane below the interface, thus causing a phase shift in

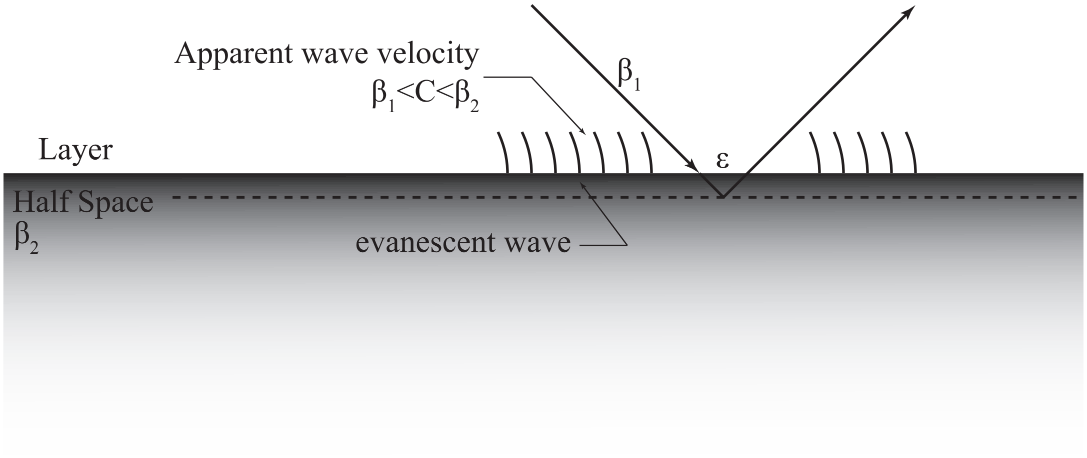

Figure 1.3: Phase shift in a post-critical wave. The apparent phase velocity, C, of a post-critical wave impinging on the interface will be less than half-space velocity, β_2, and greater than layer velocity, β_1. This mis-match causes a shallow stress field and and evanescent wave in the top of the half space that induces a phase delay, ε. The effect is as if the interface were moved to the bottom of the evanescent wave. The evanescent wave depth is greater for longer wavelengths (after Heaton (2005)).

the reflected wave. Thus, a Love wave can properly be thought of as the product of constructive interference resulting from the interaction of a reflected wave with the evanescent wave.

The phase shift effect is also evident in the reflection coefficient of a post-critical wave, which is a complex number with a modulus of unity. The phase delay, ε, is the same for all frequencies; however, because wavelength is a function of frequency, the effect is to create a thicker evanescent wave in the half-space. In effect, longer wavelengths *see* a thicker layer than is seen by shorter wavelengths. This unequal treatment contributes to the dispersive behavior of Love waves: Love wave velocity, C_L, is frequency dependent, with the apparent surface velocities of low frequency waves greater than those of high frequency waves. The reader seeking a more rigorous treatment of evanescent waves and post-critical phase shift is referred to Section 2.6 of Stein and Wysession (2003).

Like a guitar string, a Love wave system can resonate at a fundamental mode and a number of overtones; however, the interpretation of each system's fundamental mode and overtones is different. For a guitar string, the fundamental mode produces the single lowest frequency which can form a standing wave, and each overtone represents an integral multiple of the fundamental frequency. By contrast, an elastic layer over a half space can resonate at any frequency. As noted above, phase shift depends on incidence angle, so it is always possible to find at least one post-critical angle for which a given frequency can resonate. Of course, as noted in (1.2), each incidence angle is associated with a unique apparent velocity between β_1 and β_2, so a mode can be described by an infinite set of unique frequency-velocity pairs.

For a single elastic layer over a half-space, the fundamental mode exists for all frequencies, from zero to infinity, with low frequencies propagating at velocities near the half-space velocity, β_2, and high frequencies propagating at velocities closer to the layer velocity, β_1. Throughout this text, we will refer to the lowest mode ($n = 0$) as the fundamental mode, and subsequent modes as the first overtone ($n = 1$), second overtone ($n = 2$), etc. Unlike the fundamental mode, the first overtone only exists at frequencies above a cut-off frequency, f_{cn}. For an elastic layer over a half-space, the apparent velocity at f_{cn} is equal to β_2. The cut-off frequency is given by (adapted from Stein and Wysession (2003)):

$$f_{cn} = \frac{n\beta_1}{2h_1\sqrt{1 - \frac{\beta_1^2}{\beta_2^2}}} \tag{1.3}$$

In Chapter 4, we will explore the dispersive relationships for each mode. Because these relationships are dependent on material properties, Love wave dispersion curves can provide information about layer properties. In Chapters 5 and 6, we will develop methods for determining layer structure and material properties using Love wave dispersion and attenuation curves.

Ernst Meissner (1921) first proposed a general model for elastic Love wave propagation in heterogeneous media. Aichi (1922) proposed a general solution using Bessel's functions, and extended the method to layered media. Bateman (1928) offered a formulation and solution that differed somewhat from that of either Meissner or Aichi. Further work by Gutenberg, Jeffreys, and Stoneley was focused on correlating observed Love wave dispersion with a two-layer model of Earth's crust (Stoneley, 1948). Interest in surface waves was rekindled during the late 1940s when Dobrin (1951) and other researchers used surface and Airy waves generated by the Bikini atomic test to derive a partial model of ocean sediments and crustal rock in the vicinity of the explosion. Thomson (1950) published a matrix formulation of the elastic surface wave problem that could be applied either to Love or Rayleigh waves. Haskell (1953) modified Thomson's method and showed that it could generate Rayleigh wave dispersion curves that compared favorably to those obtained from actual earthquake data. Although he derived a treatment for Love waves, he did not compare it to actual data. After developing a method for analyzing the dispersion curves obtained from Love waves, Takahashi (1955a) extended it to Rayleigh waves (Takahashi, 1955b).

The preceding models assume Earth materials to be purely elastic. *Elastic Waves in Layered Media* (Ewing *et al.*, 1957), a popular text that focused primarily on determination of the layering structure of Earth's crust, devoted a scant three pages to the Voigt model of *internal friction*; however, by the early 1960s, research on constitutive models incorporating friction was burgeoning.

1.2 Constitutive Soil and Rock Models

In the following discussions, we will make use of *lumped parameter models* to explain soil behavior. Lumped parameter models represent constitutive behavior using a system of elements such as springs, masses, dashpots, and frictional dampers. It is important to recognize that individual lumped parameter systems, such as are illustrated on the left side of Figures 1.5, 1.6, and 1.7 can only represent temporal behavior at a single point in space.

1.2.1 Coulombic Soil Damping Models

In 1773, Charles Augustin de Coulomb returned to Paris from a posting as a military engineer on the Island of Martinique. While on Martinique, Coulomb developed a theory of soil mechanics based on the theory of friction developed by Guillaume Amontons (1699). In short, Amontons' three laws stated that frictional force was proportional to the applied normal force, that it was independent of contact area, and that frictional force is independent of sliding velocity. Coulomb's work eventually earned him the sobriquet, *Father of Soil Mechanics*, but at the time, Amontons' theories were controversial, so although Coulomb's theory of soil mechanics was widely read (Coulomb, 1773), many believed its reliance on Amontons' tribology to be a critical flaw. The theory of contact friction in soils began with controversy and, and as we will see, that is still the case more than two centuries later.

Not surprisingly, Coulomb's next major work began with a lengthy section that used the results of his own detailed experiments to explain and defend Amontons' theory (Coulomb, 1781). This paper won a major prize from the French Academy of Sciences, and Coulomb's defense of Amonton's theory was so successful, that the theory is now usually referred to as the Coulombic theory of friction.

It was the second of Amontons' laws that caused the most controversy. Amontons, believed friction to be due to very small scale interactions between surface asparities: Frictional force, he believed, was the result of little bumps sliding over each other; however, Desagulier's work showed that highly polished objects often exhibited frictional coefficients that were greater than those for less highly polished objects made from the same material, and Desagulier concluded that frictional forces were due to adhesion. Although Desagulier generally agreed with Amontons' frictional theory, he

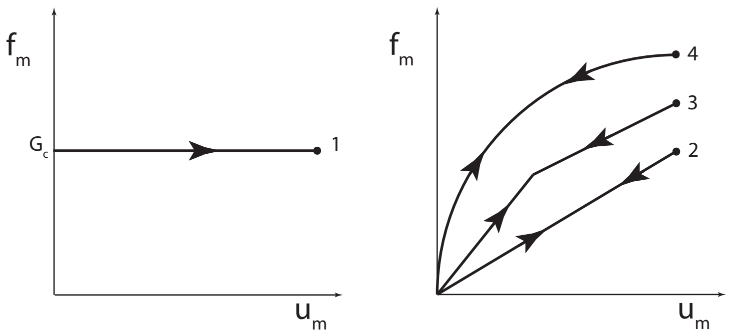

Figure 1.4: (*l*) After displacement, a purely Coulombic system (*1*) will not return to its original state. (*r*) After displacement, a purely elastic system returns to its original state along the path taken to its displaced configuration. Common elastic modeling elements include linear (*2*), bi-linear elastic (*3*), and non-linear (*4*) models.

never could completely reconcile it with his own observations.

It was Musschenbroek (1762) who pointed out that if friction were due to adhesion, then frictional forces would be a function of area. By Coulomb's day, this criticism was taken very seriously. Noting that des Camus (1722) and Desaguliers (1719) had observed the frictional retardation of moving objects to be less than that of objects at rest, Coulomb developed the concepts of static and sliding friction. Under Coulomb's model, static friction is due, primarily, to adhesion, and sliding friction is due to a different mechanism. Under this reformulation of Amontons' third law, the coefficient of *sliding* friction is independent of sliding velocity.

Coulomb's work in soil mechanics was primarily concerned with the design of statically determinate structures such as moats and embankments, and his constitutive soil models included no elastic term. A purely Coulombic system does not return to its original form after displacement (Figure 1.4*l*). Modeling clay is a material that could be described using a Coulombic term: After deformation, modeling clay does not return to its original configuration.

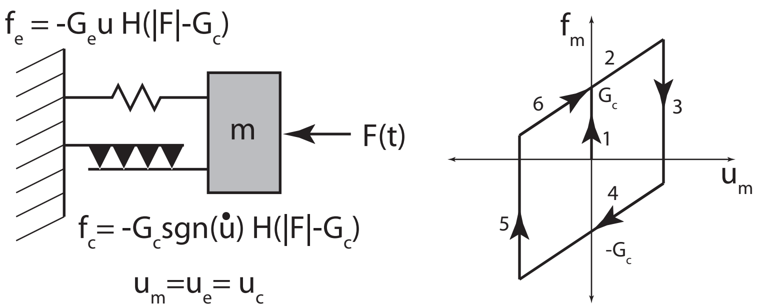

Figure 1.5: (*l*) Coulombic damping model. (*r*) When a unidirectional force, $F(t)$, is applied to the system, it follows the force-displacement relationship indicated by paths 1 and 2. When $F(t)$ is a periodic force, it follows hysteretic loop of paths 2, 3, 4, 5, and 6, and then repeats.

A purely elastic system tends to return to its original configuration without dissipating any energy. On a force-displacement plot, a purely elastic system follows the same path to and from its displaced configuration (figure 1.4*r*). Since a purely elastic system contains no mechanism for dissipating energy, once perturbed, it will vibrate indefinitely around its original configuration. No completely elastic systems exist in the macroscopic world: When struck, a bell may ring for a very long time, but it will eventually dissipate energy, and stop ringing (Lai *et al.*, 1993).

There are two obvious ways to include an elastic term in a Coulombic friction model. In the Coulombic damping model, elastic and Coulombic elements are in parallel. In the elasto-plastic model, they are situated in series (Morrison, 2002).

In an idealized Coulombic damping system (Figure 1.5), spring displacement (u_e) and displacement of the Coulombic friction element (u_c) are both equal to the displacement of the mass (u_m). If we apply an external force, $F(t)$ to the mass, no displacement occurs until the external force equals the frictional force of the Coulombic element (G_c), after which both the spring and dashpot exert a force on the element. This behavior, dubbed *stiction* by tribologists, is represented by a Heaviside step

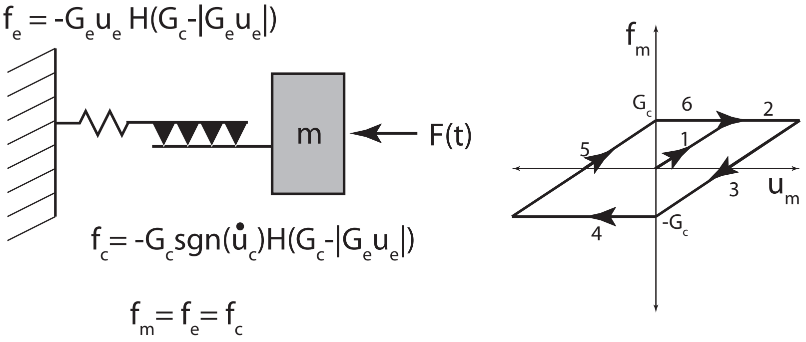

Figure 1.6: (l) Elasto-plastic system: Elastic and Coulombic elements in series. (r) When a unidirectional force, $F(t)$, is applied to the system, it follows the force-displacement relationship indicated by paths 1 and 2. When $F(t)$ is a periodic force, it follows the hysteretic loop of paths 2, 3, 4, 5, and 6, and then repeats the cycle.

function $H(|F(t)| - G_c)$. Once in motion, the frictional element exerts a constant force, G_c, opposite the direction of motion, and the elastic spring exerts a force that is equal to the relative displacement of the spring times the spring (Hooke's) constant, G_e. A signum function, $sgn(\dot{u})$, ensures that the frictional term acts opposite the direction of motion (Figure 1.5). A physical analogue to this system might be a sponge, which, if deformed, will return to its original shape, albeit with a loss in the mechanical energy of the system.

If driven by an oscillating driving force, $F(t)$, the force-displacement curve will assume the shape shown in Figure 1.5r. The area bounded by this curve is called a hysteresis loop, and it represents the energy lost by the system during each oscillatory cycle. When the maximum displacement amplitude is u_{max}, the total hysteresis energy will just be the area inside the parallelogram ($E_H = 4u_{max}G_c$). If the driving force is removed, the system will oscillate, but its amplitude will decay with time.

For an idealized elasto-plastic system, the forces acting on the mass and spring are both equal to the frictional force of the Coulombic element (Figure 1.6); however, the displacement of each element will be different (Iwan, 1961). The spring deforms to a maximum displacement equal to $u_e = sgn(\dot{u}_c)G_c/G_e$ before the Coulombic element begins sliding, and the force on the spring, mass, and Coulombic element will all equal G_c. If driven by an oscillating force, the force-displacement curve will assume the shape shown in Figure 1.6r. If the driving force is removed from a serially damped system, the system will oscillate and decay until $f_m < G_c$. After that point, decay will be zero for an ideal system. The elasto-plastic constitutive model is widely employed by geotechnical engineers (Desai and Christian, 1977).

An important characteristic of any frictional model is its dependence on loading. Under the original Amontons-Coulomb theory, G_c is a linear function of normal force. For soils, this translates into a dependency on effective stress, which, itself, is a function of depth, soil density, and pore water pressure (Das, 2011). Recall that elasto-plastic behavior remains elastic until the total force on the system exceeds G_c: For a soil exhibiting elasto-plastic behavior, we expect depth to increase the force necessary to induce Coulombic behavior. On the other hand, once this threshold has been reached, and particles begin moving against each other, we would expect the effects of damping to be enhanced with depth. In practice, although we see a delayed onset of Coulombic behavior at depth, this is not as pronounced as Amontons-Coulomb theory, alone, would predict (Ishihara, 1996).

The main appeal of the Coulombic damping and elasto-plastic models is their conceptual simplicity. It is easy to see how the microscopic action of individual soil particles scraping against each other could be extended to macroscopic scales. Unfortunately, real soils often deviate significantly from this behavior (Ishihara, 1996): In the elasto-plastic model, soils can be permanently deformed, and deformation that can alter material properties (Morrison, 2002). Perhaps more importantly, a fundamental assumption of Amontons-Coulomb theory is that the contact surfaces be dry: In the real world, soil particles tend to be wet. Even in the vadose zone, most soil particles are coated with a thin water film (Fetter, 2001). Depending on film thickness, contact velocity, and contact surface geometry, this film can either act as a viscous lubricant, or as a hydrodynamic bearing surface (Burr, 1995).

Probably the largest obstacle to adoption of models with Coulombic elements is their computational difficulty. Mathematical models of Coulombic elements tend to be highly non-linear, and they are not generally amenable to closed-form analytical solution (Iwan, 1961). Even after the wide spread availability of digital computers, calculations involving Coulombic elements remain computationally expensive. A common solution is to approximate Coulombic elements using visco-elastic elements.

1.2.2 Viscoelastic Models

In his *Principia Philosophiae*, Renée Descartes proposed that the orbital motion of the Sun was due to a sort of fluid vortex (Descartes, 1644). Seeking to disprove this view, Isaac Newton conducted numerous experiments on fluid behavior, and in the process established several important principles of fluid dynamics (Newton, 1687). Indeed, a large portion of the second volume of Newton's *Principia* is devoted to the topic of fluid behavior. Of particular interest to us, he formulated his eponymous law of viscosity, which states that the shear force transmitted between two objects in a fluid will be proportional to fluid viscosity, inversely proportional to the distance between the two objects, and proportional to the relative velocity of the two objects.

William Thomson (Lord Kelvin) proposed that viscosity could explain oscillatory

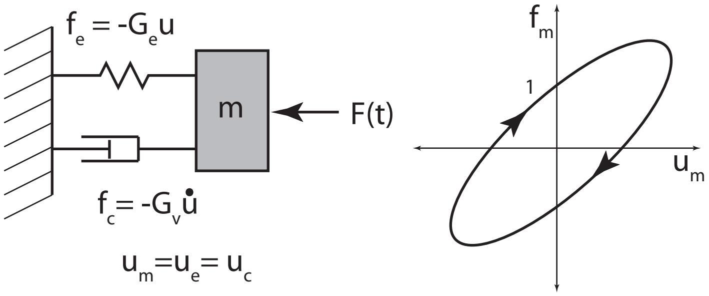

Figure 1.7: (*l*) Kelvin-Voigt viscoelastic model. (*r*) When subject to an oscillating driving force, *F(t)*, the force-displacement curve of a Kelvin-Voigt system describes a Lissajous curve.

damping and creep behavior that he observed in metal wires (Thomson, 1865). Thomson's viscoelastic model was a simple one-dimensional model similar to that shown in Figure 1.7. While working to explain the elastic behavior of crystalline solids, Voigt (1889) proposed a comprehensive viscoelastic model that is now generally referred to as either the Kelvin-Voigt model, or the Voigt model.

The Kelvin-Voigt (KV) model consists of an elastic element and a viscous element in parallel. The viscous term is characterized by the product of a viscosity factor, G_v and a velocity, $\dot{u}$, so that:

$$F_m = -G_e u - G_v \frac{du}{dt} = m \frac{d^2u}{dt^2} \tag{1.4}$$

Rearranging Equation (1.4), and equating it in terms of a driving force, $F(t)$:

$$\frac{d^2u}{dt^2} + \frac{G_v}{m}\frac{du}{dt} + \frac{G_e}{m}u = F(t) \tag{1.5}$$

which is a second order non-homogeneous linear differential equation. Solution for the homogeneous (harmonic) left-hand side can be found in any book on differential equations, e.g. Asmar (2000). For an underdamped system (discussed in Chapter 2), the solution is:

$$u = e^{-Dt}\left(C_1 cos(\omega_d t) + C_2 sin(\omega_d t)\right) \tag{1.6}$$

where:

$$\omega_d = \sqrt{\frac{G_v^2}{4m^2} + \omega_0^2} \tag{1.7}$$

$$D = \frac{G_v}{2m} \tag{1.8}$$

where D is a damping factor, ω_d is the resonant frequency of the damped system, and ω_0 is the resonant frequency of the corresponding undamped system, i.e. $G_v = 0$. We will devote much of Chapter 2 to derivation of a viscoelastic soil model and wave equation analogous to Equation 1.6, but for now, we will consider some consequences of the Kelvin Voigt model of a lumped parameter system.

First, we note that the exponential term in (1.6) is a damping factor that depends on the ratio $G_v/(2m)$. Second, we note that the resonant frequency of a damped system will always be higher than the resonant frequency of the corresponding undamped system. This second, somewhat counterintuitive, result and its implications for wave propagation will be discussed extensively in the following chapters.

The Kelvin-Voigt model accurately describes a variety of time-dependent behaviors observed in engineering materials (Equation 1.8) and it is a basic model for representing fatigue and creep behavior in metals and polymers (Stephens *et al.*, 2000). It has also seen widespread use as a soil model by geotechnical engineers (Ishihara,

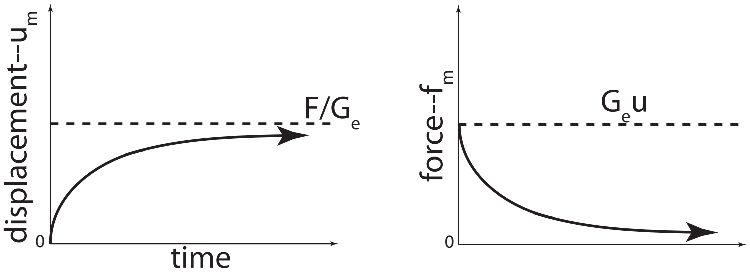

Figure 1.8: (l) When subject to a constant force, F, displacement of a Kelvin-Voigt system will approach, asymptotically, F/G_e. (r) When subject to a rapid displacement, the force on the mass will decrease, asymptotically, to zero. Materials Scientists refer to this behavior as creep.

1996), although competing models abound.

Much of the Kelvin-Voigt model's appeal is its amenability to treatment by analytical methods (Michaels, 1998), and it is possible to reformulate other models in terms of a Kelvin-Voigt model. For example, it is common practice to expres the Coulombic damping model in terms of a Kelvin-Voigt model that disperses the same hysteretic energy per cycle. As stated earlier, the total hysteretic energy lost by a single Coulombically damped cycle is $E_c = 4G_c u_{max}$. The energy dissipated in a single viscoelastic cycle, found by integrating one cycle of the ellipse in 1.7, is $E_{ve} = \pi G_v \omega u_{max}^2$. Under an equivalent hysteretic energy formulation, we could impress the viscoelastic model into service as a Coulombic damping model by making the viscosity factor a function of frequency and displacement amplitude (Equation 1.9).

$$G_{veq}(\omega, d) = 4G_c/(\pi \omega u_{max}) \tag{1.9}$$

where G_{veq} is the equivalent viscosity. This is common practice when using viscoelastic formulations of cyclic fatigue in engineering materials, e.g. the Coffin-Manson

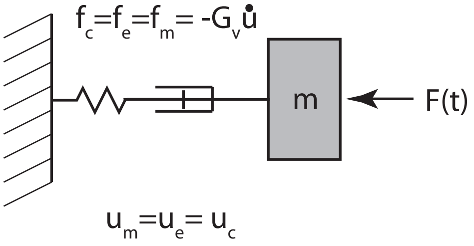

Figure 1.9: Maxwell viscoelastic model.

model (Stephens *et al.*, 2000). We will discuss a variant of this technique that is in common use by practitioners reducing data from resonant column experiments. Arslan and Sihayi (2006) have outlined a generalized technique for incorporating non-linear behavior into KV constitutive models.

Of course, it is also possible to arrange the viscous and elastic elements in a series (Figure 1.9). This model was originally formulated by James Clerk Maxwell (1866) while developing a constitutive model for gas behavior, but it has gained widespread use as a rheological model for fluids and for solids that exhibit low-shear strain dependent behavior.

An interesting consequence of the Maxwell model is its prediction that at sufficiently high frequencies, fluids might be able to transmit shear waves. Indeed, Han *et al.* (2005) have demonstrated the ability of heavy, high viscosity oils to transmit shear waves at frequencies in the 100s of KHz to MHz range.

Maurice Biot developed a theory of wave propagation in porous media that accounted for interactions between the fluid and frame. At low frequencies, Biot proposed that fluid-frame interactions could be treated as oscillating Poiseuille flow (Biot, 1956a). Poiseuille flow is the sort of fluid flow that occurs when viscous liquids move through relatively long tubes at relatively low velocities, and oscillating Poisueille

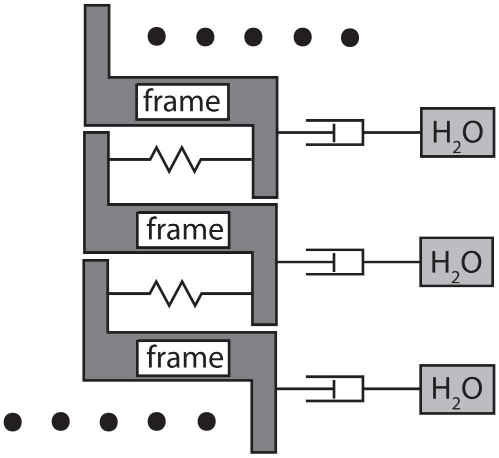

Figure 1.10: Assemblage of Kelvin-Voigt-Maxwell-Biot (KVMB) systems (after Michaels (2006a))

flow is one of the few transient cases for which a closed-form analytical solution exists. As envisioned by Biot, the fluid and frame act as coupled oscillating systems. An interesting consequence of Biot theory is the prediction that there exist two types of P-waves: One that exists primarily in the frame, but that is slowed somewhat by its interaction with the fluid, and another that exists primarily in the fluid, but that is sped-up somewhat by its interaction with the frame. Biot noted that at high frequencies, the assumptions of Poiseuille flow break-down, and published a second paper treating high frequency wave transmission (Biot, 1956b). Biot theory is appealing because it is derived from fundamental mechanical principles. Unfortunately, as noted by Michaels (1998), implementation of Biot theory can be computationally cumbersome.

Models combining various lumped parameter elements abound. For example, Michaels (2006b) has proposed a lumped parameter model that combines the Maxwell and Kelvin-Voigt models in a manner that emulates the fluid-frame coupling proposed by Biot: The Kelvin-Voigt-Maxwell-Biot (KVMB) model.

1.3 Testing Methods

We will briefly review two standardized methods for estimating viscoelastic soil parameters: The resonant column test, which is described in ASTM-D-4015 (1996), *Standard Test Methods for Modulus and Damping of Soils by the Resonant-Column Method*, and the crosshole method, which is described in ASTM-D-4428 (1996), *Standard Test Methods for Crosshole Seismic Testing*. We will also discuss in-situ tests that have been proposed as alternatives to these standardized methods.

1.3.1 The Resonant Column Test

Imagine suspending a dumb bell shaped object using a wire. After permitting the wire to relax, the dumb bell could be rotated slightly, and then released. The elasticity of the wire would exert a torque on the dumb bell, causing it to oscillate about the axis of the wire. Using the period of oscillation, inertial moment of the dumb bell, and dimensions of the wire, it is possible to calculate the shear modulus of the wire material, and by observing the decay rate of its oscillations, it is possible to determine its viscosity. This instrument, called a torsional balance oscillator, was originally developed by Coulomb in the late 18th century. Working from his laboratory at the University of Tokyo's *Earthquake Research Institute*, Kumizi Iida made several improvements to the device that allowed him to make precise measurements of the shear modulus and viscosity of earth materials such as quartz and sandstone (Iida, 1935). The natural frequency of thicker speciments will generally be much greater than those of wire, so Iida added an electrical torsion motor and optical detector that allowed him to drive the system at much higher frequencies. He could determine the natural frequency of the system from the frequency that produced the maximum

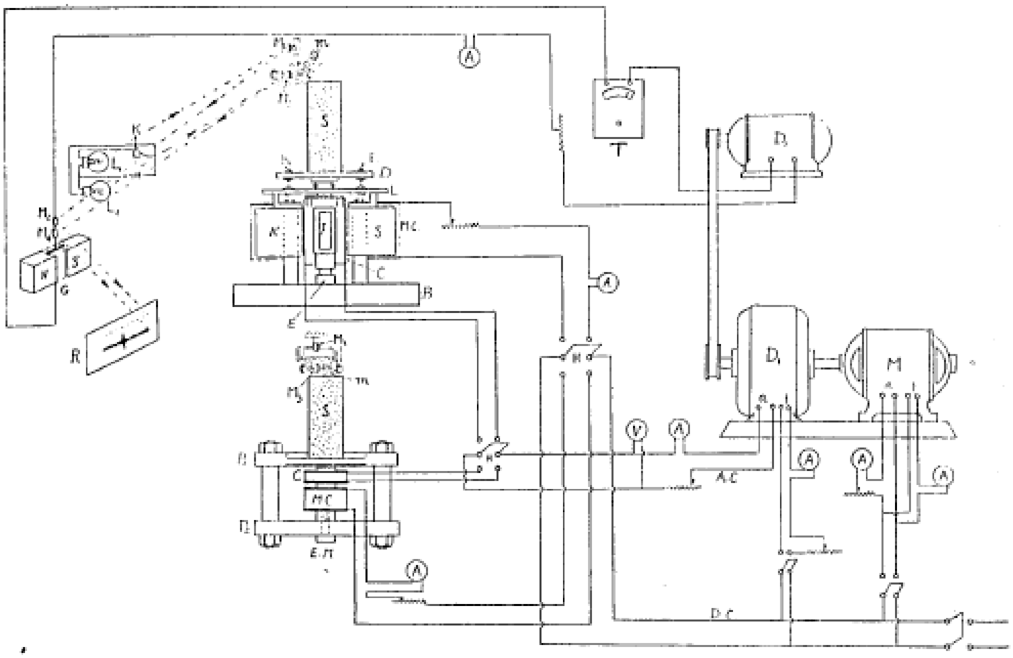

Fig. 2. Schematic diagram of arrangement of the apparatuses for producing the torsional and the longitudinal vibrations of soils.

a: Armature terminal.
A: Ampere-meter.
A.C.: Alternating current circuit.
B: Steel block.
B_1, B_2: Brass bolt.
C: *A.C.* coil.
D: Circular brass disc.
D_1: Alternating generator.
D_2: Dynamo of the Weston tachometer.
D.C.: Direct current circuit.
E: End of the pivot.
E.M.: Electromagnet.
F: Solid cylindrical iron stick.
f: Field terminal.
G: Galvanometer.
H: Switch.

K: Key.
L_1, L_2: Light source.
m: Magnet.
M: *D.C.* motor.
M_1, M_3: Lens mirror.
M_2, M_4: Plane mirror.
M.C.: *D.C.* coil for electromagnet.
N, *S*: Pole piece of electromagnet.
P_1: Circular iron disc for vibration.
P_2: Circular iron disc with electromagnet.
R: Bromide paper for record.
S: Soil specimen.
T: Voltmeter of the Weston tachometer.

Figure 1.11: Resonant Column Apparatus used by Ishimoto and Iida (1937).

response in his optical detector. In a collaboration, Ishimoto and Iida (1936) modified the device so that it could be used to determine the resonant frequency of soil samples and other unconsolidated media (Figure 1.11).

The resulting resonant column device consisted of an iron disk (base), on which was affixed a cellophane tube containing the soil sample (sample tube). Atop the soil sat another iron disk that compressed the soil sample into the tube (weight). The iron base was oscillated by means of an oscillating magnet. Iidra improved his resonant column device several times. Initially, oscillation of the weight was monitored mechanically, but in later versions, oscillation was monitored using a light and mirror. An advantage of the latter apparatus was that it could be used with moving photographic film to record transient signals. The device could also include an axial excitation mechanism and sensor, so that dilational properties could be measured, as well.

Iidra would vary the excitation frequency until he either obtained a maxima or a null point, calculate the dilational or shear wave velocity necessary for resonance, and then use the velocities so obtained to estimate Young's modulus, shear modulus, Poisson's ratio, and Lame's parameters. By turning-off the instrument, and monitoring its transient response, he could calculate both normal and shear viscosity values. Iida's last paper using a resonant column device, *On the Elastic Properties of Soil, Particularly in relation to its Water Content*, was published in September 1940 (Iida, 1940)

Interest in the resonant column method resumed in the United States, with researchers such as Shannon, Yamane, Dietrich, Hall, Richart, and Hardin publishing many papers on the method and results obtained from it in the 1950s and 1960s

(Richart *et al.*, 1970). Most instruments followed the general pattern set by Iidra; however, researchers often changed the methods for exciting the sample or measuring sample response. In most cases, the column was either excited or its response monitored using some sort of magnetic inductor. Such instruments are called *free-free* instruments, because both their base and weighted top are free (Figure 1.12). A second variant, with a fixed base and free top, was developed by Hall (Hall and Richart, 1963). In 1981, the American Society for the Testing of Materials adopted a standardized test using the free-free instrument, ASTM-D-4015 (1996). The method has been updated twice since that date.

In practice, a specimen is prepared, weighed, and its physical dimensions measured. The resonant frequency is determined, and then machine power is cut-off. Vibrational decay is measured, and then the operator uses uses a series of calculations, curves, or a Fortran program, to determine modulii and the damping ratio, defined as:

$$DR = \frac{\eta\omega}{2\mu} \tag{1.10}$$

where η is soil viscosity, ω is angular frequency is radians per second, and μ is the shear modulus. Note that we have altered ASTM's symbology to be consistent with that used throughout the rest of this paper.

One of the most frequent criticisms of ASTM-D-4015 involves Equation 1.10. An influential early practitioner of the resonant column method in the U.S. was Bobby O. Hardin of the University of Kentucky. His paper, *The nature of damping in sands*, included a thorough treatment of the mathematics and calculations necessary to implement the resonant column method (Hardin, 1965). Using experiments based

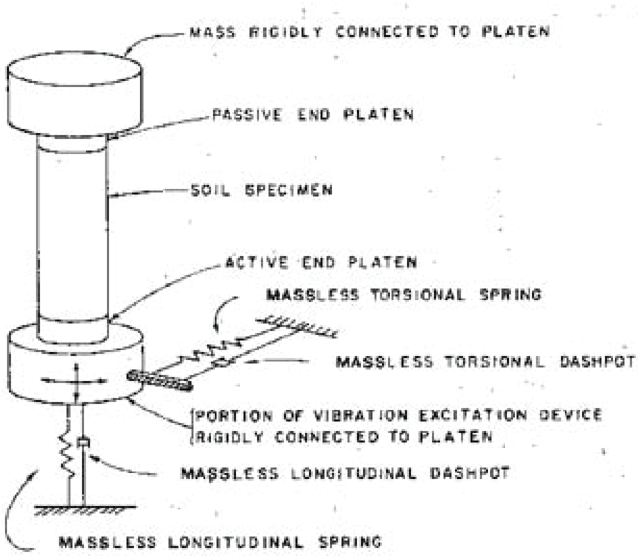

Figure 1.12: Resonant Column Apparatus (excerpted from ASTM-D-4015 (92)).

on dry Ottawa sands, he concluded that soil viscosity varies inversely with frequency, such that $\eta\omega/G$ is a constant. This is, essentially, Equation (1.10). The 2 in the denominator of Equation (1.10) aligns the definition of damping ratio with that of a related quantity called the *damping capacity.* Hardin seems to have been surprised by this finding, and emphasized that this result was for dry sands only, and that this assumption probably only holds near the measurement frequency.

Rearranging Equation 1.10, we arrive at the surprising result that for a given soil sample, its viscosity is inversely proportional to the frequency at which the resonant column test was conducted: $\eta = 2G(DR)/\omega$. This very odd result, a material property that is dependent on test conditions, seems to belie a problem with the ASTM-D-4015 methodology.

In response to Hardin's article, Weissmann (1965) suggested that Hardin's frequency dependent viscosity actually indicates that Hardin used the wrong model.

Indeed, the requirement that the product of viscosity and frequency be constant is exactly what we would expect of a Coulombic damping model. In any event, it is difficult to reconcile a constant $\eta\omega/G$ with the static viscosity values that were published for the same materials in Hardin's paper.

We should note that a resonant column instrument is a very crude device for determining frequency-material property relationships. For a given material, we are limited to the column's resonant frequency and its overtones. Hardin indicated that he used the fundamental and first two overtones to arrive at his conclusion, but he didn't actually publish any of the frequencies that he used; instead, he published normalized frequencies without giving the normalization factor. In another discussion, about confining pressure relationships, he gave a frequency of $\omega = 1290\ rad/s$, which is about 205 Hz. Given this frequency, his first and second overtones would have been about 610 Hz and 1025 Hz, respectively. In a discussion of one of Hardin's earlier papers (Hardin and Richart, 1963), Rao (1964) asked whether, given Hardin's caveat about the limited frequency range over which the constant $\eta\omega/G$ assumption is valid, measurements taken at frequencies that are two or more orders of magnitude greater than what might be expected in an earthquake are really worthwhile.

Data obtained by Ishimoto and Iida data showed an overwhelming dependence of soil viscosity on moisture conditions, with high moisture content soils (approx 50%) exhibiting viscosities nearly two orders of magnitude less than their dry counterparts. Furthermore, they found that this relationship held across dozens of soil types (Ishimoto and Iida, 1936). By using columns of several different heights, they were able to take measurements at approximately a dozen different fundamental mode frequencies, and concluded that the relationship between frequency and measured viscosity was much flatter for dry samples than for moist samples–This is consistent with the idea that a Coulombic model might be appropriate for dry soils.

Other criticisms have been leveled at the resonant column apparatus, itself. H.D. McNiven and C.B. Brown suggested that some of the resonant behavior being observed might be due to tube waves (McNiven and Brown, 1963). Viscosity measurements typically are made by switching off the power to the device; however, Wang *et al.* (2003) demonstrated that it could take several seconds for the magnetic field used by the inductor to collapse, and that during that time, the system would create a counter-emf that could explain some or all of the frequency-dependent viscosity effect. In other words, it is quite likely that the amplitude decay measurements used to determine damping ratio are at least partially due to the resonant column device, itself.

A final criticism could be leveled at nearly any laboratory test: It is difficult to know whether or not a laboratory sample is behaving as it would in-situ. Ishimoto and Iida (1936 and 1937), collected soil samples in a carefully designed sampling jar. After making a resonant column with a sample, they would disturb the same soil sample, and repack it into the same sampling jar. They determined that repacking the sample usually effected a 2x to 10x decrease in viscosity.

1.3.2 In-Situ Methods

The preferred in-situ method for determining elastic material properties is the seismic crosshole test ASTM-D-4428 (1996). Because it is an in-situ test, it avoids many of the potential problems of laboratory testing. Soils are measured under field conditions, and aside from the material immediately adjacent to the boreholes, the soil is

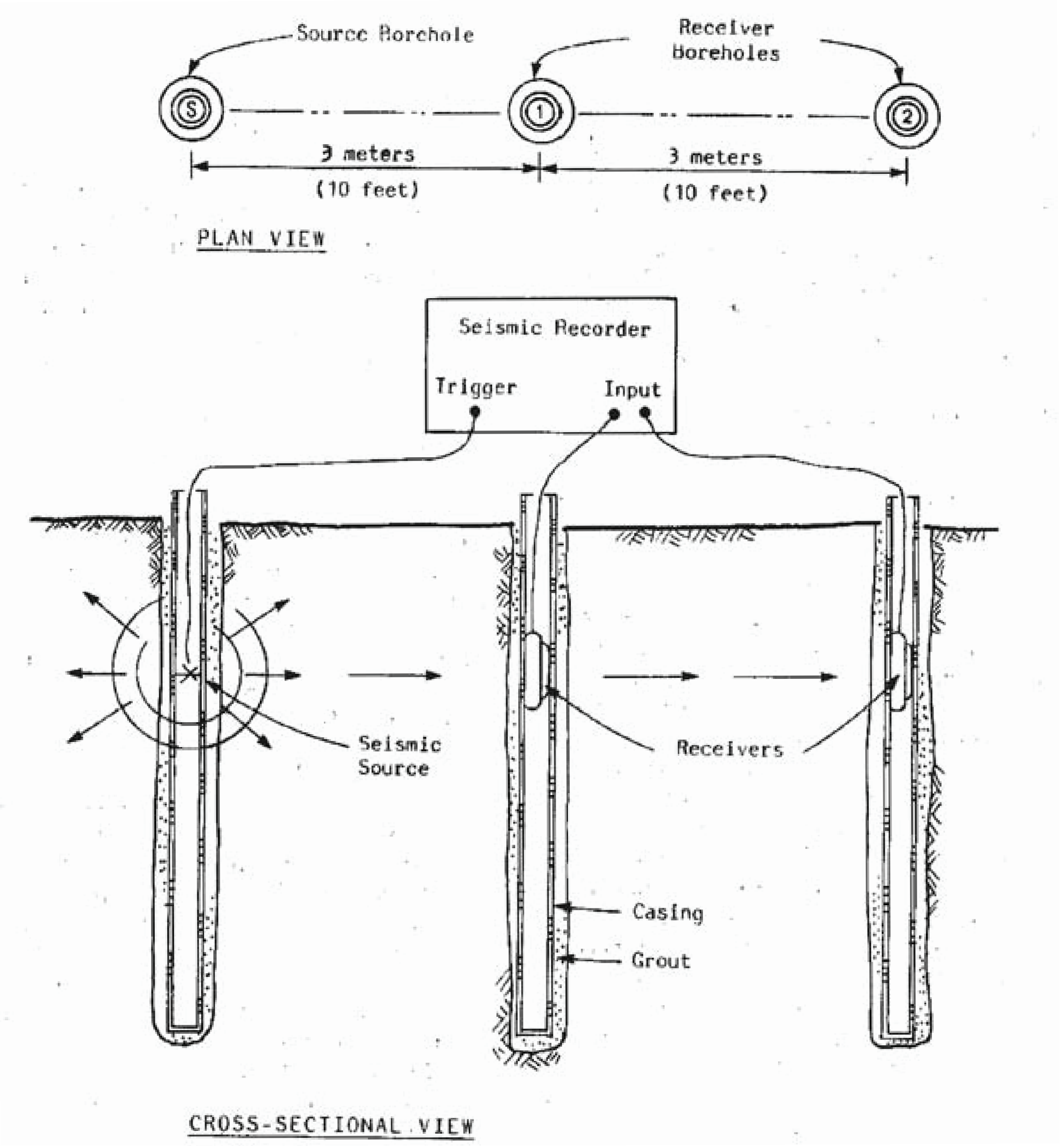

Figure 1.13: Preferred borehole configuration for crosshole testing (excerpted from ASTM-D-4428(91)).

undisturbed. In practice, three boreholes are drilled along a line at 3 *m* intervals, taking care to disturb soils adjacent to each borehole as little as possible (Figure 1.13). Each hole is carefully cased and grouted. A seismic source is lowered into one of the outside holes, and receivers lowered into the two remaining holes so that all three are at the same height below the datum. The seismic source is triggered, and the signal recorded at each of the receivers. The process is repeated for several different heights using both p and s-wave sources. The data for each height and source is analyzed by using the difference in arrival times at the two receivers to determine the wave velocity at each level. Using either assumed or measured soil densities, material properties such as shear modulus, Young's modulus, and Poisson's ratio can be determined.

Although not specified by ASTM-D-4428, it should be possible to determine attenuation coefficients provided that each receiver's response characteristics are sufficiently well characterized.

The crosshole test's main disadvantage is cost, and because the preferred spacing for the boreholes is relatively close (3 *m*), multiple test locations might be necessary to survey an entire area of interest. ASTM-D-4428 provides a two hole method that can reduce costs somewhat; however, it would not generally be possible to extract attenuation information without at least three boreholes. Also, as was pointed out by Michaels (1998), the crosshole method is susceptible to the wave guide effect, which could cause elastic waves to experience dispersion, which would be easily confused for attenuation.

Robertson *et al.* (1985) have integrated a small rugged shear wave seismometer into a standard cone penetrometer, and demonstrated its ability obtain a shear-wave profile of up to 40 meters depth. They have called this the Seismic Cone Penetrometer

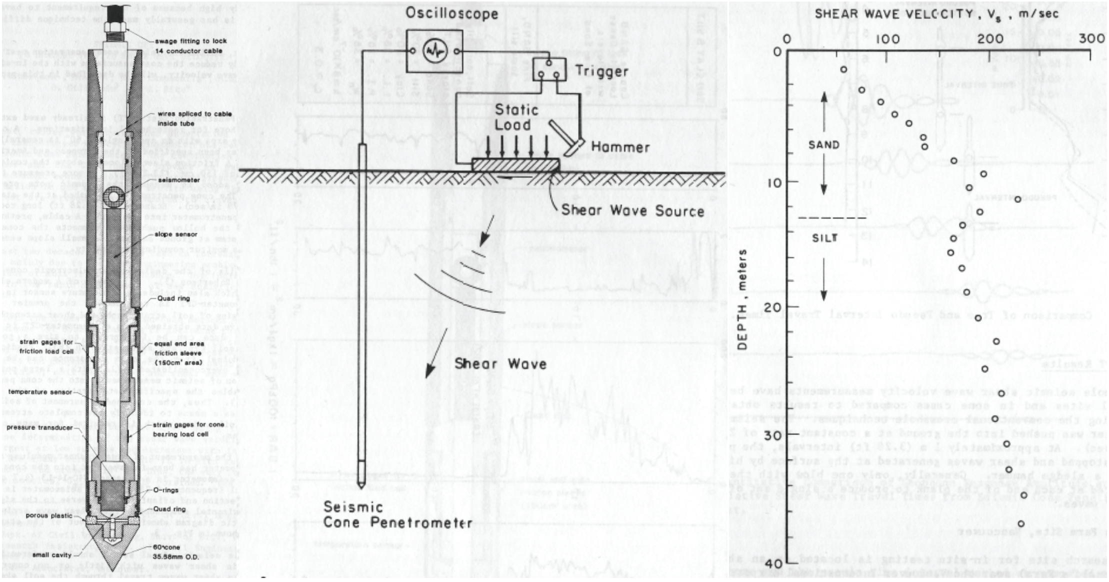

Figure 1.14: Seismic Cone Penetrometer Test (SCPT) developed by Robertson *et al.* (l) Cone penetrometer equipped with a rugged shear-wave seismometer. (c) Field test set-up. (r) Typical velocity-depth profile. Illustrations excerpted from Robertson *et al.* (1985).

Test (SCPT). The penetrometer is driven into the soil, and stopped at intervals so that its seismometer can be used to measure a signal generated by a horizontal shear wave source at the surface 1.14. The cone penetrometer test is less expensive than crosshole testing, and it has the advantage of producing correlative data that can be used to impute pore water pressure, median grain size (D_{50}), relative density (D_r), unconsolidated shear strength (c_u), overconsolidation ratio (OCR), drained friction angle (ϕ'), and bearing capacity factor (N_k) (Das, 2011). Although the authors did not do so, there would seem to be no impediment to using SCPT data to estimate damping coefficients. The main disadvantage of penetrometer tests is that the cone can have difficulty negotiating large cobbles or gravels.

Michaels (1998) developed a joint inversion routine that he used to estimate shear modulus and damping factors from downhole seismic data. As noted by the author,

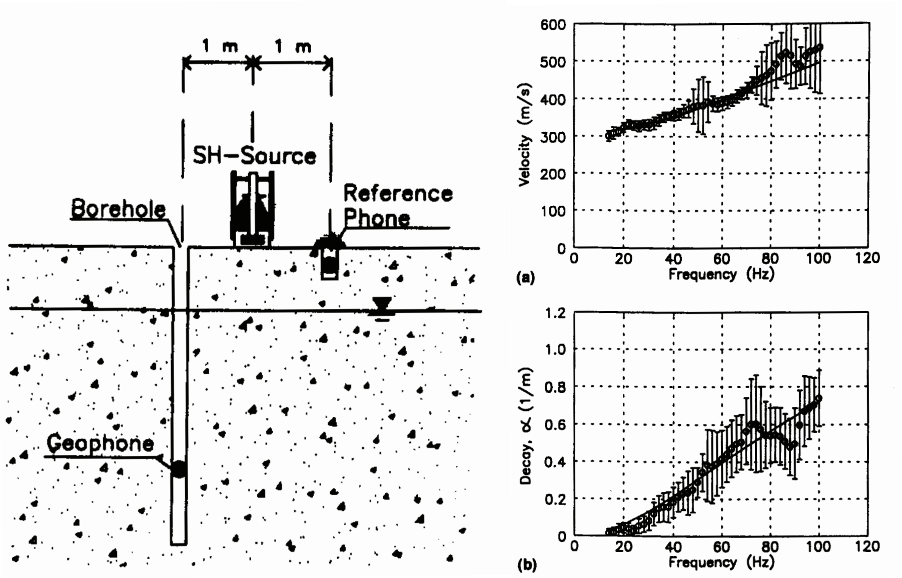

Figure 1.15: (*l*) Field set-up used by Michaels to obtain downhole data. (*r*) Typical dispersion (top) and attenuation (bottom) curves obtained from Michaels' Idaho field tests. Illustrations excerpted from Michaels (1998).

there is no reason that this technique could not also be used with SCPT data. A receiver is lowered down a borehole and used to measure a signal generated by a horizontal shear wave source on the surface. The measured data is then inverted in a manner that best fits both the dispersion and attenuation curves obtained from the model (Michaels, 1998). These curves were obtained assuming a Kelvin-Voigt soil model.

The downhole method is a better choice for gravely soils than the SCPT method, and because it only uses one borehole, it is less costly than the crosshole method. It is also probably less susceptible to the effects of layering (wave-guide formation).

1.3.3 Surface Wave Methods

Jones (1962) described methods for determining the thickness and modulii of roadway materials using Rayleigh waves. Although not central to his proposal, his development included a discussion of the Voigt viscoelastic model, with methods for correcting data for viscous attenuation. In 1981, J. Scott Heisey (1981), a graduate student at the University of Texas at Austin, wrote a Master's thesis entitled, *Determination of in situ shear wave velocities from spectral analysis of surface waves* (Heisey, 1981). The next year, he and his collaborators published an extensive report of the same title for the Texas Department of Transportation, in which they detailed potential uses for the method (Heisey *et al.*, 1982). That same year, they published a paper entitled, *Modulii of pavement systems from spectral analysis of surface waves* in ASCE's *Transportation Research Record*. Kenneth Stokoe II, one of Heisey's collaborators, has since published many papers on the Spectral Analysis of Surface Waves (SASW) technique.

Rayleigh waves propagating in homogeneous media are not dispersive. In other words, velocity is not a function of frequency. As noted by Love (1911), Rayleigh waves become dispersive when they propagate in layered media. High frequency waves tend to penetrate to shallower depths and be less influenced by deep layers than their low frequency kin. SASW takes advantage of this property of Rayleigh waves in order to determine the layered structure beneath the surface. The SASW method typically uses a source and two receivers located some distance away. Velocity information is imputed from travel times between the two receivers and correlated with frequency information to obtain dispersion relationships. Multichannel Analysis of Surface Waves (MASW), a related method pioneered by Gabriels *et al.* (1987), employs multiple channels in order obtain two or three dimensional depth profiles of surface layers in an area. Several researchers, including Xia *et al.* (1999), have promoted the MASW method as a shallow-surface exploration tool. Although often advertised as a stand-alone method, SASW and MASW are probably best used in conjunction with techniques such as downhole, crosshole, or cone penetrometer tests.

An important motivator for the use of shear wave techniques has been the Uniform Building Code (ICBO, 1997) and its successor, the International Building Code (ICC, 2000). In order to estimate a structure's earthquake response, both codes require that the shear wave profile of the soils for any expensive or critical building project be determined to a depth of at least 30 m. Averaged shear velocity values then are used to impute earthquake site response and site amplification factors used for structural lateral load calculations. A 5% soil damping factor is used in base calculations; however, this may be adjusted depending on local soil conditions, or from the results of resonant column tests such as ASTM-D-4015 (1996). There currently is no requirement that damping ratio be imputed from in-situ tests; hence, there is little impetus to use SASW and MASW to estimate soil damping factors.

A second deterrent to using SASW/MASW to determine soil damping factors is the complexity of data inversion. Both methods use Rayleigh waves, which are dependent on dilational as well as shear properties. An inversion scheme using Rayleigh waves to determine shear properties would need to separate the effects of soil density, shear modulus, shear viscosity, bulk modulus, and bulk viscosity.

Most attempts at inverting surface wave data obtained from earthquakes have focused on purely elastic models. Pei (2007) has developed an interesting method that jointly inverts data from Love and Rayleigh waves to determine elastic parameters.

The importance of soil damping is appreciated by the geophysical community, and there have been many efforts to model regional earthquake behavior using viscoelastic models. Most forward models employ finite difference methods. For example, Jemberie (2002) modeled Rayleigh wave behavior using a Voigt-type model, and then used a least squares technique to determine the viscoelastic coefficients that best fit earthquake seismic data. Olson *et al.* (2000) have used earthquake surface wave data to refine a viscoelastic model that used data from borehole logs as a control. Ho-Liu (1988) applied tomographic techniques to develop a viscoelastic model of crustal blocks in California's Imperial valley; however, this study focused on the horizontal, rather than vertical structure of crustal blocks.

Chakravarthy (2008) has studied Love wave propagation in a single viscoelastic layer over a half-space. The difference between Love wave behavior of a single viscoelastic layer and its purely elastic counterpart is striking. In Chapter 4, we will extend the study of a single viscoelastic layer to multiple viscoelastic layers.

1.4 The Need for Accurate Viscoelastic Soil Property Estimates

The method prescribed by the International Building Code is a variant of the base shear force model: The structure is considered to be a stationary mass, under which, the soil and foundation oscillate with displacement, u, velocity $\dot{u}$, and acceleration $\ddot{u}$. For most calculations, the building is considered to be rigid, and the transverse force, shear, and moment on a given member are calculated using Newton's third law. Thus, the acceleration at the structure's base is a function of the soil geometry and properties. We will illustrate soil response using an idealized lumped parameter soil model with a single degree of freedom (SDOF) and a sinusoidal force $F(t)$ acting at its base (Figure 1.16).

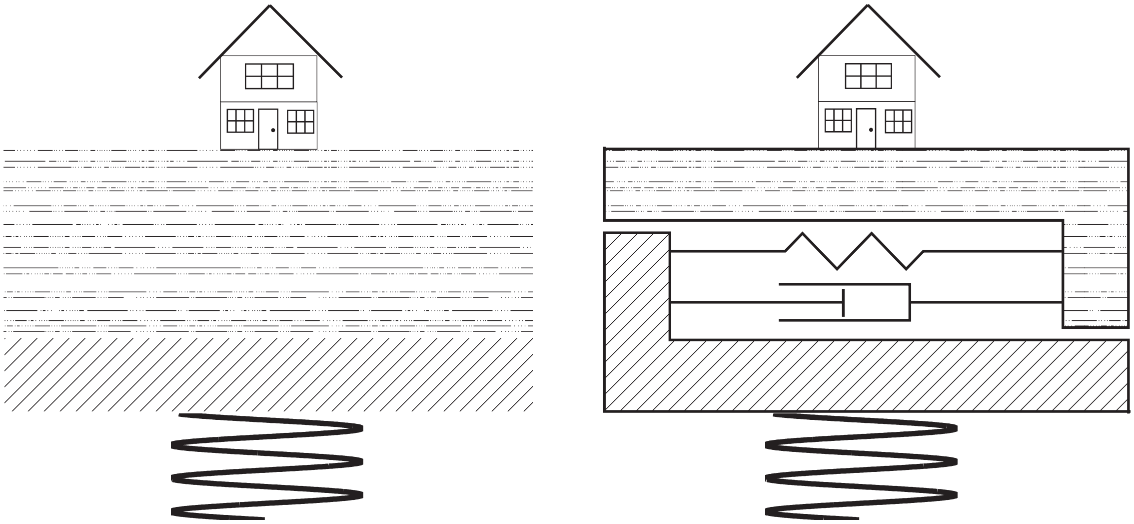

Figure 1.16: (l) Idealized viscoelastic soil model with a sinusoidal wave traveling upwards to the surface. (r) Lumped parameterization of an idealized SDOF soil model.

Recall Equation 1.5. Setting $F(t) = sin(\omega t)$ we obtain:

$$\frac{d^2u}{dt^2} + \frac{G_v}{m}\frac{du}{dt} + \frac{G_e}{m}u = sin(\omega t) \tag{1.11}$$

for which we define the magnification factor (MF) as the ratio of peak resonant amplitude to that of an untuned system. We will also define the critical damping ratio (DR_c) for a lumped parameter SDOF system as the ratio of the damping coefficient to the damping coefficient that would effect critical damping. We note that definition differs from the ASTM definition used in resonant column testing (Equation 1.10). A complete derivation is found in the appendices of Kramer (1996):

$$MF = \frac{1}{\sqrt{\left(1 - \frac{\omega}{\omega_0}\right)^2 + \left(\frac{2DR_c\omega}{\omega_0}\right)^2}} \tag{1.12}$$

As the forcing frequency, ω, approaches the undamped resonant frequency, ω_0,

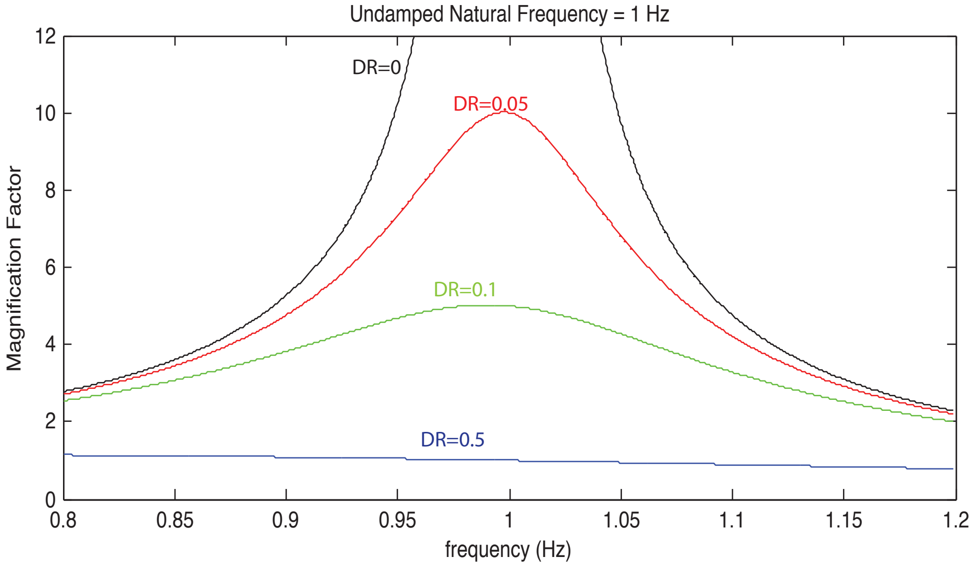

Figure 1.17: Magnification factor versus frequency for an idealized viscoelastic system with a natural resonance frequency of 1 Hz.

the magnification factor increases. Indeed, with no damping, it increases to infinity (Figure 1.17). Not surprisingly, magnification factor decreases rapidly with increasing damping ratio.

Idriss and Seed (1968) developed the SHAKE computer algorithm, which estimates surface displacement, velocity, and acceleration for layered soils over an oscillating bedrock base. SHAKE has been immensely popular, and it has been the progenitor of several generations of software designed to estimate surface motion. As of this writing, SHAKE91 and SHAKE2000 are in common use. We should note that the various iterations of SHAKE use a bilinear hysteretic model–A variant of the Coulombic damping model. Nevertheless, the frequency dependence of magnification factors obtained using SHAKE are similar to those obtained using the viscoelastic model.

Recall that Ishimodo and Iida found that the damping properties of disturbed soils, as measured by resonant column tests, could be from one half to one tenth the value obtained from an undisturbed sample of the same soil. It is possible that a soil with a measured damping ratio of 0.5 could actually have a damping ratio of 0.05, so instead of a magnification factor near unity, the true, in-situ value might actually be closer to 10 (Figure 1.17). Even if it were possible to gather an undisturbed soil sample, that soil sample would represent just one point in the area of interest. Adjacent soils, or soils at different depths might be considerably different.

Crosshole and downhole tests avoid most of the pitfalls associated with laboratory testing; however, they are expensive. The seismic cone penetrometer test is less expensive, but can only be used with a limited range of soil types. Furthermore, crosshole, downhole, and seismic cone penetrometer tests only provide a velocity-depth profile for one point. MASW is a relatively inexpensive way to obtain v_{s30} information over a fairly large area. Unfortunately, the complexity of Rayleigh waves has made determination of viscoelastic properties using either SASW or MASW problematic.

Unlike Rayleigh waves, which result from the interactions of both shear and dilational waves, Love waves arise from the interactions of shear waves alone. In the present work, we explore a method for inverting Love waves to obtain viscoelastic properties.

CHAPTER 2:

THE VISCOELASTIC SHEAR WAVE EQUATION

In this chapter, we discuss our choice of the viscoelastic shear wave model, derive the viscoelastic wave equation, and then show how the viscoelastic wave equation can be transformed into a variant of the more common elastic wave equation. We will then solve the viscoelastic wave equation for a homogeneous half-space.

2.1 Choosing a Constitutive Soil Model

An overarching consideration in our selection of a constitutive model is utility. As we saw in Chapter 1, Coulombic damping models, viscoelastic models, and their many variants all see common use, and there seems to be no consensus about which of these best models soil behavior. For example, ASTM-D-4015 (1996) specifies the use of a viscoelastic model that has been modified in such manner that it approximates Coulombic damping. As we noted, such a model might be appropriate for dry sands, but an unmodified viscoelastic would probably be more appropriate for moist or saturated soils. Stoll (1985) conducted resonant column experiments using the same Ottawa sands as Hardin. He found that dry sands exhibited the frequency indifference reported by Hardin; however, he also found that moist and saturated sands and inorganic silts exhibited the sort of frequency dependence that would be expected for a viscoelastic model.

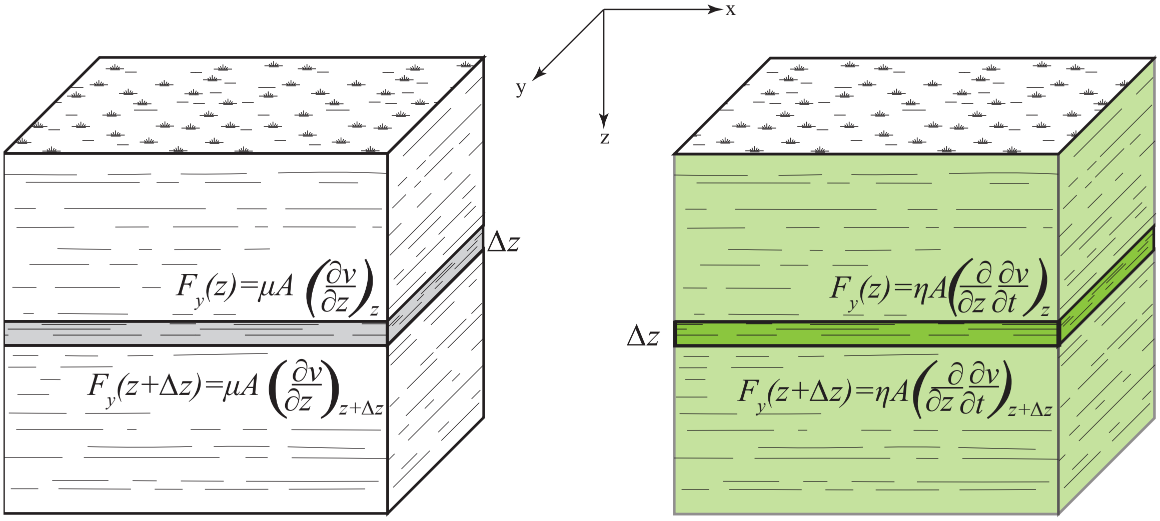

Figure 2.1: (l) Elastic shear forces acting on a horizontal soil element with thickness Δz and area A. (r) Viscous shear forces acting on the same element.

Most soils are damp; thus, the viscoelastic model seems more appropriate for most geotechnical applications. Furthermore, as noted in Chapter 1, the viscoelastic model can be used to approximate Coulombic behavior, so data obtained from the viscous model can be readily converted for use with the Coulombic damping model or its derivatives.

2.2 The Viscoelastic Equation of Motion

Consider a thin horizontal layer within a homogeneous, isotropic material with density ρ and shear modulus, μ. The top and bottom surfaces of the layer are at depths z and $z + \Delta z$, respectively. Now suppose that a shear wave passes vertically through the material, and that the wave's particle motion is in the y-direction. We denote the y-displacement of a particle from its initial position with the letter v. The stress on the surface of a layer is equal to the product of the shear modulus and the shear strain at that depth. The total force acting on the layer is the sum of the forces acting on the top and bottom faces (Figure 2.1(l)). In general, the forces at the top and bottom faces of the layer act in opposite directions, so that the net elastic shear force on the layer is given by:

$$F_{ye} = F_{ye}(z + \Delta z) - F_{ye}(z) = \mu A \left(\frac{\partial v}{\partial z_{z+\Delta z}} - \frac{\partial v}{\partial z_z} \right) \tag{2.1}$$

We approximate the right-hand side of Equation 2.1 with a differential formulation.

$$F_{ye} \approx \mu A \frac{\partial}{\partial z} \left(\frac{\partial v}{\partial z} \right) \Delta z = \mu A \frac{\partial^2 v}{\partial z^2} \Delta z \tag{2.2}$$

The mass of the layer is $m = \rho A \Delta z$. Applying Newton's second law, and taking the limit as Δz approaches zero:

$$F_{ye} = \rho A \Delta z \frac{\partial^2 v}{\partial t^2} = \lim_{\Delta z \to 0} \mu A \frac{\partial^2 v}{\partial z^2} \Delta z \tag{2.3}$$

Dividing both sides of Equation 2.2 by $\rho A \Delta z$, we obtain the one dimensional shear wave equation for a homogeneous, isotropic, linearly elastic material:

$$\frac{\partial^2 v}{\partial t^2} = \frac{\mu}{\rho} \frac{\partial^2 v}{\partial z^2} \tag{2.4}$$

Now consider a viscoelastic material. In addition to elastic stress, there is also a rate dependent shear stress due to the viscous effects at each surface. From Newton's law of viscosity, the force on each surface equals the product of viscosity η, area, and the velocity gradient at that surface. Thus, the net viscous shear force is:

$$F_{yv} = F_{yv}(z + \Delta z) - F_{yv}(z) = \eta A \left(\frac{\partial}{\partial z} \frac{\partial v}{\partial t_{z+\Delta z}} - \frac{\partial}{\partial z} \frac{\partial v}{\partial t_z} \right) \tag{2.5}$$

Using arguments similar to those for the purely elastic case, we obtain an equation of motion for the viscous forces that is analogous to Equation 2.3:

$$F_{yv} = \rho A \Delta z \frac{\partial^2 v}{\partial t^2} = \lim_{\Delta z \to 0} \eta A \frac{\partial^2}{\partial z^2} \frac{\partial v}{\partial t} \Delta z \tag{2.6}$$

The total force on the layer is $F_y = F_{ye} + F_{yv}$. Adding these forces, applying Newton's second law, and dividing both sides by $\rho A \Delta z$, we obtain the one dimensional viscoelastic wave equation for a homogeneous, isotropic, linearly elastic, and linearly viscous material:

$$\frac{\partial^2 v}{\partial t^2} = \frac{\mu}{\rho} \frac{\partial^2 v}{\partial z^2} + \frac{\eta}{\rho} \frac{\partial^3 v}{\partial z^2 \partial t} \tag{2.7}$$

We will solve (2.7) using the method of separation of variables (Asmar, 2000) by letting $v(z,t) = Z_v(z)T_v(t)$. Thus separated, we obtain two differential equations:

$$\frac{\partial^2 Z_v}{\partial_z^2} + k^{*2} X_v = 0 \tag{2.8}$$

$$\frac{\partial^2 T_v}{\partial t^2} + k^{*2} \left(\frac{\eta}{\rho} \frac{\partial T_v}{\partial t} + \frac{\mu}{\rho} T_v \right) = 0 \tag{2.9}$$

for which k^* is the complex eigenvalue used to separate the variables. The solutions to Equations 2.8 and 2.9 are:

$$Z_v(z) = A_1 e^{ik^*x} + A_2 e^{-ik^*z} \tag{2.10}$$

$$T_v(t) = B_1 e^{i\omega t} + B_2 e^{-i\omega t} \tag{2.11}$$

where $k^* = k_r + ik_i$ is called the complex wave number, and k_r and k_i are given by:

$$k_r = \omega \left(\rho \frac{\mu + \sqrt{\mu^2 + \eta^2\omega^2}}{2(\mu^2 + \eta^2\omega^2)} \right)^{1/2} \tag{2.12}$$

$$k_i = \omega \left(\rho \frac{-\mu + \sqrt{\mu^2 + \eta^2\omega^2}}{2(\mu^2 + \eta^2\omega^2)} \right)^{1/2} \tag{2.13}$$

2.2.1 An Alternative Formulation of the Viscoelastic Wave Equation

The solutions of Equation 2.7 are harmonic, and of the form $e^{i(\omega t - k^*x)}$. Substituting this into the third order term of (2.7) and differentiating with respect to time yields:

$$\frac{\eta}{\rho}\frac{\partial^3 v(z,t)}{\partial z^2 \partial t}\frac{\eta}{\rho}\frac{\partial^3 e^{i(\omega t - k^*z)}}{\partial z^2 \partial t} = i\omega\frac{\eta}{\rho}\frac{\partial^2 e^{i(\omega t - k^*z)}}{\partial z^2} = i\omega\frac{\eta}{\rho}\frac{\partial^2 v(z,t)}{\partial z^2} \tag{2.14}$$

This suggests a method for transforming Equation 2.7 into a second order differential equation. Substituting the result from (2.14) into (2.7), we obtain:

$$\frac{\partial^2 v}{\partial t^2} = \frac{\mu}{\rho}\frac{\partial^2 v}{\partial z^2} + \frac{i\omega\eta}{\rho}\frac{\partial^2 v}{\partial z^2} = \frac{\mu + i\omega\eta}{\rho}\frac{\partial^2 v}{\partial z^2} = \frac{\mu^*}{\rho}\frac{\partial^2 v}{\partial z^2} \tag{2.15}$$

where $\mu^* = \mu + i\omega\eta$ is called the complex shear modulus. The complex shear modulus permits us to express the viscoelastic wave equation as a variant of the complex wave equation:

$$\frac{\partial^2 v(x,z,t)}{\partial t^2} = \frac{\mu^*}{\rho}\nabla^2 v(x,z,t) \tag{2.16}$$

2.2.2 Shear Wave Velocity and Wave Number Relationships

We denote the complex shear velocity as $\beta^* = \sqrt{\frac{\mu^*}{\rho}}$. For shear waves, the complex velocity is given by:

$$\beta^* = \sqrt{\frac{\mu^*}{\rho}} = \sqrt{\frac{\mu + i\omega\eta}{\rho}} = \beta_r + i\beta_i \tag{2.17}$$

where:

$$\beta_r = \left(\frac{\mu + \sqrt{\mu^2 + \eta^2\omega^2}}{2\rho}\right)^{\frac{1}{2}} \tag{2.18}$$

$$\beta_i = \left(\frac{-\mu + \sqrt{\mu^2 + \eta^2\omega^2}}{2\rho}\right)^{\frac{1}{2}} \tag{2.19}$$

The shear wave phase velocity, β_s, is:

$$\beta_s = \frac{\beta_r^2 + \beta_i^2}{\beta_r} = \frac{\sqrt{\frac{\mu^2}{\rho^2} + \frac{\omega^2\eta^2}{\rho^2}}}{\left(\frac{\mu + \sqrt{\mu^2 + \omega^2\eta^2}}{2\rho}\right)^{1/2}} = \beta\frac{\sqrt{1 + \frac{\omega^2\eta^2}{\mu^2}}}{\left(\frac{1 + \sqrt{1 + \frac{\omega^2\eta^2}{\mu^2}}}{2}\right)^{1/2}} \tag{2.20}$$

where β is the elastic shear wave velocity ($\beta = \sqrt{\mu/\rho}$).

The complex wave number, k^* is:

$$k^* = k_r + ik_i = \frac{\omega}{\beta^*} = \frac{\omega}{(\beta_r + i\beta_i)}\frac{(\beta_r - i\beta_i)}{(\beta_r - i\beta_i)} = \frac{\omega\beta_r - i\omega\beta_i}{\beta_r^2 + \beta_i^2} \tag{2.21}$$

where:

$$k_r = \frac{\omega\beta_r}{\beta_r^2 + \beta_i^2} \tag{2.22}$$

$$k_i = \frac{-\omega\beta_i}{\beta_r^2 + \beta_i^2} \tag{2.23}$$

We define the shear wave attenuation coefficient, α_s, to be the negative of k_i:

$$\alpha_s = -k_i \tag{2.24}$$

2.2.3 Viscoelastic Damping

We define the shear wave loss tangent, ξ_s, to be the negative of the ratio of the imaginary and real component of the complex wave number, k^*:

$$\xi_s = \frac{-k_i}{k_r} = \frac{\beta_i}{\beta_r} = \left(\frac{-\mu + \sqrt{\mu^2 + \eta^2\omega^2}}{\mu + \sqrt{\mu^2 + \eta^2\omega^2}}\right)^{\frac{1}{2}} = \left(\frac{\sqrt{1 + \frac{\eta^2\omega^2}{\mu^2}} - 1}{\sqrt{1 + \frac{\eta^2\omega^2}{\mu^2}} + 1}\right)^{\frac{1}{2}} \tag{2.25}$$

When the loss tangent is zero, there is no decay, and the wave is said to be undamped. When the loss tangent is between zero and unity, the wave has the shape of an exponentially decaying sinusoid, and the wave is said to be underdamped. As can be seen when $\xi = 0.5$ (Figure 2.2), underdamped materials may effect so

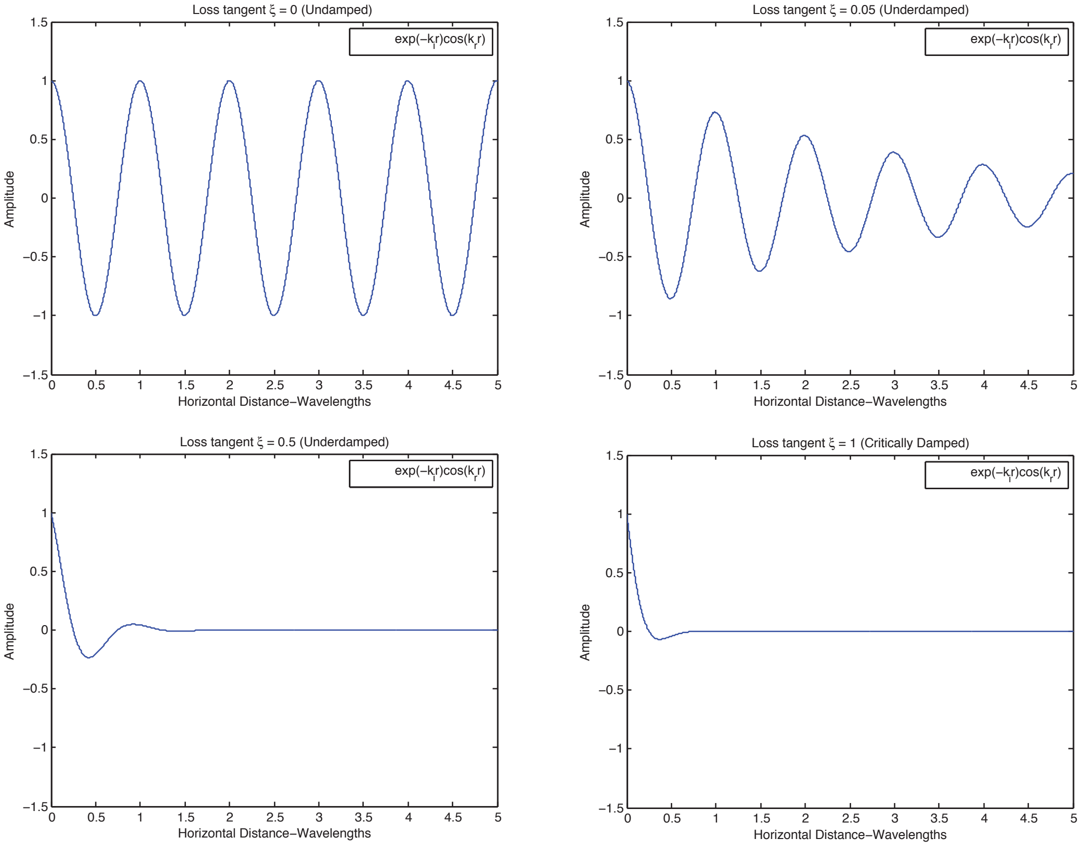

Figure 2.2: Viscoelastic attenuation of a plane wave with different loss tangents.

much attenuation that signals may become unmeasurable a few wavelengths from the source. When the loss tangent is equal to (critically damped) or greater than unity (overdamped), sinusoidal motion is completely suppressed within one wavelength of the source (Figure 2.2).

The loss tangent is analogous to the damping ratio (DR) used by geotechnical engineers (Kramer (1996) or ASTM-D-4015 (1996)):

$$DR = \frac{\omega\eta}{2\mu} \tag{2.26}$$

There are, however, important differences between the loss tangent and damping ratio. First, we note that the damping ratio is properly defined only for the temporal decay of an oscillating system, while the loss tangent represents spatial decay as a function of wave number or wavelength. Inspection of Equations 2.25 and 2.26 also reveals that for real values of η, μ, and ω, the loss tangent can only attain values between zero and unity, while the damping ratio can assume any value greater than or equal to zero. Thus, although it may be possible for a simple oscillator to be overdamped, it isn't possible for a simple shear wave to be overdamped. It is, however, possible for a Love wave to be overdamped (Chapter 3).

2.3 The 2-D Viscoelastic Shear Equation for a Homogeneous Medium

Consider a horizontally polarized shear wave propagating within a half-space. Particle displacement, v, is in the y-direction, perpendicular to the direction of propagation. We take z to be perpendicular to the plane of Earth's surface, with the positive z-axis in the downward direction (Figure 2.3). We rewrite Equation (2.16), the complex shear equation, as:

$$\frac{\partial^2 v(x,z,t)}{\partial t^2} = \frac{\mu^*}{\rho}\left(\frac{\partial^2 v(x,z,t}{\partial x^2} + \frac{\partial^2 v(x,z,t)}{\partial z^2}\right) \tag{2.27}$$

Equation 2.27 can be solved using the method of separation of variables. We begin by separating the solution to Equation 2.27 into three independent function of x, z, and t:

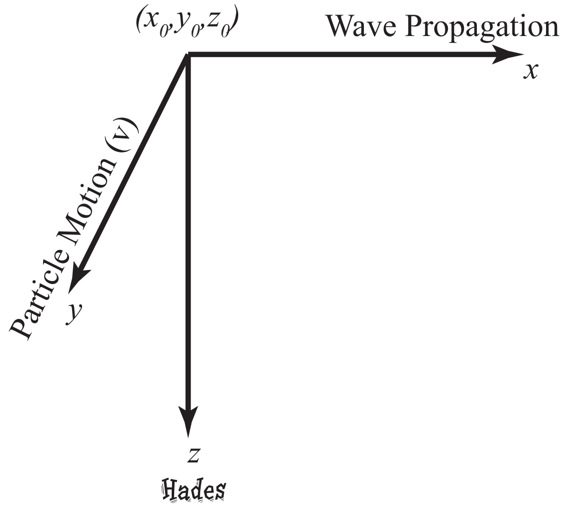

Figure 2.3: Coordinate system used in the derivation of shear and Love wave equations.

$$v(x,z,t) = R(x)L(z)T(t) \tag{2.28}$$

Substituting Equation 2.28 into Equation 2.27 and rearranging yields:

$$\frac{1}{T(t)}\frac{\partial^2 T(t)}{\partial t^2} = \frac{\mu^*}{\rho}\left(\frac{1}{R(x)}\frac{\partial^2 R(x)}{\partial x^2} + \frac{1}{L(z)}\frac{\partial^2 L(z)}{\partial z^2}\right) \tag{2.29}$$

Because T(t), R(x), and L(z) are independent functions, the only way for the left and right-hand sides of (2.29) to be equal to each other is for each side to equal a constant, which we will denote $-\omega^2$. Thus, Equation 2.29 can be decomposed into two differential equations:

$$\frac{1}{T(t)}\frac{\partial^2 T(t)}{\partial t^2} = -\omega^2 \tag{2.30}$$

$$\frac{1}{R(x)}\frac{\partial^2 R(x)}{\partial x^2} + \frac{1}{L(z)}\frac{\partial^2 L(z)}{\partial z^2} = \frac{-\omega^2}{\beta^{*2}} \tag{2.31}$$

Similarly, (2.31) can be decomposed into two independent differential equations:

$$\frac{\mu}{\rho}\left(\frac{1}{R(x)}\frac{\partial^2 R(x)}{\partial x^2}\right) = -K^{*2} \tag{2.32}$$

$$\frac{1}{L(z)}\frac{\partial^2 L(z)}{\partial z^2} = K^{*2} - \frac{\omega^2}{\beta^{*2}} \tag{2.33}$$

where K^* is the horizontal wave number.

The solutions to Equations 2.30, 2.32, and 2.33 are:

$$\begin{aligned} T(t) = & \quad a_1 e^{-\omega t} + a_2 e^{\omega t} \\ R(x) = & \quad b_1 e^{-K^* x} + b_2 e^{K^* x} \\ L(z) = & \quad (s_d e^{-\nu z} + s_u e^{\nu z}) \end{aligned} \tag{2.34}$$

where the eigenvalue $\nu = \sqrt{K^{*2} - \frac{\omega^2}{\beta^{*2}}}$ is the vertical wave number, and the coefficients s_d and s_u are coefficients for the down-going and up-going z-components of the wave, respectively.

For a wave moving in the positive x direction, a_2 and b_1 are zero. We set $a_1 = b_2 = 1$ to obtain:

$$v(x,z,t) = L(z)R(x)T(t) = \left(s_d e^{-\nu z} + s_u e^{\nu z}\right) e^{i(K^* x - \omega t)} \tag{2.35}$$

By substituting $K^* = K_r + iK_i$ into (2.35), we obtain:

$$v(x,z,t) = L(z)R(x)T(t) = L(z)e^{K_i x} e^{i(K_r x - \omega t)} \tag{2.36}$$

which describes damped oscillation propagating in the x direction. Thus, the imaginary wave number component, K_i, is a spatial attenuation factor.

CHAPTER 3:

LOVE WAVE PROPAGATION IN LAYERED VISCOELASTIC MEDIA

3.1 Introduction

In Chapter 11 of his essay, *Some Problems of Geodynamics*, Love derived equations for transverse waves in a single superficial layer over a half-space (Figure 3.1), and demonstrated that such a system produces a series of laterally polarized, large amplitude waves with well defined periodicity (Love, 1911). Love attributed this behavior to the formation of standing waves in the superficial layer, and demonstrated that efficient standing wave formation requires that S-wave velocity in the superficial layer be less than that of the half space ($\frac{\beta_1}{\beta_2} < 1$).

Chapter 7 of Aki and Richards (2009) is a general discussion of surface waves in a vertically heterogeneous medium, and it includes models for Love and Rayleigh waves in layered, as well as continuously varying elastic media. In this chapter, we will extend their treatment to propagation in layered viscoelastic media, but confine our derivation to the case of horizontally polarized shear waves (S-H waves) in a vertically layered medium over a half-space.

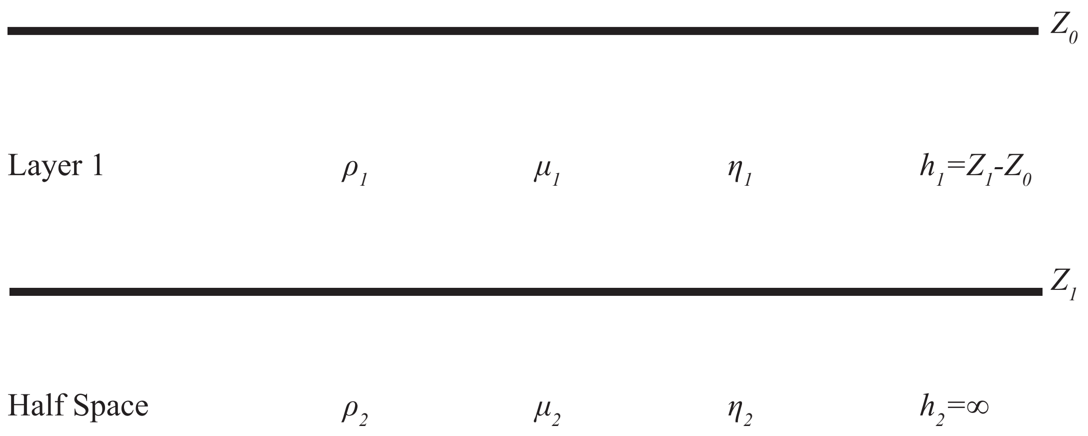

Figure 3.1: Nomenclature and layer properties for a single layer over a half-space. ρ_j, μ_j, and η_j are, respectively, the density, shear modulus, and viscosity of layer j.

3.2 The Shear Wave Equation for a Layered Viscoelastic Medium over a Half-Space

In the previous section, we derived a relationship for particle displacement, v, in a homogeneous viscoelastic medium. We would like to extend this treatment to a horizontally layered medium. For layered media, density, shear modulus, and viscosity are functions of depth (Figure 3.2). In our derivation for a single homogeneous layer, we defined $T(t)$ and $R(x)$ in such a way that they are independent of depth; thus, we need only derive a relationship for $L(z)$ to extend our theory to layered media.

A layered structure represents a coupled system in which adjacent layers are connected to each other. At each interface, we will impose a no-slip condition, such that both the displacement and stress on each side of the interface must be equal. We will find it convenient to define two new terms: A motion term, and a stress term. The

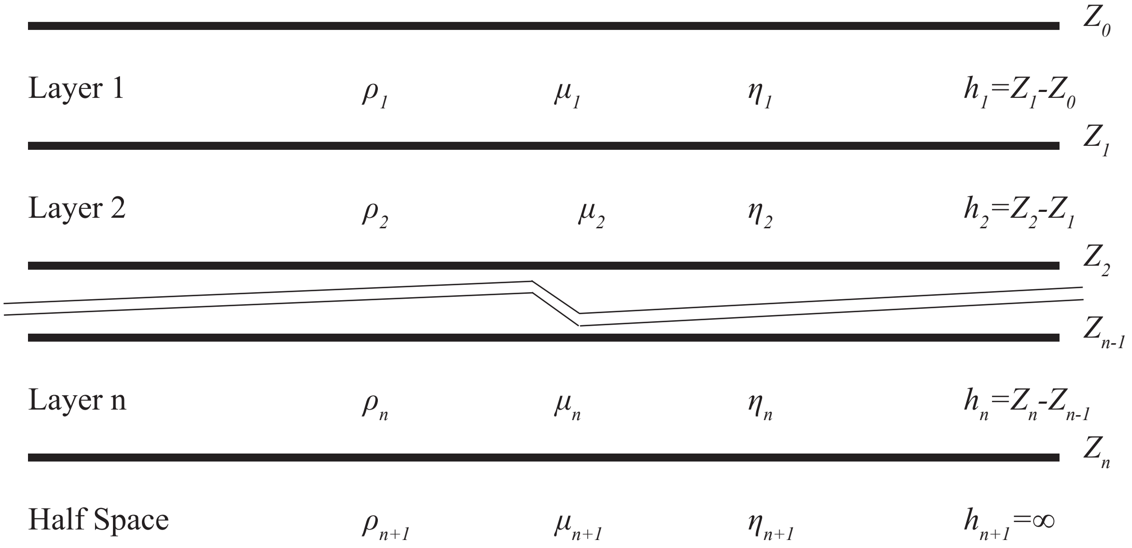

Figure 3.2: Nomenclature and layer properties for a layered system over a half-space. ρ_j, μ_j, and η_j are, respectively, the density, shear modulus, and viscosity of layer j.

motion term, $l_{m,j}(z)$ denotes the value of $L(z)$ for layer j at depth z. The stress term denotes the $\tau_{z,y}$ stress at the same location, and is given by:

$$l_{s,j}(z) = \mu \frac{\partial l_{m,j}(z)}{\partial z} \tag{3.1}$$

Applying Equation 3.1 to Equation 2.35, we see that stress within a homogeneous layer is given by:

$$\tau_{z,y}(z) = \mu \frac{\partial v(x,z,t)}{\partial z} = \mu^* \nu \left(-s_d e^{-\nu z} + s_u e^{\nu z} \right) e^{i(k^* x - \omega t)} \tag{3.2}$$

The motion and stress terms can be combined into a single motion-stress vector:

$$l_j(z) = \begin{bmatrix} l_{m,j}(z) \\ l_{s,j}(z) \end{bmatrix} \tag{3.3}$$

The no-slip condition assures that the displacement of two adjacent layers is the same at each interface: $L_j(z) = L_{j+1}(z)$, where j and $j+1$ are layer indices. Similarly, the interfacial stress must also be equal. Expressed in terms of motion-stress vectors, this is:

$$\boldsymbol{l_j(z) = l_{j+1}(z)} \tag{3.4}$$

In the following sections, we will develop a propagator matrix, $\boldsymbol{P(z_a, z_b)}$ that will represent the coupling relationship between any two arbitrary depths, z_a and z_b:

$$\boldsymbol{l(z_a) = P(z_a, z_b) l(z_b)} \tag{3.5}$$

There is no stress at the free surface ($z = 0$); thus, we can impose the Dirichlet boundary condition that $\tau_{y,z} = 0$ at z = 0. We will use the subscript j to denote the lower interface of layer j, so that the surface will be z_0, the bottom of the first layer will be z_1, and so-on until the bottom of layer n, z_n.

$$\tau_{y,z} = \mu \frac{\partial v}{\partial z} = \mu \frac{\partial L(0)}{\partial z} = l_{s,1}(0) = 0 \tag{3.6}$$

For an n-layer system, a propagator representing the coupling between the free surface and the bottom of the n^{th} layer will be:

$$\boldsymbol{l(z_n) = P(z_n, z_0) l(z_0)} \tag{3.7}$$

Of course, z_n also denotes the top of the half-space. At the boundary between the n^{th} layer and the half-space, a down-going wave is generated, but because the half-space is theoretically infinite, there will be no corresponding wave traveling upward through the half-space to the interface, so our formulation of a propagator matrix for the half-space will differ from that in the layered zone. We will denote the propagator matrix for the half-space as $\boldsymbol{P(z_\infty, z_n)}$, and the relationship between the motion-stress vector at the surface and the up-going and down-going displacement amplitudes in the half space as:

$$\begin{bmatrix} s_d \\ s_u \end{bmatrix} = \boldsymbol{P(z_\infty, z_n)P(z_n, z_0)l(z_0)} \tag{3.8}$$

For a single layer over a half-space, these two boundary conditions are sufficient. Alternative solutions for a single elastic layer over a half space can be found in Section 7.1 of Aki and Richards (2009) and Section 5.3.2 of Kramer (1996).

3.2.1 Propagator Matrix for a Layered Medium–$\boldsymbol{P(z_n, z_0)}$

Thomson (1950) developed a generalized matrix formulation for dilational and rotational elastic waves in layered media. Haskell (1953) refined Thomson's model and used it to study Love and Rayleigh waves in Earth's crust. Haskel demonstrated the method's utility by comparing two-layer Rayleigh wave models to data obtained from North American earthquakes and rock slides; however, he neither attempted a formal data inversion, nor did he extend his demonstration to Love waves.

The method developed by Thomson and Haskell assembled submatrices into a single large matrix that could be solved by numerical integration; however, truncation errors could cause the method to become unstable (Dunkin, 1965), and several authors proposed modifications to ameliorate numerical errors (Rosenbaum, 1964). Knopoff (1964) suggested an entirely new matrix formulation using the method of propagator matrices. First proposed by Volterra (1887) as a method for solving systems of coupled linear differential equations, the propagator method provides a systematic procedure for creating separate matrices for each layer, and then combining them into a single matrix via matrix multiplication.

Gilbert and Backus (1966) collated the methods of Thomson, Haskell, Rosenbaum, and Knopoff into a cogent procedure for obtaining a propagator matrix suitable for trial-and-error solution by numerical integration. The method involved numerical integration of the propagator matrix from a location deep in the half-space to the top of the layer stack. The integration is repeated using different values of the Love or Rayleigh wave number until the correct surface boundary conditions are obtained. Aki and Richards (2009) outline a clever method for tying boundary conditions at the surface to the surface that permits solution of the Gilbert and Backus propagator matrix without numerical integration.

Chapter 7 of Aki and Richards (2009) is a general discussion of surface wave propagation in heterogeneous media. Their methods are general, and include solutions for both Love and Rayleigh waves in continuously changing, as well as layered media. In the present treatment, we focus on Love waves in layered media, so it will be possible to simplify both the derivation and the nomenclature. In their propagator matrix solution, Aki and Richards employed the Sylvester-Lagrange formula. In our derivation, we will follow the method used by Sadun (2001), since it uses matrix methods that will be familiar to any reader with an elementary knowledge of linear algebra.

We begin by rearranging and rewriting (2.33) in terms of $l_{m,j}$ and $l_{s,j}$:

$$\begin{aligned} \frac{\partial^2 L(z)}{\partial z^2} - L(z)\left(K^{*2} - \frac{\omega^2}{\beta^{*2}}\right) &= 0 \\ \frac{\partial}{\partial z}\left(\frac{l_{s,j}}{\mu^*}\right) - l_{m,j}\left(K^{*2} - \frac{\omega^2}{\beta^{*2}}\right) &= 0 \end{aligned} \tag{3.9}$$

We can now write (3.9) in terms of motion-stress vectors:

$$\frac{\partial}{\partial z}\begin{bmatrix} l_{m,j} \\ l_{s,j} \end{bmatrix} = \begin{bmatrix} 0 & \frac{1}{\mu^*} \\ \left(K^{*2} - \frac{\omega^2}{\beta^{*2}}\right)\mu^* & 0 \end{bmatrix}\begin{bmatrix} l_{m,j} \\ l_{s,j} \end{bmatrix} \tag{3.10}$$

Equation 3.10 could be integtrated, numerically, to find values of the motion-stress vector, and thus, L(z). The method is outlined in Aki and Richards (2009) Section 7.2.1, as well as in texts on numerical integration like Desai and Christian (1977) Section 17. It is an iterative method that assumes values for K^*, and then integrates from a position deep in the half-space to the surface of the top layer. A value of K^* is assumed to be correct when the value of the stress vector is zero at the surface.

The propagator matrix is an analytical method for determining the motion-stress vector and L(z). We rewrite (3.10) in matrix form:

$$\frac{\partial \boldsymbol{l_j}}{\partial z} = \boldsymbol{A l_j} \tag{3.11}$$

For a single, homogeneous layer, a solution to this first order linear differential equation is the propagor matrix (Sadun, 2001):

$$\boldsymbol{P(z_j, z_{j-1})} = e^{(z_j - z_{j-1})\boldsymbol{A}} = e^{h_j \boldsymbol{A}} \tag{3.12}$$

where h_j is the thickness of layer j.

Chapter 5 of Sadun (2001) discusses the properties of the propagator matrix. A most useful property is the ability to combine propagator matrices in a sort of chain:

$$\boldsymbol{P(z_n, z_0) = P(z_n, z_{n-1)} P(z_{n-1}, z_{n-2)} ... P(z_2, z_1) P(z_1, z_0)} \tag{3.13}$$

Thus, a solution for an entire stack of layers can be found given $\boldsymbol{P}$ for each of its constituent layers. A difficulty computing $\boldsymbol{P}$ arises when using Equation 3.12. The exponent of a matrix is not generally defined in terms of elementary functions, and direct computation requires the use of a matrix Taylor series. A simpler computation is obtained by diagonalizing $\boldsymbol{A}$ (Sadun, 2001):

$$\boldsymbol{A = Q \Lambda Q^{-1}} \tag{3.14}$$

where $\boldsymbol{\Lambda}$ is a diagonal matrix of eigenvalues, and $\boldsymbol{Q}$ is a matrix of eigenvectors.

Sadun (2001) demonstrates that the exponent of a square diagonal matrix such as $\boldsymbol{\Lambda}$ is:

$$e^{\boldsymbol{\Lambda}} = \begin{bmatrix} e^{\nu_1} & 0 \\ 0 & e^{\nu_2} \end{bmatrix} \tag{3.15}$$

where ν_1 and ν_2 are the eigenvalues in Λ. A second useful result is that, for a diagonalized matrix:

$$e^{\boldsymbol{Q \Lambda Q^{-1}}} = \boldsymbol{Q e^{\Lambda} Q^{-1}} \tag{3.16}$$

We find the eigenvalue matrix of $\boldsymbol{A}$:

$$e^{\boldsymbol{\Lambda}} = \begin{bmatrix} e^{\nu} & 0 \\ 0 & e^{-\nu} \end{bmatrix} \tag{3.17}$$

Where $\pm\nu$ are the eigenvalues of $\boldsymbol{A}$, and

$$\nu = \sqrt{K^{*2} - \frac{\omega^2}{\beta^{*2}}} \tag{3.18}$$

The eigenvector matrix, $\boldsymbol{Q}$ and its inverse are:

$$\boldsymbol{Q} = \begin{bmatrix} 1 & 1 \\ \nu\mu^* & -\nu\mu^* \end{bmatrix} \tag{3.19}$$

$$\boldsymbol{Q^{-1}} = \frac{1}{2}\begin{bmatrix} 1 & \frac{1}{\nu\mu^*} \\ 1 & -\frac{1}{\nu\mu^*} \end{bmatrix} \tag{3.20}$$

We can rewrite Equation (3.12) as:

$$\boldsymbol{P(z_{j+1}, z_j) = Qe^{h_j\Lambda}Q^{-1}} = \begin{bmatrix} cosh(\nu h_j) & \frac{1}{\nu\mu^*}sinh(\nu h_j) \\ \nu\mu^* sinh(\nu h_j) & cosh(\nu h_j) \end{bmatrix} \tag{3.21}$$

3.2.2 Propagator Matrices for a Half-Space and for an Arbitrary Depth–$\boldsymbol{P(z_\infty, z_n)}$ and $\boldsymbol{P(z, z_n)}$

Because the half space is infinite, $h_{n+1} = \infty$, applying Equation 3.21 results in infinite values of all four matrix elements. Recall that our solution to Equation 3.11 resulted in two sets of eigenvalues/eigenvectors that tacitly represent both up-going and down-going waves, and as noted earlier, there are no up-going waves in the half-space. Thus, the positive eigenvalue in Equation 3.15 goes to zero, and in the half-space:

$$e^{\mathbf{\Lambda}} = \begin{bmatrix} 0 & 0 \\ 0 & e^{\nu_2} \end{bmatrix} \tag{3.22}$$

The equation for a propagator element $P(z, z_n)$ at an arbitrary depth, z, in the half-space can be derived in a manner analogous to our derivation of Equation 3.21:

$$\boldsymbol{P(z, z_n) = Qe^{h_{n+1}\Lambda}Q^{-1}} = \frac{1}{2} \begin{bmatrix} e^{-\nu h_{n+1}} & \frac{-1}{\nu\mu^*} e^{-\nu h_{n+1}} \\ -\nu\mu^* e^{-\nu h_{n+1}} & e^{-\nu h_{n+1}} \end{bmatrix} \tag{3.23}$$

The boundary conditions at Earth's surface are formulated in terms of a motion-stress vector, while those in the half-space are formulated in terms of the upward and downward propagation coefficients, s_d and s_u. In order to reconcile the boundary conditions at the surface with those in the half-space, we will rewrite Equations 2.35 and 3.2 as a motion-stress vector:

$$l_j(z) = \begin{bmatrix} l_m(z_n) \\ l_s(z_n) \end{bmatrix} = \begin{bmatrix} e^{-\nu z_n} & e^{\nu z_n} \\ -\nu\mu^* e^{\nu z_n} & \mu^* \nu e^{\nu z_n} \end{bmatrix} \begin{bmatrix} s_d \\ s_u \end{bmatrix} \tag{3.24}$$

so that Equation 3.24 gives the motion-stress vector at the top of the half-space as a function of the up-going and down-going displacement functions. Inverting this, we obtain an equation for the upgoing and downgoing displacement functions in terms of the motion-stress vector at the top of the half-space:

$$\begin{bmatrix} s_d \\ s_u \end{bmatrix} = \frac{1}{2} \begin{bmatrix} e^{\nu z_n} & -\frac{1}{\nu\mu^*} e^{\nu z_n} \\ e^{-\nu z_n} & \frac{1}{\nu\mu^*} e^{-\nu z_n} \end{bmatrix} \begin{bmatrix} l_m(z_n) \\ l_s(z_n) \end{bmatrix} = \boldsymbol{P(z_\infty, z_n) l(z_n)} \tag{3.25}$$

Substituting for $\boldsymbol{l(z_n)}$ using Equations (3.8) and (3.13):

$$\begin{bmatrix} s_d \\ s_u \end{bmatrix} = \boldsymbol{P(z_\infty, z_n)} \prod_{j=0}^{n} \boldsymbol{P(j+1, j) l(z_0)} \tag{3.26}$$

3.2.3 The Objective Function

Multiplying the propagator matrices in (3.26), and applying the boundary conditions that the stress vector be zero at the surface, and that the upward displacement vector vanish in the half-space:

$$\begin{bmatrix} s_d \\ 0 \end{bmatrix} = \begin{bmatrix} B_{1,1} & B_{1,2} \\ B_{2,1} & B_{2,2} \end{bmatrix} \begin{bmatrix} l_m(z_0) \\ 0 \end{bmatrix} \tag{3.27}$$

Note that for Equation 3.27 to be true, it is necessary that $B_{2,1}$ always equal zero. Eigenvalues (ν) correspond to the values of ω, and K^* for which $B_{2,1} = 0$. We will refer to $B_{2,1}$ as the objective function, and for a given set of layer and half-space properties, our strategies for finding eigenvalues will be to search for values of K^* that drive the objective function to zero.

$$\begin{aligned} u &= 0 \\ v(x,z,t) &= \left(s_d e^{-\nu z} + s_u e^{\nu z}\right) e^{i(K^* x - \omega t)} = L(z) e^{i(K^* x - \omega t)} \\ w &= 0 \end{aligned} \tag{3.28}$$

For a single layer over a half-space, Equation 3.28 reduces to Equation 2.35.

As is generally the case for shear waves, normal stresses in the x, y, and z directions will be zero:

$$\tau_{x,x} = \tau_{y,y} = \tau_{z,z} = 0 \tag{3.29}$$

Shear stresses can be found by differentiating the displacement relationships of (3.28), and multiplying by the shear modulus, μ:

$$\begin{aligned}
\tau_{x,z} &= 0 \\
\tau_{y,z} &= \mu \frac{dL(z)}{dz} e^{i(K^* x - \omega t)} \\
\tau_{y,x} &= iK^* \mu L(z) e^{i(K^* x - \omega t)}
\end{aligned} \tag{3.30}$$

3.2.4 Love Wave Velocity and Wave Number Relationships

Love wave velocity/wave number relationships are similar to those derived for shear waves in Chapter 2. The complex Love Wave velocity is $C^* = C_r + iC_i$, where C_r and C_i are the real and imaginary components, respectively. We can obtain the complex wave number from frequency and complex wave velocity using the following relationship:

$$K^* = \frac{\omega}{C^*} = \frac{\omega}{(C_r + iC_i)} \frac{(C_r - iC_i)}{(C_r - iC_i)} = \frac{\omega C_r - i\omega C_i}{C_r^2 + C_i^2} \tag{3.31}$$

so the real and imaginary components of the Love wave complex wave number are:

$$K_r = \frac{\omega C_r}{C_r^2 + C_i^2} \tag{3.32}$$

$$K_i = \frac{-\omega C_i}{C_r^2 + C_i^2} \tag{3.33}$$

We will define the Love wave attenuation coefficient, α_L to be the negative of K_i:

$$\alpha_L = -K_i \tag{3.34}$$

The Love wave phase velocity can be found by inserting (3.32) into the relationship between velocity, wave number, and frequency (Chakravarthy, 2008):

$$C_L = \frac{\omega}{K_r} = \frac{C_r^2 + C_i^2}{C_r} \tag{3.35}$$

We define the Love wave loss tangent, ξ_L::

$$\xi_L = \frac{-K_i}{K_r} = \frac{C_i}{C_r} \tag{3.36}$$

We should note that, unlike the shear wave loss tangent, it is possible for the Love wave loss tangent to exceed unity.

3.3 Geometric Dispersion

In order to separate the effects of material damping from attenuation due to geometric spreading, it will be necessary to adjust our model for the attenuation that occurs when waves radiate from a finite source. To this point, our derivation has assumed

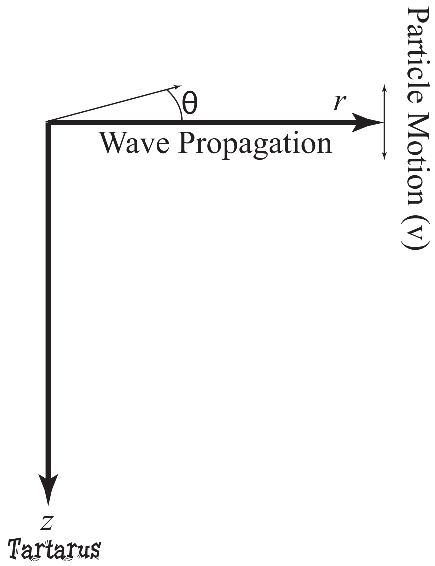

Figure 3.3: Coordinate system used in the polar coordinate derivation of the shear and Love wave equations.

plane waves of infinite lateral extent, and thus no geometric spreading. This is a reasonable assumption when applied to small regions far from the source; however, most near-surface geophysical investigation is conducted over regions that are relatively large and in close proximity to the seismic source. In this section, we will rederive Equation 2.35 in cylindrical coordinates. The result will be a type one, zero order Bessel function, which can be reasonably approximated by dividing Equation 2.35 by the square root of the radial distance from the source.

3.3.1 The Wave Equation in Cylindrical Coordinates

In Cartesian coordinates, the 3-D wave equation is:

$$\frac{\partial^2 v(x,y,z,t)}{\partial t^2} = \frac{\mu^*}{\rho}\nabla^2 v(x,y,z,t) \tag{3.37}$$

In cylindrical coordinates, the particle displacement function becomes $v(r, \theta, z, t)$. When r and θ are written as functions of x and y, this becomes: $v(r(x, y), \theta(x, y), z, t)$. Consider a horizontally polarized shear wave propagating along Earth's surface in the r-direction. Particle displacement, v, is in the θ-direction, perpendicular to the direction of propagation. As was the case in our Cartesian derivation, we take z to be perpendicular to the plane of Earth's surface, with the positive z axis in the downward direction (Figure 3.3). Assuming displacement angles to be small, and v to be symmetric about the source, we can neglect θ dependence: $v(r(x, y), z, t)$.

The relationship between x, y, and r is:

$$r^2 = x^2 + y^2 \tag{3.38}$$

Single and double integration of Equation 3.38 with respect to x gives:

$$\frac{\partial r}{\partial x} = \frac{x}{r} \tag{3.39}$$

$$\frac{\partial^2 r}{\partial x^2} = \frac{1}{r}\left(1 - \left(\frac{\partial r}{\partial x}\right)^2\right) = \frac{1}{r}\left(1 - \left(\frac{x^2}{r^2}\right)^2\right) \tag{3.40}$$

Similar relationships are obtained for y:

$$\frac{\partial r}{\partial y} = \frac{y}{r} \tag{3.41}$$

$$\frac{\partial^2 r}{\partial y^2} = \frac{1}{r}\left(1 - \left(\frac{\partial r}{\partial y}\right)^2\right) = \frac{1}{r}\left(1 - \left(\frac{y^2}{r^2}\right)^2\right) \tag{3.42}$$

By the chain rule, partial derivatives of v(r(x,y),z,t) with respect to x and y are:

$$\frac{\partial^2 v(r(x,y),z,t)}{\partial x^2} = \frac{\partial^2 r}{\partial x^2}\left(\frac{\partial v}{\partial r}\right) + \left(\frac{\partial r}{\partial x}\right)^2\left(\frac{\partial^2 v}{\partial r^2}\right) \tag{3.43}$$

$$\frac{\partial^2 v(r(x,y),z,t)}{\partial y^2} = \frac{\partial^2 r}{\partial y^2}\left(\frac{\partial v}{\partial r}\right) + \left(\frac{\partial r}{\partial y}\right)^2\left(\frac{\partial^2 v}{\partial r^2}\right) \tag{3.44}$$

Substituting these into the Cartesian wave equation (3.37), and simplifying using Equations 3.38 through 3.42 gives us:

$$\frac{\partial^2 v(r,\theta,z,t)}{\partial t^2} = \frac{\mu^*}{\rho}\left(\frac{1}{r}\frac{\partial}{\partial r}\left(r\frac{\partial v}{\partial r}\right) + \frac{\partial^2 v}{\partial z^2}\right) \tag{3.45}$$

3.3.2 Solution to the Wave Equation in Cylindrical Coordinates

Our approach to solving the wave equation in cylindrical coordinates will be analogous to our approach for Cartesian coordinates. We begin again by separating the solution to (3.45) into three independent functions of r, z, and t:

$$v(r,z,t) = L(z)S(r)T(t) \tag{3.46}$$

Applying the method of separation of variables, we find that the cylindrical solutions for $L(z)$ and $T(t)$ are the same as those for (2.33) and (2.30); however, we obtain the following differential equation for $S(r)$:

$$r^2\frac{\partial^2 S(r)}{\partial r^2} + r\frac{\partial S(r)}{\partial r} + k^{*2}r^2 S(r) = 0 \tag{3.47}$$

This has the general form of a Bessel's equation of order zero (Asmar, 2000). We can put it in standard form using a change of variables. Let $s = k^*r$, so that:

$$\frac{\partial S(s)}{\partial r} = \frac{\partial s}{\partial r}\frac{\partial S(s)}{\partial s} = k^*\frac{\partial S(s)}{\partial s} \tag{3.48}$$

$$\frac{\partial^2 S(s)}{\partial r^2} = \left(\frac{\partial s}{\partial r}\right)^2 \frac{\partial^2 S(s)}{\partial s^2} = k^{*2}\frac{\partial^2 S(s)}{\partial s^2} \tag{3.49}$$

Substituting these into (3.47), dividing the entire equation by k^{*2}, and substituting $s = k^*r$, we obtain:

$$s^2\frac{\partial^2 S(s)}{\partial s^2} + s\frac{\partial S(s)}{\partial s} + s^2 S(s) = 0 \tag{3.50}$$

$$s = k^*r$$

for which the solution is a zero order Bessel function of the first type (Wylie and Barrett, 1982):

$$S(s) = J_0(s) = J_0(k^*r) \tag{3.51}$$

A complete solution to (3.45) is:

$$v(x, z, t) = L(z)S(r)T(t) = \left(s_d e^{-\nu z} + s_u e^{\nu z}\right) e^{-i\omega t} J_0(k^*r) \tag{3.52}$$

3.3.3 Correction for Geometric Spreading

Equation 3.52 is not amenable to signal-processing techniques in common use by geoscientists and engineers, and we will find it convenient to devise a method for approximating it using trigonometric functions.

The complex Bessel's function on the right-hand side of (3.52) can be approxi-

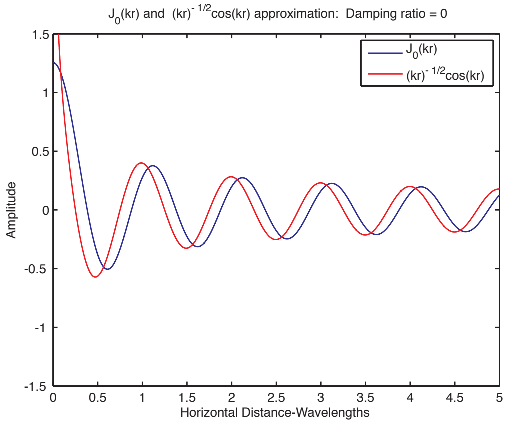

Figure 3.4: Bessel function and an approximation using Equation (3.54).

mated by $J_0(k^* r) \approx e^{k_i r} J_0(k_r r)$ (Cohen, 1908), so:

$$v(x,z,t) \approx \left(s_d e^{-\nu z} + s_u e^{\nu z}\right) e^{-i\omega t} e^{k_i r} J_0(k_r r) \tag{3.53}$$

At large values of kr, $J_0(kr)$ converges to the quotient of a cosine function and the square root of kr (Wylie and Barrett, 1982), so Equation 3.53 can be rewritten:

$$v(x,z,t) \approx \left(s_d e^{-\nu z} + s_u e^{\nu z}\right) e^{k_i r} \frac{e^{i(kr - \omega t + \pi/4)}}{\sqrt{kr}} \tag{3.54}$$

which suggests a data transformation based on the square root of radial distance from the source. In fact, such transformations are commonly used to transform surface wave data. Their justification typically involves the conservation of energy: As a surface wave expands, its energy is distributed over an increasingly large annulus whose volume is proportional to radius. Amplitude decreases with the square root of energy density; thus, amplitude should decrease with the square root of radial distance.

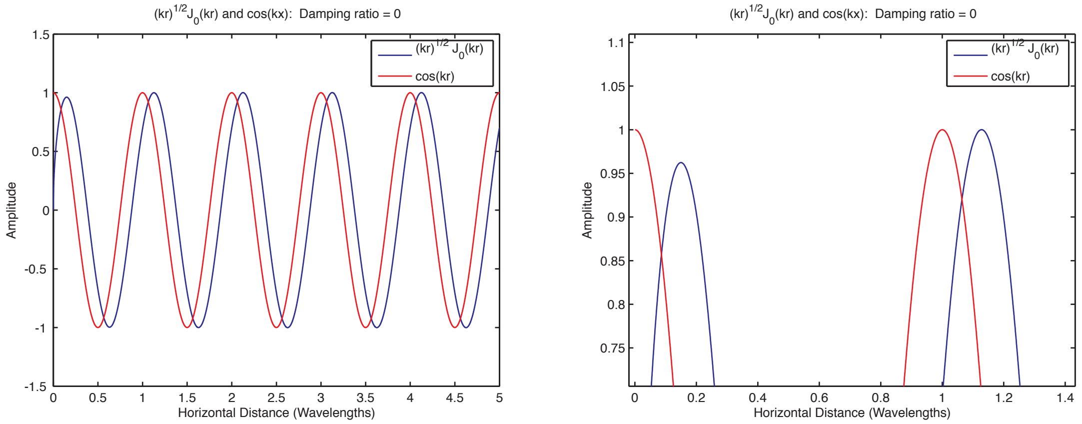

Figure 3.5: Bessel function multiplied by $\sqrt{kx}$ compared to $cos(kx)$. Aside from distortion during the first cycle, the result of the $\sqrt{kx}$ transformation is nearly sinusoidal. $(right)$ Detail of the first two cycles.

In Figure 3.4, we see that after the first complete wavelength, Equation 3.54 provides a remarkably good approximation to Equation 3.52.

At the end of the first cycle, the value obtained from the approximation is 3.9% greater than that of the exact solution, and by the end of the second cycle, the discrepancy has fallen to less than 0.1%, and it decreases by at least an order of magnitude with each subsequent cycle. The transformed Bessel function lags the cosine function by $\frac{\pi}{4}$ radian.

Published values of the damping ratio are typically between 1% and 10% per cycle (Hardin, 1965), so transformed data obtained from Equation (3.5) should be a satisfactory transformation, so long as all data used in analysis is obtained beyond one or two wavelengths of the source.

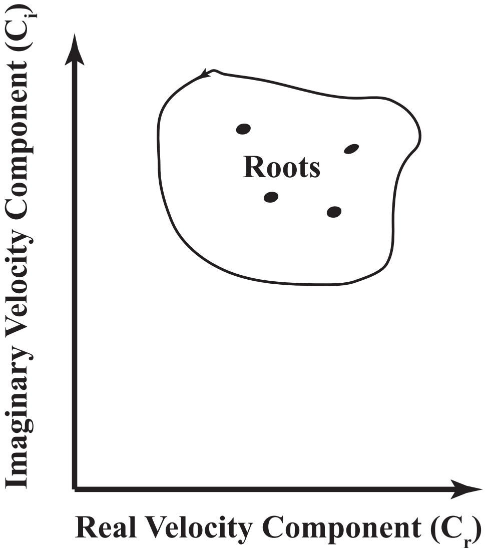

Figure 3.6: Equation 3.56 yields a numerical value equal to the number of points enclosed by the arbitrary closed curve. In this case, $I(z)$=4.

3.3.4 Finding Solutions to the Love Wave Equation

Each eigenvenvalue of Equation 3.18, represents a Love wave normal mode. As we will see in Chapter 4, the complex velocity associated with each normal mode is a complicated function of frequency, soil properties, and layer structure. Finding a normal mode is tantamount to finding the complex velocity for which the objective function equals zero. Chakravarthy (2008) found roots of a single-layer model using a point-by-point grid search, and subsequent path of steepest descent (PSD) method to refine his complex velocity estimate. This is a reasonably robust method, but it requires that a new grid search be conducted for each frequency increment, and for each time that soil parameters are changed: For a multi-layer model, this can be a computationally expensive approach.

Our method for finding and tracking normal modes will rely on the argument principle from the calculus of residues. The reader interested in more detail is referred to texts on analysis or complex variables. We will rely on Ablowitz and Fokas (2003) for the following discussion.

A function is said to be analytic at a point z_0 on the complex plane if it is differentiable at that point. It is said to be analytic in a region if it is differentiable at every point over that region. Isolated, undifferentiable points in a region that is otherwise analytic are called singularities. Of interest to the present discussion are singularities that occur when the denominator of the function goes to zero, as occurs at z_0 for $f(z) = \frac{1}{z-z_0}$.

Polynomial and exponential functions are analytic, as are functions created by the sums or products of these functions, so the trigonometric and hyperbolic sine and cosine functions are analytic, too. In fact, ratios of these functions are analytic except at the singularities that result when a denominator becomes zero. Perusal of the propagator matrices derived earlier in this chapter reveals that these are, indeed, functions comprised of sums and products of exponential and hyperbolic functions. Thus, the objective function, $B_{2,1}$ is also analytic.

Love wave normal modes correspond to complex roots of the objective function. That is, points where $B_{2,1}$ equals zero. Thus, the reciprocal of the objective function, $\frac{1}{B_{2,1}}$, will have singularities at each root. A consequence of this is the argument principle, which states that for an analytic function, the following relation holds:

$$I(z) = \frac{1}{2\pi i} \oint_C \frac{f'(z)}{f(z)} dz = N - P \tag{3.55}$$

where $f(z)$ is meromorphic: That is, $f(z)$ is well-behaved and analytic except at a few singularities. N is the number of zeros enclosed within the contour C, and P is the

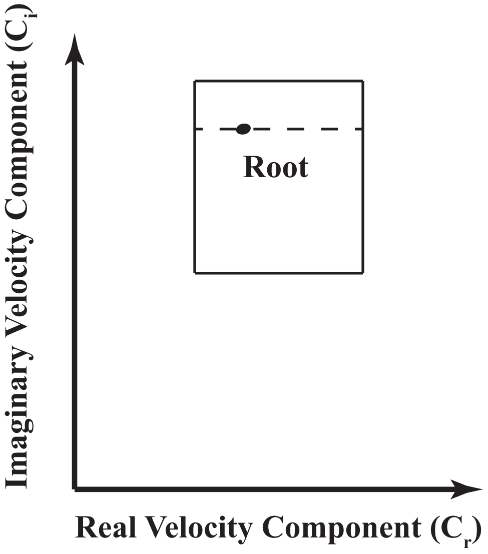

Figure 3.7: By shrinking the top edge of a rectangular contour until the path integral is equal to zero, we can determine the root's imaginary coordinate. Repeating the procedure with a vertical edge allows us to determine the root's real coordinate.

number of poles. We should also note that an assumption of the argument principle is that no poles or zeros can occur on the contour, C, itself. Since there are no poles in the objective function, Equation 3.55 can be restated as:

$$I(z) = \frac{1}{2\pi i} \oint_C \frac{B'(z)}{B(z)} dz = N \tag{3.56}$$

Rather than calculating the objective function for every point in a region, we can determine the number of roots by computing a path integral around the region (Figure 3.6). If a region has only one root, we can determining its location by systematically collapsing the path integral: The point at which $I(z) = 0$ corresponds to the coordinates of the root. This is illustrated in Figure 3.7

CHAPTER 4:

LOVE WAVE MODES IN LAYERED VISCOELASTIC SOILS

In Chapter 1, we described, qualitatively, Love wave behavior in a single elastic layer over an elastic half space. In Chapter 3, we extended the theory of Love wave propagation to multiple viscoelastic layers. In the present chapter, we will examine the ramifications of layering and viscoelasticity, while paying particularly close attention to the surface expression of these changes.

After examining elastic and viscoelastic systems consisting of a single layer over a half-space, we will introduce a simple scaling heuristic that can be extended to multi-layered systems. We will use this heuristic to develop multi-layered homologues of single-layered systems, and then compare the behaviors of these systems.

4.1 Single Elastic Layer over a Half-Space

In Chapter 1, we noted that a necessary condition for Love wave propagation is the existence of a relatively slow surface layer over a faster half-space. Above the critical incidence angle, θ_c, Love waves result from constructive interference of waves trapped within the layer. An interesting feature of the Love wave system is the formation of an angle-dependent stress field at the top of the half-space. The evanescent wave formed in this stress field induces a phase shift that causes different frequencies to *see* different layer thicknesses, leading to the characteristic dispersive behavior of Love

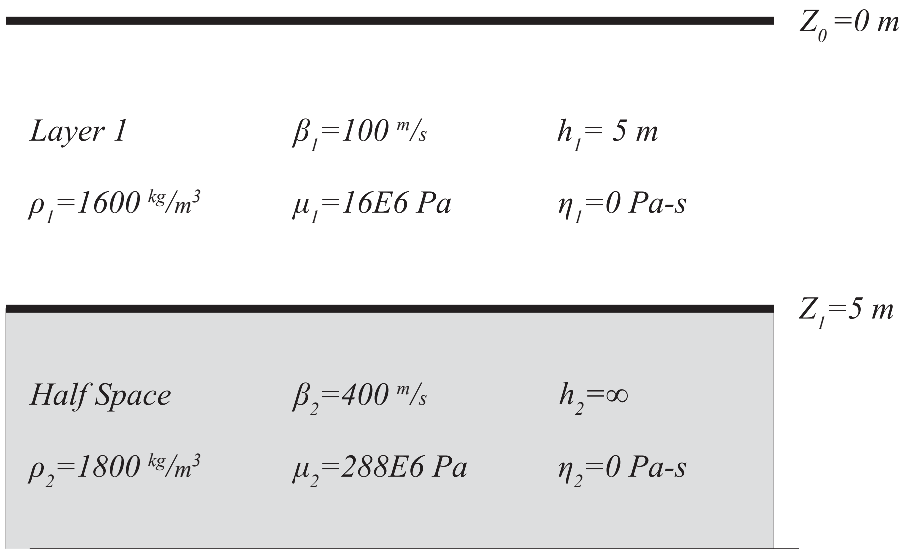

Figure 4.1: Soil properties used to model a single elastic layer over a half-space.

waves. For systems consisting of a single layer over a half-space, apparent Love wave velocities are restricted to the range, $\beta_1 < C_L < \beta_2$.

4.1.1 Love Wave Modes and Depth Dependent Behavior

When deriving Equations 2.35 and 2.36, we separated the displacement relationship into three independent functions, $v(x, z, t) = R(x)L(z)T(t)$, and introduced the variables ω and K^*, which link and constrain the behavior of these three functions so that each value of angular frequency, ω, is associated with a particular value of horizontal angular wave number, K^*. The vertical wave number, $\nu = \sqrt{K^{*2} - \frac{\omega^2}{\beta^{*2}}}$, is a function of both K^* and ω, and it constrains the behavior of $L(z)$. The function $L(z)$ is periodic in the layer, so that valid solutions of Equation 2.35 exist at $n\pi$ increments of its argument. Thus, it is possible for ω to be associated with more than one value of K^*. The first (fundamental) mode occurs when $n = 0$, the second mode (first over-

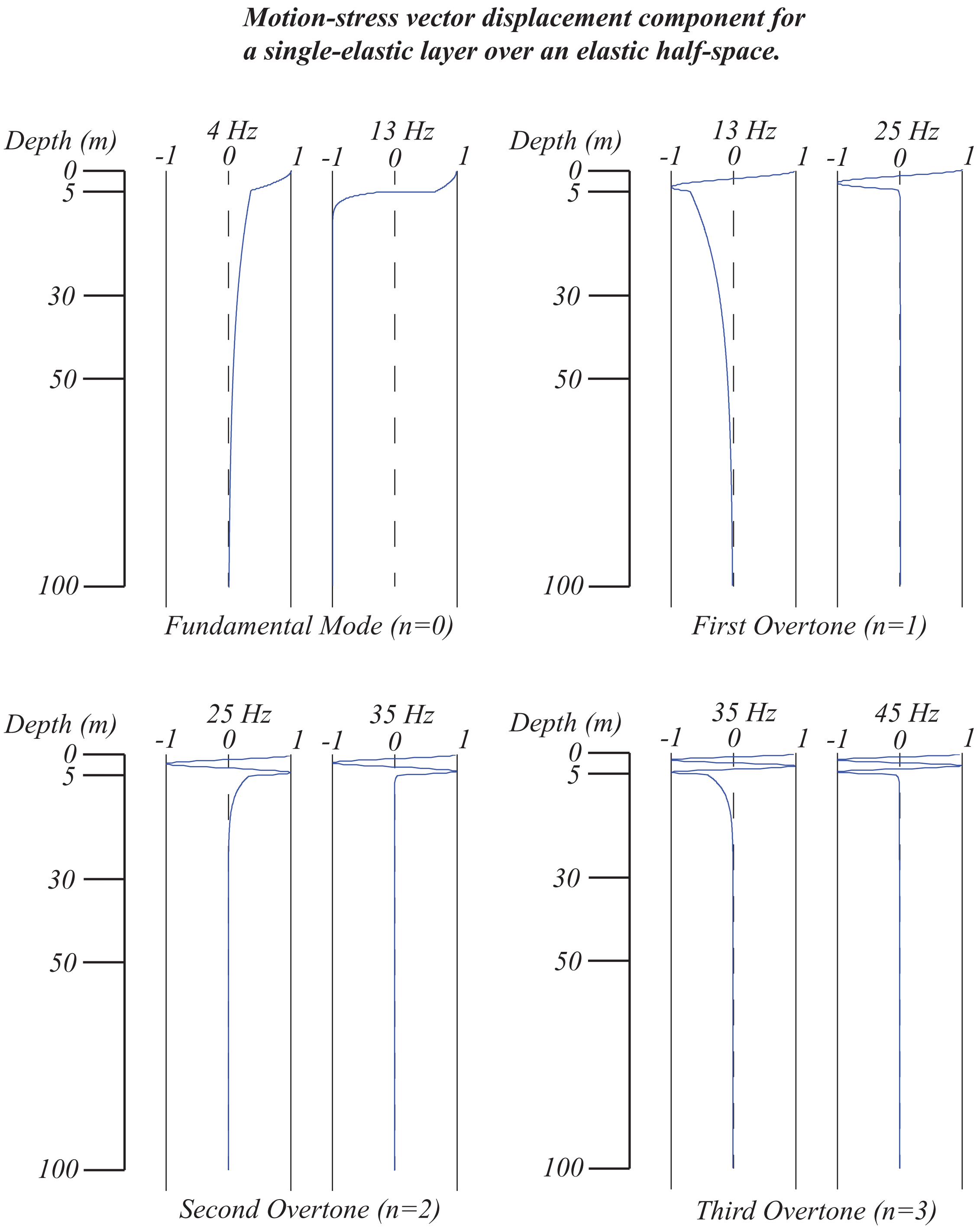

Figure 4.2: Motion stress vector displacement component for a single-elastic layer over an elastic half-space. Each mode number corresponds to the number of phase changes in the layer.

tone), when $n = 1$, and so-on. For the system shown in figure 4.1, overtones appear at approximately 10.33 Hz intervals (equation 1.3). Because its cut-off frequency is effectively zero, the fundamental mode exists at all frequencies.

Near its cut-off frequency, a mode's influence extends more deeply into the half-space than it does at higher frequencies (Figure 4.2). This is especially true for the fundamental mode, whose effects can extend many layer thicknesses into the half-space. This zone represents the depth of the stress field, or evanescent wave, that is responsible for the angle-dependent phase changes that occur when post-critical waves impinge on the interface. As would be expected, the differences in stress field depth result in a concomitantly greater phase delay for low frequencies than for high frequencies.

For a purely elastic system, only real values of K^* are possible. At low frequencies, the fundamental mode is associated with small wave numbers and relatively large Love wave velocities (Equation 3.33). As frequency increases, the fundamental mode's Love wave velocity decreases from a maximum near the half-space shear wave velocity, β_2, to a minimum near the layer shear wave velocity, β_1. Overtones come into existence at higher frequencies and velocities than the fundamental mode, but otherwise exhibit similar behavior (figure 4.3).

Dispersion curves for the purely elastic system of Figure 4.1 are illustrated in Figure 4.4. As expected, the low frequencies of each mode correspond to Love wave velocities near $C_L = \beta_2$. C_L decreases rapidly with increasing frequency before approaching the top-layer velocity, β_1, asymptotically. At high frequencies, many modes may be crowded into the region near β_1, and discriminating between modes becomes problematic.

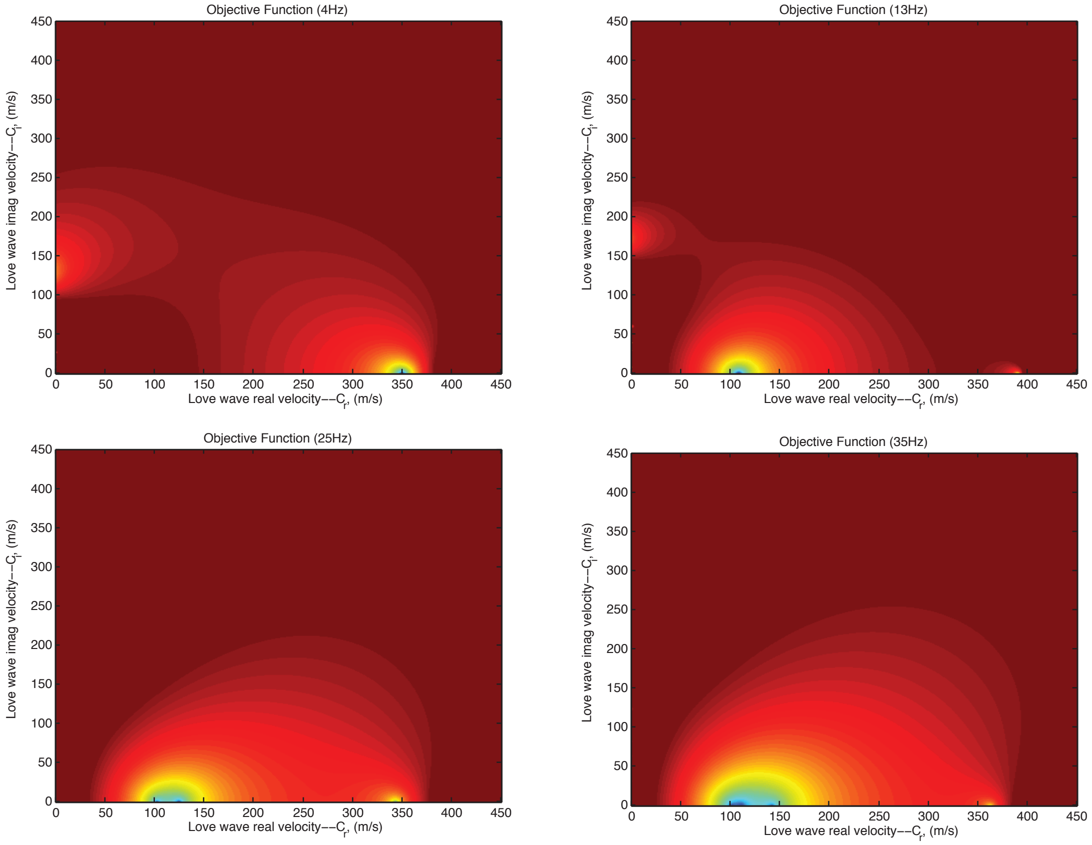

Figure 4.3: Elastic mode evolution with increasing frequency for a single-elastic layer over a half-space (Figure 4.1). At 4 Hz, only the fundamental mode exists. At 13 Hz, the fundamental mode has moved to approximately 110 m/s, and the first overtone has just come into existence. Similarly, at 25 Hz, the second overtone has come into existence, and the first overtone is visible at approximately 120 Hz; the fundamental mode is barely visible near 100 Hz (β_1). The process repeats at 35 Hz, when the third overtone comes into existence.

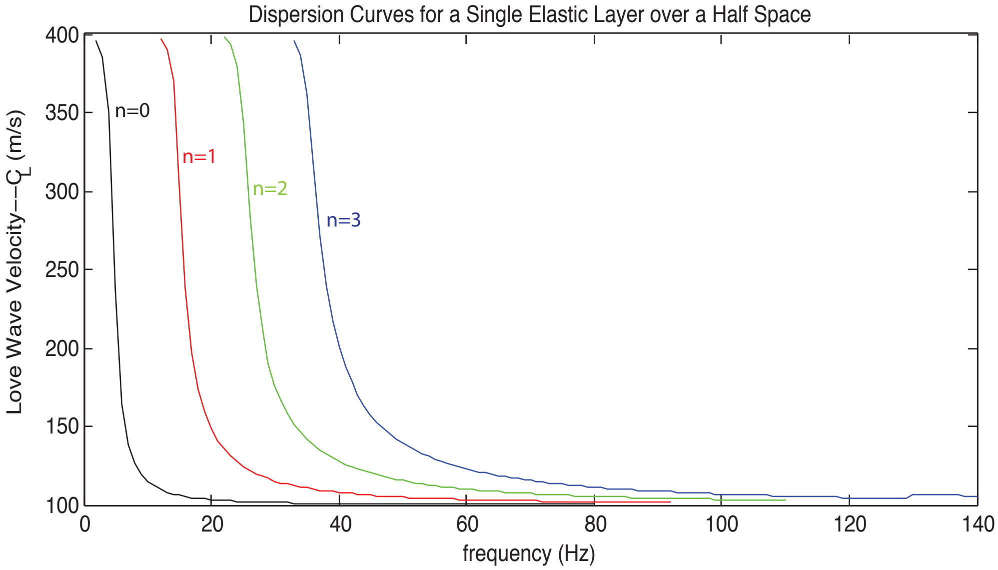

Figure 4.4: Dispersion curves of the fundamental mode and first three overtones for a single elastic layer over a half-space (Figure 4.1).

4.1.2 Elastic Scaling Relationships

We rearrange Equation 1.3 to obtain a useful heuristic for scaling layered Love wave systems:

$$f_{sc} = \frac{2fh_1\sqrt{1-\frac{\beta_1^2}{\beta_2^2}}}{\beta_1} \tag{4.1}$$

where f_{sc} is the scaled frequency. Love (1911) alluded to scaling in his original paper, and Aki and Richards (2009) made use of a similar scaling factor when describing the behavior of a single layer over a half-space. Equation 4.1 gives exact results when layer and half-space velocities are the same for both systems being scaled. For example, we might wonder what would happen if the layer thickness of the system illustrated in Figure 4.1 were increased from 5 m to 10 m. At 35 Hz, the scaled frequency of the original system is $f_{sc} = 3.39$. For the corresponding system with a 10 m layer, achieving the same scaled frequency requires that frequency be reduced by a factor of two. At 17.5 Hz, the 10 meter layer system would have four roots at exactly the same velocities displayed in the 35 Hz panel of Figure 4.3; however, the associated frequencies, and frequencies of corresponding dispersion curves, would be halved.

When the ratio β_1/β_2 is the same for both systems, roots will appear at the same relative velocities for systems with the same scaled frequency. For example, doubling both the layer and half-space velocities in Figure 4.1 to 200 and 800 m/s, respectively, and increasing layer thickness to 10 m results in a doubling of all root velocities: The root at 360 m/s in the 35 Hz panel of Figure 4.3 will correspond to a root at 720 m/s in the 10 m layer model, and so-on. In this case, the phase velocities of roots in the high velocity system are exactly twice those in the original system.

Scaling is only approximate when β_1/β_2 is not the same for both systems.

4.2 Evolution of Complex Modes with Viscosity

We should note that even for a purely elastic system, both real and imaginary roots are evident (Figure 4.5). Each time that frequency increases beyond a cut-off frequency, a real mode originates near the half-space velocity (β_2), and then moves along the real axis until approaching, asymptotically, layer velocity (β_1). Simultaneously, a companion mode appears along the real axis, and moves rapidly toward infinity. It is difficult to impute a physical significance to these purely imaginary solutions with no real velocity; however, as we will see, inclusion of a viscous term in our model induces these purely imaginary roots to evolve into complex roots for which we can ascribe a physical interpretation.

For a purely elastic model, solutions are symmetric about both the real and imag-

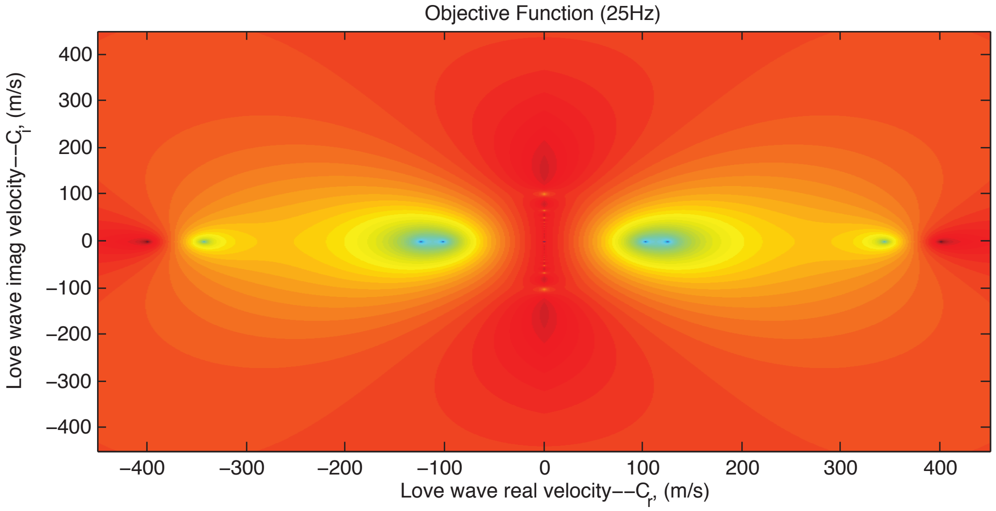

Figure 4.5: Objective function at 25 Hz for a single elastic layer over a half-space (Figure 4.1) showing all four quadrants of the complex plane. Note the faint roots along the vertical (imaginary) axis.

inary axes. Adding viscosity changes this symmetry so that the first and third quadrant pair, and the second and fourth quadrant pair, remain symmetric about the origin.

Importantly, under all conditions tested, no roots crossed quadrant boundaries, and all roots either originated along the imaginary axis, or they originated at a point near half-space velocity along the real axis. This is somewhat at odds with the three root types described by Chakravarthy (2008). The Type III root he describes and illustrates (Chakravarthy (2008), Figure 3.6) is, in reality, the system's fundamental mode, which originated along the real axis at 400 m/s.

We now alter our model by adding viscosity to the layer (Figure 4.8). An obvious consequence of this addition is that Love waves will attenuate with time and distance; however, a more subtle effect is an increase in the apparent stiffness, and hence layer shear wave velocity. Qualitatively, this can be thought of as a consequence of the

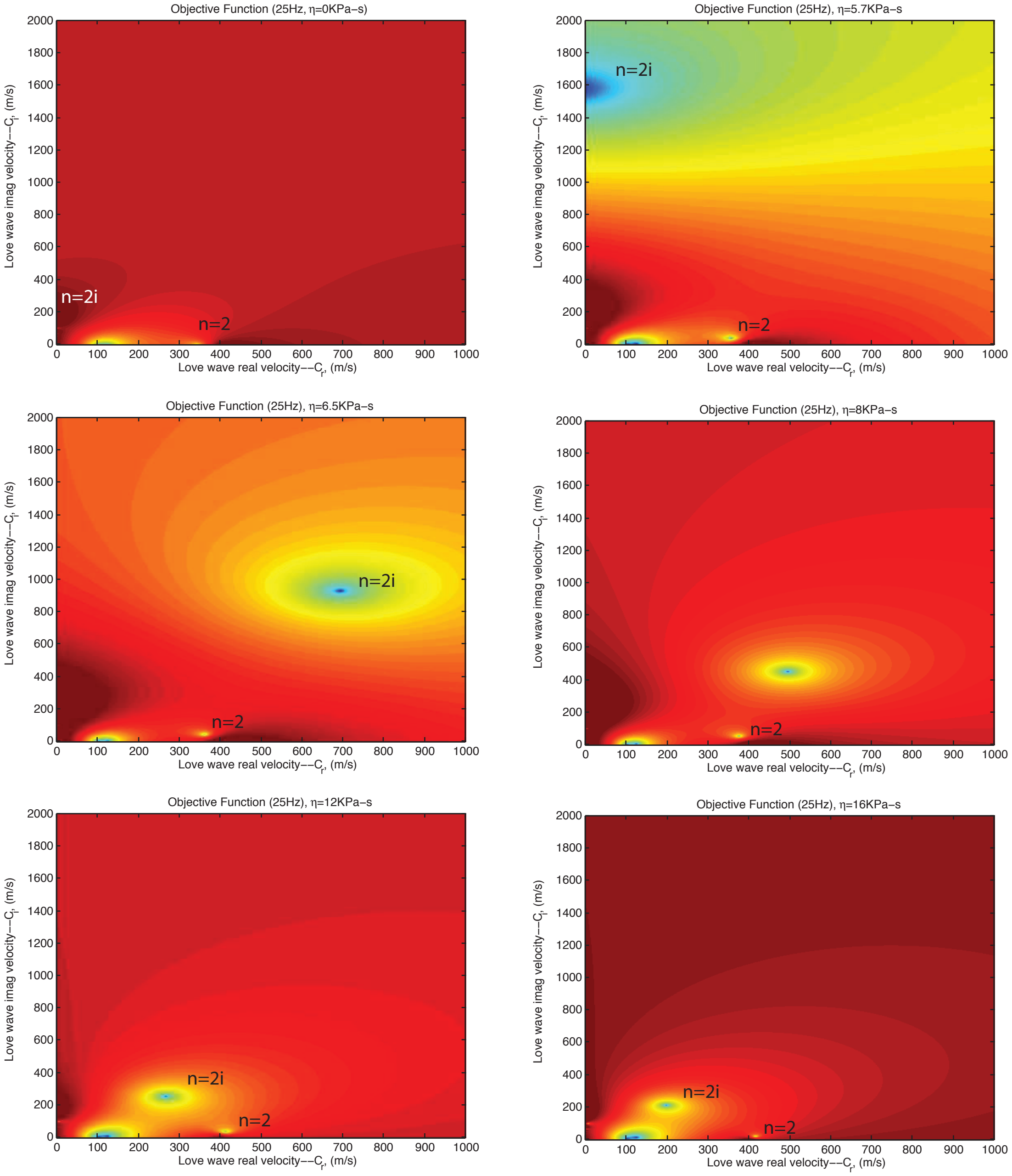

Figure 4.6: Effect of viscosity on complex velocity. In the purely elastic model ($\eta = 0KPa - s$), we see three modes along the real axis. As viscosity increases, the second overtone (n=2) rotates clockwise, into the complex plane, until it disappears beyond 400 m/s (real). Meanwhile, a corresponding overtone (n=2i) appears on the imaginary axis, and rotates through the complex plane until approaching the fundamental mode and first overtone.

increased shear resistance that results from viscous forces within a material. We infer from the frequency dependence of the viscous term in Equation 3.35 that the apparent stiffness of a viscoelastic material will increase with frequency.

The general effect of inclusion of a small viscosity term is to add a small imaginary component to the real velocity of lower order elastic Love wave modes; otherwise, modes behave much as they do for the purely elastic case. At sufficiently high viscosities, a very interesting phenomena occurs: A root with its origins on the real axis may disappear, but be replaced by a corresponding root whose provenance is the imaginary axis. We will refer to roots originating on the real axis as principal roots, and designate them using real numbers (n=0, n=1, n=2, etc.). We will refer to roots originating along the imaginary axis as companion roots, and designate them with imaginary numbers (n=1i, n=2i, etc.).

The effect becomes more pronounced with increasing overtone number. In Figure 4.6, we can see this evolution take place: The fundamental mode and first overtone behave analogously to their elastic counterparts, but the second and higher overtones rotate to a velocity above the half-space velocity (β_2) before disappearing.

This behavior can be explained in terms of viscous stiffening. Increasing viscosity effects an increase in Love wave phase velocity. This causes the principal overtone's location to shift right (higher real velocity). When phase velocity exceeds that of the half-space, we expect it to become an evanescent mode as described in Chapter 1. Similarly, viscous stiffening also causes the erstwhile imaginary companion root to don a real component, and move rightward into the complex plane.

We should note that the fundamental mode (n=0) behaves somewhat differently. Although the fundamental mode may experience substantial displacement, it never

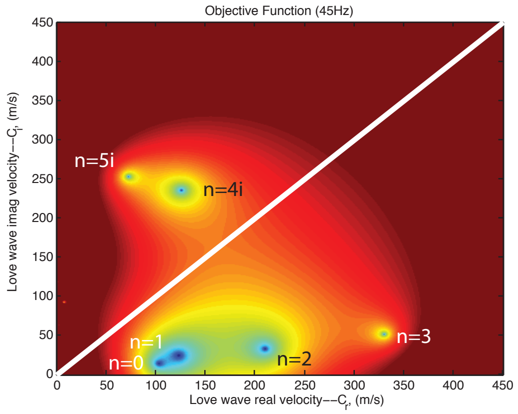

Figure 4.7: The loss tangent is greater than unity when $C_i > C_r$. We would not expect the two companion roots (n=4i and n=5i) that are above the diagonal line to be expressed as propagating waves.

completely disappears. This explains how a fundamental mode could have evolved into Chakravarthy's Type III root, as noted above.

As discussed in Section 3.3, no Love wave can be transmitted when the loss tangent, $\xi_L = \frac{C_i}{C_r}$, is greater than or equal to unity, suggesting that there will be no measurable expression of a mode when its imaginary velocity component, C_i, exceeds its real component, C_r: We would not expect a companion mode to manifest itself until the real component of its complex velocity exceeds its imaginary component (Figure 4.7). Thus, when the loss tangent of a root is greater than unity, it will not be manifested as a propagating wave. For all cases studied, this occurs almost immediately after the corresponding principal overtone has exceeded half-space velocity. In no test did both a principal and its companion mode simultaneously exhibit a ξ_L less than unity.

Despite their differing provenance, companion modes and their principal counterparts share many important traits. Importantly, depth and frequency-dependent

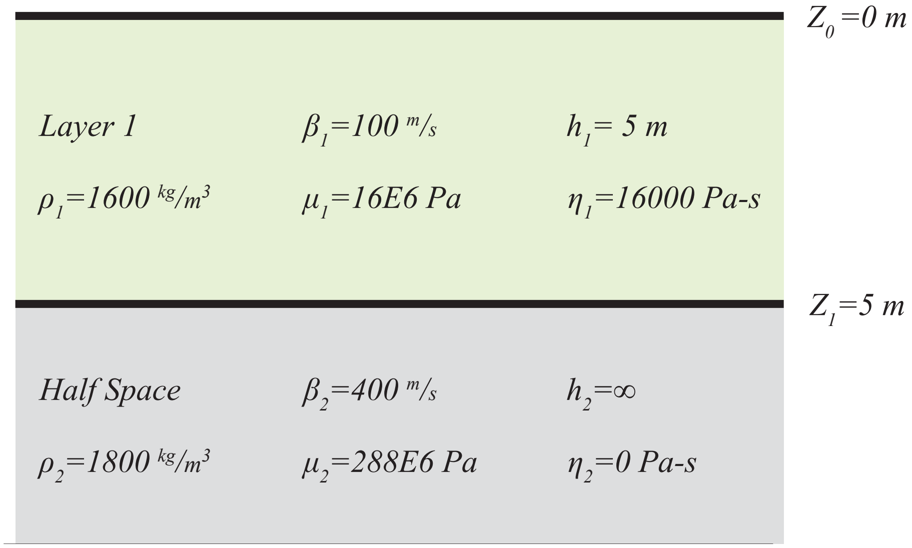

Figure 4.8: Soil properties used to model a single viscoelastic layer over a half-space.

behavior are similar: Each principal mode and its counterpart exhibit similar motion-stress behavior with depth, and the same number of phase changes in the layer (Figure 4.2).

4.3 Single Viscoelastic Layer over a Half-Space

We now turn our attention to a single visoelastic layer over a half-space (Figure 4.8), and note the effects of changing frequency. As we saw for the purely elastic case, each mode comes into existence shortly after its cut-off frequency. Unlike the purely elastic case, viscoelastic Love wave mode velocity includes both real and imaginary components, so as frequency increases, Love wave modes appear to move in an arc (Figure 4.9). The behavior is analogous to that obtained when viscosity was increased. This is not surprising, since the viscous component of the complex shear modulus is equal to the product of frequency and viscosity ($\mu_i = i\omega\eta$).

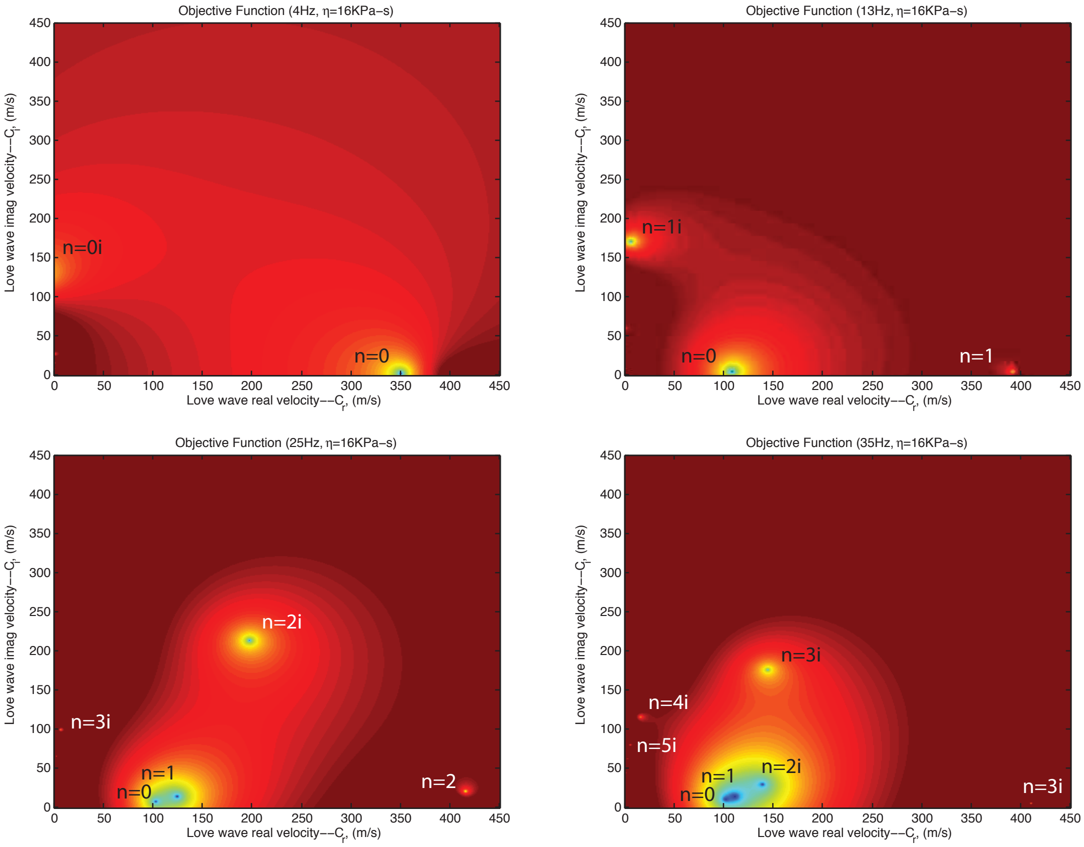

Figure 4.9: Viscoelastic mode evolution with increasing frequency for a single viscoelastic layer over a half-space (Figure 4.8). As frequency increases, both the fundamental mode (n=0) and first overtone (n=1) behave much like their elastic counterparts. Companion modes (n=0i and n=1i) appear, but move beyond the plotted area. On the other hand, the second and third overtones (n=2 and n=3) rotate clockwise and eventually disappear above 400 m/s, while their companion modes (n=2i and n=3i) take their places.

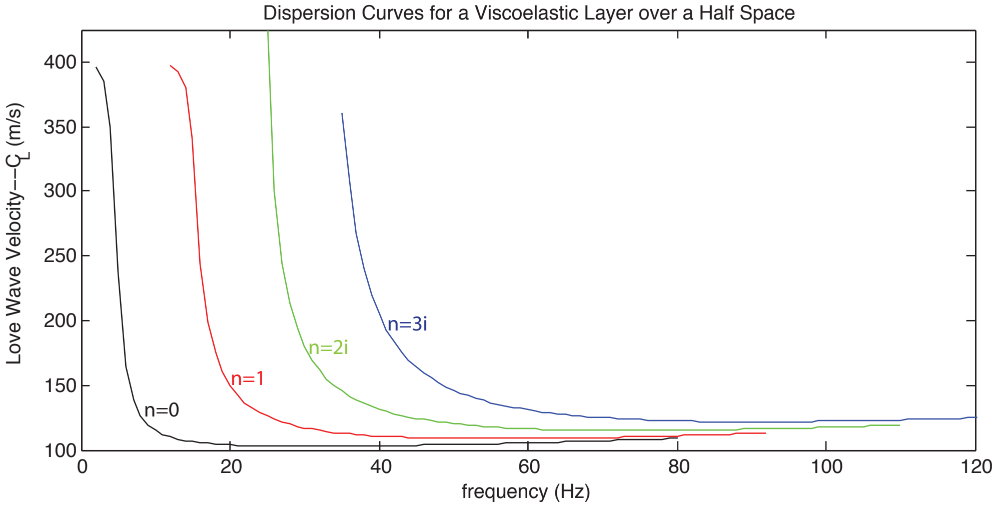

Figure 4.10: Dispersion curves for a single viscoelastic layer over a half-space (Figure 4.8). Companion mode behavior (n=2i, 3i) is only displayed in the region where loss tangent is less than unity.

Overall, dispersion curves derived from the viscoelastic model (Figure 4.10) resemble their purely elastic counterparts (Figure 4.4). Beyond the contumacious region near the cut-off frequency, each curve is well behaved until the curves converge to the shear wave phase velocity of the topmost layer (Equation 2.20).

Near its cut-off frequency, a companion mode exhibits a large attenuation coefficient (Figure 4.11). High loss tangents imply that there will be no physical manifestation of companion modes near the cut-off frequency (Figure 4.12). As frequency increases, the attenuation coefficients and loss tangents of all modes asymptotically approach that of the layer (Equations 2.23 and 2.25).

4.3.1 Effects of Half-Space Viscosity

We found that half-space viscosity has little, if any, effect on the behavior of a viscoelastic Love wave system. We examined the dispersion and attenuation curves of

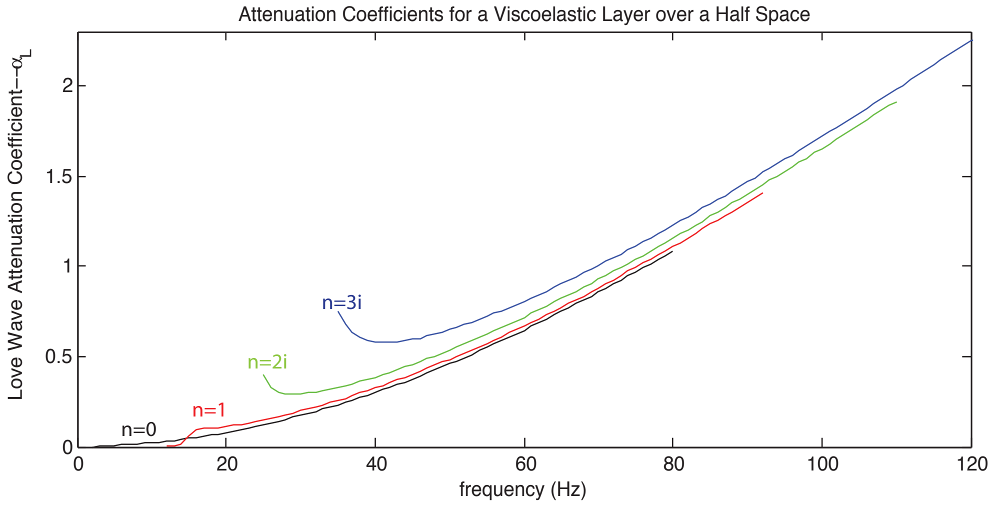

Figure 4.11: Attenuation as a function of frequency for a single viscoelastic layer over a half-space (Figure 4.8). Companion mode behavior (n=2i, 3i) is only displayed in the region where the loss tangent is less than unity.

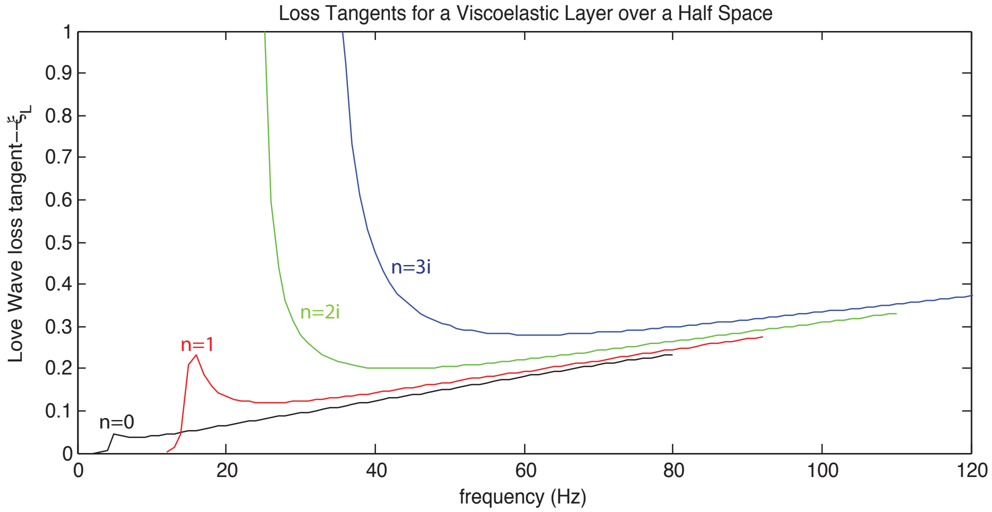

Figure 4.12: Loss tangent as a function of frequency for a single viscoelastic layer over a half-space Figure 4.8).

layered models with β_2 =400 m/s and β_1 =140 m/s, 200 m/s, and 400 m/s, with and without a viscosity term (η =288E3 Pa-s). In no instance did lower modes exhibit observable differences in either phase velocity, C_L, or attenuation, α. The differences observed in higher modes (n=2, 3) were very small, and only in the non-linear region near the cut-off frequency. This is consistent with the findings of Chakravarthy (2008).

Half-space viscosity also had little, if any, effect on the motion-stress vector. Indeed, the imaginary components of the motion-stress vector are almost entirely absent at all depths in a viscoelastic half-space.

The lack of sensitivity to half-space viscosity can be explained as follows. First, Love waves are the result of shear waves trapped within the layer, and the only time that the wave interacts with the half-space is when reflecting from it. Second, recall that when developing boundary conditions for the half-space (Sub-section 3.3.2), we expressly excluded the upward wave component, s_u, so no wave component from the half-space enters the layer.

4.3.2 Viscoelastic Scaling Relationships

In Sub-section 4.1.2, we discussed elastic scaling relationships. By using the corresponding complex velocities in Equation 4.1, these can be applied to a viscoelastic system, as well. Because the effect of half-space viscosity on the system is negligible, we need only substitute β_1^* for β_1. Because β_1^* is a function of $\omega\eta$ (Equations 2.19 and 2.20), scaling requires a change in viscosity when frequency is changed.

When only the layer thickness is changed, scaling can be accomplished by applying Equation 4.1 to the corresponding elastic system (using β_1), and then adjusting viscosity in inverse proportion to the frequency change (e.g., if frequency is doubled, viscosity should be halved). For example, increasing layer thickness of the system illustrated in Figure 4.8 from 5 *m* to 10 *m*, decreasing frequency from 35 *Hz* to 17.5 *Hz*, and increasing viscosity from 16,000 *Pa-s* to 32,000 *Pa-s* will result in complex root velocities that are identical to those of the 35 *Hz*, 5 *m*, 16,000 *Pa-s* system shown in the 35 *Hz* panel of Figure 4.9.

As was the case for the elastic system, the technique will also work when the ratio of layer to half-space velocity is constant. In this case, the vector representing the complex velocity of a root will be transformed by a scalar that is equal to the ratio of elastic layer velocities. As was the case for the elastic system, the method yields only approximate results when the ratio of layer to half-space velocity is not held constant.

4.4 Two Layers over a Half-Space

4.4.1 Two Elastic Layers over a Half-Space

In Section 1.1, we discussed Love wave propagation for a single layer over a half-space. Apparent Love wave phase velocity, C_L, is a function of layer velocity and incidence angle (Equation 1.2). We obtain a relationship between the apparent love wave phase velocity and the incidence angle at the half-space interface by combining this with Snell's Law (Figure 4.13):

$$C_L = \frac{\beta_1}{sin\theta_1} = \frac{\beta_1}{\frac{\beta_1 sin\theta_2}{\beta_2}} = \frac{\beta_2}{sin\theta_2} \tag{4.2}$$

At the critical incidence angle, $sin\theta_2 = \beta_2/\beta_3$, so the maximum possible Love wave phase velocity is the half-space velocity, β_3. By extension, we can show that

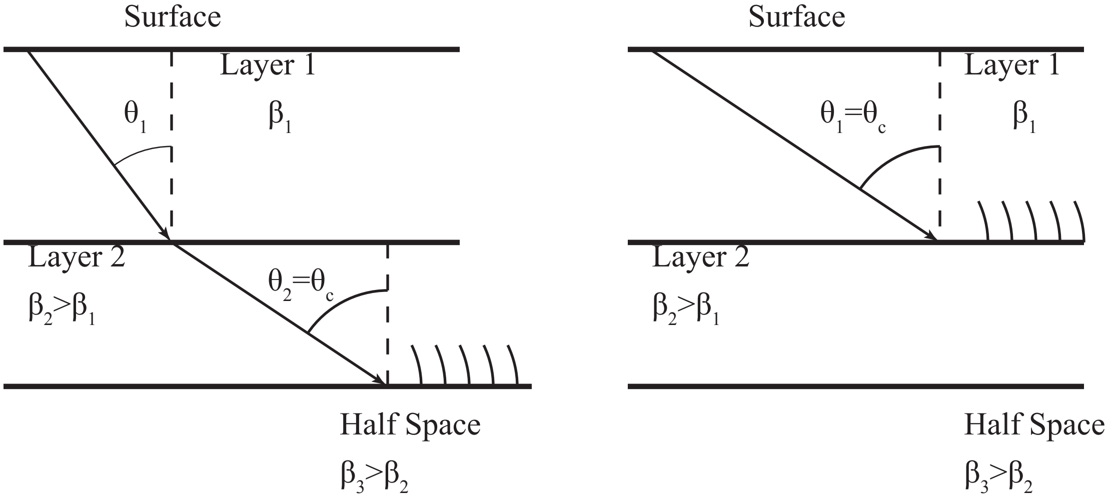

Figure 4.13: (Left) Two layer ray path when the incidence angle at the half-space interface is critical. (Right) When the incidence angle at the layer-one/layer-two interface exceeds its critical angle, layer two takes the role of the half-space, and the wave may propagate in a manner similar to that of a head-wave.

regardless of the number of layers, the maximum possible Love wave phase velocity will be that of the half-space.

At low incidence angles, either of two possibilities may occur. It is possible for the wave to be refracted, and then interact with the half-space, in which case, the minimum velocity is still that of the surface layer. On the other hand, when the incidence angle exceeds the critical angle at the layer-one/layer-two interface, the Love wave may be conducted in a manner akin to a head-wave. For elastic layers, this manner of propagation usually spans a finite range of frequencies, and results in a temporary *shelf* in the dispersion curve, before the mode again heads asymptotically toward the top-layer velocity. Thus, for elastic media, Love wave phase velocities are bounded by the range: $\beta_1 < C_L < \beta_{hs}$. When viscosity is added to the model, viscous stiffening can greatly increase the range of frequencies over which the shelf occurs.

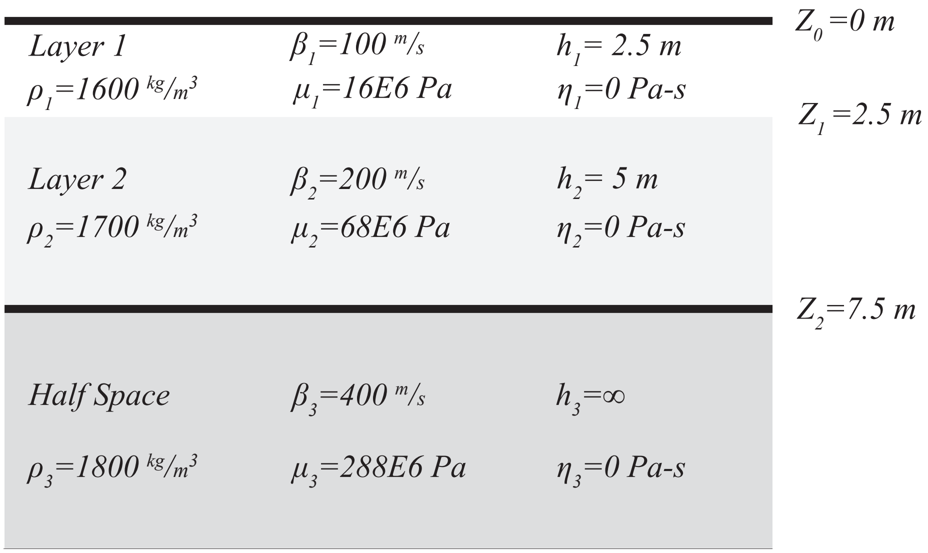

Figure 4.14: Soil properties used to model two elastic layers over a half-space.

From Equation 4.1, we infer that the effect of increasing layer velocity is similar to that of decreasing layer thickness. For a layered elastic model, substituting an equivalent single layer thickness, $\overline{h}$, for h_1 in Equations (1.3), and (4.1) gives good results:

$$\overline{h} = \sum_{j=1}^{n} h_j \frac{\beta_1}{\beta_j} \tag{4.3}$$

The soil profile illustrated in Figure 4.14 has an equivalent layer thickness of 5 m, so we can compare the frequency response obtained with this model to that of the single-layered elastic model (Figure 4.1).

The soil model in Figure 4.14 is homologous to that of Figure 4.1. That is, the two layers were scaled using Equation 4.3. For both models, cut-off frequencies are the same; however, we can see that as frequency increases (Figure 4.15), modes from the two-layer model do not move as quickly from the half-space velocity, β_3, to the

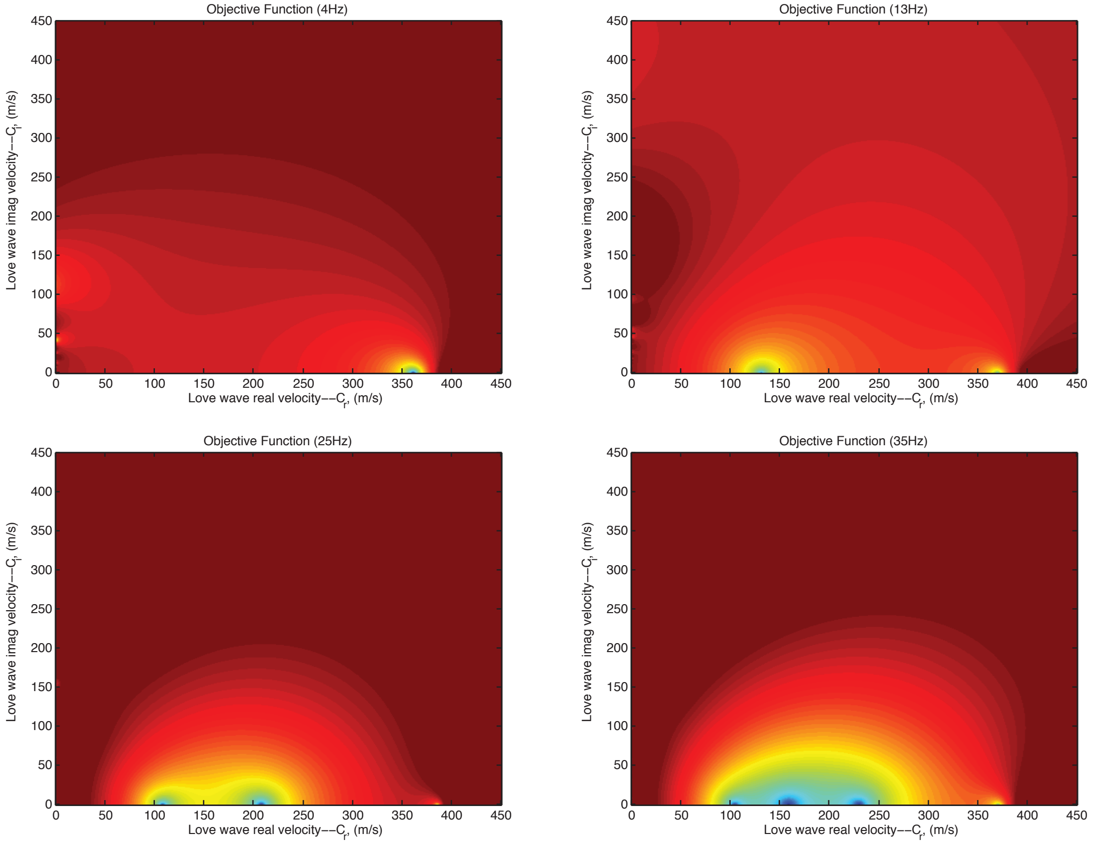

Objective Function (4Hz)

Objective Function (13Hz)

Objective Function (25Hz)

Objective Function (35Hz)

Figure 4.15: Mode evolution with frequency for the two elastic layer/half-space system illustrated in Figure 4.14. Compared to the single-layer model, velocities do not change as quickly (see Figure 4.3).

surface-layer velocity, β_1. The effect is most pronounced for higher order overtones. Examination of the dispersion curves (figure 4.17) suggests an explanation: When frequency increases to the point that Love wave phase velocity, C_L, is approximately equal to the velocity of the second layer, the angle of incidence at the second layer becomes equal to the critical angle, and virtually all of the wave's energy is now channeled by the wave-guide formed by the layer-one/layer-two interface. Layer two, effectively, becomes a half-space.

Examination of the motion-stress vector (Figure 4.16) illustrates the effect. At

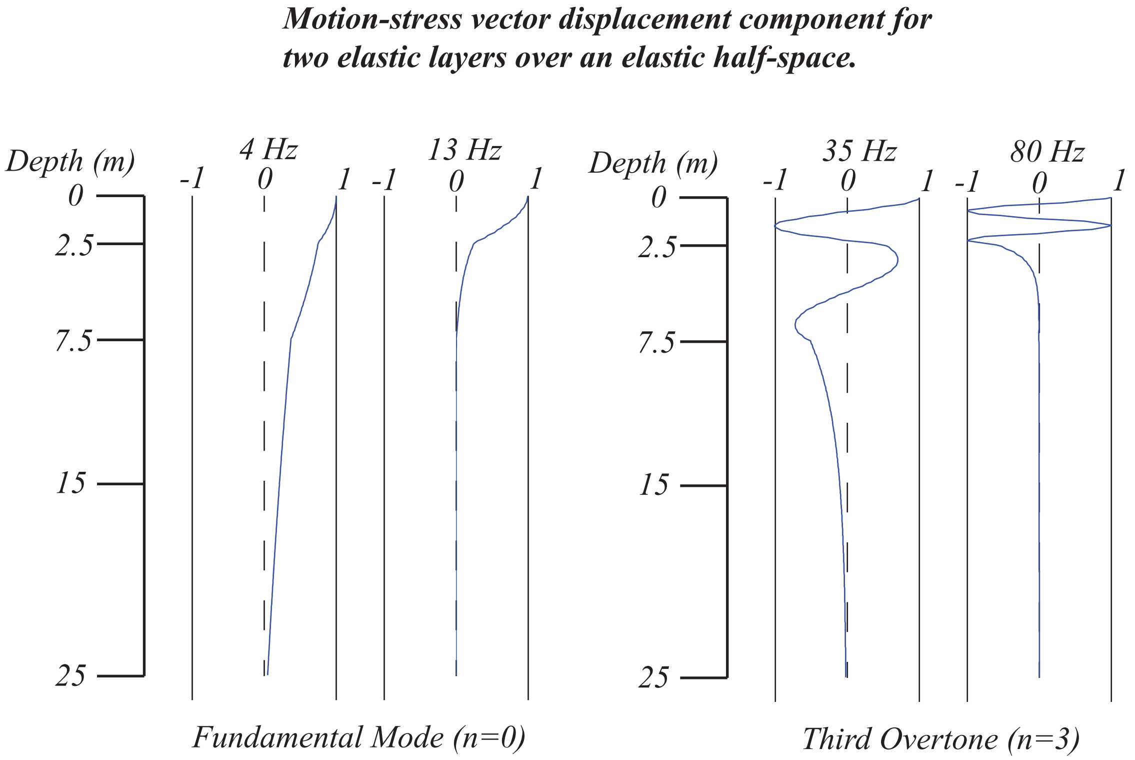

Figure 4.16: Motion-stress vector displacement component for two elastic layers over a half-space (Figure 4.14). At low frequencies, the null points are distributed across both layers; however, as frequency increases, the null points become confined to the top layer.

low frequencies, the motion-stress vector is distributed across both layers, but as frequency increases, the oscillating portion of the motion-stress vector moves entirely into the top layer.

The effect of the intermediate wave guide acting as a new half-space is clearly visible in dispersion curves. The dispersion curve for the fundamental mode shows a pronounced thickening at its base, and higher order overtones show an obvious *shelf* corresponding to the shear wave velocity of the intermediate layer.

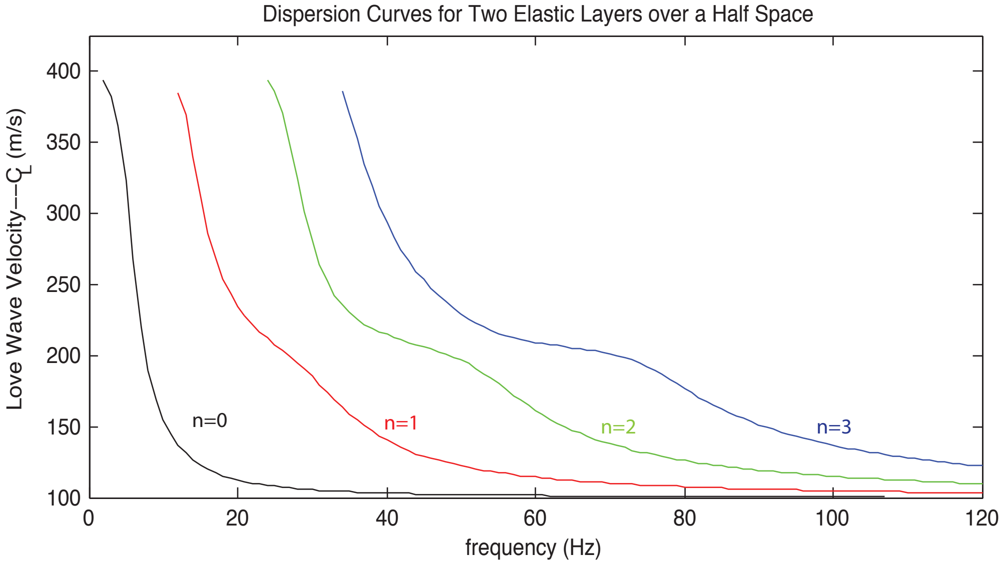

Figure 4.17: Dispersion curves for two elastic layers over an elastic half-space (Figure 4.14). Note the obvious *shelves* corresponding to the layer two shear wave velocity (200 m/s).

4.4.2 Two Viscoelastic Layers over a Half-Space

Adding viscosity to our two layer model has little effect on the fundamental mode or first overtone (Figure 4.18). As frequency increases, they move from the half-space velocity to surface layer velocity, albeit at a slightly retarded pace (Figure 4.19). The effect on the second and third overtones, however, is remarkable. Unlike the one-layer model, for which the second and third overtones originated as companion modes from the imaginary axis (n=2i, 3i), the second and third overtones of the two-layer model originate as principal overtones from the real axis. Also, as a result of viscoelastic stiffening, the range of frequencies over which the second and third overtones remain above the layer two velocity is greatly extended (Figure 4.20): The shelves persist to frequencies as high as 200 Hz.

We should pointout that a small increase in layer viscosities will effect the mode

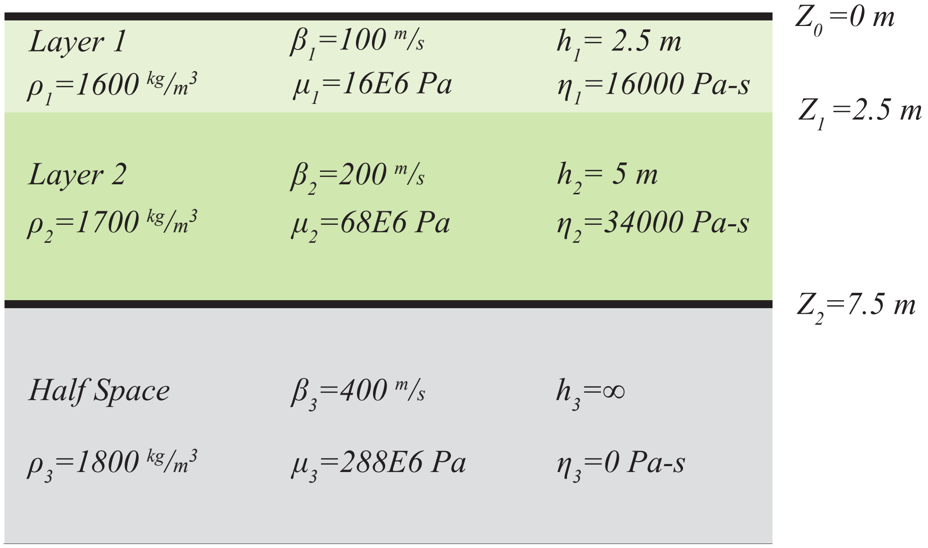

Figure 4.18: Soil properties used to model two viscoelastic layers over a half-space.

swapping behavior that is evident in the single-layer model, while decreasing layer viscosities will decrease the span of frequencies over which the shelf persists.

Attenuation coefficients for the two-layer viscoelastic model show an even more marked departure from the behavior observed in the one-layer model. The most obvious difference is the transposition of mode order. At high frequencies, the attenuation coefficient (and loss tangent) of the two lower order modes is approximately that computed for the layer one shear wave (Equations 2.24 and 2.25). On the other hand, the second and third overtones appear to converge to a value that is an amalgam of the top two layer properties.

A graph of the loss tangent shows similar transposition and juxtaposition of modes.

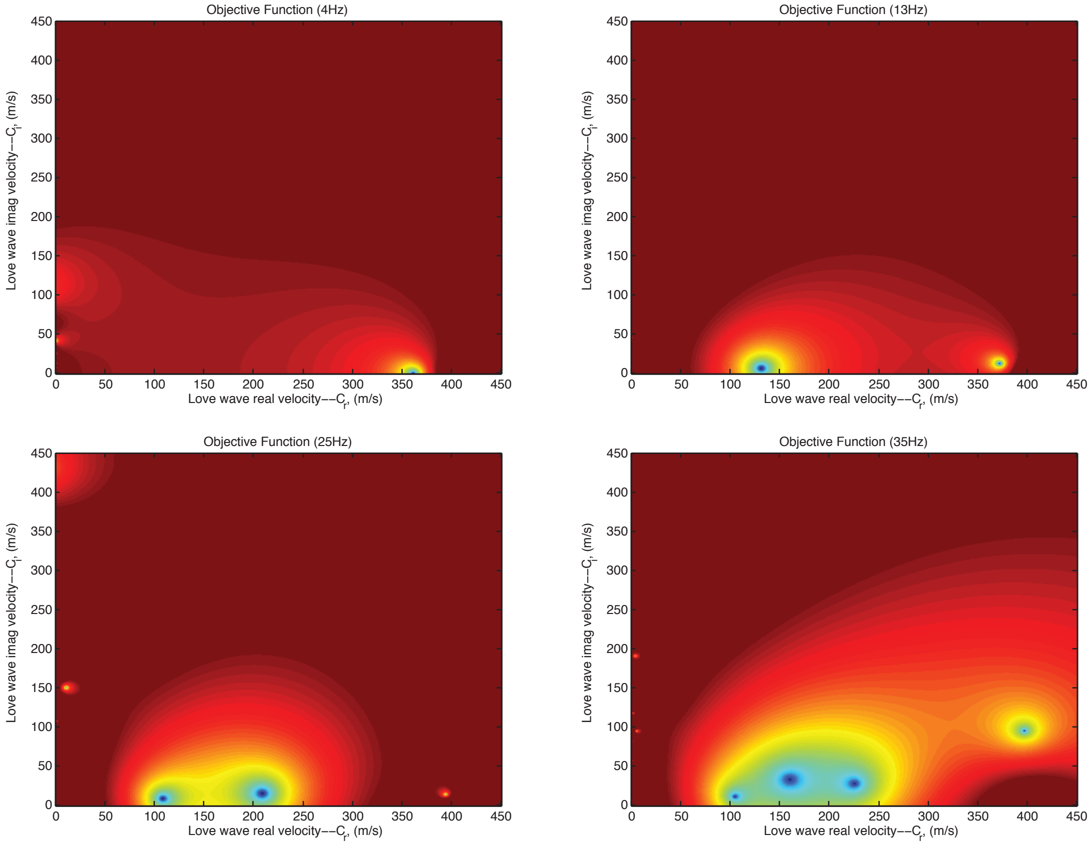

Figure 4.19: Viscoelastic mode evolution with increasing frequency for two viscoelastic layers over a half-space (Figure 4.18). All of the modes displayed with real velocity components between 100 and 400 m/s originated along the real axis.

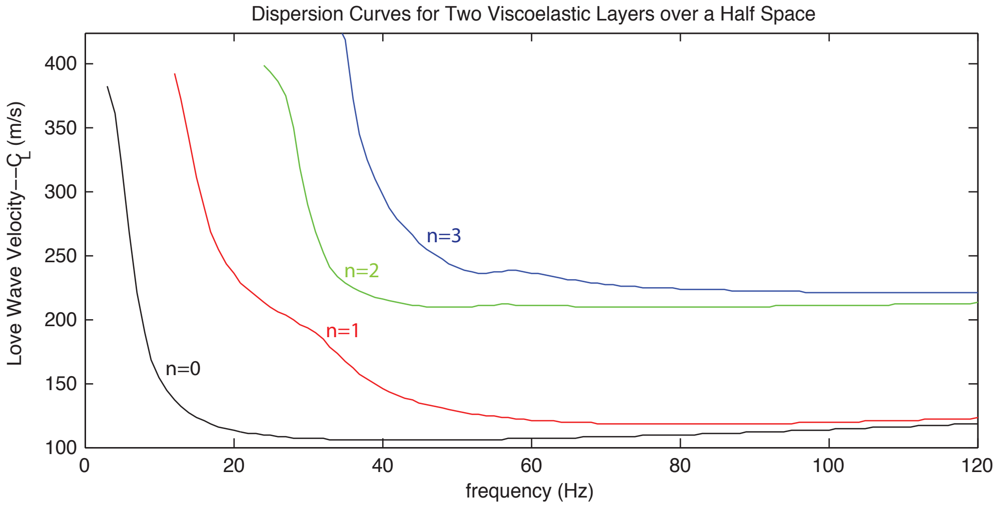

Figure 4.20: Dispersion curves for two viscoelastic layers over a half-space (Figure 4.18). Note that velocities of the second and third overtones never fall below layer 2 velocity (200 m/s).

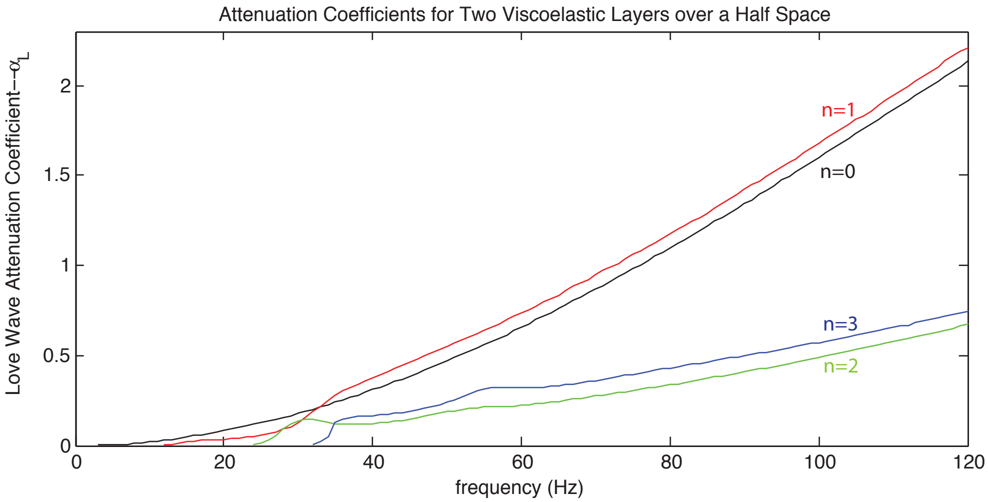

Figure 4.21: Attenuation as a function of frequency for two viscoelastic layers over a half-space (Figure 4.18). Note the transposition of mode order with respect to the single-layer viscoelastic model (Figure 4.11).

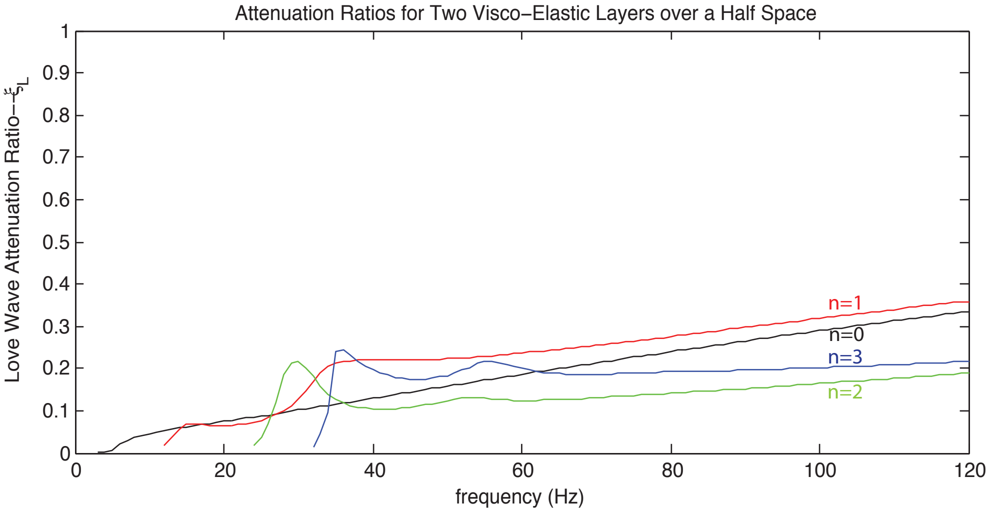

Figure 4.22: Loss tangent as a function of frequency for two viscoelastic layers over a half-space (Figure 4.18). As was the case for attenuation coefficients, mode order is transposed with respect to that observed in the single-layer model (Figure 4.12).

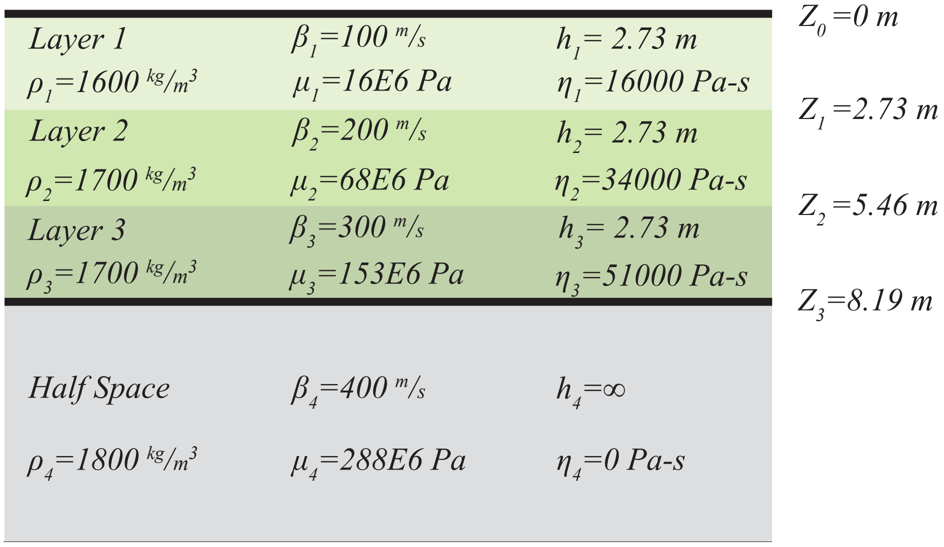

Figure 4.23: Soil properties used to model three viscoelastic layers over a half-space.

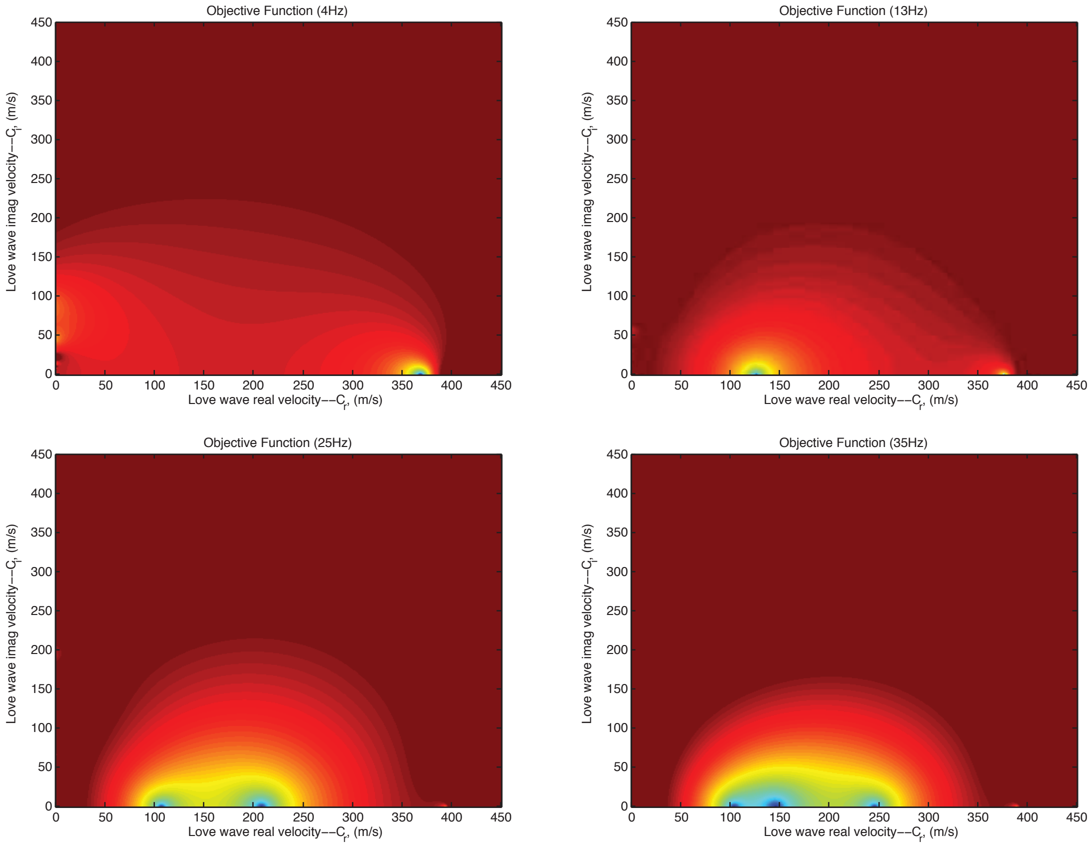

Figure 4.24: Love wave modes as a function of frequency for a three-layer elastic system (Figure 4.23).

4.5 Three Layers over a Half-Space

Our three-layer model is homologous with the two and one layer models that we have already discussed, so we expect modes to evolve at approximately the same cut-off frequencies (Figure 4.24). As was the case for the two-layer model, all four modes pictured originated as principal modes along the real axis.

For a three-layer model, we would expect to see shelves at 200 and 300 m/s. The second and third overtones exhibit fairly obvious shelves corresponding to 200 m/s; however, nothing but a slight thickening at 300 m/s belies the existence of the high

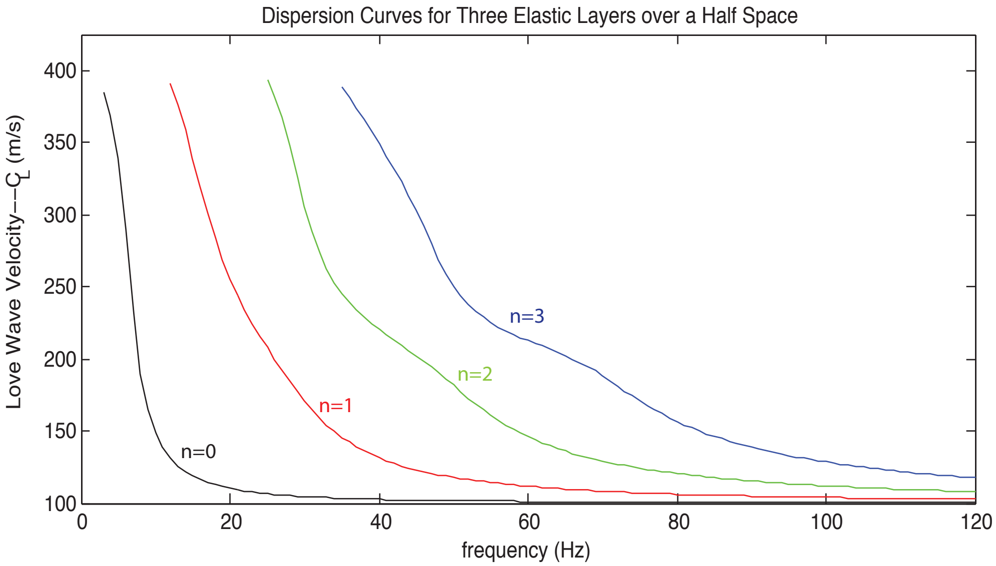

Figure 4.25: Dispersion curves for three elastic layers over a half-space (Figure 4.23). Note the thickening relative to the one and two layer models.

velocity layer. Indeed, it is difficult to find any discernable difference between the shapes of the fundamental modes displayed in two-layer and three-layer dispersion curves.

Behavior of the three-layer viscoelastic system is similar to that of the two-layer system, albeit with a slower progression of modes from half-space velocity to top-layer velocity (figure 4.26).

As was the case for the two-layer viscoelastic model, the second and third overtones level out at approximately 200 m/s, although the third overtone exhibits a pronounced shelf at around 340 m/s. The diminutive response at 300 m/s can probably be explained by the rapid frequency response that modes exhibit near their cut-off frequencies: The 300 m/s shelf is overpowered by the rapid rate of change in this region.

The attenuation curve scarcely differs from that of the two-layer model, suggesting

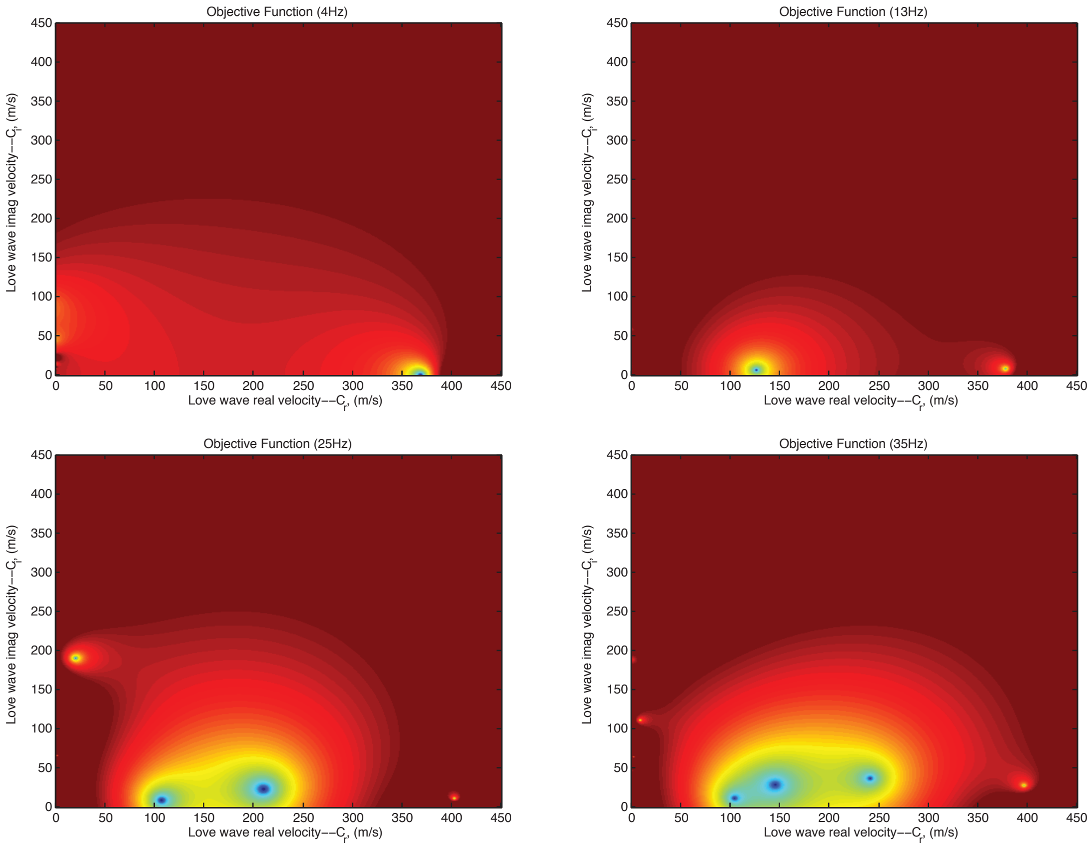

Figure 4.26: Love wave modes as a function of frequency for a three layer viscoelastic system (Figure 4.23). The first four modes all originated at a real velocity of approximately 400 m/s. Those modes visible along the imaginary axis eventually depart the plotted area.

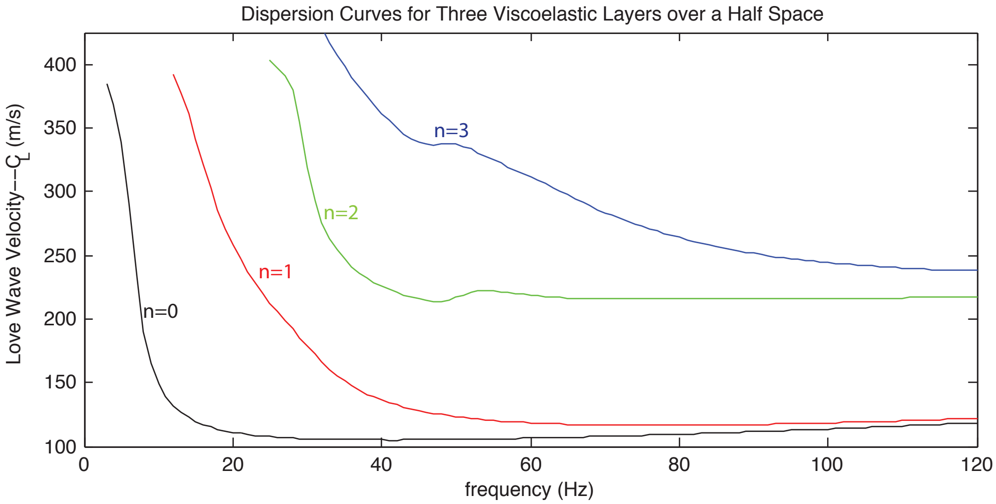

Figure 4.27: Dispersion curves three viscoelastic layers over a half-space (Figure 4.23). Note the pronounced third overtone shelf at 340 m/s

.

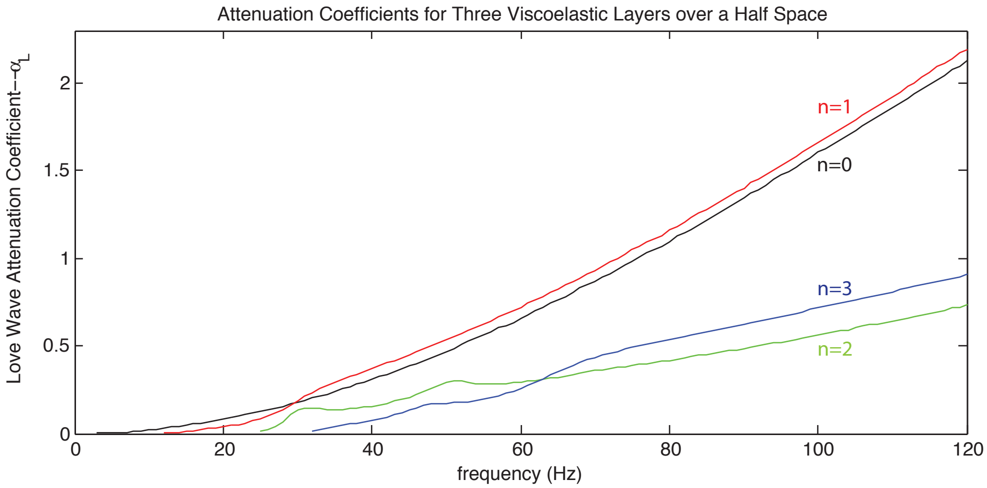

Figure 4.28: Attenuation as a function of frequency for three viscoelastic layers over a half-space (Figure 4.23). Note the similarity to the two-layer model (Figure 4.11).

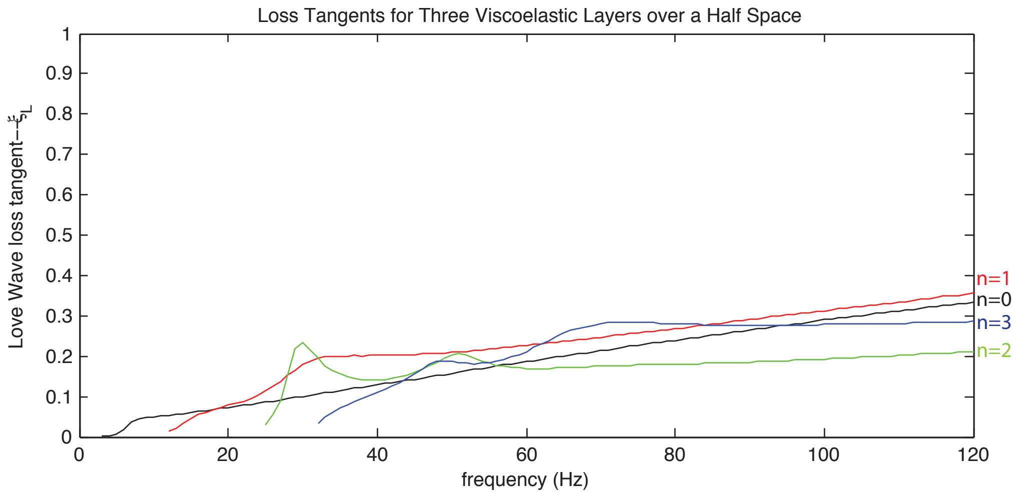

Figure 4.29: Loss tangent as a function of frequency for three viscoelastic layers over a half-space (Figure 4.23). Note the transposition of mode order with respect to the single-layer viscoelastic model (Figure 4.12).

that very little information about viscosity in the bottom layer has found its way into the curves. Likewise, the loss tangent curves are so similar to those of the two-layer model that they could be mistaken for the same curves. Only the third overtone differs markedly from its two-layer counterpart.

4.5.1 Some Observations on Higher Order Modes

Figure 4.30 illustrates the evolution of higher order modes for the three-layer viscoelastic system described above. The fundamental mode and first three overtones are all principal modes: They originate from along the real axis. The fourth principal mode has been replaced by its companion from the imaginary axis (n=4i), and has traveled in a relatively tight arc. Note, however, that although the second and third overtones languish on a shelf at around 200 m/s, we find the fourth overtone approaching surface-layer velocity (100 m/s). Likewise, the fifth and sixth companion overtones

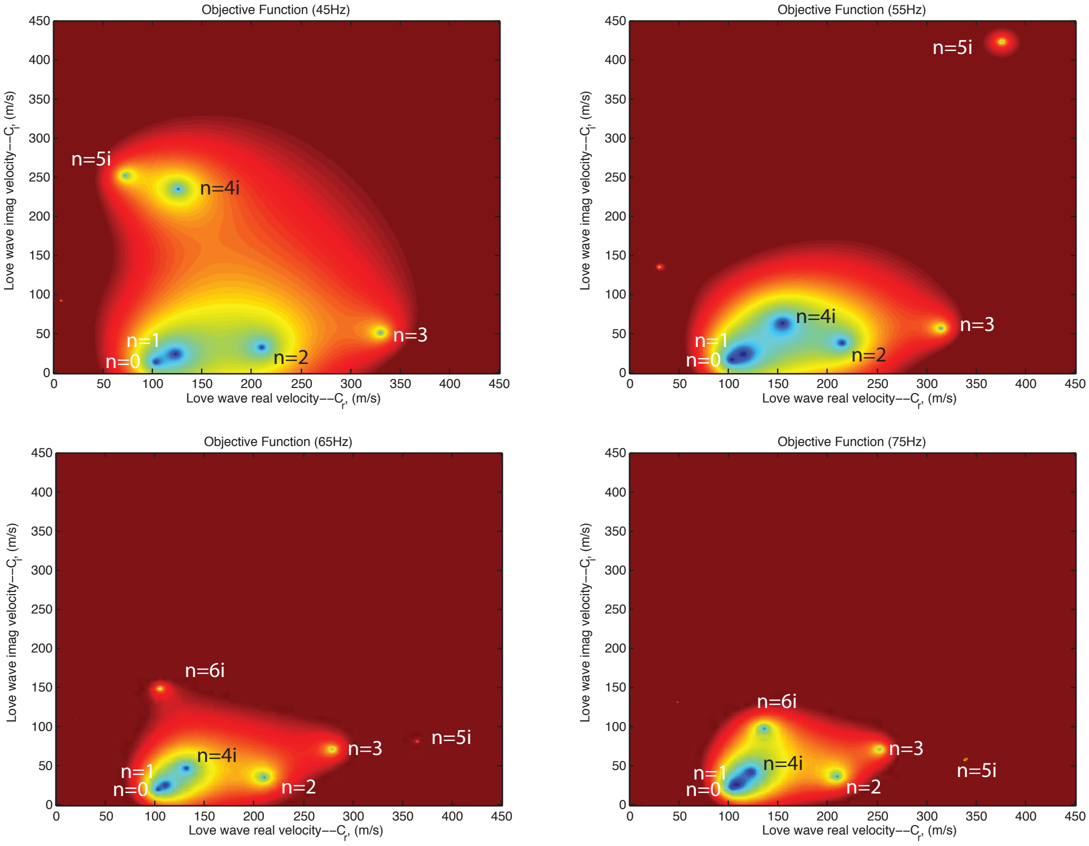

Figure 4.30: Higher order Love wave modes as a function of frequency for a three-layer viscoelastic system (Figure 4.23).

(n=5i, n=6i) replace their principal counterparts in the lineup. Interestingly, the 6th overtone (n=6i) does so quickly, while the fifth overtone (n=5i) takes a rather large detour before settling-down at the 300 m/s shelf. Placement of subsequent modes is even more haphazard.

After observing the first fifteen modes of the viscoelastic systems described in this chapter (as well as others), we can make some general observations. In all cases, the principal mode originated from the real axis at a velocity corresponding to that of the half-space, and all subsequent overtones originated either from this spot, or from the imaginary axis. The modes that made their way into the region where $\xi_L < 1$ followed a definite pattern: The earliest modes originated from the real axis, but mode origin would inevitably shift, permantly, to the imaginary axis. For high viscosity systems, this could happen as early as the first overtone.

CHAPTER 5:

DATA COLLECTION AND REDUCTION

In the previous chapters, we discussed Love wave mode behavior as a function of geometry, layer properties, and frequency. For each mode, this behavior was expressed using dispersion and attenuation curves. Field data, however, are collected in the form of signals representing time domain waveforms obtained from measurement devices such as geophones or seismometers. These signals are a function of more than just layer geometry and material properties: They are also a function of the source waveform, source-ground coupling, source-receiver geometry, receiver-ground coupling, and receiver response. In the present chapter, our goal will be to extract information that can be reduced into dispersion and attenuation curves.

The process of reducing Love wave data to dispersion curves is complicated by the fact that more than one mode may operate at a given frequency. Aside from the very lowest frequencies, at which only the fundamental mode operates, a signal's frequency response represents the sum of two or more modes. Separating the contributions of multiple modes will require two data transformations: From time domain to frequency domain, and then from spatial domain to wave number domain. We can then deduce phase velocity from the resulting wave number-frequency (K-f) relationship.

Obtaining the amplitude information necessary to produce attenuation curves is a more daunting task requiring that special attention be given to field data acquisition. In this chapter, we will discuss methods for collecting field data, and then demonstrate one of these techniques using synthetic Love wave data.

It will be helpful to begin with a discussion of how a source waveform is partitioned into disparate modes.

5.1 Partitioning Waveforms

Section 7.4 of Aki and Richards (2009) discusses techniques for producing synthetic data using a Green's function. For the current discussion, we will simplify and adapt Aki and Richards' Equation 7.143 by assuming that source and receiver height are the same, and that the source produces shear waves that propagate along the source-receiver axis. For an angular frequency, ω, the wave form will be:

$$v(r,t,z,\omega) = \sum_n \frac{l_m(K^*,z,\omega)}{8cUI_1}\sqrt{\frac{2}{\pi K^* r}}e^{i(K^* r-\omega t+\pi/4)} \tag{5.1}$$

$$I_1 = \frac{1}{2}\int_0^\infty \rho(z) l_m^2 dz \tag{5.2}$$

$$I_2 = \frac{1}{2}\int_0^\infty \mu(z) l_m^2 dz \tag{5.3}$$

$$U = \frac{I_2}{cI_1} \tag{5.4}$$

Rearranging Equation 5.4, we see that $cUI_1 = I_2$. Substituting this into the denominator of (5.1), we obtain:

$$v(r,t,z,\omega) = \sum_n \frac{l_m(K^*,z,\omega)}{8I_2}\sqrt{\frac{2}{\pi K_r r}}e^{K_i r}e^{i(K_r r-\omega t+\pi/4)} \tag{5.5}$$

Note the relationship between Equation 5.5 and Equation 3.54, which we derived

Mode	4 Hz	13 Hz	25 Hz	35 Hz	45 Hz	80 Hz
0	1.00	4.41	3.10	2.59	2.27	1.46
1	n/a	0.19	3.40	2.75	2.37	1.77
2i	n/a	n/a	4.90	3.08	2.54	1.83
3i	n/a	n/a	n/a	4.44	2.87	1.88

Table 5.1: Normalized amplitudes of the partition function for a single viscoelastic layer over a half-space (Figure 4.8). Values have been divided by the 4 *Hz* fundamental mode amplitude (6.36E-10).

to account for geometric spreading. We can create a synthetic wave form by summing Equation 5.5 over all frequencies.

In Equations 5.1 and 5.5, I_1, I_2, and K_r are functions of mode (n) and frequency (ω). We define a partition function,$\Gamma(n, \omega)$ as:

$$\Gamma(n,\omega) = \frac{1}{8I_2(n,\omega)}\sqrt{\frac{2}{\pi K_r(n,\omega)}} \tag{5.6}$$

Also recall that we we defined the Love wave attenuation coefficient as $\alpha_L = -K_i$, so that (5.5) can be written as:

$$v(r,t,z,\omega) = \sum_n \Gamma(n,\omega) l_m(K^*, z, \omega)\frac{e^{-\alpha_L r}e^{i(K_r r - \omega t + \pi/4)}}{\sqrt{r}} \tag{5.7}$$

The partition function, $\Gamma(n, \omega)$, is proportional to the fraction of displacement (v) that can be ascribed to a given mode-frequency combination. Recall the depth-dependent behavior of the motion-stress vector (Figure 4.2): For a given mode, the displacement vector in the half-space becomes less pronounced with increasing frequency. The function I_2 in the denominator of (5.6) provides a measure of the influence that the shear modulus of each layer has on the wave form. At low frequencies, deep layers exert a stronger influence on I_2 than they do at high frequencies. Given the Love wave requirement for a velocity structure that generally increases with depth, we would expect I_2 to be greater for low frequencies than for high frequencies. The behavior of I_2 is offset to some extent by the behavior of K_r, which varies directly with frequency, and is inversely proportional to phase velocity. The general tendency of Γ is to decrease with increasing frequency; however, the velocity dependence of K_r complicates this behavior in the interval immediately after the cut-off frequency.

Table 5.1 demonstrates this behavior for each mode. Initially, a new mode will be relatively weak; however, its strength increases to a maximum shortly before the next mode makes its debut. Aside from the first few Hertz after its cut-off frequency, each new overtone has approximately the same strength as its precedessors.

5.2 Practical Considerations

In this section, we discuss the criteria for planning a viscoelastic Love wave experiment. As an example, we will use the geometry and properties from the three-layer viscoelastic model discussed in Chapter 4 (Figure 4.23). We will assume the use of *10 Hz* geophones; i.e., that the geophones are capable of accurately measuring signals with frequencies as low as 10 *Hz*.

5.2.1 Depth vs. Wavelength

In Chapter 4, we discussed Love wave behavior as a function of depth. Near its cut-off frequency, a given mode will be more strongly influenced by deep layers than is the case at higher frequencies (Figure 4.2). Near its own cut-off frequency, a mode's velocity is close to that of the half-space; however, at that same frequency, a lower order mode's phase velocity will approach the shear wave velocity of the upper layers (Figure 4.4). The frequency scaling relationship of Equation 4.1 can be interpreted as the number of half-wave lengths between the surface and the top of the half-space. The fundamental mode (n=0) *sees* the top of the half-space when frequency approaches zero *Hz*. Given that the lower frequency limit of economical, commercially available geophones is in the 8 to 10 *Hz* range, it may be a better plan to use the first or higher overtones to glean information about deeper layers. Another factor militating against the use of the fundamental mode for peering into deep layers is its relative insensitivity to layering. Compare, for example, the dispersion curves for a single 5 *meter* elastic layer over a half-space (Figure 4.4) to the dispersion curves for three elastic layers over a half-space (Figure 4.25): There is little difference between the two fundamental mode dispersion curves; however, there is a marked difference in the dispersion curves for higher modes, which display *shelves* near the shear wave velocity of each layer.

We can rearrange Equation 4.1 to determine the lowest possible mode that could be used to explore a given layer depth. Because this is a multilayer model, we will use Equation 4.3 to estimate equivalent thickness, $\overline{h}$. For the three-layer viscoelastic model, all three layers are 2.73 m thick, and shear wave velocities are $\beta_1 = 100\ m/s$, $\beta_2 = 200\ m/s$, and $\beta_3 = 300\ m/s$. $\overline{h}$=5 m, and:

$$n_{min} = ceil\left(\frac{2f\overline{h}\sqrt{1-\frac{\beta_1^2}{\beta_2^2}}}{\beta_1}\right) = ceil\left(\frac{2(5)(10)\sqrt{1-\frac{100^2}{400^2}}}{100}\right) = 1 \tag{5.8}$$

suggesting that the first overtone will the lowest mode that will be completely visible to our 10 *Hz* receivers.

5.2.2 Temporal and Spatial Resolution and Aperture

In the introduction to this chapter, we suggested that our approach to separating Love wave modes would require that spatial and temporal data be transformed to frequency and wave number domain, and that the resulting K-f plot be used create dispersion curves. Thus, when designing a Love wave field experiment, the data must span the wave numbers and frequencies of interest to the investigator, and have sufficient resolving power to enable the investigator to distinguish between the frequencies and wave numbers of neighboring modes.

The temporal Nyquist criterion places an upper limit on the frequency that can be resolved with a given sampling rate:

$$\Delta t_{nyq} = \frac{1}{2f_{max}} = \frac{\pi}{\omega} \tag{5.9}$$

where Δt_{nyq} is the Nyquist sampling interval, and f_{max} is the highest frequency being measured. In practice, it is usually desirable to use sampling intervals that are considerably less than dictated by the Nyquist criterion. For the present discussion, we will use $\Delta t = 1/(5f_{max})$ as an experimental design criterion. At the other end of the frequency spectrum, resolving low frequencies requires that data be collected over a duration comparable to a complete cycle of the lowest frequency of interest. For the present discussion, we will use a duration equal to twice the low frequency period as our design criteria. This duration, called the temporal aperture, is equal to $(n_t - 1)\Delta t$, so the minimum number of samples, n_t, necessary to achieve a temporal aperture twice the longest wavelength being studied is:

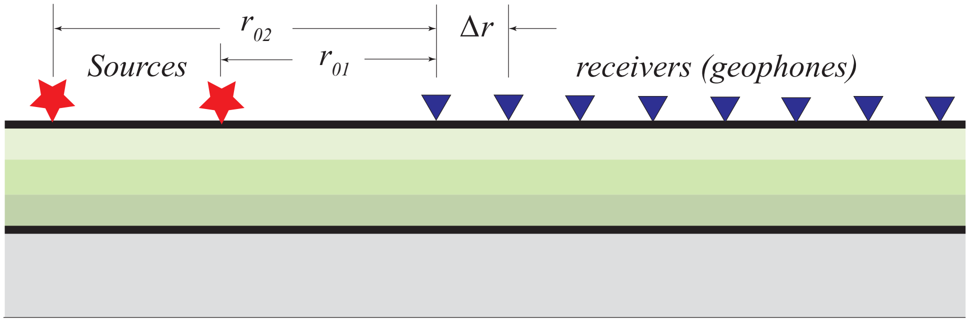

Figure 5.1: Source and receiver lay-out. The distance between a source and the first receiver, r_{0j}, is called the *offset distance.* Δr is the *receiver spacing.*

$$n_t = \frac{2}{f_{min}\Delta t} + 1 \tag{5.10}$$

We denote the spatial wavelength of a signal using the Greek letter λ, so that the spatial wave number, $1/\lambda$, represents the number of complete oscillations in a unit length. The spatial wavelength is related to the angular wave number, K_r by the relationship:

$$K_r = \frac{2\pi}{\lambda} \tag{5.11}$$

The angular wave number is expressed in terms of *radians* per unit length, while frequency is expressed as *cycles* per unit time. To simplify the following discussion, we will introduce a cyclic wave number, $K = K_r/(2\pi)$, so that the Love wave phase velocity is:

$$C_L = \frac{\omega}{K_r} = f\lambda = \frac{f}{K} \tag{5.12}$$

(see also Equation 3.35).

A spatial analogue to the temporal Nyquist criterion is:

$$\Delta r = \frac{1}{2K} = \frac{\lambda}{2} = \frac{C_L}{2f} \tag{5.13}$$

where Δr is the spatial sampling interval (receiver spacing). As was the case with Δt, it is usually desirable to use sampling intervals that are considerably smaller than those dictated by the Nyquist criterion. We will use the following receiver spacing as an experimental design criterion:

$$\Delta r = \frac{1}{5K} = \frac{\lambda}{5} = \frac{C_L}{5f} \tag{5.14}$$

Spatial aperture is analogous to temporal aperture, and is equal to $(n_r - 1)\Delta r$. In order to resolve long wavelengths, we would like to have a receiver line of sufficient length (spatial aperture) to capture at least two wavelengths, so the minimum number of receivers, n_r, will be:

$$n_r = \frac{2}{K\Delta r} + 1 = \frac{2C_L}{f\Delta r} + 1 \tag{5.15}$$

In our discussion of the three-layer model, we examined dispersion and attenuation curves for frequencies as high as 120 *Hz*, which corresponds to a sampling interval of 0.00167 *s*. Although we explored the behavior of the system at frequencies as low as 4 *Hz*, our use of 10 *Hz* geophones obviates the need to design a data collection scheme for frequencies lower than 10 *Hz*. The minimum number of time samples (Equation 5.10) is 121. These sampling requirements are well within the capabilities of off-the-shelf hardware.

Determining an economical receiver spacing interval becomes more problematic.

lay-out	Vel (m/s)	Low Frequency Limit (Hz)	High Frequency Limit (Hz)
low den	100	2.1	50
low den	400	8.4	200
hi den	100	12.6	300
hi den	400	50.4	300*

Table 5.2: Frequency ranges for the low density (1 *m* receiver spacing) and high density (0.167 *m* receiver spacing) lay-outs. * The high density lay-out upper limit is constrained by the temporal Nyquist frequency.

Receiver spacing corresponding to 120 *Hz* and 100 *m/s* is a very tight 0.167 *m*, and the number of receivers necessary to measure a 400 *m/s* phase velocity at 10 *Hz* is 480. Given the cost of receivers, we would like to reduce this number. Inspection of Figures 4.27 and 4.28 suggests that we could increase receiver spacing to *0.2 m*, which corresponds to a frequency of 60 *Hz* and velocity of 100 *m/s*, and still see the important features of each curve, but this plan still requires 201 receivers.

More importantly, this exercise in fine tuning required such detailed a-priori knowledge of layer geometry and material properties as to obviate the need for an investigation using Love waves. Realistically, collecting Love wave data may require more than one receiver lay-out. In this chapter, we will assume two separate receiver lay-outs, each using 96 receivers: A high density lay-out using 0.167 *m* spacing (6 receivers per meter), and a low density lay-out using 1 *m* spacing. We will use these two lay-outs in this chapter's simulations.

Throughout this discussion, we have implicitly assumed a flat, horizontally homogeneous layer geometry. Although increasing aperture size improves resolution, it also increases the risk that the survey area will include discontinuities or asperities of sufficient magnitude to violate the assumption of horizontal homogeneity.

5.2.3 Measuring Attenuation

The majority of seismic work done by geotechnical engineers or shallow-subsurface researchers involves reflection and refraction seismology; thus, common equipment and techniques are usually optimized for problems that involve purely elastic properties. In reflection or refraction seismology, arrival times, phase velocity, and dispersive properties are important (Burger *et al.*, 2006); however, the exact amplitude of any particular signal is usually of less importance. We will find the derivation of dispersion curves from seismic data to be a relatively straight-forward process, but because of source/receiver variability, we will find extracting attenuation information to be more challenging.

As noted earlier, the signal recorded along a line of receivers is a function of much more than just the properties of the intervening materials. More often than not, the source used in geotechnical work is a hammer blow, which we hope will generate a signal approximating a unit pulse–Or at least a sufficiently broadband pulse to capture essential information from a few Love wave modes. In the field, the hammer may be wielded by one or more human beings, and the blow-to-blow amplitude variation may be considerable. If we were measuring a non-dispersive, monochromatic signal, we might consider a source and receiver lay-out consisting of a single source and two receivers (Figure 5.1). We could determine the attenuation coefficient using Δr and the amplitude at each receiver. So long as the measurement is taken using a single hammer blow, this scheme avoids any problems associated with source variability.

On further reflection, however, we see that the signal recorded by each receiver is a function of ground motion, receiver-ground coupling, and the receiver, itself. Only ground motion is of interest to us, and to isolate the amplitude of ground motion from the variability of receiver-ground coupling and the inner workings of the receiver, we might consider determining the attenuation coefficient by applying linear regression to data obtained from a line of multiple receivers. Indeed, as we saw in the previous subsection, such a line will be necessary if we are to have an aperture sufficient to effect mode separation. We will refer to this sort of data collection scheme as a *single-source* design.

In practice, receiver-to-receiver variability can be quite large relative to the attenuation values being measured, and the number of receivers necessary to obtain an accurate regression estimate using a single-source design could be prohibitive.

We could eliminate receiver-to-receiver variation, and minimize receiver-ground coupling effects, by using a single receiver that is moved to carefully prepared locations along the receiver line. Because this experimental design requires multiple hammer blows, we will need to include a fixed reference receiver near the source. Amplitude information from the reference receiver can be used to compensate for blow-to-blow variation. We will refer to this scheme as a *receiver walk-away* design.

By reciprocity (Aki and Richards, 2009), it should be possible to *walk-away* the source from a single, stationary receiver. As was the case for the receiver walk-away design, each change of source position will be accompanied by a new, and unknown source-ground coupling constant. Moving a reference receiver with the source may allow us to compensate for blow-to-blow and source-ground coupling variability, but moving the reference receiver also introduces variability from changes in the reference receiver-ground coupling constant.

For the discussion in this and subsequent chapters, we will assume that data has been gathered using a *source walk-away* design consisting of a fixed receiver line, and a source that is moved to different receiver offsets (Figure 5.1). In the next section, we will see that this design is robust to receiver variability.

The reader can probably imagine other combinations of source and receiver walkaway, and the proper choice of whether it is best to keep source or receiver fixed will ultimately depend on equipment capability and local soil conditions.

5.2.4 Near Field Considerations

In Section 3.3, we derived the wave equation in cylindrical coordinates, and found the exact solution to be a Bessel function. Most common geophysical data processing techniques assume that the underlying wave forms are sinusoidal, and we found that beyond about one wavelength, a transformation based on Equation 3.54 gives good results.

A second near-field consideration concerns the need for the Love wave to be completely developed before it reaches the receiver array. As we discussed in the introduction to Chapter 1, a Love wave results from the interaction between a reflecting shear wave and the evanescent wave formed at the top of the half-space. It is thus necessary that the shear wave be able to make one complete round trip from the surface, to the half-space, and back to the surface. Assuming a velocity structure that monotonically increases with depth, a source-receiver offset distance greater than or equal to the depth of the top of the half-space should assure full Love wave field development.

Thus, the minimum source-receiver offset should either be equal to one wavelength, or to the depth to the top of the half-space, whichever is greater.

5.3 Data Reduction

The continuous Fourier transformation of a periodic function, Θ, over a finite interval can be expressed as (Snieder, 2004):

$$F(K,f) = \int_{-L/2}^{L/2} e^{-2\pi iKr} \int_{-T/2}^{T/2} e^{2\pi ift}\Theta(r,t)dtdr \tag{5.16}$$

where $K = 1/\lambda$, L and T are, respectively, spatial and temporal limits of integration, and $\Theta(r,t)$ can be written as:

$$\Theta(r,t) = Ae^{i(K^*r-\omega t)} \tag{5.17}$$

where A is the signal amplitude. $F(K,f)$ can be rewritten as $F(K,f) = F(K)F(f)$, where $F(K)$ and $F(f)$ are, respectively, spatial and temporal Fourier transforms. Equation 5.16 can be rewritten as:

$$F(K,f) = \int_{-L/2}^{L/2} e^{-2\pi iKr} \int_{-T/2}^{T/2} e^{2\pi ift}Ae^{i(K^*r-\omega t)}dtdr = AF(f)\int_{-L/2}^{L/2} e^{i(K^*-2\pi K)}dr \tag{5.18}$$

Recalling that the complex wave number $K^* = K_r + iK_i$, and that $\alpha = -K_i$, Equation 5.18 becomes:

$$F(K,f) = AF(f)\int_{-L/2}^{L/2} e^{-\alpha r}e^{i(K_r-2\pi K)}dr \tag{5.19}$$

In practice, we will be using discrete, digital data, which we will process using a discrete analogue of Equation 5.16. Denoting the discrete analogues of $F(K,f)$ and $F(f)$ as $F'(K,f)$ and $F'(f)$, a discrete form of 5.19 can be written as:

$$F'(K,f) = AF'(f)\sum_{j=0}^{n-1} e^{-\alpha(r_0+j\Delta r)} e^{i(K_r-2\pi K)(r_0+j\Delta r)} \tag{5.20}$$

where r_0 and Δr are, respectively, receiver offset and spacing (Figure 5.1). The right side of Equation 5.20 can be rewritten:

$$F'(K,f) = AF'(f)e^{-\alpha r_0} e^{i(K_r-2\pi K)r_0} \sum_{j=0}^{n-1} e^{i(K_r-2\pi K+i\alpha)j\Delta r} \tag{5.21}$$

When applied to real data, the modulus of values obtained from Equation 5.21 will achieve local maxima when $\omega = 2\pi f$ and $K_r = 2\pi K$: We will find wave number-frequency pairs corresponding to Love wave modes by looking for maxima on a K-f plot of data obtained from the Fourier transformation of Equation 5.21.

Examination of the right-hand side of Equation 5.21 reveals that the summation is a function of receiver spacing, whereas the exponential factors outside the summation are functions of offset distance. This suggests a technique for determining α that can be used with data collected using a source walk-away experimental design: When multiple offsets (r_{0j}) are used, we can obtain alpha from the regression coefficient (slope) of the logarithm of the absolute value of the left-hand side of Equation 5.21 with respect to r_{0j}. When only two offsets are used, alpha can be obtained using:

$$\alpha = \frac{ln|F_2'(K)| - ln|F_1'(K)|}{r_{01} - r_{02}} \tag{5.22}$$

where $F_1'(K)$ and $F_2'(K)$ are the temporal-spatial Fourier transforms of data taken at offset distances r_{01} and r_{02}, respectively. With more than two offsets, we could obtain α from the regression coefficient (slope) of $ln|F_j'(K)|$ with r_{0j}.

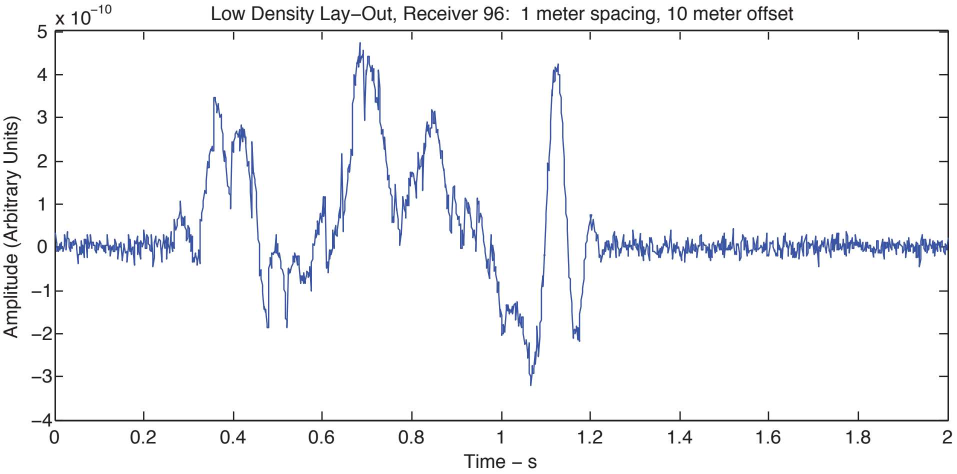

Figure 5.2: Gaussian white noise was added to the data from each trace.

5.4 Synthetic Data and Data Reduction Methods

We will demonstrate the data reduction methods of the previous section using synthetic data generated using the wave form partitioning techniques presented in Section 5.1.

5.4.1 Synthetic Data

We will generate synthetic data using the earth models presented in Chapter 4, and the waveform partitioning techniques presented in Section 5.1. The source waveform will be a unit pulse generated by superposition of sinusoidal waves with frequencies varying, in $\frac{1}{4}$ Hz increments, between 4 and 120 Hz. We will add Gaussian white noise, with a standard deviation equal to 10% of the RMS signal strength of the most distal receiver, to the data (Figure 5.2).

Our simulated data will be collected over a 2 second interval using a of sampling rate of 600 *samples/s*, which corresponds to a Nyquist frequency of 300 Hz. We will

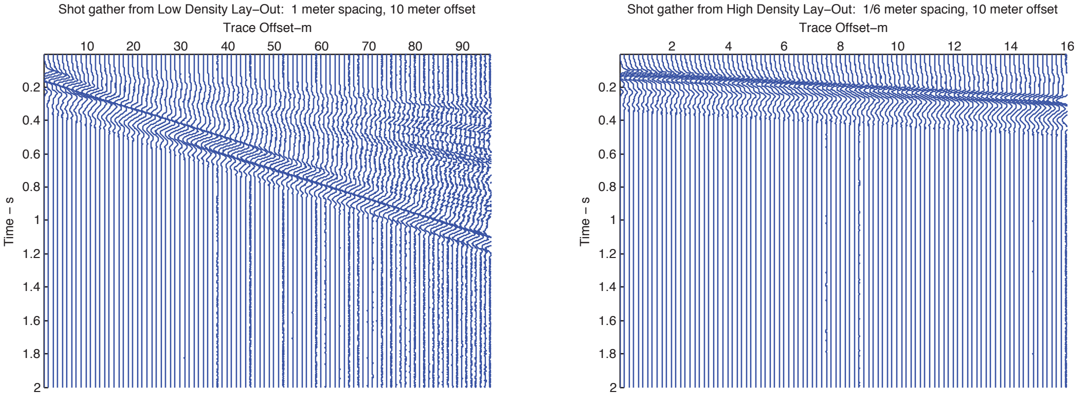

Figure 5.3: Comparison of low density (l) and high density (r) synthetic data shot gathers for a single viscoelastic layer over a half-space (Figure 4.8). Gaussian white noise has been added to both data sets.

use two different receiver spacings: A low density lay-out with a receiver spacing of 1 m and a 95 m aperture, and a high density lay-out with 6 receivers per meter, and a 15.84 m aperture. Both lay-outs employ 96 receivers. See Table 5.2 for the frequency and velocity ranges of each lay-out. For each lay-out, we will simulate a source walk-away experimental design using two different receiver offsets: The first at 10 m and the second at 20 m. More information about the methods and code (*SignalBuilder.m*) used to create synthetic data can be found in Appendices A and B.

5.4.2 Reducing Source Walk-Away Data

We will use the following procedure to reduce data from our source walk-away experiment.

- Apply a geometric correction to the data from each receiver. This can be done by multiplying the data from each receiver by the square root of its distance from the source, $\sqrt{r_{0j} + k\Delta r}$.

- For each source offset distance, create a K-f plot using successive time and space domain Fourier transforms. Use the absolute value of the transformed data to create the K-f plots and frequency slices described below. Detailed procedures for creating a K-f plot can be found in Appendix C.

  ◇ For each of these plots, visually identify each mode (Figure 5.5).

  ◇ For each wave number, create a slice of frequency domain data, and determine the frequency and amplitude corresponding to each mode (Figure 5.6). More detailed procedures for creating a constant wave number slice can be found in Appendix C.

  ◇ For each wave number-frequency pair, determine velocity using $v = f/k$. Use these values to create a dispersion curve.

  ◇ When using only two source offsets, Equation 5.22 can be used to determine the attenuation coefficient, α, for each frequency. When using more than two source offsets, use the regression technique described in the previous section. Use these values to create an attenuation curve.

5.4.3 Reducing Receiver Walk-Away Data

The process of obtaining a dispersion curve from receiver walk-away data is similar to that for source walk-away data, but because only one source position is used, we will need to use a different method for obtaining attenuation data.

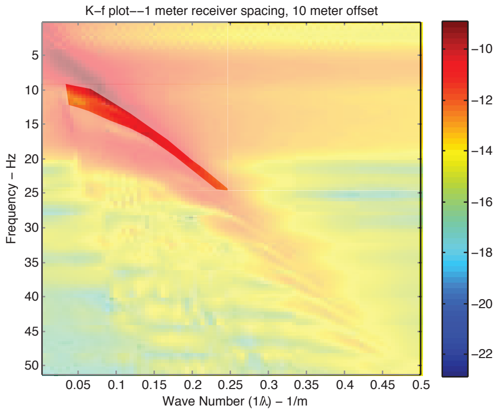

Figure 5.4: Before receiver walk-away data is transformed from K-f domain to frequency-space domain, information not associated with the mode should be excluded. In this case, we have *masked-out* all data not associated with the first harmonic (n=1). Figure 5.5 illustrates unmasked data.

- Apply a geometric correction to the data from each receiver. This can be done by multiplying the data from each receiver by the square root of its distance from the source, $\sqrt{r_{0j} + k\Delta r}$.
- Using the data from all receiver positions, create a K-f plot using successive time and space domain Fourier transforms.
  - ◇ Visually identify each mode (Figure 5.5).
  - ◇ For each wave number, create a slice of frequency domain data. Identify the frequency corresponding to each mode (Figure 5.6).
  - ◇ For each wave number-frequency pair, determine velocity using $v = f/k$. Use these values to create a dispersion curve.
- For a receiver walk-away experiment, we will obtain attenuation coefficients in frequency-space domain. Do the following for each mode:

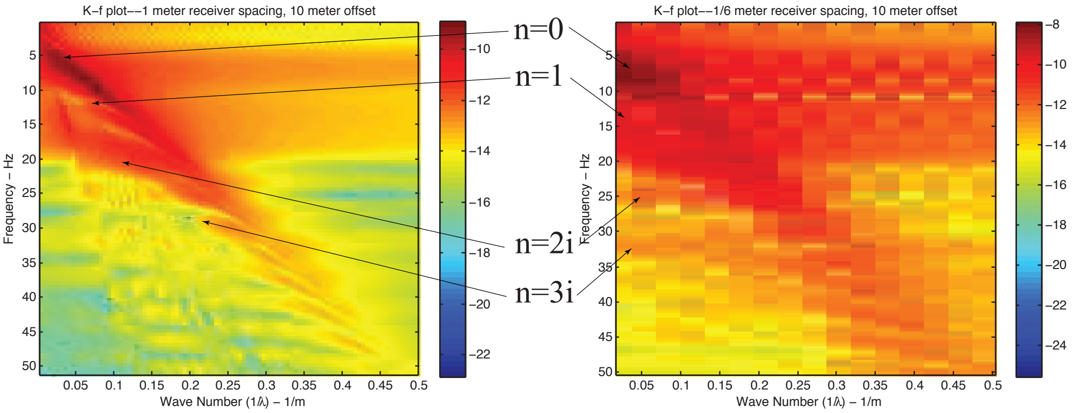

Figure 5.5: Comparison of K-f plots obtained using the low density (*left*) and high density (*right*) lay-outs. Note the logarithmic color scale.

◇ In K-f domain, *mask-out* all data not associated with the mode of interest (Figure 5.4).

◇ Use a single Fourier transformation to convert the *masked* data to frequency-space domain.

◇ For each receiver, determine the amplitude of each frequency.

◇ For each frequency, determine the attenuation coefficient from the regression coefficient (slope) of the logarithm of amplitude versus receiver offset.

5.5 Results

In this section, we will demonstrate the data reduction process for synthetic data produced using the one, two, and three layer viscoelastic models presented in Chapter 4.

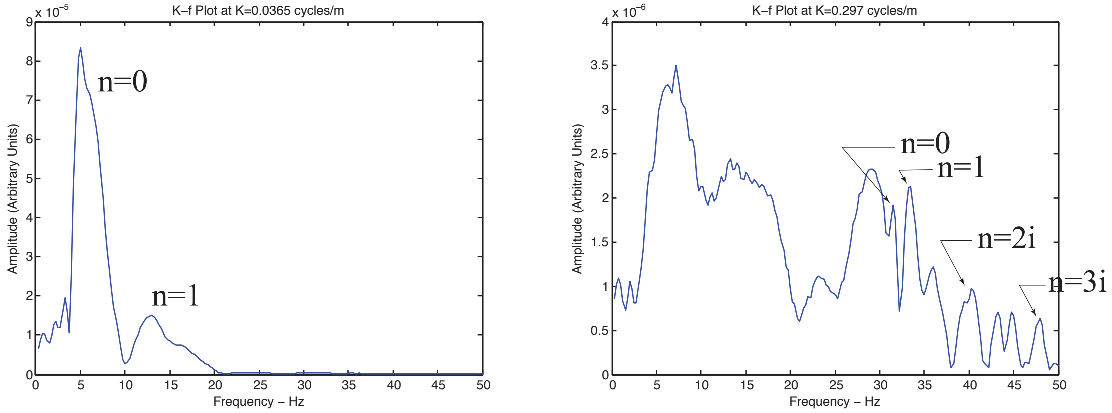

Figure 5.6: Constant wave number *slices* obtained from Figure 5.5.

5.5.1 One-Layer Model

Examination of K-f plots (figure 5.5) confirms that at low frequencies, data obtained using the low density lay-out provide better resolution than data obtained from the high density lay-out. It is possible to visually identify modes using K-f plots alone, and satisfactory dispersion curves can be so obtained; however, this procedure does not yield data of sufficient accuracy to calculate attenuation. In practice, we can identify approximate relationships visually using K-f plots, and then refine them using either constant frequency or constant wave number plots such as shown in figure 5.6.

Given the general orientation of modes (Figure 5.5), constant wave number plots are less noisy than their constant frequency counterparts. Peak identification is relatively easy at low wave numbers, but becomes increasingly difficult as wave number increases. By approximately 0.4 *cycles/m*, corresponding to a 100 *m/s* phase velocity frequency of 40 *Hz*, peaks become so difficult to isolate, that mispicks are likely. Beyond 0.4 *cycles/m*, data from the high density lay-out can be used (Figure 5.7), permitting the frequency range of dispersion and attenuation curves to be extended

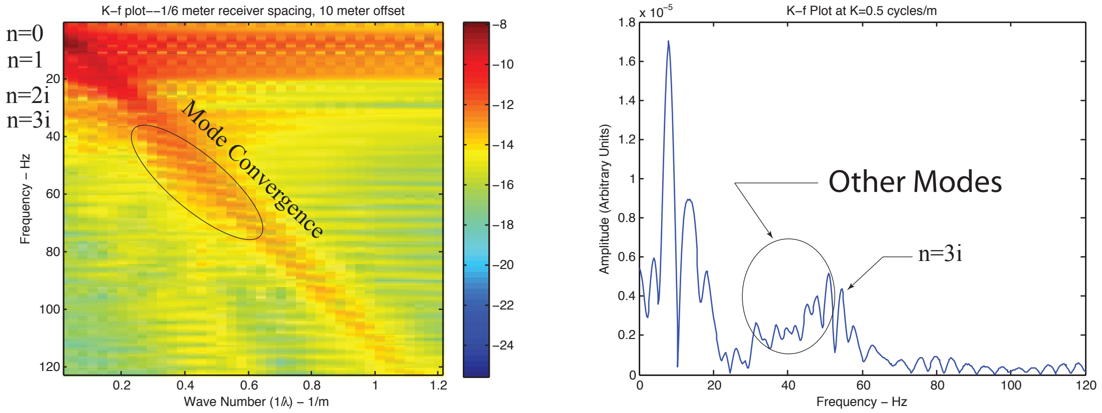

Figure 5.7: Expanded K-f plot of high density lay-out data. This data permitted marginally better discrimination of modes in the region of mode convergence than could be obtained from low density lay-out data.

by a few Hertz. Beyond wave numbers of about 0.6 *cycles/m*, modes converge into a single, inchoate blob. For the low density lay-out, this corresponds reasonably well to our design criteria (Figure 5.8). Somewhat surprisingly, the high density lay-out only extends this limit a few Hertz (Figure 5.8).

After correcting for geometric dispersion (Sub-section 3.3.3), we find attenuation values for each frequency by applying Equation 5.22 to the absolute value of corresponding K-f pairs from both 10 *m* and 20 *m* offset distances. Accurate amplitude measurement is hampered by noise appearing at around 20 *Hz* (Figure 5.10). By about 30 *Hz*, little meaningful amplitude information can be gleaned from either the low or high density lay-outs.

In general, useful attenuation data are only available for the fundamental mode and first harmonic (figure 5.11).

Attenuation information from the high density lay-out is unusable (figure 5.12).

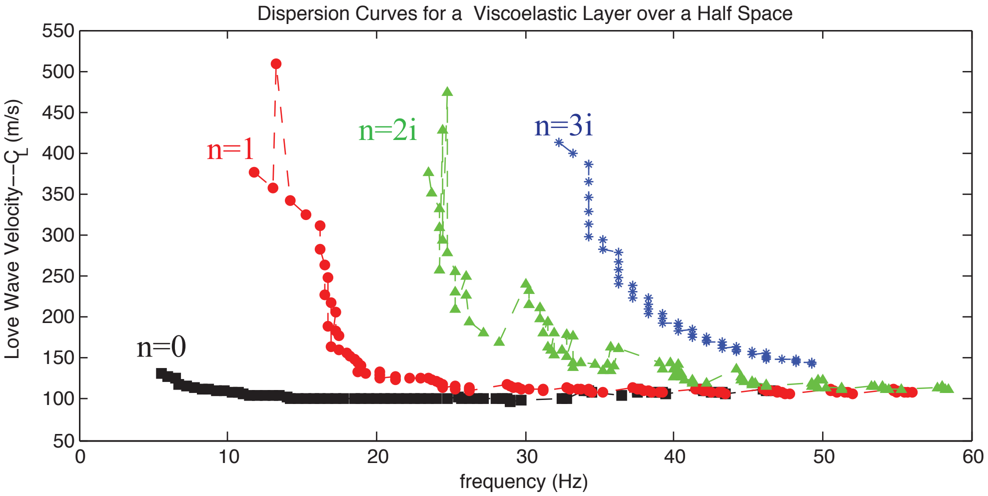

Figure 5.8: Dispersion curves obtained from the low density lay-out. Synthetic data were generated using the one-layer viscoelastic model illustrated in Figure 4.8. Compare with the theoretical curves for the same model (Figure 4.10).

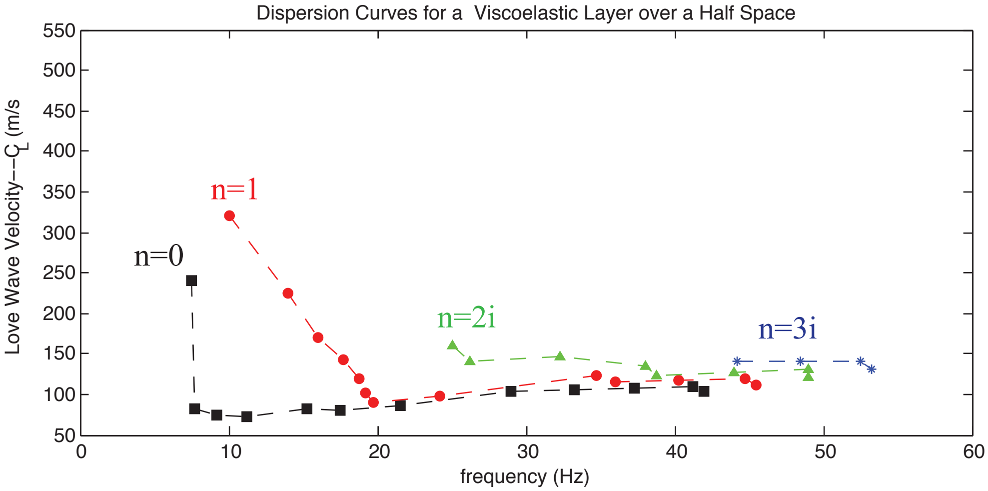

Figure 5.9: Dispersion curves obtained from the high density lay-out. Synthetic data were generated using the one-layer viscoelastic model illustrated in Figure 4.8. Compare with the theoretical curves for the same model (Figure 4.10).

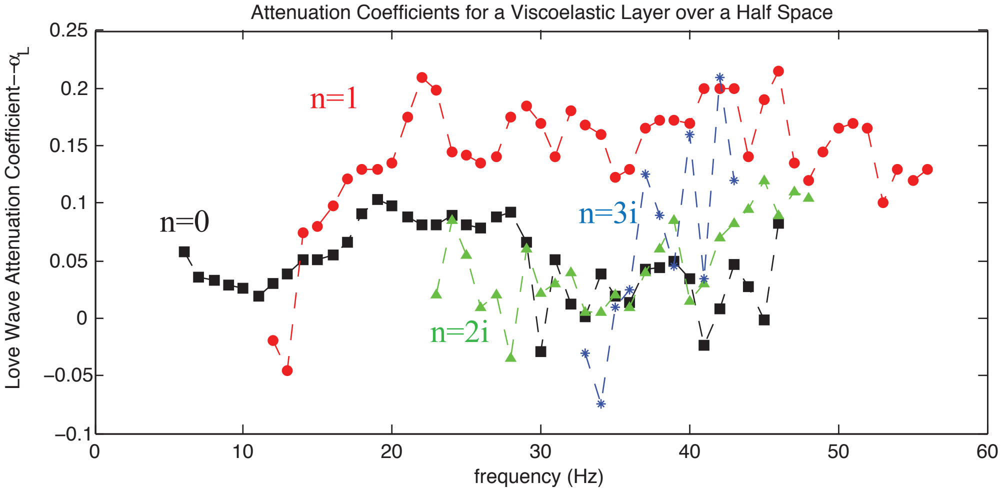

Figure 5.10: Attenuation curves obtained from the low density lay-out. Synthetic data were generated using the one layer viscoelastic model illustrated in Figure 4.8. Compare with the theoretical curve for the same model (Figure 4.11).

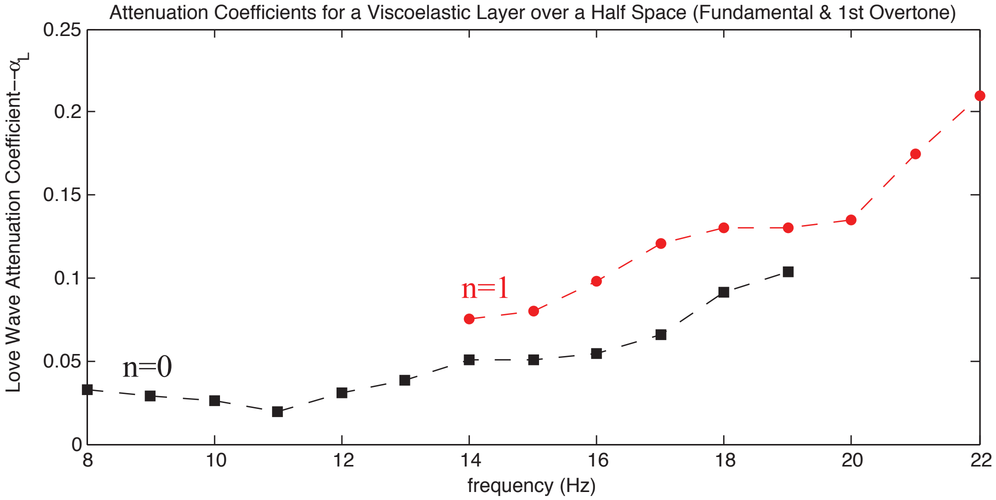

Figure 5.11: Selected attenuation curves extracted from Figure 5.10.

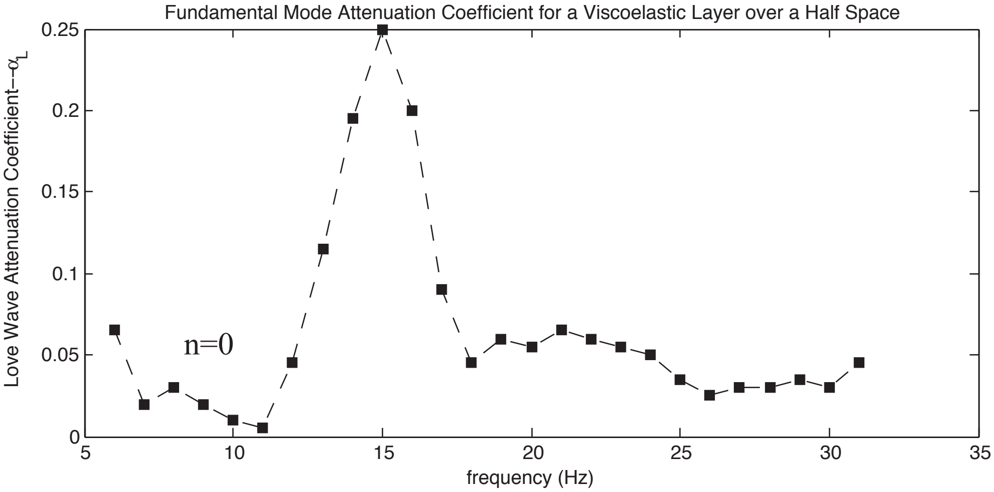

Figure 5.12: Attenuation curve obtained for the fundamental mode using the high density lay-out. Attenuation values obtained from the remaining modes were completely unsable. Synthetic data were modeled using the one-layer viscoelastic model illustrated in Figure 4.8. Compare with the theoretical curve for the same model (Figure 4.11).

5.5.2 Two-Layer Model

The data reduction procedures for the two-layer model are similar to those used for the single-layer model. Dispersion curves for the second and third overtones capture the layer two *shelf* at approximately 200 *m/s*. It is possible to obtain dispersion curves for the second and third overtones up to a frequency of 60 *Hz*. Recall that for a two-layer viscoelastic model, attenuation curves for higher level modes were inverted with respect to the one-layer elastic model (Figure 4.21). Evidently, this inversion effect permits higher order modes to remain viable to higher frequencies than either the fundamental or first harmonic. Unfortunately, this means that there is little difference in the signals obtained at 10 *m* and 20 *m* source offsets, so beyond about 30 *Hz*, the calculated attenuation coefficients for the second and third harmonics (n=2,3) are either zero or negative (Figure 5.10).

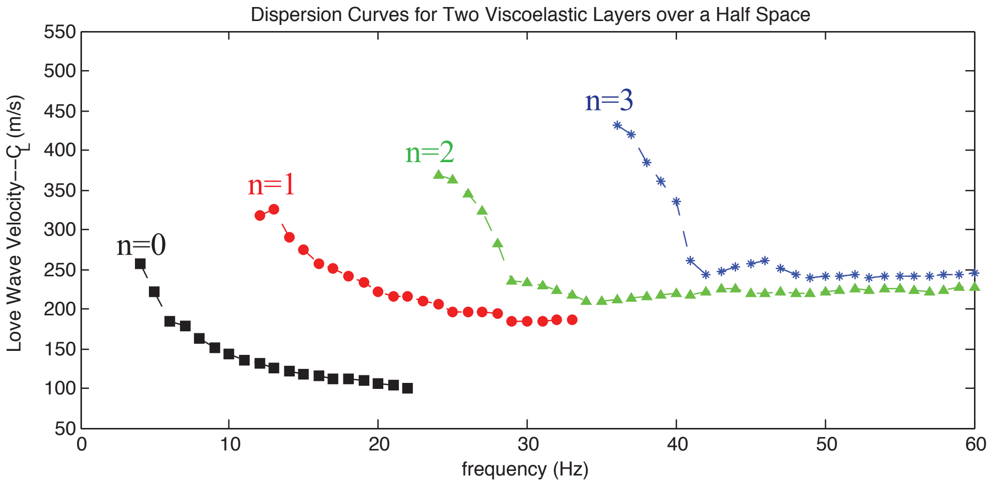

Figure 5.13: Dispersion curves for synthetic two-layer viscoelastic data (Figure 4.18) obtained from the low density lay-out. Compare with the theoretical curve for the same model (Figure 4.20).

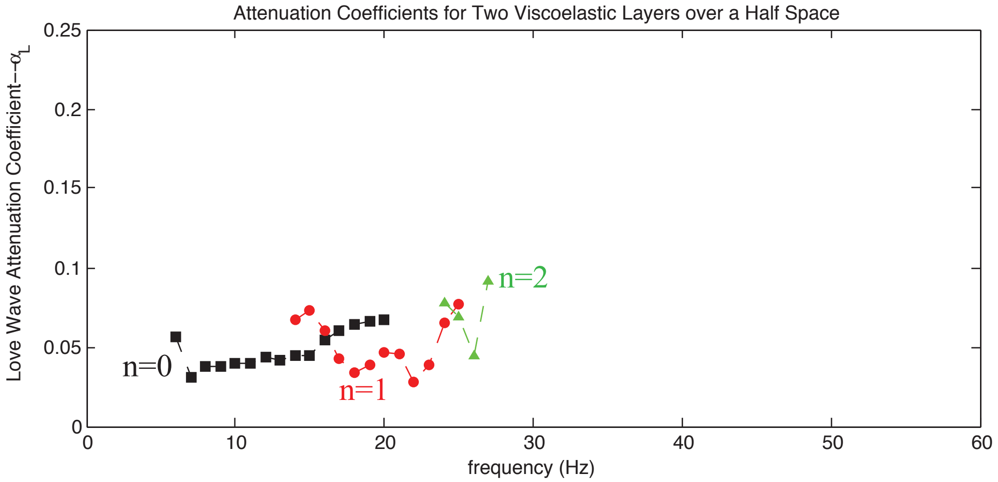

Figure 5.14: Attenuation curves for synthetic two-layer viscoelastic data (Figure 4.18) obtained from the low density lay-out. Compare with the theoretical curve for the same model (Figure 4.21).

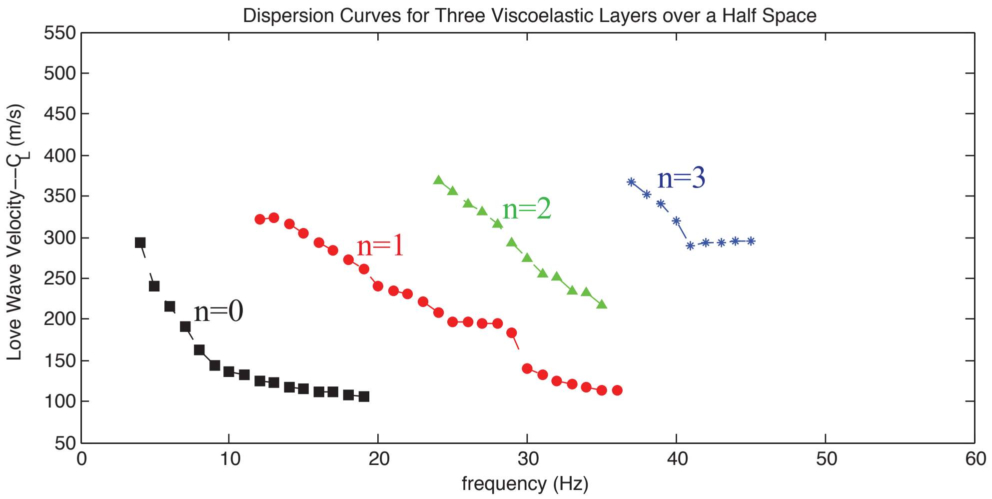

Figure 5.15: Dispersion curves for synthetic three-layer viscoelastic data (Figure 4.23) obtained from the low density lay-out. Compare with the theoretical curve for the same model (Figure 4.27).

5.5.3 Three-Layer Model

Data reduction procedures and results for the three-layer model are similar to those obtained for the two-layer model. Although the attenuation coefficients experience the same inversion effect as was observed for the two-layer model, this does not translate into an increase in the frequency over which dispersion data can be obtained. The *shelves* associated with layers 2 and 3 are evident, but not particularly pronounced.

5.6 Summary: Data Reduction

In this chapter, we discussed considerations for the design of field experiments, and demonstrated a method for obtaining dispersion curves and attenuation plots from data obtained using a source walk-away field experiment. Obtaining data suitable for generating dispersion curves is a straightforward process, but obtaining data from

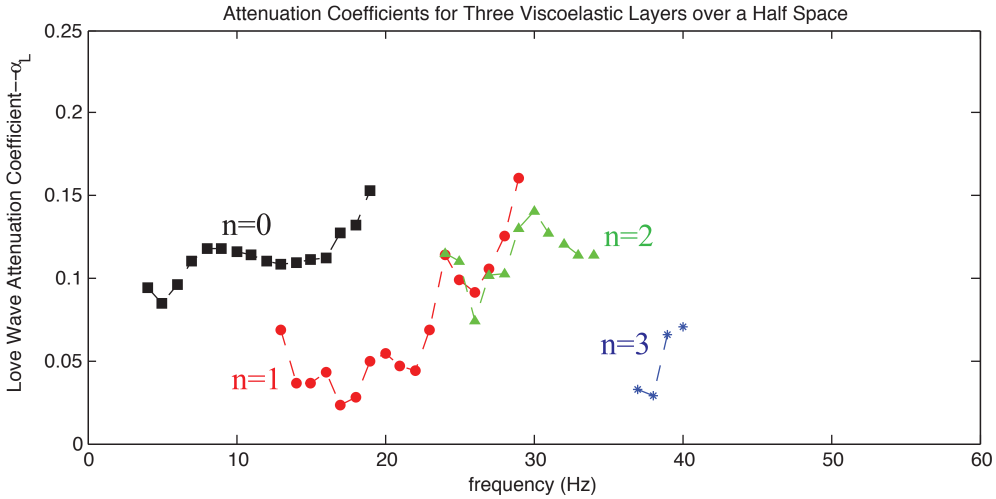

Figure 5.16: Attenuation curves for synthetic three-layer viscoelastic data (Figure 4.23) obtained from the low density lay-out. Compare with the theoretical curve for the same model (Figure 4.28).

which attenuation information can be generated requires that special care be taken when designing and conducting a field experiment.

We compared the performance of two different receiver lay-outs using 96 receivers each. It had been hoped that the high density lay-out would extend the frequency range of the experiment; however, because of its small aperture, the high density lay-out was unable to satisfactorily resolve modes at high frequencies. On the other hand, the low density lay-out, with its large aperture, produced usable data over a much wider range of frequencies and wave numbers.

Using the low frequency lay-out, we were able to obtain dispersion curves for all modes and all three models over an interval from 10 *Hz* to about 50 *Hz*. Our ability to evince attenuation information from the data was more limited. For the one and two-layer models, we were only able to obtain accurate attenuation from the first two modes. Beyond about 25 *Hz*, modes were sufficiently close to each other that partitioning amplitude information became difficult. Prominent *shelves* in the three-layer model kept peaks separated over a larger range of frequencies, and reasonably good attenuation information could be obtained at frequencies up to about 35 *Hz*.

CHAPTER 6:

DATA INVERSION

In the previous chapter, we reduced field data into a form that can be represented by dispersion and attenuation curves. In this chapter, we will be concerned with finding layer geometry and material properties that provide a plausible explanation for the dispersion and attenuation curves and, by extension, the field data. This process is called inversion.

6.1 Joint Inversion Using the Gauss-Newton Method

We will briefly discuss the Gauss-Newton method for inverting non-linear data. A more thorough treatment can be found in most elementary texts on inversion, such as Aster *et al.* (2013). In the present exposition, we follow the treatment of Michaels (1998), who used the method to invert shear wave dispersion and attenuation data obtained from downhole studies.

Consider the general, non-linear relationship, $\mathbf{G}(f, \mathbf{m}) = \mathbf{d}(f)$, where $\mathbf{d}(f)$ is a data vector, f is frequency, and $\mathbf{m}$ is a vector of model parameters such as thickness (h), density (ρ), shear modulus (μ), and viscosity (η) for each layer. For the present discussion, the data vector, $\mathbf{d}(f)$, contains measurements taken at a specific frequencies from either dispersion or attenuation curves. Note that the data vector includes error, and is equal to $\mathbf{d_{true}}(f) + \epsilon$, where $\mathbf{d_{true}}(f)$ is a vector of error-free values, and

ϵ is a vector of errors.

Our task will be to find an estimate of $\mathbf{m}$, which we will call $\hat{\mathbf{m}}$, that best fits the data vector. Our approach will be to use an iterative procedure, and we will denote successive trial values our estimate as $\hat{\mathbf{m}}_k$. The residual, or difference between the measured data and an estimate made using our assumed value, is given by:

$$\mathbf{r_k} = \mathbf{d}(f) - \mathbf{G}(f, \hat{\mathbf{m}}_\mathbf{k}) \tag{6.1}$$

where $\mathbf{r_k}$ is a vector of residual values. Under the least-squares criterion for best fit, we could obtain an estimate of $\mathbf{m}$ by adjusting $\hat{\mathbf{m}}_\mathbf{k}$ until we find a value for which the sum of squared residuals is minimized. Given the potential number of model parameters, this could be a time-consuming process, indeed.

We note that $\mathbf{r_k}$ is a vector pointing from $\mathbf{G}$ to the data, $\mathbf{d}(f)$. Assuming $\mathbf{G}$ to be differentiable, and reasonably linear in the vicinity of $\mathbf{d}(f)$ and $\mathbf{G}$, $\mathbf{r_k}$ is approximately equal to:

$$\mathbf{r_k} \approx \begin{bmatrix} \frac{\partial \mathbf{G}(f_1,\mathbf{m})}{\partial m_1} & \frac{\partial \mathbf{G}(f_1,\mathbf{m})}{\partial m_2} & \cdots \\ \frac{\partial \mathbf{G}(f_2,\mathbf{m})}{\partial m_1} & \frac{\partial \mathbf{G}(f_2,\mathbf{m})}{\partial m_2} & \cdots \\ \vdots & \vdots & \ddots \end{bmatrix} \Delta\mathbf{m_k} = \mathbf{J}(f, \mathbf{m})\Delta\mathbf{m_k} \tag{6.2}$$

where $\Delta\mathbf{m_k} = \mathbf{m} - \hat{\mathbf{m}}_\mathbf{k}$, and the matrix of partial derivatives is called the Jacobian, $\mathbf{J}$, of $\mathbf{G}$. Use of the Jacobian effectively linearizes the problem. The relationship, $\mathbf{r_k} = \mathbf{J}\Delta\mathbf{m_k}$, is amenable to linear least squares regression techniques (Aster *et al.*, 2013). We should mention a few important assumptions of least squares regression: The errors in the data vector, (ϵ), should be random, independent, and normally and identically distributed. The last assumption, that the errors be normally and identically distributed, is a fairly weak assumption so long as variance is equal (Rice, 1995).

We will typically have more than one dispersion and attenuation curve at our disposal, and we would like to be able to use the data from all of these when estimating parameters. Such a procedure is referred to as joint inversion. We restate the Jacobian matrix with a separate section (set of rows) for each curve:

$$\begin{bmatrix} \mathbf{J}(f,\mathbf{m})_{curve1} \\ \mathbf{J}(f,\mathbf{m})_{curve2} \\ \vdots \end{bmatrix} \Delta\mathbf{m_k} = \begin{bmatrix} \mathbf{r_k}_{curve1} \\ \mathbf{r_k}_{curve2} \\ \vdots \end{bmatrix} \tag{6.3}$$

Given the large differences in scale between the velocity vector (∼100s of meters per second), and the attenuation coefficient (∼0.1 per meter), we expect large disparities in the variances of the data vectors associated with each section of (6.3), thus violating the equal variance assumption of least squares regression. To ameliorate this situation, we resort to a row weighting scheme using a square, diagonal matrix with dimensions equal to the number of data points, and diagonal entries equal to the reciprocal of the standard deviation of each block of data (Brandal, 1991):

$$\mathbf{W} = \begin{bmatrix} 1/\sigma_1 & 0 & 0 & 0 & 0 & 0 & \dots & \\ 0 & 1/\sigma_1 & 0 & 0 & 0 & 0 & \dots & \\ 0 & 0 & 1/\sigma_1 & 0 & 0 & 0 & \dots & \\ \dots & 0 & 0 & 1/\sigma_2 & 0 & 0 & \dots & \\ \dots & 0 & 0 & 0 & 1/\sigma_2 & 0 & \dots & \\ \dots & 0 & 0 & 0 & 0 & 1/\sigma_2 & \dots & \\ \vdots & \vdots & \vdots & \vdots & \vdots & \vdots & \vdots & \ddots \end{bmatrix} \tag{6.4}$$

Although unrelated to the statistical assumptions of least squares regression, computational instability may arise when there are large differences between the typical values of each column of the Jacobian (Brandal, 1991). We can reduce the risk of computational instability by scaling columns so that their typical values are of similar magnitude. This is tantamount to multiplying the Jacobian by a diagnal matrix with dimensions equal to the number of columns of the Jacobian, and diagonal entries equal to the reciprocal of the mean value of each column:

$$\mathbf{Y} = \begin{bmatrix} 1/\overline{x}_1 & 0 & 0 & 0 & 0 & \dots & \\ 0 & 1/\overline{x}_1 & 0 & 0 & 0 & \dots & \\ \dots & 0 & 1/\overline{x}_2 & 0 & 0 & \dots & \\ \dots & 0 & 0 & 1/\overline{x}_2 & 0 & \dots & \\ \vdots & \vdots & \vdots & \vdots & \vdots & \vdots & \ddots \end{bmatrix} \tag{6.5}$$

Applying weighting factors, (6.3) can be rewritten as:

$$(\mathbf{WJY})\mathbf{Y^{-1}}\Delta\mathbf{m_k} = \mathbf{Wr_k} \tag{6.6}$$

and the least squares solution is:

$$\begin{aligned} \Delta\hat{\mathbf{m}}_\mathbf{k} &= \mathbf{H}\Delta\mathbf{r_k} \qquad (6.7) \\ \mathbf{H} &= \mathbf{Y}[(\mathbf{WJY})^\mathbf{T}(\mathbf{WJY})]^{-\mathbf{1}}(\mathbf{WJY})^\mathbf{T}\mathbf{W} \end{aligned}$$

The algorithm is applied iteratively, adding $\Delta\hat{\mathbf{m}}_\mathbf{k}$ from the previous iteration to calculate a new estimate of $\mathbf{m}$.

6.1.1 Estimating Error

Error estimates can be found using:

$$\mathbf{C_m} = \mathbf{HC_dH^T} \tag{6.8}$$

where $\mathbf{C_m}$ is a covariance matrix for estimates of $\mathbf{m}$, and $\mathbf{C_d}$ is the data covariance matrix. Diagonal entries of $\mathbf{C_m}$ represent the variance of each parameter represented by $\hat{\mathbf{m}}$ (Michaels, 1998). Off-diagonal entries indicate the correlation, or interaction, between terms (Rice, 1995).

Similarly, the diagonal terms of the data covariance matrix represent the variance of each data point, and the off-diagonal terms indicate the degree to which these terms may not be independent. Diagonal terms correspond to the variance that can be computed by taking multiple measurements at a single point.

Aster *et al.* (2013) recommend that a model resolution test be conducted to evaluate model resolution. The resolution matrix obtained from such a test is an *nxn* matrix, where n is equal to the dimension of the model space. In this instance, the model space will equal the number of parameters used in the inversion. Aster *et al.* give the trace of the resolution matrix as a quantitative measure of resolution: The trace should be close to the model space.

6.1.2 Constraining Layer Thickness

We will see that inversion estimates of shear modulus and viscosity are sensitive to the layer thickness used in the model. Incorporating layer thicknesses from other sources, such as borehole information, can substantially improve viscoelastic parameter estimates.

Even when individual layer thicknesses are not known, borehole information may suggest a total thickness for the layer stack. Alternatively, a useful estimate of effective total layer thickness can also be obtained by inspection of dispersion curves. Recall that the spacing between cut-off frequencies is a function of top layer velocity, half-space velocity, and layer thickness (Equation 1.3). This can be used to find the equivalent single-layer thickness of a layered structure. In either case, we can constrain the model using a modified Jacobian matrix.

Recall that we defined equivalent layer thickness using Equation 4.3.

$$\overline{h} = \sum_{j=1}^{n} h_j \frac{\beta_1}{\beta_j}$$

where $\overline{h}$ is obtained using Equation 1.3. β_1 can be obtained from the asymptotic velocity of the dispersion relationships. Accurate estimates of β_1 and β_2 can be obtained from shot gathers.

When no information about layer structure is available, satisfactory partitions can be obtained by dividing the equivalent layer into two or more layers with a modulus that is similar to the modulus of the top layer. To avoid the possibility of a producing a hidden layer (velocity decreasing with depth), the assumed modulii of the initial model should increase monotonically.

As discussed later in this chapter, it is usually best to overestimate the number of layers. In tests on synthetic data, modeling a single, homogeneous layer using a two layer model provided reasonable results. Modeling a two-layer structure with a one-layer model tended to produce thickness and modulus estimates that were an amalgam of the two-layer properties; however, the viscosity estimate obtained from the one-layer model was neither representative of the *true* viscosity of either layer individually, nor was it a value intermediate between the layer viscosities.

For simplicity, we assume a multi-layer inversion model with only layer heights as parameters. For the current discussion, then, $\Delta \mathbf{h_k} = \Delta \hat{\mathbf{m}}_\mathbf{k}$, and Equation 6.2 becomes:

$$\mathbf{r_k} = \mathbf{J}(f, \mathbf{m})\boldsymbol{\Delta}\mathbf{h} \tag{6.9}$$

where $\boldsymbol{\Delta}\mathbf{h_k}$ is a vector of differential heights. For a model that is constrained by Equation 4.3, only n-1 heights can be varied independently. The change in the n^{th} layer height is a function of the changes of the other layers in the model. Rearranging (4.3), we obtain a relationship for the thickness of the n^{th} layer:

$$h_n = \overline{h}\frac{\beta_n}{\beta_1} - h_1\frac{\beta_n}{\beta_1} - h_2\frac{\beta_n}{\beta_2} - \ldots \tag{6.10}$$

The change in layer n thickness is:

$$\Delta h_n = -\Delta h_1\frac{\beta_n}{\beta_1} - \Delta h_2\frac{\beta_n}{\beta_2} - \ldots \tag{6.11}$$

If we denote the Jacobian elements of (6.9) with $J_{i,j}$, a single row multiplication could be represented as:

$$r_i = J_{i,1}\Delta h_1 + J_{i,2}\Delta h_2 + \ldots + J_{i,n}\Delta h_n \tag{6.12}$$

Substituting (6.11) into (6.12):

$$r_i = J_{i,1}\Delta h_1 + J_{i,2}\Delta h_2 + \ldots + J_{i,n}(-\Delta h_1 \frac{\beta_n}{\beta_1} - \Delta h_2 \frac{\beta_n}{\beta_2} - \ldots) \tag{6.13}$$

which can be rearranged into:

$$r_i = (J_{i,1} - \frac{\beta_n}{\beta_1} J_{i,n})\Delta h_1 + (J_{i,2} - \frac{\beta_n}{\beta_2} J_{i,n})\Delta h_1 + \ldots \tag{6.14}$$

We will refer to:

$$J'_{i,j} = (J_{i,j} - \frac{\beta_n}{\beta_j} J_{i,n}) \tag{6.15}$$

as a modified Jacobian element. The modified Jacobian matrix is formed by substituting a modified Jacobian element for each Jacobian element computed using a layer thickness parameter. Layer n thickness is then removed from the model. For example, suppose that are using a three-layer model with layer thickness and shear modulus as parameters. The model could be represented as:

$$\mathbf{r} = \begin{bmatrix} J_{1,h_1} & J_{1,h_2} & J_{1,h_3} & J_{1,\mu_1} & J_{1,\mu_2} & J_{1,\mu_3} \\ J_{2,h_1} & J_{2,h_2} & J_{2,h_3} & J_{2,\mu_1} & J_{2,\mu_2} & J_{2,\mu_3} \\ \vdots & \vdots & \vdots & \vdots & \vdots & \vdots \end{bmatrix} \begin{bmatrix} \Delta h_1 \\ \Delta h_2 \\ \Delta h_3 \\ \Delta \mu_1 \\ \Delta \mu_2 \\ \Delta \mu_3 \end{bmatrix} \tag{6.16}$$

Using a modified Jacobian matrix, the constrained model is rewritten:

$$\mathbf{r} = \begin{bmatrix} J'_{1,h_1} & J'_{1,h_2} & J_{1,\mu_1} & J_{1,\mu_2} & J_{1,\mu_3} \\ J'_{2,h_1} & J'_{2,h_2} & J_{2,\mu_1} & J_{2,\mu_2} & J_{2,\mu_3} \\ \vdots & \vdots & \vdots & \vdots & \vdots \end{bmatrix} \begin{bmatrix} \Delta h_1 \\ \Delta h_2 \\ \Delta \mu_1 \\ \Delta \mu_2 \\ \Delta \mu_3 \end{bmatrix} \tag{6.17}$$

The n^{th} layer thickness can then be found using Equation 6.10.

If the thickness constraint is an actual thickness, such as might be obtained from borehole data, then (6.15) simplifies to:

$$J'_{i,j} = (J_{i,j} - J_{i,n}) \tag{6.18}$$

6.2 Methods

We will evaluate the inversion procedure by applying it to the dispersion and attenuation curves obtained from the low density lay-out, as described in the previous chapter.

6.2.1 Inversion Procedure

The general inversion process begins with data matrices representing dispersion and attenuation curves, and an initial model, $\hat{\mathbf{m}}_\mathbf{0}$, of assumed layer properties such as thickness, shear modulus, and viscosity, a delta properties matrix, and a data covariance matrix.

- For each inversion iteration:

◇ Use the assumed model to produce theoretical seed matrices representing dispersion and attenuation curves as discussed in Chapter 4. Tools and procedures for producing seed matrices can be found in Appendix A.

◇ The delta properties matrix is used to calculate the Jacobian. For each property being estimated, the delta properties matrix includes a delta value that will be used to approximate the Jacobian in Equations 6.2 and 6.3. More information about the delta properties matrix can be found in Appendix C.

◇ Calculate the Jacobian using the seed model and the delta properties matrix. Tools and techniques for calculating the Jacobian can be found in Appendix C.

◇ For models with constrained layer properties (e.g., total layer thickness, or effective layer height), we will need to produce a modified Jacobian using the procedures discussed in Section 6.1.2

◇ The data covariance matrix will be used to compute a model covariance matrix. See the Section, *Parameter Error Estimates*, for a discussion of the method used to create the data covaraince matrix.

◇ Solve Equation 6.3 for $\Delta\mathbf{m_k}$ using the methods described in Section 6.1. Tools and techniques for solving Equation 6.3 and for obtaining a matrix of covariance estimates can be found in Appendix C.

◇ Add the vector, $\Delta\mathbf{m_k}$ to the assumed model to obtain a new assumed model ($\hat{\mathbf{m}}_\mathbf{k}$), and repeat until the model reaches the desired level of convergence.

6.2.2 Characterization Models

We will characterize the reduction/inversion process by evaluating its behavior with respect to the one, two, and three-layer viscoelastic models presented in Chapter 4. Characterization experiments will include the following:

- ◇ Data from all three models will be inverted using initial estimates of layer thickness, shear modulus, or viscosity that differ from their *true* values.

- ◇ Data from the single layer model will be also be inverted using a model in which initial estimates of viscosity are zero.

- ◇ In order to investigate the effects of including incorrect/biased assumptions, the single-layer model will be inverted by either holding incorrect values of layer thickness or shear modulus constant.

- ◇ Data from the single-layer model will be inverted to demonstrate the procedure's ability to invert data using dispersion and attenuation information from a single mode, two modes, and all modes.

- ◇ Data from the single layer model will be inverted to demonstrate the procedure's ability to obtain parameter estimates using either just dispersion information or just attenuation information.

- ◇ Using the single-layer model, joint inversion will be compared to a sequential inversion process. In a sequential inversion cycle, data is first inverted for thickness and shear modulus using dispersion data, and then inverted for viscosity using attenuation data.

◇ Data from the two-layer model will be inverted using fundamental mode data, data from the fundamental mode and first harmonic, and data from all modes.

◇ Data from the two-layer model will be inverted for viscosity using only dispersion information.

◇ Data from the two and three-layer models will also be inverted using a modified Jacobian that constrains either total layer thickness or effective layer thickness.

◇ Subsets of data obtained from the one-layer model will be inverted to demonstrate the method's ability to estimate parameters using either dispersion data alone, or using attenuation data alone.

◇ In order to investigate the effects of making incorrect assumptions about the number of layers used in the model, two-layer data will be inverted using an inversion model with only one layer, and one-layer data will be modeled using an inversion model with two layers.

6.3 Single Layer Property Estimates Using Only Fundamental Mode Data

Only the fundamental mode is present at the lowest frequencies, and it is possible that the only usable dispersion and attenuation information obtained from field data will be from the fundamental mode. We will apply our inversion procedure to the fundamental mode data obtained from the single-layer viscoelastic model (Figure 4.8).

Dispersion and attenuation data can be seen in Figures 5.8 and 5.11. The usable data for both of these curves occurs between 9 and 19 *Hz*. For this inversion, we varied layer thickness, shear modulus, and viscosity. The remaining properties were fixed at those of Figure 4.8.

Applying our joint inversion procedure to this data, we obtain the convergence history illustrated in Figure 6.1. All three estimates converged quickly to reasonable values. A two parameter inversion model, which held layer thickness at a constant 5 *m* while varying shear modulus and viscosity, converged to similar values.

6.3.1 Effects of Varying Half-Space Parameters

Varying the half-space shear modulus by ± 50 % of its base value (288 MPa) has no discernable effect. Even after row and column scaling, the values of the Jacobian column associated with half-space modulus remain at least four orders of magnitude smaller than the values in the other columns.

In Chapter 4, we noted that half-space material properties only exert a significant effect near the cut-off frequency: When the Love wave phase velocity was near that of the half-space. Inspection of Figures 5.8 and 5.11 reveals that the data used in the previous inversion were obtained for phase velocities far from half-space velocity, so the relative unimportance of half-space parameters is not surprising. This lack of sensitivity to half-space properties held for this and all other models tested, and in subsequent inversion tests, half-space parameters were fixed at their *true* values.

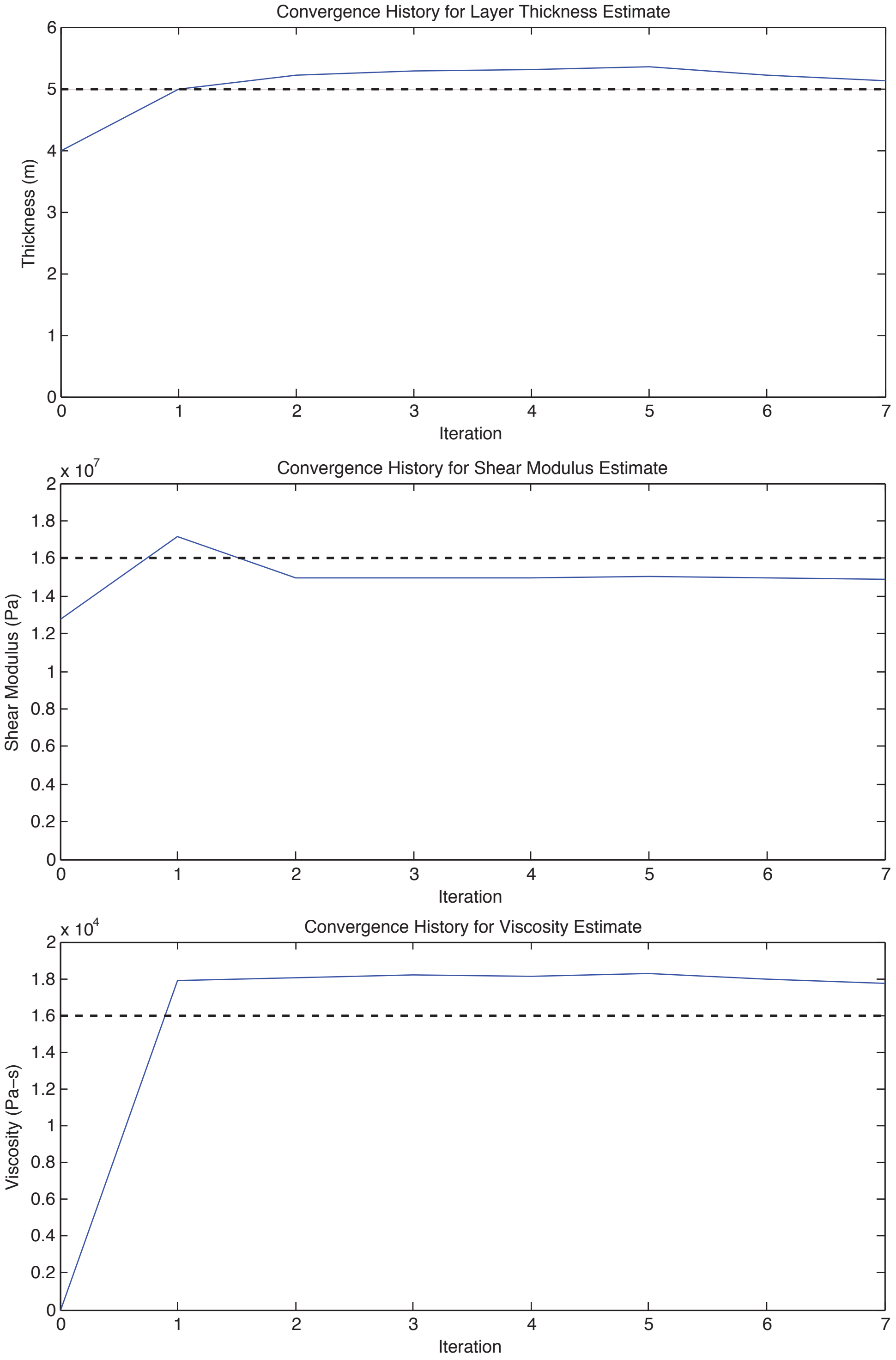

Figure 6.1: Convergence history for single mode data for a soil model consisting of a single viscoelastic layer over a half-space. Dashed lines indicate the value used to create synthetic data.

6.3.2 Effects of Model Bias

Model bias occurs when we assume an incorrect fixed parameter value in our model. For example, we might have obtained a 4 *meter* estimate of layer thickness using bore hole data, and used this, instead of the true 5 *meter* value, as a fixed model parameter. For the present inversion problem (one layer and one mode), this has very little effect. In fact, estimates of modulus and viscosity only changed about 5% when layer thickness was changed from a fixed value of 4 *meters* to a fixed value of 6 *meters*; however, we will see that including more modes and more layers in the model greatly increases the sensitivity of the shear modulus estimate to assumed layer thickness.

On the other hand, the effect of using an incorrect fixed value for shear modulus has a substantial effect on the viscosity estimate. Holding layer thickness at 5 *meters*, and fixing shear modulus at 12.8 MPa (20% low), results in a viscosity estimate that is about 13% low (13,960 *Pa-s*). Using a fixed value of 19.2 MPa (20% high) results in a viscosity estimate that is nearly 60% high (25,400 *Pa-s*).

6.3.3 Models Using Only Dispersion Data

As noted in Chapter 5, accurate attenuation data is difficult to obtain, and is not generally available over as wide a range of frequencies as dispersion data. Comparison of dispersion curves for the one layer elastic and viscoelastic models shows some subtle differences, and it might be hoped that these differences could be used to ascertain underlying values of viscosity. Applying a three-parameter model (thickness, modulus, and viscosity) to the fundamental mode provides an excellent estimate of layer thickness (4.998 m), and a reasonable estimate of shear modulus (14.81 MPa); however, the model failed to converge to a meaningful value of viscosity. Estimates obtained from subsequent iterations vary by as much as 50,000 *Pa-s*.

6.3.4 Models Using Only Attenuation Data

We also evaluated the quality of parameter estimates obtained using attenuation data, alone. A three-parameter model (thickness, modulus, and viscosity) was applied to fundamental mode attenuation data. The model was unable to obtain a meaningful layer thickness estimate.

By using a fixed, 5 m thickness, reasonable estimates of shear modulus (17.62 MPa) and viscosity (19,900 *Pa-s*) were obtained using a two parameter model (modulus and viscosity).

Usable phase velocity information can be gleaned from from the shot gather (Figure 5.3). The slopes of the upper and lower boundaries of the envelope containing the waveforms are equal to the half-space and layer shear wave velocities, respectively. Using these slopes, and assuming a material density for each layer, we can obtain an accurate estimate of the shear modulii for both the layer and half-space.

6.4 Single-Layer Property Estimates Using Several Modes

6.4.1 Joint Inversion of Dispersion and Attenuation Data

Joint inversion of dispersion and attenuation information obtained from a single-layer model failed to yield stable property estimates.

The main culprit preventing convergence was the labile behavior of overtones.

In Chapter 4, we saw that at low viscosities, overtones typically evolved along the real axis. At higher viscosities, these overtones could disappear, and be replaced by a companion mode originating from the imaginary axis. The point at which this transition occurs is dependent on layer geometry, shear modulus, and viscosity. In the case of the one layer model presented in Chapter 4, the first overtone is a primary mode (n=1), and the second and third overtones are companion modes (n=2i, n=3i). While attempting to invert the data, we found that combinations of layer thickness, shear modulus, and viscosity that best fit first overtone data were inconsistent with the existence of companion second and third overtones. Conversely, model parameters that were consistent with companion second and third overtones were inconsistent with a primary first overtone.

A model using a 4 *meter* layer thickness, 12.8 MPa shear modulus, and 12,800 *Pa-s* viscosity resulted in a fundamental and first three overtones that originated along the real axis. A model using a 6 meter layer thickness, 19.2 MPa shear modulus, and 12,800 *Pa-s* viscosity induced all overtones to originate along the imaginary axis. If the initial values used in the inversion process produced the wrong combination of modes, the inversion was doomed. When this happened, the model became unstable, oscillated between mode type, and failed to converge.

It is possible to force the model to use information from a particular overtone; however, this presupposes a knowledge of layer geometry and properties that normally would be unavailable to researchers working with field data.

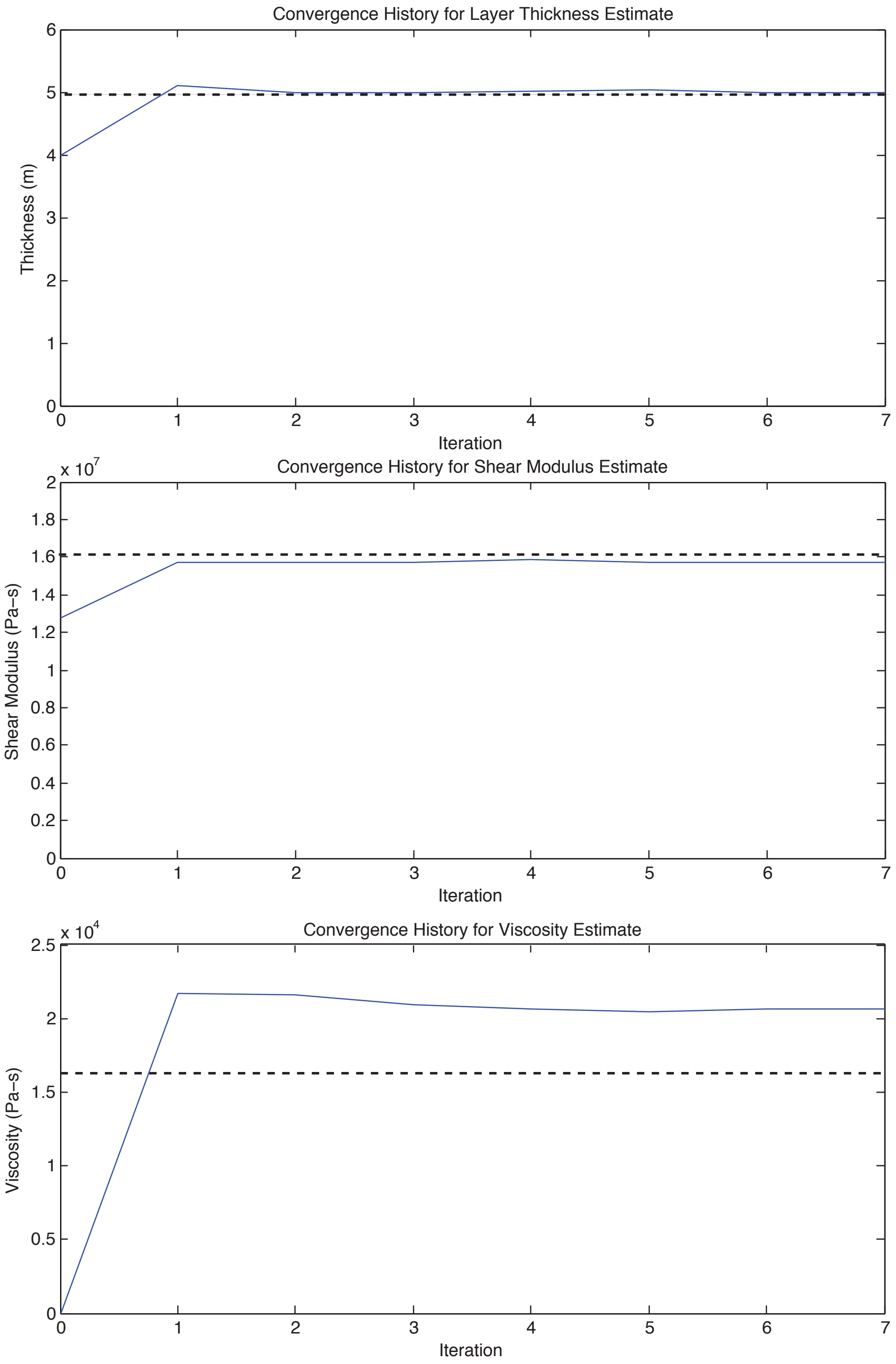

Convergence History for Layer Thickness Estimate

Convergence History for Shear Modulus Estimate

Convergence History for Viscosity Estimate

Figure 6.2: Convergence history for sequential inversion of data from all four modes for a soil model consisting of a single viscoelastic layer over a half-space. Dashed lines indicate the values used to create synthetic data.

6.4.2 Sequential Inversion of Dispersion and Attenuation Data

In sequential inversion, a model using only dispersion information is inverted to estimate layer thickness and shear modulus. This is followed by an inversion using only attenuation information to estimate viscosity. In order to eliminate the labile overtone problem described in the previous sub-section, it is necessary to initiate the model with a value of viscosity that guaranteed convergence to the proper (primary vs. companion) overtone.

Sequential inversion proved far more effective than joint inversion. In all single layer cases, this dispersion model converged quickly (Figure 6.2). For the single-layer model, sequential inversion gave reasonable results when information from only the fundamental mode and first overtone were used.

Applying sequential inversion to a three-parameter model using only first overtone dispersion and attenuation data, the model converged to a viscosity estimate of 17,701 *Pa-s*–About 11% higher than the *true* value.

6.4.3 Notes on Single-Layer Inversion

Inversion for thickness and shear modulus using dispersion information proved to be a reasonably robust procedure that converged quickly to values that are reasonably close to *true* values. When inverting multi-mode data for shear modulus, alone, it was found that the final estimate of shear modulus could be sensitive to assumed layer thickness. Although a one-parameter inversion for viscosity, alone, is insensitive to the assumed value of layer thickness, it is quite sensitive to the assumed value of shear modulus. Thus, in a three-parameter inversion (layer thickness, shear modulus, and viscosity), small errors in the final estimate of layer thickness can lead to large errors in viscosity. We noted that in a three-parameter model, these errors were accompanied by instability.

Accurate single-layer thickness and velocity information may be available from other sources. Top layer and half-space phase velocities can be obtained from measurements on the shot gather; these, in turn, can be used with assumed density values to find estimates of shear modulus.

Measuring the distances between the three cut-off points in Figure 5.13, we find an average cut-off interval of 11 *Hz*. The lowest fundamental mode velocities obtained from the data used to generate this figure averaged about 103 *m/s*. With an accurate estimate of half-space velocity, we can solve Equation 1.3 to obtain a 4.84 m layer thickness estimate. Absent a half-space velocity estimate, we can ignore the square root term in (1.3) and obtain a 4.69 m estimate, which can be used as an initial value for the inversion process.

6.5 Two-Layer Model

Reasonably good parameter estimates were obtained from the two-layer model. Unlike inversion using single mode data from a single-layer model, single-mode inversion estimates of shear modulus and viscosity from the two-layer model were quite sensitive to layer thickness. When total layer thickness constraints were included in the model, even inversion using fundamental mode data, alone, could yield useful viscoelastic layer property estimates.

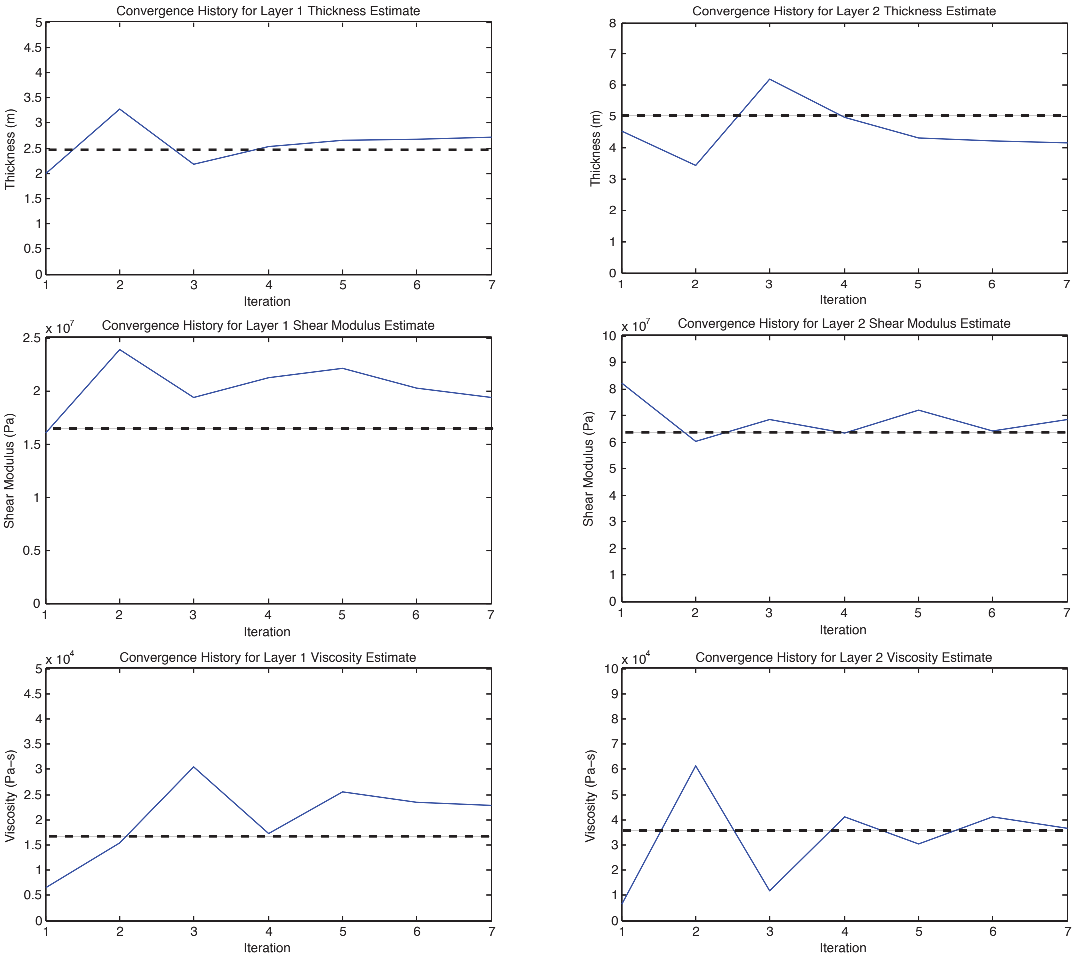

Figure 6.3: Convergence history for sequential inversion using data from all modes for a model consisting of two viscoelastic layers over a half space. Dashed lines indicate the values used to create synthetic data.

6.5.1 Two-Layer Model Using Only Dispersion Data

When using sequential inversion, it was necessary to add a viscosity term in order to produce the *shelf* observed in the mode 2 and 3 dispersion curves. Given this viscosity dependence of the dispersion curves, it was hoped that reasonable viscosity estimates might be evinced from the dispersion data. In fact, very satisfactory viscosity estimates were obtained by an inversion model incorporating layer thickness, shear modulus, and viscosity (Table 6.2).

6.5.2 Using a One-Layer Model with Two-Layer Data and Vice Versa

It is possible that the layer structure of field data could be misinterpreted. Absent the obvious shelves of the second and third overtones (Figure 5.13), it would be difficult to ascertain, a-priori, the number of layers to be used in a model. Inverting the two layer viscoelastic data using a one layer model yielded a thickness estimate of 4.24 m, a shear modulus estimate of 21.4 Pa, and a viscosity estimate of 7,780 Pa-s.

Model Parameter	True	Initial Value	Mode 0*	Modes 0,1*	All Modes
h_1 (m)	2.50	2.00	2.17	2.44	2.74
μ_1 (Pa)	16E6	12.8E6	14.3E6	14.5E6	19.4E6
η_1 $(Pa\text{-}s)$	16E3	6.57E3	15.7E3	16.8E3	22.9E3
h_2 (m)	5.00	4.50	5.27	5.70	4.15
μ_2 (Pa)	68.0E6	82.2E6	41.9E6	63.1E6	68.3E6
η_2 $(Pa\text{-}s)$	34E3	6.5E3	52.0E3	51.3E3	36.5E3

Table 6.1: Results from the sequential inversion of two layer data using one, two, or all modes. * indicates that total layer thickness was constrained to an effective height of $\overline{h} = 5m$. Convergence history for the all-mode model is also displayed in Figure 6.3.

Model Parameter	True	Initial Value	Dispersion Data
h_1 (m)	2.50	2.00	2.59
μ_1 (Pa)	16E6	16E6	14.7E6
η_1 $(Pa\text{-}s)$	16E3	6.57E3	12.6E3
h_2 (m)	5.00	4.50	5.61
μ_2 (Pa)	68.0E6	82.2E6	68.7E6
η_2 $(Pa\text{-}s)$	34E3	6.5E3	38.8E3

Table 6.2: Reasonable viscosity estimates could be obtained using dispersion data, alone with two-layer data.

Both the thickness and shear modulus estimates are between the *true* values for layers one and two; however, the viscosity estimate seems anomalously low. The standard deviation for this estimate was 41,200 *Pa-s*.

Applying a two-layer model to the one layer data of the previous section gives better results. Ideally, the estimates of shear modulus and viscosity for both layers would be 16E6 and 16E3, respectively. By constraining total layer thickness to the *true* value of 5 *m*, the resulting two-layer model yields good estimates of modulus, and reasonable viscosity estimates: Both the layer one and layer two shear modulus estimates are, respectively, 15.5E6 and 15.4E6 *Pa*. Viscosity estimates are 12.1E3 and 33.7E3 *Pa-s* for both layers.

6.5.3 Three-Layer Model

For the three-layer model, layer thickness, shear modulus, and viscosity estimates obtained using an unconstrained inversion model were very poor. In fact, the unconstrained inversion yielded negative values for shear modulus and viscosity, and the inversion model never actually converged (Table 6.3). Obtaining reasonable viscoelastic parameter estimates required that layer thickness be constrained. Including

Model Parameter	True	Initial Value	Unconstrained	$\overline{h} = 5$	Fixed h
h_1 (m)	2.73	2.5	2.03	2.55	2.73
μ_1 (Pa)	16E6	12.8E6	10.86E6	12.9E6	14.7E6
η_1 $(Pa\text{-}s)$	16E3	6.57E3	22.9E3	21.1E3	19.66E3
h_2 (m)	2.73	2.5	2.17	0.56	2.73
μ_2 (Pa)	68.0E6	54.4E6	-33E6	58.9E6	77.8E6
η_2 $(Pa\text{-}s)$	34E3	6.57E3	-39.5E3	41.1E3	37.9E3
h_3 (m)	2.73	3.75	7.0	4.095	2.73
μ_3 (Pa)	153.0E6	122.4E6	36.2E6	96.1E6	94.2E6
η_3 $(Pa\text{-}s)$	51.0E3	6.57E3	-44,473	44.0E3	50.0E3

Table 6.3: Parameter estimates obtained for the three-layer model. Constraining effective height to $\overline{h} = 5$ m improved model stability. Fixing layer thicknesses at their *true* values (2.73 m) yielded the best estimates of all.

either the constraint that effective total layer thickness equal 5 m, or that each layer thickness be fixed at its *true* value of 2.73 m greatly improved the model.

6.6 Parameter Error Estimates

Parameter covariance estimates were obtained for all models using Equation 6.8. Data error estimates could be obtained by running the experiment several times, making a separate dispersion or attenuation curve for each run, and then computing a separate variance for each point. Given the amount of time necessary to run the experiment a single time, this was not feasible. For the following analyses, we assumed that no correlation (hence, no covariance) exists between the elements of the data vector. Data error estimates were obtained using the root mean square of residuals from best-fit polynomials taken for segments of each dispersion or attenuation curve. Because similar analyses were performed using the same data sets, these estimates tended to be similar. Except where noted, these estimates apply to all models (Table 6.4).

Layer	h (m)	μ (Pa)	η $(Pa\text{-}s)$
1	0.05 (1.0%)	0.48E6 (3.0%)	260 (1.6%)
2	0.06 (1.2%)	0.92E6 (1.36%)	1,500 (4.4%)
3	0.7 (25.6%)	3.7E6 (2.4%)	6,000 (11.8%)

Table 6.4: Typical standard deviations of estimated model parameters obtained from the model covariance matrix.

Note that error estimates tend to increase with depth.

Model resolution tests (see Sub-section 6.1.1) were performed on Jacobians from inversion models using thickness, shear modulus, and viscosity for the one, two, and three layer soil models. For one, two, and three-layer soil models, the model spaces, are 3, 6, and 9, respectively. For the three Jacobians tested, the traces of the resolution matrices were, respectively, 3.0000, 6.0000, and 9.0000. These values compare favorably with the criterion (Aster *et al.*, 2013) that the trace of the resolution matrix should be close to the model space.

6.7 Summary

As a result of our synthetic data experiments, we make the following generalizations:

◇ Reasonable single layer estimates can be obtained using dispersion and attenuation from only the fundamental mode.

Varying half space by ± 50 % had no discernable effect on other parameter estimates.

For a single-layer model, assuming an incorrect *fixed* value of layer thickness has a modest effect on estimates of shear modulus and viscosity;

however, assuming an incorrect *fixed* value of shear modulus can effect a very large error in viscosity estimates.

Labile changes from primary to companion modes (and vice versa) could cause the inversion process to converge to the wrong mode, entirely. Avoiding this problem requires that the model be initialized using viscosities near the *true* values, and that a sequential inversion process be employed.

Attempts to estimate viscosity using dispersion data, alone, were only successful when inclusion of viscosity created an obvious *shelf* that was not present in the purely elastic model.

Attempts to estimate layer thickness and shear modulus using only attenuation information were unsuccessful.

It is better to assume a model with too many layers than it is to assume a model with too few layers.

For two and three-layer models, the inversion procedure is sensitive to initial assumptions about layer thickness. For the two-layer model, constraining total layer thickness or effective layer thickness improved estimates of shear modulus and viscosity. For the three-layer model, reasonable (non-negative) estimates of shear modulus and layer thickness could not be obtained without constraining either total layer thickness or effective layer thickness.

CHAPTER 7:

CONCLUSIONS AND RECOMMENDATIONS FOR FURTHER RESEARCH

We set out to determine whether or not Love wave inversion could be a viable means for determining viscoelastic soil properties. The answer is a qualified *yes.* We demonstrated a method for winnowing Love wave modes from the types of data typically collected in the field, and we developed a straightforward inversion process that can be used to identify and characterize soil layering. As we have seen, the inversion process is relatively stable, and almost always yields a solution. For single-layer models, the method gives reasonable estimates of layer thickness, shear modulus, and viscosity, even when dispersion and attenuation information is only available for a single mode. As the number of layers increases, accurate estimates of shear modulus and viscosity require that constraints on layer thickness be incorporated into the model. This suggests that surveys using Love waves should be used in conjunction with downhole or crosshole methods: With layer thicknesses from these latter methods as a control, Love wave seismic methods can be used to extend the area of investigation.

We saw that the process for determining dispersion information was relatively straightforward; however, obtaining amplitude information of sufficient quality to estimate attenuation coefficients requires that extra care be used in the design and conduct of field experiments. Given a sufficient level of care, we have shown how data from a source walk-away experiment can be used to extract attenuation information of sufficient quality to estimate viscous soil parameters.

Depending on local conditions and equipment availability, a receiver walk-away experiment may afford better reproducibility, and we have suggested a method for estimating dispersion curves and attenuation coefficient for receiver walk-away experiments.

Our analyses in Chapters 4 through 6 were conducted using layer thicknesses between 5 and 10 *m*, and useful data was obtained from modes between about 10 and 50 *Hz*. As discussed in Chapter 1, V_{s30} calculations specified by the *International Building Code* require that viscoelastic properties be measured to a depth of at least 30 *m*. Using the scaling rules derived in Chapter 4, the first four modes of a 30 *meter* layer structure would make their appearances at frequencies less than about 10 *Hz*. Higher modes might be detectable above this frequency range, but as we saw at the end of Chapter 4, the behavior of higher modes can very difficult to predict. Receivers with a two to three *Hertz* lower limit should be considered for V_{s30} surveys.

Mode ambiguity was an impediment to inverting the data. The potential for a mode to transition from a primary to a companion mode, or vice versa, was the usual culprit when the inversion process became bistable. Nevertheless, choosing initial values of layer thickness, shear modulus, and viscosity that ensured the proper mode type (primary vs. companion) prevented this issue.

The current inversion process is very labor intensive, and requires between sixteen and twenty hours per inversion. In particular, the process of identifying and tracking roots in order to create predictive dispersion curves is very time consuming, and it is only automated at frequencies far from each mode's cut-off frequency. Attempts to fully automate the procedure in the cut-off frequency region were unsuccessful.

When analyzing K-f plots, modes are fairly easy to identify visually; however, the task of separating and measuring their amplitudes is both labor intensive and prone to error. Many attempts were made to filter the data; however, most of these schemes required a-priori knowledge of the system's dispersive behavior.

7.1 Lessons Learned

We will recapitulate some of the more important lessons learned in the course of our investigation:

◇ Although single-layer viscoelastic property estimates can be obtained using only fundamental mode information, estimates for multi-layer systems require that higher order mode information be used.

◇ Love waves are relatively insensitive to half-space parameters, and it is probably not possible to obtain meaningful half-space viscosity estimates by means of Love wave inversion.

◇ Roots representing the complex velocities of Love wave modes evolve in pairs, with a primary mode originating from along the real axis, and a companion mode originating from along the imaginary axis. In all cases studied, only one root from each pair exhibited a loss tangent less than unity, and was expressed as a propagating wave.

◇ Most meaningful information is obtained at low frequencies and long wave numbers. The information obtained by the high density array was of no use in either the data reduction or inversion processes. By design, 10 Hz receivers and 1 m spacing was about right for the 5 to 10 m depths explored in the current work; however, deeper investigation will require a concomitant decrease in receiver frequency and increase in receiver spacing.

◇ Attenuation coefficients can only be derived from dispersion curves when the layer structure is conducive to large, viscoelastically induced, changes in dispersion curves. This will generally only be true for higher order modes. A more general approach to obtaining attenuation information requires accurate amplitude measurements, which, in turn, require a well-designed and carefully executed experiment.

◇ Inversion estimates of viscosity are sensitive to assumptions about layering. Accurate viscosity estimates require constraints on the inversion model that can either be obtained through inclusion of information from higher order modes, or from external information about total layer height and structure.

◇ Simultaneous inversion using both dispersion and attenuation information can be unstable. A better approach is to sequentially invert dispersion curves to obtain layer thickness and shear modulus, and to invert attenuation curves to obtain viscosity. Periodically, updating the model, and repeating the process until it converges. It may be necessary to include a viscosity term in the initial parameter estimate to assure that the model converges to the correct (primary/companion) mode.

7.2 Recommendations for Further Research

Before Love wave inversion can become a viable means for estimating viscoelastic soil properties, the following work will be necessary:

◇ Research should be done to better understand and predict the pairing of companion roots, with particular emphasis on understanding how to identify and incorporate this knowledge into the inversion model.

◇ Work should be done to fully automate the root-tracking procedure near the cut-off frequency. This would enable the entire inversion cycle to be automated.

◇ The process of identifying and tracking modes in K-f plots is labor intensive and prone to error. At low frequencies (near the cut-off frequency), modes are fairly easy to identify; however, identifying modes and measuring their amplitudes becomes much more difficult with increasing frequency. Work should be done to determine the best ways to filter and measure root amplitudes.

◇ Work should be done to understand layer structures not explored in this investigation. For example, we did not explore the effects of a layer structure in which velocity does not increase monotonically with depth (hidden layers).

◇ We adopted a viscoelastic constitutive model, in part, because of its wide use. As noted in Chapter 1, other constitutive models exist. In particular, it appears that a Coulombic model is a better fit to data from dry soils. Work should be done to extend the method to dry soils.

- ◇ Work should be done to characterize and minimize the variability of source walk-away and receiver walk-away experiments.
- ◇ Before using the attenuation data reduction method described for receiver walk-away experiments, it should be characterized using synthetic data.

7.3 Concluding Remarks

In summary, we must conclude that while Love wave inversion is feasible, several technical challenges must be overcome before it can become a viable research tool.

REFERENCES

Ablowitz, M. J., and Fokas, A.S. 2003. *Complex Variables: Introduction and Applications*. Second edn. Cambridge University Press.

Aichi, K. 1922. On the Transversal Seismic Waves Traveling Upon the Surface of a Heterogeneous Material. *Proceedings of the Physico-Mathematical Society of Japan*, **4**, 137–142.

Aki, K., and Richards, P. 2009. *Quantitative Seismology*. Second edn. University Science Books.

Amontons, G. 1699. Moyen de substituer commodément l'action du feu a la force des hommes et des chevaux pour mouvoir les machines. *Memoires de l'Academie royale des sciences, Paris.*

Arslan, H., and Sihayi, Bilge. 2006. A comparative study on linear and nonlinear site response analysis. *Journal of Environmental Geology*, **50**, 1193–1200.

Asmar, N. H. 2000. *Partial Differential Equations and Boundary Value Problems*. Upper Saddle River, N.J., USA: Prentice Hall.

Aster, R.C., Borchers, B., and Thurber, C. 2013. *Parameter Estimation and Inverse Problems*. Second edn. 225 Wyman Street, Waltham Ma. 02451, USA: Elsevier Academic Press.

ASTM-D-4015. 1996. Standard Test Methods for Modulus and Damping of Soils by the Resonant Column Method. *Annual Book of ASTM Standards*, **4.08 Soil and Rock**.

ASTM-D-4428. 1996. Standard Test Methods for Crosshole Seismic Testing. *Annual Book of ASTM Standards*, **4.08 Soil and Rock**.

Bateman, H. 1928. Trasverse Seismic Waves on the Surface of a Semi-Infinite Solid Composed of a Heterogeneous Material. *Bulletin of the American Mathematical Society*, **34**, 343–348.

Biot, M.A. 1956a. Theory of Propagation of Elastic Waves in a Fluid-Saturated Porous Solid. I. Low Frequency Range. *Journal of the Acoustical Society of America*, **28**(2), 179–191.

Biot, M.A. 1956b. Theory of Propagation of Elastic Waves in a Fluid-Saturated Porous Solid. II. Higher Frequency Range. *Journal of the Acoustical Society of America*, **28**(2), 168–178.

Brandal, W. 1991. *Numerical Linear Algebra.* Moscow, Idaho, USA: BCS Associates.

Burger, H., Sheehan, A.F., and Jones, C.H. 2006. *Introduction to Applied Geophysics.* First edn. New York, N.Y., USA.: Norton.

Burr, A.H. 1995. *Mechanical Analysis and Design.* Second edn. Upper Saddle River, N.J., USA.: Prentice Hall.

Chakravarthy, G. 2008. *Love Wave Propagation in Viscoelastic Media.* Ph.D. thesis, Boise State University.

Cohen, L. 1908. Note on the approximate values of Bessel's functions for large arguments. *NBS Bulletins*, **5**(2), 227–230.

Coulomb, C.A. 1773. Sur une aplication des régles de maximis e minimis a quelques problm̀es de statique, relatifs a l'architecture. *Memoires de l'Academie royale des sciences, Paris.*

Coulomb, C.A. 1781. Theorie des Machines Simples. *Memoires de l'Academie royale des sciences, Paris.*

Das, B. 2011. *Principles of Foundation Engineering.* Seventh edn. Stamford, Ct. 06902, USA: Cenage Learning.

des Camus, F.J. 1722. *Traité des forces mouvantes pour la pratique des arts et mètiers.* First edn.

Desaguliers, J.T. 1719. *A Course in Experimental Philosophy.* First edn.

Desai, C. S., and Christian, J.T. 1977. *Numerical Methods in Geotechnical Engineering.* First edn. New York, N.Y., USA: McGraw Hill Book Company, Advanced Book Program.

Descartes, R. 1644. *Principia Philosophiae: English Tr. by John Veitch.* First edn. Salt Lake City, Utah, USA: Project Gutenberg.

Dobrin, M.G. 1951. Dispersion in Seismic Surface Waves. *Geophysics*, **16**, 63–80.

Dunkin, J.W. 1965. Computation of modal solutions in layered, elastic media at high frequencies. *Bull. Seism Soc. Am.*, **55**, 335–358.

Ewing, W.M., Jardetzky, W.S., and Press, F. 1957. *Elastic Waves in Layered Media.* New York, N.Y., USA: McGraw Hill.

Fetter, C.W. 2001. *Applied Hydrogeology.* Fourth edn. Upper Saddle River, N.J., USA: Prentice Hall.

Fowler, C.M.R. 2005. *The Solid Earth: An Introduction to Gobal Geophysics.* Second edn. The Edinburgh Building, Cambridge, U.K.: Cambridge University Press.

Gabriels, P., Snider, R., and Nolet, G. 1987. In situ measurements of shear wave velocity in sediments with higher mode Rayleigh waves. *Geophysical Prospecting*, **35**, 187–196.

Gilbert, F., and Backus, G.E. 1966. Propagator Matrices in Elastic Wave and Vibration Problems. *Geophysics*, **XXXI(2)**(April), 326–332.

Hall, J.R., and Richart, F.E. 1963. Dissipation of Elastic Wave Energy in Granular Soils. *J. Soil Mech and Found. Div.*, **89**(November), 33–57.

Han, D., Liu, J., and Batzle, M. 2005. Measurement of shear wave velocity in heavy oil. *Pages 1513–1516 of: SEG/Houston 2005 Annual Meeting.* Society of Explorational Geophysics, Houston.

Hardin, B.O. 1965. The nature of damping in sands. *J. Soil Mech. and Found. Div.*, **91(1)**, 63–97.

Hardin, B.O., and Richart, F.E. 1963. Elastic wave velocities in granular soils. *J. Soil Mech. and Found. Div.*, **89(1)**, 33 – 65.

Haskell, N.A. 1953. The Dispersion of Surface Waves on Multilayered Media. *Bull. Seism Soc. Am.*, **43**(Jan.), 17 – 34.

Heaton, T.J. 2005. *Engineering Seismology Notes.* California Institute of Technology.

Heisey, J.S. 1981. *Determination of in situ shear wave velocities from spectral analysis of surface waves.* M.Phil. thesis, University of Texas at Austin.

Heisey, J.S., II, K.H. Stokoe, Hudson, W. R., and Meyer, A.H. 1982. Determination of in situ shear wave velocities from spectral analysis of surface waves. *Texas Department of Highways and Public Transportation, Research Study 3-8-80-256.*

Ho-Liu, P.H. 1988. *Attenuation tomography. Modelling regional Love waves: Imperial Valley to Pasadena.* Ph.D. thesis, California Institute of Technology.

ICBO, International Council of Building Officials. 1997. *Uniform Building Code.* Washington D.C., USA: ICBO.

ICC, International Code Council. 2000. *International Building Code.* Washington D.C., USA: ICC.

Idriss, I.M., and Seed, H.B. 1968. Seismic Response of Horizontal Soil Layers. *J. Soil Mech. and Found. Div.*, **94**, 1003–1028.

Iida, K. 1935. Changes in Rigidity and Internal Friction of Amorphous Silica with Temperature. *Bulletin of the Earthquake Research Institute*, **13**, 665–680.

Iida, K. 1940. On the Elastic Properties of Soil, particularly in relation to its Water Content. *Bulletin of the Earthquake Research Institute*, **118**, 60–78.

Ishihara, K. 1996. *Soil Behavior in Earthquake Geotechnics.* Third edn. New York, N.Y., USA: Oxford University Press, Inc.

Ishimoto, M., and Iida, K. 1936. Determination of Elastic Constants of Soils by means of Vibration Methods: Part I. Young's Modulus. *Bulletin of the Earthquake Research Institute*, **14**, 632–657.

Ishimoto, M., and Iida, K. 1937. Determination of Elastic Constants of Soils by means of Vibration Methods: Part II. Modulus of Rigidity and Poisson's Ratio. *Bulletin of the Earthquake Research Institute*, **15**, 67–88.

Iwan, W.D. 1961. *The Dynamic Response of Bilinear Hysteretic Systems.* Ph.D. thesis, California Institute of Technology.

Jemberie, A.L. 2002. *Shear-Wave Attenuation and Velocity Studies in Southeastern Asia.* Ph.D. thesis, Saint Louis University.

Jones, R. 1962. Surface wave technique for measuring the elastic properties and thickness of roads: Theoretical Development. *British Journal of Applied Physics*, **13**(1), 21–29.

Knopoff, L. 1964. A matrix method for elastic wave problems. *Bull. Seism Soc. Am.*, **54**, 431–438.

Kramer, S .L. 1996. *Geotechnical Earthquake Engineering.* Upper Saddle River, N.J., USA: Prentice-Hall.

Lai, W .M., Rubin, D., and Krempl, E. 1993. *Introduction to Continuum Mechanics.* Third edn. Butterworth Heinemann.

Lamb, H. 1882. Vibrations of an Elastic Sphere. *Pages 189–212 of: Proceedings of the London Mathematical Society*. London Mathematical Society, Oxford University Press.

Love, A.E.H. 1911. *Some Problems of Geodynamics: Being an Essay to which the Adams Prize in the University of Cambridge was Adjudged in 1911.* London, England: Cambridge University Press.

Maxwell, J.C. 1866. On wave propagation in two dimensions. *Pages 167–171 of: Proceedings of the Royal Society of London*, vol. 15. Royal Society of London, Oxford University Press.

McNiven, H.D., and Brown, C.B. 1963. Elastic Wave Velocities in Granular Soils. *J. Soil Mech and Found. Div.*, **89**(September), 103–118.

Meissner, E. 1921. Elastische Oberflchenwellen mit Dispersion in einem inhomogenen Medium. *Vierteljahrsschrift der Naturforschenden Gesellschaft*, **66**, 158.

Michaels, P. 1998. In Situ Determination of Soil Stiffness and Damping. *Journal of Geotechnical and Geoenvironmental Engineering*, **124(8)**, 709–719.

Michaels, P. 2006a. Comparison of Damping in Unsaturated Soils, Compression and Shear. *Pages 565–576 of: Unsaturated Soils 2006, Proceedings of the Fourth International Conference on Unsaturated Soils (GSP 147)*, vol. 1. ASCE, Reston, VA.

Michaels, P. 2006b. Relating Damping to Soil Permeability. *International Journal of Geomechanics*, **6(3)**, 158–165.

Morrison, M.W. 2002. *A Reliability Model for Creep Induced Fatigue in Load Bearing Tin/Lead Solder Joints.* M.Phil. thesis, University of Idaho.

Musschenbroek, P. Van. 1762. *Introductio ad Philosophiam Naturalem.* First edn. Leiden: J. Lulofs.

Newton, I. 1687. *Newton's Principia: English Tr. by Andrew Motte.* First edn. 45 Liberty Street, New York, N.Y., USA: Daniel Adee,.

Oldham, R. D. 1900. On the propagation of earthquake motion to great distances. *Philosophical Transactions of the Royal Society*, **194**.

Olson, K.B., Nigbor, R., and Konno, T. 2000. 3D Viscoelastic wave propagation in the Upper Borrego Valley, California, Constrained by Borehole and Surface Data. *Bulletin of the Seismological Society of America*, **90**, 134–150.

Pei, D. 2007. *Modeling and Inversion of Dispersion Curves of Surface Waves in Shallow Site Investigations.* Ph.D. thesis, University of Nevada, Reno.

Poisson, S. D. 1830. *Mémoire sur la propagation du movement dans les milieux élastiques.* Paris, France: l'Acadmie des sciences.

Rao, H.A.B. 1964. Dissipation of Elastic Wave Energy in Granular Soils. *J. Soil Mech. and Found. Div.*, **90**(July), 195–197.

Rayleigh, Lord. 1887. On waves propagated along the plane surface of an elastic solid. *Page 441 of: Scientific Papers*, vol. II.

Rice, J.A. 1995. *Mathematical Statistics and Data Analysis.* Second edn. Belmont, Ca., USA.: Duxbury Pres (Wadsworth).

Richart, F.E., Hall, J.R., and Woods, R.D. 1970. *Vibration of Soils and Foundations.* Englewood Cliffs, New Jersey, USA: Prentice Hall.

Robertson, P.K., Campanella, R.G., Gillespie, D., and Rice, A. 1985. Seismic CPT to Measure In-Situ Shear Wave Velocity. *Measurement and Use of Shear Wave Velocity for Evaluating Dynamic Soil Properties, R.D. Woods ed.*, 34–48.

Rosenbaum, J.H. 1964. A note on the computation of Rayleigh wave dispersion curves for layered elastic media. *Bull. Seism Soc. Am.*, **54**, 1013–1019,1578.

Sadun, L. 2001. *Applied Linear Algebra: The Decoupling Principle.* Upper Saddle River, New Jersey, USA: Prentice Hall.

Snieder, R. 2004. *Mathematical Methods for the Physical Sciences.* First edn. Cambridge, U.K.: Cambridge University Press.

Stein, S., and Wysession, M. 2003. *An Introduction to Seismology, Earthquakes, and Earth Structure.* Malden, Ma., USA: Blackwell Publishing.

Stephens, R.I., Fatemi, A., Stephens, R.R., and Fuchs, H.O. 2000. *Metal Fatigue in Engineering.* Second edn. New York, N.Y., USA: Wiley Interscience.

Stokes, G. G. 1849. On the dynamical theory of diffraction. *Trans. Phil. Soc.*

Stoll, R.D. 1985. Computer-Aided Studies of Complex Soil Modulii. *Measurement and Use of Shear Wave Velocity for Evaluating Dynamic Soil Properties, R.D. Woods ed.*, 18–33.

Stoneley, R. 1948. The Continental Layers of Europe. *Bulletin of the Seismological Society of America*, **38**, 263–274.

Takahashi, T. 1955a. Analysis of the Dispersion Curves of Love Waves. *Bulletin of the Earthquake Research Institute*, **33**(3), 287–296.

Takahashi, T. 1955b. The Dispersion of Rayleigh Waves in Heterogeneous Media. *Bulletin of the Earthquake Research Institute*, **35**(2), 297–308.

Thomson, W. 1865. On the elasticity and viscosity of metals. *Pages 289–297 of: Proceedinigs of the Royal Society of London*, vol. 14. Royal Society of London, London.

Thomson, W.T. 1950. Transmission of Elastic Waves through a Stratified Solid Medium. *Journal of Applied Physics*, **21**(Feb.), 89–93.

Voigt, W. 1889. Ueber de beziehung zwichen den beiden elasticitätsconstanten isotroper körper. *Annalen der Physik*, **274(12)**, 573–587.

Volterra, V. 1887. Sui fondamenti della teoria delle equzaioni differenziali lineari. *Mem. Soc. Ital. Sci.*, **6**, 1–104.

Wang, Y.H., Cascante, G., and Santamarina, J.C. 2003. Resonant Column Testing: The Inherent Counter EMF Effect. *Geotechnical Testing Journal*, **26**(3), 1–11.

Weissmann, G.F. 1965. The nature of damping in sands: Discussion. *J. Soil Mech. and Found. Div.*, **92**(July), 232–236.

Wylie, C.R., and Barrett, L.C. 1982. *Advanced Engineerng Mathematics*. Fifth edn. New York, U.S.A.: McGraw Hill.

Xia, J., Miller, R.D., and Park, C.B. 1999. Estimation of near-surface shear-wave velocity by inversion of Rayleigh waves. *Geophysics*, **64**, 691–700.

APPENDIX A:
FORWARD MODELING UTILITIES:
DOCUMENTATION

The forward modeling utilities are a group of related MATLAB® scripts and functions. In this appendix, we will outline the procedures used to create a complex velocity plot (Figure 4.9), dispersion plot (Figure 4.10), attenuation plot (Figure 4.11), and loss tangent plot (Figure 4.12). We will also discuss the procedure for creating synthetic data (Figure 5.3). Along the way, we will learn to use a few additional utilities. The code for each utility described in this appendix can be found in Appendix B.

A.1 Getting Started

First, be sure that all required functions are loaded into the same directory. All utilities, except *PropagateZ.m* and *RootReports.m*, require the function *Propagate.m*. *RootFinder.m*, *RootTracker.m*, *RootHunter.m*, and *FineRoot.m* also require the function, *Cauchy.m*. *RootTracker.m* and *RootHunter.m* require *FineRoot.m*

All utilities require an n x 4 layer properties matrix. Row 1 contains properties for the top layer, row 2 contains properties for the second layer, and so-on. The last row contains properties for the half space. The first column contains the layer thickness in *meters*, the second contains the layer density in kg/m^3, the third contains the shear modulus in *Pascals*, and the fourth row contains viscosity in *Pa-s*. The half-space thickness isn't used, so the user can set it to any value. The layer properties matrix for the single viscoelastic layer over a half-space illustrated in Figure 4.8 is:

$$layer\_props = \begin{bmatrix} 5 & 1600 & 16E6 & 16000 \\ 0 & 1800 & 288E6 & 0 \end{bmatrix}$$

- The basic steps for creating dispersion curves and attenuation plots are:
  - ◇ Use *LoveObjects.m* to become familiar with root behavior. Pay particular attention to the frequencies at which new modes evolve, and the frequencies at which they begin to approach layer velocity (Figure 4.9).
  - ◇ Use *RootFinder.m* to determine the approximate complex velocities of each root. These will be used as starting points for *RootTracker.m* and *RootHunter.m*.
  - ◇ Use *RootTracker.m* or *RootHunter.m* to obtain complex velocities over the desired interval. Both of these utilities use the same inputs, and give the same outputs; however, *RootTracker.m* is optimized for roots that originate along the real axis. For roots originating along the imaginary axis, *RootHunter.m* is a better choice.
  - ◇ Use *RootReports* to obtain summary layer and Love wave data. This includes frequency, phase velocity, and attenuation values that can be plotted to create dispersion curves and attenuation plots (Figures 4.10 and 4.11).
- The basic steps for creating displacement and stress vectors by depth (Figure 4.2) are:

◇ Use *FineRoot.m* to obtain a precise (at least 2 decimal places) estimate of a root's location for a desired mode and frequency.

◇ Use *PropagateZ.m* to generate a matrix of displacement/stress vectors over the desired range of depths.

A.2 LoveObjects

For a given frequency, *LoveObjects.m* creates a complex velocity plot such as those displayed in Figure 4.9, and returns a matrix of objective function values used to create that plot. *LoveObjects.m* requires a matrix defining the real and imaginary boundaries for the root search. The first row contains values for the real axis, and the second contains values for the imaginary access. Columns contain the lower limit, upper limit, and number of velocity increments for each axis. The matrix used to create the panels in Figure 4.9 is:

$$search\_limits = \begin{bmatrix} 100 & 450 & 350 \\ 0 & 100 & 100 \end{bmatrix}$$

This matrix instructs *LoveObjects.m* to calculate the objective function at one meter per second increments in both the real and imaginary directions. A larger number of increments can be used, but it is probably more efficient to use *LoveRoots.m* to determine approximate locations for each root, and then use *FineRoot.m* to determine the root's exact location.

Absolute values of the objective function can span several decades, so the color values displayed on the complex velocity plot represent the logarithm of the absolute value of the objective function. The squelch feature sets upper and lower limits to the values displayed on the color axis. If both the high and low squelch values are equal to each other, no squelch will be used. The function call used to create the 35 Hz panel of Figure 4.9 is:

```
obj_fun=LoveObjects(35,layer_props,search_limits,-12.5, -6);
```

A.3 RootFinder

RootFinder.m locates roots in a user defined search search window and returns the locations of roots to a 3xm matrix. The user defines the number and width of boxes in the real and imaginary directions. *RootFinder.m* searches each box, and only returns a result if it detects one or more roots in that box. If there is only one root in the box, *RootFinder.m* returns its real velocity, imaginary velocity, and a *quality number* that should be approximately unity. If the box contains more than one root, *RootFinder.m* returns ambiguous real and complex values, and a quality number that should be approximately equal to the number of roots in the box. If a box contains more than one root, the user can either decrease the dimensions of the boxes used in the search, or use *FineRoot.m* to discriminate between roots.

The command:

```
roots=RootFinder(35,layer_props,100,0,20,10,15,8);
```

looks for roots at 35 Hz using the layer_props matrix. The lower-left hand corner of the search window is at 100 m/s (real), and 0 m/s imaginary. Each box has dimensions of 20 m/s (real) by 10 m/s (imaginary) There are 15 boxes in the real search direction and 8 boxes in the imaginary direction. This command returns:

$$roots = \begin{bmatrix} 110.5000 & 138.5000 \\ 11.5000 & 30.5000 \\ 2.0591 & 0.9928 \end{bmatrix}$$

The first column of *roots* contains the real and imaginary velocities, 110.5000 and 11.5000, respectively; however, the quality number 2.0591 in the third row indicates that there were two roots in this search box. The 0.9928 quality number in row 3, column 2 indicates that there is a unique root at 138.5000 (real) and 30.5000 (imaginary). Rerunning *RootFinder.m* using a finer search box allows us to separate the double root:

```
roots=RootFinder(35,layer_props,100,0,5,5,5,5);
```

$$roots = \begin{bmatrix} 101.5000 & 110.5000 \\ 11.5000 & 14.5000 \\ 1.0777 & 1.0798 \end{bmatrix}$$

RootFinder.m uses the argument principle (Chapter 5) for finding roots, and the quality number in row 3 is computed numerically using the path integral described by Equation 3.56. The quality number can be used to assess the quality of the real and complex values obtained by *RootFinder.m*: A quality number between about 0.85 and 1.15 suggest a high quality solution, while values outside this range should probably be verified using slightly different search parameters, or by using *FineRoot.m*.

The default interval ($\Delta z = \Delta x + i\Delta y$) used in the path integration is 1 m/s in each direction. These values can be adjusted by changing xi and yi inside the MATLAB® script; however, this can cause *RootFinder.m* to run very slowly. A better practice is to use *FineRoot.m* when a high degree of precision is required.

A.4 RootTracker

RootTracker.m tracks the complex velocity of a single root with respect to changing frequency. As we noted in Section 4.2, the frequency dependent behavior of an individual root can be very non-linear, especially in the region near cut-off frequency. *RootTracker.m* is optimized for following roots that originate along the real axis. For roots originating along the imaginary axis, use *RootHunter.m*. A root's viscosity dependent behavior is reasonably linear, so *RootTracker.m* works by first finding the system's purely elastic real root, and then tracking its complex velocity while slowly varying its viscoelastic parameters. After each viscosity increment, the root's location is recalculated using *FineRoots.m*.

Given an initial frequency, elastic root position, layer properties, and search parameters, *RootTracker.m* will find both the elastic and complex velocities of the root at subsequent frequencies. For example, given the input matrix:

$$love\_roots = \begin{bmatrix} 0 \\ 0 \\ 0 \\ 30 \\ 176.4 \end{bmatrix}$$

The command:

```
love_roots=RootTracker(love_roots, 35,1,layer_props,3,5,10);
```

will track a root from 30 Hz to 35 Hz at 1 Hz intervals. The 176.4 m/s value in row 5 is an initial velocity calculated using the purely elastic model. The search window for each root is ± 3 from the root's previous real velocity component and ± 5 from the root's previous imaginary velocity component. The root will be tracked at each of 10 viscosity increments. This command returns the following matrix:

$$love\_roots = \begin{bmatrix} 0 & 158.7500 & 152.2500 & 147.0500 & 142.5500 & 138.8500 \\ 0 & 41.2500 & 37.2500 & 34.2500 & 31.9500 & 30.1500 \\ 0 & 1.0692 & 1.0689 & 1.0691 & 1.0692 & 1.0693 \\ 30 & 31 & 32 & 33 & 34 & 35 \\ 176.400 & 166.0500 & 157.9500 & 151.4500 & 146.2500 & 141.8500 \end{bmatrix}$$

where row 1 contains real velocity components, row 2 contains imaginary velocity component, row 3 contains quality numbers, row 4 contains frequency, and row 5 holds the corresponding elastic velocity. If *RootTracker.m* is unable to find a root, it will insert zeros in rows 1 and 2, and skip to the next frequency increment. Elastic root behavior is easy to follow, so even if *RootTracker.m* is unable to find the complex velocity, it usually is able to find the corresponding real velocity. The user can fill-in missing complex roots by refining search parameters and using rows 4 and 5 of the previously known good root as starting points.

A.5 RootHunter

RootHunter.m tracks the complex velocity of a single root with respect to changing frequency. *RootHunter.m* must be initiallized with three initial complex velocities.

Using those initial root locations, *RootHunter.m* predicts a root's next position using a second derivative model. *RootHunter.m* works best for roots that originate along the imaginary axis. For roots that originate along the real axis, *RootTracker.m* may be a better choice.

Given a matrix of initial frequencies, viscoelastic (complex) root positions, layer properties, and search parameters, *RootHunter.m* will find the complex velocities of the root at subsequent frequencies. For example, given the input matrix:

$$love\_roots = \begin{bmatrix} 197.3050 & 221.3500 & 204.8000 \\ 213.7550 & 132.2500 & 89.6500 \\ 1.0589 & 1.0587 & 1.0590 \\ 25 & 26 & 27 \\ 0 & 0 & 0 \end{bmatrix}$$

The command:

```
love_roots=RootHunter(love_roots, 30,1,layer_props,15,15,0.1,0.1);
```

will track a root from 27 Hz to 30 Hz at 1 Hz intervals, given the three initial root locations in *love_roots*. The search window for each root is ± 25 from the root's previous real velocity component and ± 5 from the root's previous imaginary velocity component. The large real search window is required because of the non-linear behavior of the real velocity component in the initial three values of *love_roots*. The location of each root will be determined using 0.1 m/s increments. This command returns the following matrix:

$$
love\_roots = \begin{bmatrix} 197.3050 & 221.3500 & 204.8000 & 189.1025 & 176.5813 & 166.6981 \\ 213.7550 & 132.2500 & 89.6500 & 67.9525 & 55.0563 & 47.0106 \\ 1.0589 & 1.0587 & 1.0590 & 1.0585 & 1.0148 & 1.0146 \\ 25 & 26 & 27 & 28 & 29 & 30 \\ 0 & 0 & 0 & 0 & 0 & 0 \end{bmatrix}
$$

where row 1 contains real velocity components, row 2 contains imaginary velocity component, row 3 contains quality numbers, row 4 contains frequency. *RootHunter.m* neither requires nor provides any values to row 5. If *RootHunter.m* loses track of a root, it will quit searching. The user can fill-in missing complex roots by refining search parameters and using rows 1 and 2 of the previously known good root as starting points. In this example, we note that by 30 Hz, velocity behavior has become reasonably well behaved, so it is possible to reduce the search window, thereby decreasing processing time.

A.6 RootReports

RootReports.m uses the output from either *RootTracker.m* or *RootHunter.m* to generate a report of Love wave and layer phase velocities, attenuation coefficients, attenuation ratios, and other information. Amongst other uses, this information can be used to create plots of dispersion and attenuation like 4.10, and 4.11. Using the output obtained from the previous discussion (Appendix A.5), the command:

```
love_report=RootTracker(layer_props,love_roots);
```

produces the following report:

$$love\_report = \begin{bmatrix} 30 & 31 & \dots \\ 0 & 1.0692 & \dots \\ 0 & 158.7500 + 41.2500i & \dots \\ Inf & 0.1829 - 0.0475i & \dots \\ NaN & 169.4685 & \dots \\ 0 & 0.04753 & \dots \\ 0 & 0.2598 & \dots \\ 100.4393 + 9.3836i & 100.4687 + 9.6935i & \dots \\ 1.8605 - 0.1738i & 1.9208 - 0.1853i & \dots \\ 101.3160 & 101.4040 & \dots \\ -0.0934 & -0.09648 & \dots \\ 400 & 400 & \dots \\ 0.4712 & 0.4869 & \dots \\ 400 & 400 & \dots \\ 0 & 0 & \dots \\ & & \end{bmatrix}$$

where row 1 contains the frequency, row 2 the quality number, row 3 the Love wave complex velocity, row 4 the Love wave complex wave number, row 5 the Love wave phase velocity, row 6 the Love wave attenuation coefficient, and row 7 the Love wave attenuation ratio. Rows 8 through 11 contain the layer 1 complex velocity, complex wave number, phase velocity, and attenuation ratio. Rows 12 through 15 contain the same information for layer 2, and so-on.

A.7 FineRoot

FineRoot.m is the precision root locater for *RootTracker.m* and *RootHunter.m*, but it can also be used as a stand-alone tool for finding precise root location than are given by *RootFinder.m*. The command:

```
roots=FineRoot(35,layer_props,138.85,30.15,2,3,0.01,0.01);
```

will search at 35 Hz for a complex root in the vicinity of 138.85 + 30.15i m/s. The search box will extend ± 2 in the real and ±3 in the imaginary direction. The search increments will be 0.01 in both directions. The search will return:

$$roots = \begin{bmatrix} 138.8450 \\ 30.1450 \\ 1.1058 \end{bmatrix}$$

where 138.8450 and 30.1450 are the real and imaginary velocity components, respectively, and 1.1058 is the quality number.

A.8 PropagateZ

PropagateZ.m produces a matrix of motion-stress values corresponding to each depth in a user defined depth profile matrix.

```
depth_profile=[0:0.01:100];
```

was used to create a 100 meter depth profile with 0.01 m spacing. The command:

```
ms=PropagateZ(35,layer_props,depth_profile,138.845,30.145);
```

creates plots of the displacement (Figure 4.2) and stress vectors, and the following matrix:

$$ms = \begin{bmatrix} 0 & 0.01 & \ldots \\ 1 & 1 & \ldots \\ 0 & 0.01 & \ldots \\ 1 & 0.9999 & \ldots \\ 0 & -3.9000e+05 & \ldots \end{bmatrix}$$

where the first row is the depth, the second is the layer number, the third is the thickness (depth below the previous layer boundary), row 5 is the displacement, and row 6 is the stress. The displacement at the top of the matrix is arbitrarily set to 1 meter; however, this can be altered by adjusting the first row of l_0 in *PropagateZ.m*.

The algorithm used by *PropagateZ.m* is similar to that of *Propagate.m*; however, instead of continuing calculations to the half-space, it calculates the value of the motion-displacement vector at an arbitrary depth.

A.9 Propagate

Propagate.m creates the propagator matrix (Equation 3.26) and computes its objective function (Equation 3.27) for a given frequency and complex velocity. We should note that the upper-right hand element of the matrix in Equation 3.21 can pose computational difficulties when $\nu \approx 0$. This is rectified by using the approximation, h_j/μ^* when the modulus of $\nu < 0.000001$. This is justified by the following:

$$\lim_{\nu\to\ 0} \frac{sinh(\nu h_i)}{\nu\mu^*} = \lim_{\nu\to\ 0} \frac{1}{\nu\mu^*} \sum_{k=1}^{\infty} \frac{(\nu h_j)^{2k+1}}{(2k+1)!} = \frac{h_j}{\mu^*} \tag{A.1}$$

A.10 Cauchy

Cauchy.m returns the path integral (divided by $2\pi i$) around a rectangular region in the complex plane. This is a numerical approximation of Equation 3.56. This should, ostensibly, be an integer representing the number of roots in the region, and in most cases, *Cauchy.m* yields a value within about 0.15 units of the corresponding integer. Deviations larger than this suggest that the integration path may have come close to a root (either inside or outside the path), and that the integration may have been compromised; hence, we use the term *quality number* for the value returned by *Cauchy.m*.

A.11 SignalBuilder

SignalBuilder.m creates a signal matrix of time domain synthetic data for a single mode. Each column of data represents the time domain signal obtained from a single receiver (Figure 5.3). *SignalBuilder.m* requires that *PropagateZ.m* be located in the same directory.

Signals may be added to an existing signal matrix, so that the effects of multiple modes can be superposed. In addition to a signal matrix, *SignalBuilder.m* requires a layer properties matrix, the output from *RootReports.m*, a depth profile matrix, a source properties matrix, and information about the source-receiver offset, receiver spacing, temporal sample interval, and pulse duration. As an example, we will build the fundamental mode of the signal used in our single viscoelastic layer examples. This signal will be generated for an array of 96 geophones with 1 *meter* spacing. Temporal sampling rate will be 600 *samples/s* over a 2 second interval. We will simulate an 0.25 *s* pulse by superimposing signals taken at 0.25 *Hz* intervals, between 4 *Hz* to 120 *Hz*.

We begin by preparing a signal matrix called *wiggles*:

```
wiggles=zeros(1200,96);
```

Using either *RootTracker.m* or *RootFinder.m*, we find roots at 0.25 *Hz* increments over the interval between 4 and 120 *Hz*. This information is then used by *RootReports.m* to create the following matrix:

$$love\_report = 1e{+}02{*}\begin{bmatrix} 0.0400 & 0.0425 & 0.0450 & \dots \\ 0.0113 & 0.0113 & 0.0113 & \dots \\ 3.5006+0.02701i & 3.2181+0.04681i & 2.9355+0.0661i & \dots \\ 0.0007-0.0000i & 0.0008-0.0000i & 0.0010-0.0000i & \dots \\ 3.5009 & 3.2188 & 2.9371 & \dots \\ 0.0000 & 0.0000 & 0.0000 & \dots \\ 0.0001 & 0.0001 & 0.0002 & \dots \\ \vdots & \vdots & \vdots & \ddots \\ & & & \end{bmatrix}$$

Source properties are tabulated in a 3 x n matrix. Each column corresponds to a column of love_report, with frequency in row 1, amplitude in row 2, and phase angle (in radians) in row 3. Because we are building a unit pulse, we will set amplitude and phase angle to one and zero, respectively, for all freqencies:

$$layer\_props = \begin{bmatrix} 4 & 4.2500 & 4.5000 & \dots \\ 1 & 1 & 1 & \dots \\ 0 & 0 & 0 & \dots \end{bmatrix}$$

The partition function, Γ, discussed in Section 5.1 requires that the motion-stress vector be integrated across the half-space. In practice, we find that limiting the integration to a depth equal to about 1.5 wavelengths has no observable effect on accuracy. Nevertheless, the integration is fairly quick: We will use a depth profile of 100 meters and 0.01 meter increments:

```
depth_profile=[0:0.01:100];

wiggles=SignalBuilder(wiggles,10,1,1/600,love_report,...
          layer_props,depth_profile,source_props,0.25);
```

was used to create the fundamental mode signal for 5.3. The process was repeated in order to add signals for the first three overtones.

APPENDIX B:
FORWARD MODELING MATLAB® CODE

B.1 About the Forward Modeling Utilities

The forward modeling utilities were tested using MATLAB® Student Version, R2009a on a 32 bit Apple MacBook® with an Intel core duo microprocessor, and on a 64 bit Apple i-Mac® with a Core-2 duo microprocessor.

B.2 LoveObjects

```
function obj_fun=LoveObjects(freq,layer_props,search_limits,Lsquelch,Hsquelch)
%LoveObjects produces a matrix of the objective function and and a graph
%of imaginary velocity (Ci) versus real velocity (Cr).
%Lsquelch and Hsquelch are used to adjust the color axis.

%Requires that Propagate.m be in the same directory.

%example of a layer properties matrix for 3 VE layers over a half space.
%Properties are thickness (m),density (kg/m^3), shear modulus (Pa), and
%viscosity (Pa-s)
%layer_props=[1.67 1600 16E6 16000;1.66 1700 68E6 34000; 1.67 1700 153E6
%51000; 0 1800 288E6 0]

%example of a search limits matrix.
%row 1:  lower bound, upper bound, increment for real velocity axis
%row 2:  lower bound, upper bound, increment for imaginary velocity axis
%search_limits= [100,450,350;0,100,100];

lrv=search_limits(1,1);
urv=search_limits(1,2);
nrv=search_limits(1,3);
liv=search_limits(2,1);
uiv=search_limits(2,2);
niv=search_limits(2,3);
irv=(urv-lrv)/nrv; %Real Search Increment
iiv=(uiv-liv)/niv; %Imaginary Search Increment
obj_fun=zeros(niv+1,nrv+1); %Store Objective Function Here

for ii=0:nrv
  for jj=0:niv
     rv=lrv+ii*irv; %love wave real velocity component
     iv=liv+jj*iiv; %love wave imaginary velocity component
     obj_fun(jj+1,ii+1)=Propagate(freq,layer_props,rv,iv);
  end
end
```

```
figure;
imagesc(lrv:irv:urv,liv:iiv:uiv,log(abs(obj_fun(:,:))));

if Lsquelch ~= Hsquelch
    caxis([Lsquelch Hsquelch]);
end

title(['Objective Function (',num2str(freq),'Hz)']);
xlabel('Love wave real velocity--C_r, (m/s)');
ylabel('Love wave imag velocity--C_i, (m/s)');
set(gca,'YDir','normal'); %Sets Y axis to a more conventional direction.
end
```

B.3 RootFinder

```
function Roots = RootFinder(freq,layer_props,lx,ly,wx,wy,nx,ny)
%(frequency, layer properties matrix, left-real, lower-imag, box width,
% box height, number of boxes in real direction, number of boxes in
%imaginary direction)
%Requires Propagate.m

nroots=0;
Roots=zeros(3,1);
xi=1;  %Search resolution in real direction.
yi=1; %Search resolution in imaginary direction.

for kk=0:ny
    cy=ly+kk*wy;
    for jj=0:nx
        cx=lx+jj*wx;

%cx and cy are locations of the lower left corner of each sub box.

dx=cx+wx;
dy=cy+wy;
CI=Cauchy(freq,layer_props,cx,dx,cy,dy);
        if abs(CI)>0.5
            nroots=nroots+1;

            for ii=1:wy/yi
            ey=dy-ii*yi;
            if abs(Cauchy(freq,layer_props,cx,dx,cy,ey)) < 0.5
            Ci=ey+0.5*yi;
            break;
            end
            end

            for ii=1:wx/xi
            ex=cx+ii*xi;
            if abs(Cauchy(freq,layer_props,ex,dx,cy,dy)) < 0.5
            Cr=ex-0.5*xi;
```

```
            break;
            end
            end

            Roots(1,nroots)=Cr;
            Roots(2,nroots)=Ci;
            Roots(3,nroots)=abs(CI);
        end

    end
end
end
```

B.4 RootTracker

```
function love_roots = RootTracker(love_roots,ffin,fi,layer_props,tx,ty,neta)

%Given an initial root position and Frequency, RootTracker finds subsequent
%RootPosition/Frequency pairs.  By using the input file, love_roots,
%RootTracker can add new root locations to an existing file.  fi is the
%frequency increment, and ffin is the final frequency. layer_props is an
%mxn matrix of material properties (see example), and tx and ty are the
%half search intervals.  neta is the number of viscosity increments.

    [rrows rcols]=size(love_roots);
    fstart=love_roots(4,rcols); %frequency at which search begins.
    realstart=love_roots(5,rcols);%Last real velocity at which a search began
    x=realstart;
    y=0;
    cx=realstart-tx;
    dx=realstart+tx;
    cy=y-ty;
    dy=y+ty;
    [prows pcols]=size(layer_props);
    layer_search=layer_props;
    layer_search(:,4)=0;

    for jj=fstart+fi:fi:ffin

        layer_search(:,4)=0;

        while abs(Cauchy(jj,layer_search,cx,dx,cy,dy))<0.5
            realstart=realstart-sign(fi)*2*tx;
            cx=realstart-tx;
            dx=realstart+tx;
            cy=y-ty;
            dy=y+ty;
        end

        rcols=rcols+1;
```

```
        A=FineRoot(jj,layer_search,realstart,y,tx,ty,0.1,0.1);
        love_roots(1,rcols)=A(1,1);  %Real Velocity
        love_roots(2,rcols)=A(2,1);  %Imaginary Velocity
        love_roots(3,rcols)=A(3,1);  %Cauchy Integral/(2*pi*i)
        love_roots(4,rcols)=jj;  %Frequency
        love_roots(5,rcols)=A(1,1); %Real Search Start Point

        for kk=1:prows
            for ll=1:neta
              layer_search(kk,4)=ll/neta*layer_props(kk,4);
              A=FineRoot(jj,layer_search,A(1,1),A(2,1),tx,ty,0.1,0.1);
              love_roots(1,rcols)=A(1,1);  %Real Velocity
              love_roots(2,rcols)=A(2,1);  %Imaginary Velocity
              love_roots(3,rcols)=A(3,1);  %Cauchy Integral/(2*pi*i)
            end
        end

    end
end
```

B.5 RootHunter

```
function love_roots = RootHunter(love_roots,ffin,fi,layer_props,tx,ty,xi,yi)

%Tracks and Records real and imaginary location of a root from flow in
%frequency intervals of fi given layer properties and an initial location
%for the root.

%RootHunter requires an input array with root locations corresponding to
%three different frequencies.

jcol=1; %Initialize Last Data Column

[nrows ncols]=size(love_roots); %Checking for end of data

jcol=ncols;

%real derivatives
delta=love_roots(4,jcol)-love_roots(4,jcol-1);
der1r=(love_roots(1,jcol)-love_roots(1,jcol-1))/delta;
delta=love_roots(4,jcol-1)-love_roots(4,jcol-2);
der1pr=(love_roots(1,jcol-1)-love_roots(1,jcol-2))/delta;
delta=(love_roots(4,jcol)-love_roots(4,jcol-2))/2;
der2r=(der1r-der1pr)/delta;

%imaginary derivatives
delta=love_roots(4,jcol)-love_roots(4,jcol-1);
der1i=love_roots(2,jcol)-love_roots(2,jcol-1)/delta;
delta=love_roots(4,jcol-1)-love_roots(4,jcol-2);
der1pi=love_roots(2,jcol-1)-love_roots(2,jcol-2)/delta;
delta=(love_roots(4,jcol)-love_roots(4,jcol-2))/2;
der2i=(der1i-der1pi)/delta;

fstart=love_roots(4,jcol) + fi;
x=love_roots(1,jcol) + der1r*fi+ der2r/2*fi^2;
y=love_roots(2,jcol)+ der1i*fi+ der2i/2*fi^2;
```

```
for jj=fstart:fi:ffin
    jcol=jcol+1;
    A=FineRoot(jj,layer_props,x,y,tx,ty,xi,yi);
    love_roots(1,jcol)=A(1,1);
    love_roots(2,jcol)=A(2,1);
    love_roots(3,jcol)=A(3,1);
    love_roots(4,jcol)=jj;

    delta=love_roots(4,jcol)-love_roots(4,jcol-1);
    der1r=love_roots(1,jcol)-love_roots(1,jcol-1)/delta;
    delta=love_roots(4,jcol-1)-love_roots(4,jcol-2);
    der1pr=love_roots(1,jcol-1)-love_roots(1,jcol-2)/delta;
    delta=(love_roots(4,jcol)-love_roots(4,jcol-2))/2;
    der2r=(der1r-der1pr)/delta;

    delta=love_roots(4,jcol)-love_roots(4,jcol-1);
    der1i=(love_roots(2,jcol)-love_roots(2,jcol-1))/delta;
    delta=love_roots(4,jcol-1)-love_roots(4,jcol-2);
    der1pi=(love_roots(2,jcol-1)-love_roots(2,jcol-2))/delta;
    delta=(love_roots(4,jcol)-love_roots(4,jcol-2))/2;
    der2i=(der1i-der1pi)/delta;


    x=A(1,1) + der1r*fi+der2r/2*fi^2;
    y=A(2,1)+ der1i*fi+der2i/2*fi^2;
end
end
```

B.6 RootReport

```
function love_report = RootReport(layer_props, love_roots)

%RootReport uses a material property matrix and the output from
%RootTracker to generate a report of:

%Row 1:  Frequency
%Row 2:  Quality Number
%Row 3:  Love Wave Complex Velocity
%Row 4:  Love Wave Complex Wave Number
%Row 5:  Love Wave Phase Velocity
%Row 6:  Love Wave Attenuation Coefficient
%Row 7:  Love Wave Attenuation Ratio
%Row 8:  Layer 1 Complex Velocity
%Row 9:  Layer 1 Complex Wave Number
%Row 10:  Layer 1 Phase Velocity
%Row 11:  Layer 1 Attenuation Ratio
%Row 12:  Layer 2...
%etcetera through half-space

[prows pcols]=size(layer_props);
[rrows rcols]=size(love_roots);

love_report=zeros(7+4*prows,rcols);
for jj=1:rcols
    love_report(1,jj)=love_roots(4,jj);
    love_report(2,jj)=love_roots(3,jj);
    love_report(3,jj)=love_roots(1,jj)+i*love_roots(2,jj);
    love_report(4,jj)=2*pi*love_roots(4,jj)/love_report(3,jj);
    A=real(love_report(3,jj));
    love_report(5,jj)=love_report(3,jj)*love_report(3,jj)'/A;
    love_report(6,jj)=-imag(love_report(4,jj));
    love_report(7,jj)=-imag(love_report(4,jj))/real(love_report(4,jj));
end

for jj=1:rcols
```

```
    for kk=0:prows-1
        omega=2*pi*love_roots(4,jj);
        rho=layer_props(kk+1,2);
        mu=layer_props(kk+1,3);
        eta=layer_props(kk+1,4);
        csv2=1/rho*(mu+i*omega*eta);
        love_report(7+4*kk+1,jj)=sqrt(csv2);
        love_report(7+4*kk+2,jj)=omega/love_report(7+4*kk+1,jj);
        love_report(7+4*kk+3,jj)=omega/real(love_report(7+4*kk+2,jj));
        A=-imag(love_report(7+4*kk+2,jj));
        B=real(love_report(7+4*kk+2,jj));
        love_report(7+4*kk+4,jj)=A/B;
    end
end

end
```

B.7 FineRoot

```
function A= FineRoot(freq,layer_props,x,y,tx,ty,xi,yi)
%Given a center point and box dimensions, FineRoot will find the exact
%coordinares of a root within that box.  xi and yi indicate search
%granularity.

%Requires that Cauchy.m and Propagate.m be located in the same directory.

lx=x-tx;
ly=x-ty;
A=zeros(3,1);

%x and y are centers, and tx and ty are tolerances.
cx=x-tx; %cx and cy are locations of the lower left corner of each sub box.
cy=y-ty;
dx=x+tx;
dy=y+ty;
CI=Cauchy(freq,layer_props,cx,dx,cy,dy);
        if abs(CI)>0.5

            for ii=0:yi:2*ty
              ey=dy-ii;
              if abs(Cauchy(freq,layer_props,cx,dx,cy,ey)) < 0.5
                Ci=ey+0.5*yi;
              break;
              end
            end

            for ii=0:xi:2*tx
              ex=cx+ii;
              if abs(Cauchy(freq,layer_props,ex,dx,cy,dy)) < 0.5
                Cr=ex-0.5*xi;
              break;
              end
            end
```

```
            A(1,1)=Cr;
            A(2,1)=Ci;
            A(3,1)=abs(CI);
        end

end
```

B.8 PropagateZ

```
function l_profile=PropagateZ(freq,layer_props,depth_profile,rv,iv)
%PropagateZ returns the motion-stress vector for selected depths given a
%frequency, matrix of layer properties, real Love velocity, imaginary Love
%velocity, and a matrix of desired depths.
%(frequency, layer property matrix, Love real velocity,Love imaginary
%velocity)

%depth_profile=[1,0.01:0.01:100];
[np nz]=size(depth_profile);
l_0=[1;0];% Initialize Motion Stress Vector for surface conditions


%l_profile Row 1 = depth
%l_profile Row 2 = layer
%l_profile Row 3 = thickness
%l_profile Row 4 = motion vector
%l_profile Row 5 = stress vector

[nlayers nprops]=size(layer_props);
layer_tops=zeros(1,nlayers); %Z coordinate of each layer top
layer_tops(1,1)=0;

for kk=2:nlayers
    layer_tops(1,kk)=layer_tops(1,kk-1)+layer_props(kk-1,1);
end

l_profile=zeros(5,nz);  %Initializing l_profile matrix
l_profile(1,:)=depth_profile(1,:);
l_profile(2:3,1)=[1;0];

for jj=1:nlayers
    for kk=1:nz
        if l_profile(1,kk) > layer_tops(1,jj)
            l_profile(2,kk)=jj;
            l_profile(3,kk)=l_profile(1,kk)-layer_tops(1,jj);
```

```
        end
    end
end

clv=rv+i*iv; %love wave complex velocity
clk2=(freq*2*pi()/clv)^2; %Love Wave complex wave numb. squared (K^2)

for jj=1:nz
  Pzz0=[1,0;0,1]; %Initialize Propagator Matrix
  layer=l_profile(2,jj);

  for kk=1:layer-1
    thk = layer_props(kk,1); %Layer kk thickness
    rho = layer_props(kk,2); %Layer kk density
    mu = layer_props(kk,3); %Layer kk shear modulus
    eta= layer_props(kk,4); %Layer kk effective viscosity
    muc= mu + i*eta*2*pi()*freq; %Layer kk complex effective viscosity
    csv2=muc/rho; %Shear Wave Complex Velocity (squared)
    csk2=(freq*2*pi())^2/csv2; %Shear Wave complex wave num. squared(k^2)
    nu=sqrt(clk2 - csk2); %Complex Vertical Exponent

    %Necessary to keep A[1,2] from exploding.  See Appendix C.1
    if abs(nu) <0.000001
      A=[cosh(nu*thk),thk/muc;nu*muc*sinh(nu*thk),cosh(nu*thk)];
    else
      A=[cosh(nu*thk),sinh(nu*thk)/(nu*muc)...
          nu*muc*sinh(nu*thk),cosh(nu*thk)];
    end

    Pzz0=A*Pzz0;
  end

  if layer < nlayers
    thk = l_profile(3,jj); %Layer kk thickness
    rho = layer_props(layer,2); %Layer kk density
    mu = layer_props(layer,3); %Layer kk shear modulus
    eta= layer_props(layer,4); %Layer kk effective viscosity
    muc= mu + i*eta*2*pi()*freq; %Layer kk complex effective viscosity
    csv2=muc/rho; %Shear Wave Complex Velocity (squared)
    csk2=(freq*2*pi())^2/csv2; %Shear Wave complex wave num. squared (k^2)
```

```
    nu=sqrt(clk2 - csk2); %Complex Vertical Exponent

    %Necessary to keep A[1,2] from exploding.
    if abs(nu) <0.000001
      A=[cosh(nu*thk),thk/muc;nu*muc*sinh(nu*thk),cosh(nu*thk)];
    else
      A=[cosh(nu*thk),sinh(nu*thk)/(nu*muc)...
          nu*muc*sinh(nu*thk),cosh(nu*thk)];
    end

    Pzz0=A*Pzz0;

  else
    thk=l_profile(3,jj); %Depth to top of half space
    rho = layer_props(nlayers,2); %Half space density
    mu = layer_props(nlayers,3); %Half space shear modulus
    eta= layer_props(nlayers,4); %Half space effective viscosity
    muc= mu + i*eta*2*pi()*freq; %Half Space complex effective viscosity
    csv2=muc/rho; %Shear Wave Complex Velocity (squared)
    csk2=(freq*2*pi())^2/csv2; %Shear Wave complex wave num squared (k^2)
    nu=sqrt(clk2 - csk2); %Complex Vertical Exponent

    A=0.5*[exp(-nu*thk) -1/(muc*nu)*exp(-nu*thk)...
        -muc*nu*exp(-nu*thk) exp(-nu*thk)];
    Pzz0=A*Pzz0;

  end

  l_profile(4:5,jj)=Pzz0*l_0;

end

figure; %Displacement
plot(real(l_profile(4,:)),-depth_profile(1,:));
title(['Displacement (',num2str(freq),') Hz']);

figure; %Stress
plot(real(l_profile(5,:)),-depth_profile(1,:));
title(['Stress (',num2str(freq),') Hz']);
end
```

B.9 Propagate

```
function OBJ=Propagate(freq,layer_props,rv,iv)
%(frequency, layer property matrix, Love real velocity,Love imaginary
%velocity)

[nlayers nprops]=size(layer_props);
nlayers=nlayers-1;

clv=rv+i*iv; %love wave complex velocity
clk2=(freq*2*pi()/clv)^2; %Love Wave complex wave number squared (k-squared)

Pzz0=[1,0;0,1]; %Initialize Propagator Matrix
for kk=1:nlayers
  thk = layer_props(kk,1); %Layer kk thickness
  rho = layer_props(kk,2); %Layer kk density
  mu = layer_props(kk,3); %Layer kk shear modulus
  eta= layer_props(kk,4); %Layer kk effective viscosity
  muc= mu + i*eta*2*pi()*freq; %Layer kk complex effective viscosity
  csv2=muc/rho; %Shear Wave Complex Velocity (v^2)
  csk2=(freq*2*pi())^2/csv2; %Shear Wave complex wave number squared (k^2)
  nu=sqrt(clk2 - csk2); %Complex Vertical Exponent

  %Necessary to keep A[1,2] from exploding.
    if abs(nu) <0.000001
      A=[cosh(nu*thk),thk/muc;...
         nu*muc*sinh(nu*thk),cosh(nu*thk)];
    else
      A=[cosh(nu*thk),sinh(nu*thk)/(nu*muc);...
         nu*muc*sinh(nu*thk),cosh(nu*thk)];
    end

  Pzz0=A*Pzz0;
end

%Half Space and Boundary Value Matrix
%thk=sum(layer_props(1:nlayers,1)); %Depth to top of half space.
thk=sum(layer_props(1:nlayers,1));
```

```
rho = layer_props(nlayers+1,2); %Half space density
mu = layer_props(nlayers+1,3); %Half space shear modulus
eta= layer_props(nlayers+1,4); %Half space effective viscosity
muc= mu + i*eta*2*pi()*freq; %Half Space complex effective viscosity
csv2=muc/rho; %Shear Wave Complex Velocity (squared)
csk2=(freq*2*pi())^2/csv2; %Shear Wave complex wave number squared (k^2)
nu=sqrt(clk2 - csk2); %Complex Vertical Exponent

Finv=1/(2*nu*muc)*[nu*muc*exp(nu*thk),-exp(nu*thk);...
                   nu*mu*exp(-nu*thk),exp(-nu*thk)];

H=Finv*Pzz0;

OBJ=H(2,1);

end
```

B.10 Cauchy

```
function CI=Cauchy(freq,layer_props,cx,dx,cy,dy)
%Computes Cauchy Path Integral given frequency, layer properties,
%and corner points.
%Requires that Propagate.m be located in the same directory.

CI=0; %Initialize Cauchy Integral

for ii=cx:dx
    num=Propagate(freq,layer_props,ii+1,cy)-Propagate(freq,layer_props,ii,cy);
    den=Propagate(freq,layer_props,ii+1,cy)+Propagate(freq,layer_props,ii,cy);
    CI=CI+2*num/den;

end
for ii=cy:dy
    num=Propagate(freq,layer_props,dx,ii+1)-Propagate(freq,layer_props,dx,ii);
    den=Propagate(freq,layer_props,dx,ii+1)+Propagate(freq,layer_props,dx,ii);
    CI=CI+2*num/den;
end
for ii=cx:dx
    num=Propagate(freq,layer_props,ii+1,dy)-Propagate(freq,layer_props,ii,dy);
    den=Propagate(freq,layer_props,ii+1,dy)+Propagate(freq,layer_props,ii,dy);
    CI=CI-2*num/den;
end

for ii=cy:dy
    num=Propagate(freq,layer_props,cx,ii+1)-Propagate(freq,layer_props,cx,ii);
    den=Propagate(freq,layer_props,cx,ii+1)+Propagate(freq,layer_props,cx,ii);
    CI=CI-2*num/den;
end

CI=CI/(2*pi*i);

end
```

B.11 SignalBuilder

```
function wiggles=SignalBuilder(wiggles,x0,dx,dt,love_report,layer_props,...
    depth_profile,source_props,pulse)
%SignalBuilder adds signals to an existing matrix of signal data.
%wiggles(time,vsp).
%x0 is x coordinate of first VSP, dx is x increment, dt is time increment.
%love_report is output from RootReport.m
%layer_props is a layer properties matrix.
%depth_profile is the depth profile over which I_2 is integrated.
%source_props is a 3 x n matrix with [freq1 amp1 phase1; freq2 amp2
%    phase2...]
%pulse is the duration of the source signal
%Requires that PropagateZ.m be located in the same directory.

[wrows wcols]=size(wiggles);
[rrows rcols]=size(love_report);

for kk=1:rcols
    f = love_report(1,kk);
    alpha=love_report(6,kk);
    kr=real(love_report(4,kk));

    %Calculates the partition function
    rv=real(love_report(3,kk));
    iv=imag(love_report(3,kk));
    l_profile=PropagateZ(f,layer_props,depth_profile,rv,iv);
    Kr=2*pi*f*rv/(rv^2+iv^2);

    %Computes I_sigma
    I_sigma=0;
    [nrows ncols]=size(l_profile);
    for jj=1:ncols-1
      dz=l_profile(1,jj+1)-l_profile(1,jj);
      layer=l_profile(2,jj);
      I_sigma=I_sigma+abs(l_profile(4,jj))^2*layer_props(layer,3)*dz;
    end
    Gamma=1/(8*I_sigma)*sqrt(2/(pi*Kr*1));
```

```
    v=love_report(5,kk);
    omega=2*pi*f;

    ll=1;
    while source_props(1,ll) ~= f
        ll=ll+1;
    end

    amp=source_props(2,ll);
    ph=source_props(3,ll);

      for mm=1:wcols
          r=x0+(mm-1)*dx;
          t0=r/v;
          tp=t0+pulse;
          tlast=min(wrows,floor(tp/dt));

          for nn=ceil(t0/dt):tlast
              wiggles(nn,mm)=wiggles(nn,mm)+1/sqrt(r)*Gamma*amp*...
                  exp(-alpha*r)*cos(omega*nn*dt-kr*r+ph-pi/4);

          end

      end

end

end
```

APPENDIX C:

INVERSION UTILITIES: DOCUMENTATION

The inversion utilities are a group of related MATLAB® scripts and functions. In this appendix, we will outline the procedures used to create a shot gather (figure 5.3), K-f plot (figure 5.5), and invert dispersion and attenuation curves using the Gauss-Newton inversion method. The code for each of these utilities can be found in Appendix D.

C.1 Getting Started

First, be sure that all required functions are loaded in the same directory. The utility *Jacob.m* requires that *FineRoot.m* and *Cauchy.m* be loaded in the same directory.

◇ Use *WigglePlot.m* to look at data quality. The slopes of the bottom and top portions can be used as initial estimates of the top layer and half-space shear wave velocities.

◇ Use *KFreq.m* to construct K-f plots, then visually identify patterns of maxima corresponding to Love wave modes. For each wave number (K), plot a slice of the data and manually identify, measure, and record each peak corresponding to the Love wave mode. For each peak, determine the phase velocity using the relationship $C_L = f/K$.

◇ Determining attenuation coefficient will require amplitude data from two different source offsets. Repeat the previous procedure for data taken at a second source offset distances, and then determine attenuation coefficients at each frequency using the relationship $\alpha = \frac{1}{(d_2 - d_1)} ln(\frac{A_2}{A_1})$, where A_2 and A_1 are amplitudes at two different source offsets, d_2 and d_1.

◇ Use *FilePrep.m* to prepare appropriately formatted data matrices for *Jacob.m* and *LoveInv.m*.

◇ Use *Jacob.m* to create a Jacobian for the inversion.

◇ Use *LoveInv.m* to invert the data, and obtain estimates of selected layer properties (The Inverse Problem). Repeat the process to obtain a better estimate.

C.2 WigglePlot

WigglePlot.m produces a shot gather, such as that in figure 5.3. The function call,

```
wig=WigglePlot(wiggles,lo,hi,dx,dt,nt,scale,exclud);
```

plots the data in the m x n matrix *wiggles*, where m is the number of measurement time intervals, and n is the number of receivers (geophones). Each column contains time domain data from a single receiver. Data can be plotted over a range of receiver numbers, between *lo* and *hi*. *dx* and *dt* indicate the receiver spacing (meters) and time increment (seconds). *nt* is the total interval over which the signal was gathered (in seconds). The scaling factor, *scale* allows trace magnitude to be expanded. The 1 x n matrix *exclude* allows selected traces to be excluded. If no traces are to be excluded, set exclude to []. For example:

```
wig=WigglePlot(wiggles,15,96,1.5,1/600,2,1.5,[22 35 73]);
```

will use data from the 1200 row x 96 column matrix *wiggles* to create a shot gather. The plot will only include traces from receivers 15 to 96. Receiver spacing is 1.5 meters, and data was gathered at a 600 Hz sample rate (0.00167 s sampling interval). All 2 seconds of data will be displayed. The magnitude of each trace will be magnified 1.5 times, and traces 22, 35, and 73 will be excluded from the final plot.

C.3 Kfreq

Kfreq.m creates a K-f plot like that of figure 5.5. The command:

```
[fshot ffshot]=Kfreq(wiggles,dx,dt);
```

plots data from the m x n matrix *wiggles*, where m is the number of rows of time step information, and n corresponds to the number of receivers. *dx* and *dt* are, respectively, receiver spacing and time increment. The matrices *fshot* and *ffshot* contain Fourier transformed (time domain) and double Fourier transformed (K-f domain) data. If *wiggles* is a 1200 row by 96 column matrix, the command:

```
[fshot ffshot]=Kfreq(wiggles,1/6,1/600);
```

produces a plot with a wave number axis scaled from $1/(n * dx) = 6/96 = 1/16$ to $1/dx = 6$, and frequency from $f/m = 600/1200 = 0.5$ to 600. For the plots in chapter 6, the data was plotted with an additional 1200 rows in the time direction, and 96 extra columns in the spatial direction.

Once the K-f plot has been generated, it is used to identify modes. For each mode, determine a set of K-f values visually, and then make a K-slice from *ffshot*.

This command was used to generate the K-f slice (frequency-amplitude curve) in the right panel of figure 5.7:

```
plot(600:-600/2400:600/2400,abs(ffshot(1:2400,16)));
```

The data from wiggles was padded with an additional 1200 rows and 96 columns of zeros, resulting in a 2400 x 192 matrix. *ffshot* has the same dimensions. The number 16 indicates the column number of *ffshot*. The corresponding wave number can be found: $K = \frac{colno}{dx*ncols} = \frac{16}{0.167*192} = 0.5$.

C.4 FilePrep

The utility *FilePrep.m* converts matrices to a form that is suitable for *Jacob.m* and *LoveInv.m* from an input matrix, *seed*, and a delta layer properties matrix, *dP*. *seed* is an (m+1) x (n+1) matrix of data with frequency in column 1, and a label in column 2 indicating whether the column will be used to invert velocity data (1), or attenuation data (2). The matrix:

$$seed = \begin{bmatrix} 0 & 1 & 2 & 1 & \dots \\ 9 & 117+6i & 126+3.2i & 115+4.2i & \dots \\ 10 & 112.75+6.25i & 124.2+3.8i & 114.5+4.5i & \dots \\ \vdots & \vdots & \vdots & \vdots & \ddots \end{bmatrix}$$

includes data at 9 and 10 Hz. The first column indicates the frequency corresponding to each measurement. The 1s and 2s in the first row of data indicate that the second column will be treated as dispersion information, the third column will be treated as attenuation, and the fourth column will be treated as dispersion information. The matrix:

$$dP = \begin{bmatrix} 0 & 0 & 1E5 & 500 \\ 0 & 0 & 0 & 0 \end{bmatrix}$$

is a delta layer properties matrix that instructs *FilePrep.m* to build the appropriate matrices for a two parameter model using shear modulus and viscosity. *Jacob.m* will use shear modulus and viscosity increments, respectively, of ±1E5 MPa and ±500 *Pa-s*. The function call:

```
[Lseed tune J]=FilePrep(dP,seed);
```

produces three matrices. The data from *seed* are reformatted into a four column matrix called *Lseed*. The first three columns of *Lseed* are frequency, a column/row identifier, and a flag (1 or 2) indicating whether the data will be treated as dispersion information or attenuation information. All of the data is contained within column 4. The matrix:

$$Lseed = \begin{bmatrix} 9 & 2.0010 & 1 & 117+6i \\ 10 & 2.0020 & 1 & 112.75 \\ 9 & 3.0010 & 2 & 126+3.28 \\ \vdots & \vdots & \vdots & \vdots \end{bmatrix}$$

contains the (partial) output from *FilePrep.m*. The column/row identifier of 2.0020 indicates that the data originally came from column 2 and row 2 of *seed*.

The *tune* matrix includes the same three columns of identifying information as *Lseed*, and is followed by five columns that can be used to optimize calculation of the Jacobian in *Jacob.m*. The value in column 5 modulates the values of dP for the corresponding row. Columns 4, 5, 6, and 7 are, respectively, window sizes and search increments used by *Jacob* to hunt for roots (These serve the same function as the corresponding values used by *RootTracker.m*). The output is:

$$tune = \begin{bmatrix} 9 & 2.0010 & 1 & 1 & 10 & 10 & 0.1 & 0.1 \\ 10 & 2.0020 & 1 & 1 & 10 & 10 & 0.1 & 0.1 \\ 9 & 3.0010 & 2 & 0.1 & 5 & 4 & 0.5 & 0.5 \\ \vdots & \vdots & \vdots & \vdots & & & & \end{bmatrix}$$

In this matrix, the first two rows of *tune* have been set to the defaults; however, the user has modified the parameters in the third row. When computing the corresponding Jacobian, the values of the delta properties matrix (dP) will be multiplied by 0.1. Also, the size of the window used to search for the changing root will be 5 and 4 m/s in the real and imaginary directions, respectively. The search resolution (an indicator of search accuracy) has been reduced to 0.5 m/s. More information about using the *tune* matrix is found in the section on *Jacob.m*.

FilePrep.m also produces an empty Jacobian matrix for use by *Jacob.m*.

C.5 Jacob

Jacob.m calculates the Jacobian matrix associated with a given layer properties model. *Jacob.m* requires that *FineRoots.m* and *Cauchy.m* be located in the same folder. *Jacob.m* computes the Jacobian using a central difference formulation. For each layer property used in the model, it finds the location of a root using $G(prop + \Delta prop)$ and $G(prop - \Delta prop)$, where $\Delta prop$ is obtained from the dP matrix. This is then divided by $2\Delta prop$. If $\Delta prop$ is too large, *Jacob.m* may not be able to identify the root. To correct this, the corresponding modulation factor (column 4) of *tune* can be reduced. Alternatively, the size of the search window in columns 5 and 6 can be increased. Increasing the search window can greatly increase processing time. When accuracy does not suffer, search resolution (columns 7 and 8) can be reduced with a concomitant decrease in processing time.

The command:

```
J=Jacob(layer_props,Lseed,J,tune,dP);
```

produces an m x n Jacobian matrix, where m is the number of data points being inverted, and n is the number of properties used in the model.

C.6 LoveInv

LoveInv.m inverts the data to find $\Delta\mathbf{m}$, the delta layer properties matrix. The command:

```
[dm Covm]=LoveInv(Ldata,Lseed,J,W.Y,covd);
```

invokes *LoveInv.m*. *Lseed* was discussed in the previous section. It contains values of roots for the assumed properties matrix specified in *layer_props*. *Ldata* is a matrix of data values (obtained from a dispersion or attenuation curve), and should be formatted exactly like *Lseed*. *FilePrep.m* can be used to pepare *Ldata* so that each of its entries corresponds exactly to those in *Lseed*.

W and Y are, respectively, diagonal row and column weighting matrices that are defined by the user. W should be an m x m diagonal matrix, where m is the number of rows in *Ldata*. For the inversion procedures of chapter 6, the diagonal entries were set equal to the reciprocal of the standard deviation of each group of data from the corresponding data row (for example, all mode 0 attenuation data, or all mode 1 dispersion data).

Y is a column weighting matrix that enhances stability of the solution. Y is an n x n diagonal matrix, where n is the number of independent variables in the model (i.e. the number of columns of J). When the typical values of each column are of the same order of magnitude, the diagonal entries of Y can be set to 1. For the inversion procedures of chapter 6, the diagonal entries were set equal to the average values of the corresponding columns.

Covd is an m x m data covariance matrix, where m is the number of rows in *Ldata*. Generally, covariance information was unavailable, and only the diagonal (varance) entries were used. Variance was imputed from the residuals obtained from a line or polynomial of best fit through the local data.

To obtain an estimate of layer properties, add the appropriate value of $d\mathbf{m}$ to the corresponding entry in the layer properties matrix. In general, the method converges within five or fewer iterations.

APPENDIX D:

INVERSION MATLAB® CODE

D.1 About the Inversion Utilities

The inversion modeling utilities were tested using MATLAB® Student Version, R2009a on a 32 bit Apple MacBook® with an Intel core duo microprocessor, and on a 64 bit Apple i-Mac® with a Core-2 duo microprocessor.

D.2 WigglePlot

```
function wig=WigglePlot(wiggles,lo,hi,dx,dt,nt,scale,exclud)

%displays a wiggle plot
%wiggles data from all shot points (time x vsp)
%wig=traces of shot points excluding those in exclud
%lo and hi:  lowest and highest trace to be plotted
%dx=distance between traces (use 1 to plot station)
%dt=time sampling interval
%nt=number of time increments
%scale=width of a wiggle
%e.g. exclud = [1 9 16] to exclude traces 1,9, and 16.  [] for all traces
npts=nt;
figure;
axes('XAxisLocation','top');
hold on;
[nrows ncols]=size(exclud);

trinfo=zeros(1,hi-lo+1);
wig=zeros(npts,hi-lo+1);
for ii=lo:hi
trace = ii;
trinfo(1,ii)= max(abs(wiggles(:,ii)))/scale;
wig(:,ii)=ii*dx+dx*wiggles(:,ii)/trinfo(1,ii);
for jj=1:ncols
    if exclud(1,jj)==ii;
        wig(:,ii)=0;
    end
end

plot(wig(:,ii),dt:dt:npts*dt);
end

axis([lo*dx hi*dx dt npts*dt]);
axis ij;
end
```

D.3 Kfreq

```
function [fshot ffshot]=Kfreq(wiggles,dx,dt)
%Creates a K-f plot of wiggles, and produces files of the Fourier transformed
%(time domain) and double Fourier transformed (K-f domain) data.

[nrows ncols]=size(wiggles);
fshot=zeros(nrows,ncols);
ffshot=zeros(nrows,ncols);

for ii=1:ncols
    fshot(:,ii)=fft(wiggles(:,ii));
end

for ii=1:nrows
    ffshot(ii,:)=fft(fshot(ii,:));
end

k=1/dx;
f=1/dt;

imagesc(k:-k/ncols:k/ncols,f/nrows:f/nrows:f,log(abs(ffshot)));

end
```

D.4 FilePrep

```
function [Lseed tune J]=FilePrep(dP,seed)

%FilePrep converts matrices to a form suitable for Jacob.m and LoveInv.m.
%The matrix seed must be in a format with frequency in column 1,
%and either dispersion or attenuation information in the remaining columns.
%The first row of each data column should identify the column as either
%containing velocity (1) or attenuation (2) information.  FilePrep.m
%ignores entries of zero.  FilePrep.m may be used to prepare either data
%matrices containing real velocities, or predictor files containing complex
%velocities.
%dP is an m x 4 matrix of delta layer properties used to calculate the
%Jacobian.  The entries should correspond, exactly, to those in the layer
%properties matrix.  For properties not used in a model, enter zero.
%tune is a default tuning matrix that can be used to optimize the operation
%of Jacob.m.  The first three colums of tune are intended to help the user
%navigate, and not used by any subsequent operation.  Cols 1,2,3 are the
%frequency, col.row of the seed entry, and the vel/attenuation
%flag from row 1.  Columns 4 through 8 are default values that can be
%changed in order to stabilize values of the Jacobian.  Typically, the
%values should be changed to 1/10th of their default values if data
%corresponds to a cut-off frequency.

%J is a blank input file for Jacob.m.

[lrows lcols]=size(dP);
[srows scols]=size(seed);
Lseed=zeros(1,4);
tune=zeros(1,8);
kk=0;

%default values of tuning matrix
tx=10;
ty=10;
xi=0.1;
yi=0.1;
```

```
%Determine number of cols in Jacobian
jcols=0;
for jj=1:lrows
    for kk=1:lcols
        if dP(jj,kk)~=0
            jcols=jcols+1;
        end

    end
end

%Transform seed into an n x 4 array containing frequency (row 1),
%complex velocity (row 2), a flag indicating whether this will be
%processed using dispersion (1) or attenuation (2) criteria, and an
%information column containing the corresponding row/column of seed_roots.
jrows=0;
for ii=2:scols
    for jj=2:srows
        f=seed(jj,1);
        cv=seed(jj,ii);
        flag=seed(1,ii);
        info=ii+jj/100;
        if cv ~= 0
            jrows=jrows+1;
            Lseed(jrows,:)=[f info flag cv];
            tune(jrows,:)=[f info flag 1 tx ty xi yi];

        end

    end
end

J=zeros(jrows,jcols);
end
```

D.5 Jacob

```
function J=Jacob(layer_props,Lseed,Jin,tune,dP)
%layer_props is an m x 4 matrix of layer properties
%Lseed is an m x 4 matrix containing frequency, a row/column
%identifier, a flag signaling whether the row should be treated as a
%dispersion curve (1) or as an attenuation curve (2), and complex
%velocity.
%dP is an m x 4 matrix of delta layer properties used to calculate the
%derivative (corresponds to layer_props).  A zero in a row/column of dP
%indicates that that property should not be used in the computation.


[usrows uscols]=size(Lseed);
[lrows lcols]=size(layer_props);
[jrows jcols]=size(Jin);
P=layer_props;
J=Jin;


for ii=1:usrows
    f=Lseed(ii,1);
    x=real(Lseed(ii,4));
    y=imag(Lseed(ii,4));
    flag=Lseed(ii,3);
    fact=tune(ii,4);
    tx=tune(ii,5);
    ty=tune(ii,6);
    xi=tune(ii,7);
    yi=tune(ii,8);

if flag==1
    %Calculates Jacobian for Dispersion Curves
    jcols=0;
    for jj=1:lrows
    for kk=1:lcols
        if dP(jj,kk)~=0
            jcols=jcols+1;
```

```
            PP=P;
            PM=P;
            PP(jj,kk)=P(jj,kk)+fact*dP(jj,kk);
            PM(jj,kk)=P(jj,kk)-fact*dP(jj,kk);
            A=FineRoot(f,PP,x,y,tx,ty,xi,yi);
            B=FineRoot(f,PM,x,y,tx,ty,xi,yi);
            Ca=(A(1,1)^2+A(2,1)^2)/A(1,1);
            Cb=(B(1,1)^2+B(2,1)^2)/B(1,1);
            J(ii,jcols)=(Ca-Cb)/(2*fact*dP(jj,kk));
        end

    end
    end
else
    %Calculates Jacobian for Attenuation Curves
    jcols=0;
    for jj=1:lrows
    for kk=1:lcols
        if dP(jj,kk)~=0
            jcols=jcols+1;
            PP=P;
            PM=P;
            PP(jj,kk)=P(jj,kk)+fact*dP(jj,kk);
            PM(jj,kk)=P(jj,kk)-fact*dP(jj,kk);
            A=FineRoot(f,PP,x,y,tx,ty,xi,yi);
            B=FineRoot(f,PM,x,y,tx,ty,xi,yi);
            Ca=2*pi*f*A(2,1)/(A(1,1)^2+A(2,1)^2);
            Cb=2*pi*f*B(2,1)/(B(1,1)^2+B(2,1)^2);
            J(ii,jcols)=(Ca-Cb)/(2*fact*dP(jj,kk));
        end

    end
    end

end
end
end
```

D.6 LoveInv

```
function [dm Covm]=LoveInv(Ldata,Lseed,J,W,Y,Covd)
%be sure that the data rows and unwrpt_seed rows correspond exacly to the
%Jacobian rows.
%W is an m x m Row Weighting Matrix, where m is the number of rows in
%data/J.
%Y is an n x n column weighting matrix, where n is the number of columns
% in the Jacobian.
%Cov is an n x n covariance matrix containing variances.  If covariance
%information is unknown, use a diagonal matrix with variance equal to the
%variances of the corresponding elements of the data vector.


[usrows uscols]=size(Lseed);
pred_data=zeros(usrows,1);
for ii=1:usrows
    rv=real(Lseed(ii,4));
    iv=imag(Lseed(ii,4));
    f=Lseed(ii,1);
    if Lseed(ii,3)==1
        Cl=(rv^2+iv^2)/rv;
        pred_data(ii,1)=Cl;
    else
        alpha=2*pi*f*iv/(rv^2+iv^2);
        pred_data(ii,1)=alpha;
    end

end

r=Ldata(:,4)-pred_data;

Q=W*J*Y;
H=Y*(Q'*Q)^-1*Q'*W;
dm=H*r;
Covm=H*Covd*H';

end
```